Simulation of Transient Blood Flow in Models of Arterial Stenosis and Aneurysm

Md. Abdul Hye

Simulation of Transient Blood Flow in Models of Arterial Stenosis and Aneurysm

A Thesis Submitted for the Degree
of

Doctor of Philosophy

in the
School of Engineering
of the
University of Glasgow

By

Md. Abdul Hye
BSc., MSc. & MPhil.

System, Power & Energy Research Division
School of Engineering
University of Glasgow
Glasgow, UK

October 26, 2012

This work is dedicated to
my parents.

Declaration

This dissertation is the result of my own work. No part of this dissertation has already been, or is being concurrently submitted for any other degree, diploma or qualification.

.....
Md. Abdul Hye
October 26, 2012

Abstract

The Large Eddy Simulation (LES) technique with the Smagorinsky-Lilly dynamic subgrid model and two-equation Standard k-ω Transitional turbulence model are applied to investigate non-spiral and spiral blood flow through three dimensional models of arterial stenosis and aneurysm. A spiral pattern of blood flow is thought to have many beneficial effects on hemodynamics. Previous computational studies on spiral blood flow involve only steady spiral flow in a straight stenosed pipe without considering an upstream curved section of the artery. But a spiral pattern in the blood flow may exist due to the presence of an upstream curved section in the artery. On the other hand, pressure is generally considered a constant quantity in studies on pulsatile flow through either arterial stenosis or aneurysm; however, blood pressure is a waveform in a physiological flow.

Although cosine-type or smooth regular stenoses are generally taken in investigations of blood flow in a three-dimensional model of arterial stenosis, in reality, stenoses are of irregular shape. Besides stenosis and aneurysm, another abnormal condition of the artery is the presence of stenosis with an adjacent aneurysm in the same arterial segment, especially in the posterior circulation. A study on (steady or pulsatile) flow through such arterial stenosis with an adjacent aneurysm in the same arterial segment is not available so far.

Therefore, taking above things into consideration, thorough investigations of steady and unsteady pulsatile non-spiral and spiral blood flow in three-dimensional models of stenosis and aneurysm are needed to give a sound understanding of the transition-to-turbulence of blood flow due to stenosis and aneurysm and to study the the effects of spiral velocity on the transition-to-turbulence.

The LES technique has mostly been used to investigate turbulent flow in engineering fields other than bio-fluid mechanics. In the last decade, LES has seen its excellent potential for studying the transition-to-turbulence of physiological flow in bio-fluid mechanics. Though the k-ω Transitional model is used in few instances, mainly LES is applied in this study.

Firstly, investigations of steady non-spiral and spiral blood flow through three-dimensional models of cosine-type regular stenosed tube without and with upstream curved segment of varying angles of curvature are performed by using the k-ω Transitional model and LES. A fully developed Poiseuille velocity profile for blood is introduced at the inlets of the models. To introduce a spiral effect at the inlet, one-sixth of the bulk velocity is taken as the tangential velocity at the inlet along with the axial velocity profile there.

Secondly, physiological pulsatile non-spiral and spiral blood flow through a three-dimensional model of a straight tube having cosine-type regular stenosis are

investigated by using mainly LES. A two-equation k-ω Transitional model is also used in one non-spiral flow case. The first four harmonics of the Fourier series of pressure pulse are used to generate physiological velocity profiles at the inlet. At the outlet, a pressure waveform is introduced. The effects of percentage of area reduction in the stenosis, length of the stenosis, amplitude of pulsation and Womersley number are also examined.

Thirdly, transient pulsatile non-spiral and spiral blood flow through a three-dimensional model of irregular stenosis are investigated by applying LES and comparison is drawn between non-spiral flow through a regular stenosis and that through an irregular stenosis.

Lastly, pulsatile non-spiral and spiral blood flow through a three-dimensional model of irregular stenosis with an adjacent post-stenotic irregular aneurysm in the same arterial segment are studied by applying LES and the k-ω Transitional model. The effects of variation in spiral velocity are also examined.

The results presented in this thesis are analysed with relevant pathophysioloical consequences. In steady flow through the straight stenosed tube, excellent agreement between LES results for $Re = 1000$ and 2000 and the corresponding experimental results are found when the appropriate inlet perturbations are introduced. In the models with an upstream curved segment, no significant effect of spiral flow on any flow property is found for the investigated Reynolds numbers; spiral pattern disappears before the stenosis – which may be due the rigid wall used in the models and/or a steady flow at the inlet. The effects of the curved upstream model can be seen mainly in the maximum turbulent kinetic energy (TKE), the maximum pressure drop and the maximum wall shear stress (WSS), which in the curved upstream models generally increase significantly compared with the corresponding results in the straight stenosed tube.

The maximum contributions of the SGS motion to the large-scale motion in both non-spiral and spiral flow through a regular stenosis, an irregular stenosis and an irregular stenosis with an adjacent post-stenotic irregular aneurysm are 50%, 55% and 25%, respectively, for the highest Reynolds number investigated in each model. Although the wall pressure and shear stress obtained from the k-ω Transitional model agree quite well with the corresponding LES results, the turbulent results obtained from the k-ω Transitional model differ significantly from the corresponding LES results – this shows unsuitability of the k-ω model for pulsatile flow simulation. Large permanent recirculation regions are observed right after the stenosis throat in both non-spiral and spiral flow, which in the model of a stenosis with an adjacent post-stenotic aneurysm are stretched beyond the aneurysm and the length of the recirculation regions increases with spiral velocity. This study shows that, in both steady and unsteady pulsatile flow through the straight tube model having either a stenosis (regular or irregular) or an irregular stenosis with an adjacent post-stenotic irregular aneurysm, the TKE rises significantly at some locations and phases if a

spiral effect is introduced at the inlet of the model. However, the maximum value of the TKE in a high spiral flow drops considerably compared with that in a low spiral flow. The maximum wall pressure drop and shear stress occur around the stenosis throat during all the phases of the pulsatile cycle. In the model of a stenosis only, the wall pressure rises in the immediate post-stenotic region after its drop at the stenosis throat. However, in the model of a stenosis with an adjacent aneurysm, the wall pressure does not rise to regain its undisturbed value before the start of the last quarter of the aneurysm. The effects of the spiral flow on the wall pressure and WSS are visible only in the downstream region where they take oscillatory pattern. The break frequencies of energy spectra for velocity and pressure fluctuations from $-5/3$ power slope to $-10/3$ power slope and $-7/3$ power slope, respectively, are observed in the downstream transition-to-turbulence region in both the non-spiral and spiral flow. At some locations in the transition region, the velocity spectra in the spiral flow has larger inertial subrange region than that in non-spiral flow. The effects of the spiral flow on the pressure spectra is insignificant. Also, the maximum wall pressure drop, the maximum WSS and the maximum TKE in the non-spiral flow through the irregular stenosis rise significantly compared with the corresponding results in the non-spiral flow through the regular stenosis.

When the area reduction in the stenosis is increased, the maximum pressure drop, the maximum WSS and the TKE rise sharply. As for the effects of the length of the stenosis, the maximum WSS falls significantly and the maximum TKE rises sharply due to the increase in the length of the stenosis; but the maximum pressure drop is almost unaffected by the increase in the stenosis length. The increase in the amplitude of pulsation causes both the maximum pressure drop and the maximum WSS to increase significantly under the inlet peak flow condition. While the increased amplitude of pulsation decrease the maximum TKE, it is nonetheless responsible for the sharp rise in the TKE found at some places in the transition-to-turbulence region. The decrease in the Womersley number causes the maximum TKE to increase dramatically; however, the maximum pressure drop and the maximum WSS decrease slightly under the inlet peak flow condition as a result of the decrease in the Womersley number.

The author does believe that the present study makes a breakthrough in understanding the non-spiral and spiral transient blood flows through arteries having a stenosis and a stenosis with an adjacent post-stenotic aneurysm. The findings of the thesis would, therefore, help the interested groups such as pathologists, medical surgeons and researchers greatly in gaining better insight into the transient non-spiral and spiral blood flow through models of arterial stenosis and aneurysm.

Acknowledgements

All the praises be to Allah, the Most Beneficent, the Most Merciful. I would like to express my gratitude to my supervisor, Dr Manosh C. Paul, for all his guidance, support and encouragement during this research. His stimulating comments and suggestions have been of immense benefit to me.

The financial support of ORSAS and the school of Engineering of the University of Glasgow for this study is gratefully appreciated. I'm also grateful to Shahjalal University of Science and Technology, Sylhet, Bangladesh, for granting me study leave with pay.

Grateful thanks are due to the members of IT Support Team of School of Engineering, especially Mr Walter Robinson and Mr Ken McColl for their constant effort to keep the system always running and help in fixing any problems in the computer systems.

I would like to express my sincere thanks to all the friends and colleagues, Dr Md Mamun Molla, Mr Md Foyzul Haque, Mr Najeeb Yahya, Mr Ahmed Mahboob Ferdousi, Prof Syed Shamsul Alam, Dr Rizaul Islam, Mr Rafiqul Islam, Dr Bala Boyi Bukata, Mr Ali Saad Alzwayi, Mr Blaid Alganash and Mr Ahmed Al Waaly. Their spirited support and encouragement has been of great help to me throughout the relentless endurance test of my PhD.

I am deeply indebted to my beloved parents, wife, son, siblings, maternal aunt and mother-in-law. I owe you all much more than I can possibly express. I am also grateful to all of my well-wishers for their invaluable advice and support that has helped me greatly to make it this far.

Contents

List of Figures **v**

List of Tables **xxiv**

1 Introduction **1**

2 Review of Previous Works **4**

2.1 Experimental Works on Stenosis 4

2.1.1 Post-stenotic Flow Characteristics 4

2.1.2 Pathophysiological Implications 7

2.1.3 Turbulence Energy Spectra 8

2.2 Computational Investigations on Stenosis 10

2.2.1 Laminar Flow 10

2.2.2 Turbulent Flow 13

2.3 Previous Works on Aneurysm 15

2.3.1 Experimental Works 15

2.3.2 Computational Works 16

2.4 Spiral Blood Flow in Stenosis 17

2.5 Objectives of the Project 18

2.6 Thesis Outline 20

3 Numerical Methods **22**

3.1 Governing Equations 22

3.2 Standard k-ω Transitional Model 23

3.3 Shear-Stress Transport (SST) k-ω (or k-ω-SST) model 25

3.4 Large Eddy Simulation 27

3.4.1 Filtered Governing Equations 27

3.4.2 Smagorinsky-Lilly Subgrid-scale Model 28

3.4.3 Dynamic Smagorinsky-Lilly Subgrid-scale Model 29

3.5 Boundary Conditions 30
3.5.1 Velocity Inlet 30
3.5.2 Wall 30
3.5.3 Pressure Outlet 31
3.6 Overview of Numerical Procedures 31
3.7 Data Processing and Flow Statistics 32

4 A Computational Study on Spiral Blood Flow in Stenosed Arteries with and without an Upstream Curved Section 35
4.1 Introduction 35
4.2 Flow Models and Meshing 36
4.3 Inflow Boundary Condition 38
4.4 Validation with Experiment 39
4.5 Results and Discussion 40
4.5.1 Flow Visualization 41
4.5.2 Flow Velocity 43
4.5.3 Turbulent Kinetic Energy (TKE) 44
4.5.4 Wall Pressure and Shear Stress 45
4.5.5 Summary of the other models 46
4.6 Conclusion 48

5 Simulation of Physiological Pulsatile Non-spiral and Spiral Blood Flow in a Regular Arterial Stenosis 84
5.1 Introduction 84
5.2 Problem Formulation 85
5.2.1 Physiological Inlet and Outlet Conditions and Computational Parameters 85
5.3 Grid Independence and Simulation Details 89
5.4 Results and Discussion 90
5.4.1 Contribution of the SGS Model 90
5.4.2 Instantaneous Flow Field 91
5.4.3 Phase-averaged Flow Characteristics 95
5.4.4 Turbulent Characteristics 96
5.4.5 Turbulent Energy Spectra 99

5.4.6 Effects of Percentage and Length of the Stenosis 101
5.4.7 Effects of amplitude of pulsation and Womersley number . . 103
5.5 Conclusion 104

6 LES of Physiological Pulsatile Non-spiral and Spiral Blood Flow through a Model of Irregular Arterial Stenosis 134
6.1 Introduction 134
6.2 Problem Formulation 135
6.2.1 Model Geometry and Mesh arrangement 135
6.2.2 Governing Equations and Boundary Conditions 136
6.3 Results and Discussion 136
6.3.1 Grid Resolution Study 136
6.3.2 Contributions of the SGS Dynamic Model 137
6.3.3 Instantaneous Flow Physics 138
6.3.4 Phase-averaged Flow Characteristics 143
6.3.5 Turbulent Characteristics 144
6.4 Conclusion 148

7 Physiological Pulsatile Non-spiral and Spiral Flow in a Model of a Stenosis with an Adjacent Aneurysm in Basilar Artery 168
7.1 Introduction 168
7.2 Problem Formulation 169
7.2.1 Model Geometry and Mesh arrangement 169
7.2.2 Boundary Conditions 171
7.3 Results and Discussion 171
7.3.1 Grid Resolution Study 171
7.3.2 Contributions of the SGS Dynamic Model 172
7.3.3 Instantaneous Flow Field 172
7.3.4 Phase-averaged Flow Characteristics 178
7.3.5 Turbulent characteristics 179
7.4 Conclusion 182

8 Conclusions and Suggestions for Future Research 200
8.1 Conclusions 200

8.2 Future Research 204

References **206**

List of Figures

4.1 Three dimensional view of model arteries without and with an upstream curved section of varying angles of curvature. Angles of curvature in frame (a), (b), (c) and (d), are $0°$, $60°$, $90°$ and $120°$, respectively. 50

4.2 Axial velocity comparison with the experimental data of Ahmed and Giddens [28] for non-spiral flow in model $B1$ at (a) $z/D = 0$, (b) $z/D = 1$, (c) $z/D = 2.5$, (d)$z/D = 4$, (e) $z/D = 5$ and (f) $z/D = 6$. 51

4.3 Axial velocity comparison with the experimental data of Ahmed and Giddens [27] for non-spiral flow in model $D1$ at (a) $z/D = 0$, (b) $z/D = 1$, (c) $z/D = 2.5$, (d)$z/D = 4$, (e) $z/D = 5$ and (f) $z/D = 6$. 51

4.4 Grid resolution study for LES of spiral flow in model $D1$ showing axial velocity at (a) $z/D = 0$, (b) $z/D = 1$, (c) $z/D = 2.5$, (d)$z/D = 4$, (e) $z/D = 5$ and (f) $z/D = 6$. 52

4.5 Grid resolution study for spiral flow in model $D3$ with $k - \omega$ Transitional approach showing axial velocity at (a) $z/D = 0$, (b) $z/D = 1$, (c) $z/D = 2.5$, (d)$z/D = 4$, (e) $z/D = 5$ and (f) $z/D = 6$. 52

4.6 Cross-sectional streamlines appended on the axial velocity contour for non-spiral flow in model $D1$ at (a) $z/D = -3$, (b) $z/D = -1$, (c) $z/D = 0$, (d) $z/D = 1$, (e) $z/D = 2$, (f) $z/D = 3$, (g) $z/D = 4$, (h) $z/D = 5$, (i) $z/D = 6$, (j) $z/D = 7$, (k) $z/D = 8$, (l) $z/D = 9$, (m) $z/D = 10$, (n) $z/D = 12$, (o) $z/D = 16$ and (p) $z/D = 22$. . . 53

4.7 Cross-sectional streamlines appended on the axial velocity contour for spiral flow in model $D1$ at (a) $z/D = -3$, (b) $z/D = -1$, (c) $z/D = 0$, (d) $z/D = 1$, (e) $z/D = 2$, (f) $z/D = 3$, (g) $z/D = 4$, (h) $z/D = 5$, (i) $z/D = 6$, (j) $z/D = 7$, (k) $z/D = 8$, (l) $z/D = 9$, (m) $z/D = 10$, (n) $z/D = 12$, (o) $z/D = 16$ and (p) $z/D = 22$. . . 54

4.8 Cross-sectional streamlines appended on the axial velocity contour for non-spiral flow in model $D3$ at (a) $z/D = -3$, (b) $z/D = -1$, (c) $z/D = 0$, (d) $z/D = 1$, (e) $z/D = 2$, (f) $z/D = 3$, (g) $z/D = 4$, (h) $z/D = 5$, (i) $z/D = 6$, (j) $z/D = 7$, (k) $z/D = 8$, (l) $z/D = 9$, (m) $z/D = 10$, (n) $z/D = 12$, (o) $z/D = 16$ and (p) $z/D = 22$. . . 55

4.9 Cross-sectional streamlines appended on the axial velocity contour for spiral flow in model $D3$ at (a) $z/D = -3$, (b) $z/D = -1$, (c) $z/D = 0$, (d) $z/D = 1$, (e) $z/D = 2$, (f) $z/D = 3$, (g) $z/D = 4$, (h) $z/D = 5$, (i) $z/D = 6$, (j) $z/D = 7$, (k) $z/D = 8$, (l) $z/D = 9$, (m) $z/D = 10$, (n) $z/D = 12$, (o) $z/D = 16$ and (p) $z/D = 22$. . . 56

4.10 Cross-sectional streamlines appended on the axial velocity contour for non-spiral flow in model $D2$ at (a) $z/D = -3$, (b) $z/D = -1$, (c) $z/D = 0$, (d) $z/D = 1$, (e) $z/D = 2$, (f) $z/D = 3$, (g) $z/D = 4$, (h) $z/D = 5$, (i) $z/D = 6$, (j) $z/D = 7$, (k) $z/D = 8$, (l) $z/D = 9$, (m) $z/D = 10$, (n) $z/D = 12$, (o) $z/D = 16$ and (p) $z/D = 22$. . . 57

4.11 Cross-sectional streamlines appended on the axial velocity contour for spiral flow in model $D2$ at (a) $z/D = -3$, (b) $z/D = -1$, (c) $z/D = 0$, (d) $z/D = 1$, (e) $z/D = 2$, (f) $z/D = 3$, (g) $z/D = 4$, (h) $z/D = 5$, (i) $z/D = 6$, (j) $z/D = 7$, (k) $z/D = 8$, (l) $z/D = 9$, (m) $z/D = 10$, (n) $z/D = 12$, (o) $z/D = 16$ and (p) $z/D = 22$. . . 58

4.12 Cross-sectional streamlines appended on the axial velocity contour for non-spiral flow in model $D4$ at (a) $z/D = -3$, (b) $z/D = -1$, (c) $z/D = 0$, (d) $z/D = 1$, (e) $z/D = 2$, (f) $z/D = 3$, (g) $z/D = 4$, (h) $z/D = 5$, (i) $z/D = 6$, (j) $z/D = 7$, (k) $z/D = 8$, (l) $z/D = 9$, (m) $z/D = 10$, (n) $z/D = 12$, (o) $z/D = 16$ and (p) $z/D = 22$. . . 59

4.13 Cross-sectional streamlines appended on the axial velocity contour for spiral flow in model $D4$ at (a) $z/D = -3$, (b) $z/D = -1$, (c) $z/D = 0$, (d) $z/D = 1$, (e) $z/D = 2$, (f) $z/D = 3$, (g) $z/D = 4$, (h) $z/D = 5$, (i) $z/D = 6$, (j) $z/D = 7$, (k) $z/D = 8$, (l) $z/D = 9$, (m) $z/D = 10$, (n) $z/D = 12$, (o) $z/D = 16$ and (p) $z/D = 22$. . . 60
4.14 Pathlines, coloured by the particle ID, for spiral flow in model $D2$. 61
4.15 contour plots of tangential velocity for non-spiral flow in model $D1$ at (a) $z/D = -3$, (b) $z/D = -1$, (c) $z/D = 0$, (d) $z/D = 1$, (e) $z/D = 2$, (f) $z/D = 3$, (g) $z/D = 4$, (h) $z/D = 5$, (i) $z/D = 6$, (j) $z/D = 7$, (k) $z/D = 8$, (l) $z/D = 9$, (m) $z/D = 10$, (n) $z/D = 12$, (o) $z/D = 16$ and (p) $z/D = 22$. 62
4.16 contour plots of tangential velocity for spiral flow in model $D1$ at (a) $z/D = -3$, (b) $z/D = -1$, (c) $z/D = 0$, (d) $z/D = 1$, (e) $z/D = 2$, (f) $z/D = 3$, (g) $z/D = 4$, (h) $z/D = 5$, (i) $z/D = 6$, (j) $z/D = 7$, (k) $z/D = 8$, (l) $z/D = 9$, (m) $z/D = 10$, (n) $z/D = 12$, (o) $z/D = 16$ and (p) $z/D = 22$. 63
4.17 Contour plots of tangential velocity for non-spiral flow in model $D2$ at (a) $z/D = -3$, (b) $z/D = -1$, (c) $z/D = 0$, (d) $z/D = 1$, (e) $z/D = 2$, (f) $z/D = 3$, (g) $z/D = 4$, (h) $z/D = 5$, (i) $z/D = 6$, (j) $z/D = 7$, (k) $z/D = 8$, (l) $z/D = 9$, (m) $z/D = 10$, (n) $z/D = 12$, (o) $z/D = 16$ and (p) $z/D = 22$. 64
4.18 contour plots of tangential velocity for spiral flow in model $D2$ at (a) $z/D = -3$, (b) $z/D = -1$, (c) $z/D = 0$, (d) $z/D = 1$, (e) $z/D = 2$, (f) $z/D = 3$, (g) $z/D = 4$, (h) $z/D = 5$, (i) $z/D = 6$, (j) $z/D = 7$, (k) $z/D = 8$, (l) $z/D = 9$, (m) $z/D = 10$, (n) $z/D = 12$, (o) $z/D = 16$ and (p) $z/D = 22$. 65
4.19 Contour plots of tangential velocity for non-spiral flow in model $D3$ at (a) $z/D = -3$, (b) $z/D = -1$, (c) $z/D = 0$, (d) $z/D = 1$, (e) $z/D = 2$, (f) $z/D = 3$, (g) $z/D = 4$, (h) $z/D = 5$, (i) $z/D = 6$, (j) $z/D = 7$, (k) $z/D = 8$, (l) $z/D = 9$, (m) $z/D = 10$, (n) $z/D = 12$, (o) $z/D = 16$ and (p) $z/D = 22$. 66

4.20 contour plots of tangential velocity for spiral flow in model $D3$ at (a) $z/D = -3$, (b) $z/D = -1$, (c) $z/D = 0$, (d) $z/D = 1$, (e) $z/D = 2$, (f) $z/D = 3$, (g) $z/D = 4$, (h) $z/D = 5$, (i) $z/D = 6$, (j) $z/D = 7$, (k) $z/D = 8$, (l) $z/D = 9$, (m) $z/D = 10$, (n) $z/D = 12$, (o) $z/D = 16$ and (p) $z/D = 22$. 67

4.21 Contour plots of tangential velocity for non-spiral flow in model $D4$ at (a) $z/D = -3$, (b) $z/D = -1$, (c) $z/D = 0$, (d) $z/D = 1$, (e) $z/D = 2$, (f) $z/D = 3$, (g) $z/D = 4$, (h) $z/D = 5$, (i) $z/D = 6$, (j) $z/D = 7$, (k) $z/D = 8$, (l) $z/D = 9$, (m) $z/D = 10$, (n) $z/D = 12$, (o) $z/D = 16$ and (p) $z/D = 22$. 68

4.22 contour plots of tangential velocity for spiral flow in model $D4$ at (a) $z/D = -3$, (b) $z/D = -1$, (c) $z/D = 0$, (d) $z/D = 1$, (e) $z/D = 2$, (f) $z/D = 3$, (g) $z/D = 4$, (h) $z/D = 5$, (i) $z/D = 6$, (j) $z/D = 7$, (k) $z/D = 8$, (l) $z/D = 9$, (m) $z/D = 10$, (n) $z/D = 12$, (o) $z/D = 16$ and (p) $z/D = 22$. 69

4.23 Mean axial velocity, $\langle w \rangle$, profiles for both non-spiral and spiral flow in model $D1$ at (a) $z/D = -1$, (b) $z/D = 0$, (c) $z/D = 1$, (d) $z/D = 2$, (e) $z/D = 3$, (f) $z/D = 4$, (g) $z/D = 5$, (h) $z/D = 6$, (i) $z/D = 7$, (j) $z/D = 8$, (k) $z/D = 9$, (l) $z/D = 10$, (m) $z/D = 12$, (n) $z/D = 16$ and (o) $z/D = 22$. Note that LES was also applied to this model. 70

4.24 Mean axial velocity, $\langle w \rangle$, profiles for both non-spiral and spiral flow in models $D2$, $D3$ and $D4$ at (a) $z/D = -1$, (b) $z/D = 0$, (c) $z/D = 1$, (d) $z/D = 2$, (e) $z/D = 3$, (f) $z/D = 4$, (g) $z/D = 5$, (h) $z/D = 6$, (i) $z/D = 7$, (j) $z/D = 8$, (k) $z/D = 9$, (l) $z/D = 10$, (m) $z/D = 12$, (n) $z/D = 16$ and (o) $z/D = 22$. 71

4.25 Mean x-velocity, $\langle u \rangle$, profiles for both non-spiral and spiral flow in model $D1$ at (a) $z/D = -1$, (b) $z/D = 0$, (c) $z/D = 1$, (d) $z/D = 2$, (e) $z/D = 3$, (f) $z/D = 4$, (g) $z/D = 5$, (h) $z/D = 6$, (i) $z/D = 7$, (j) $z/D = 8$, (k) $z/D = 9$, (l) $z/D = 10$, (m) $z/D = 12$, (n) $z/D = 16$ and (o) $z/D = 22$. Note that LES was also applied to this model. 72

4.26 Mean x-velocity, $\langle u \rangle$, profiles for both non-spiral and spiral flow in models $D2$, $D3$ and $D4$ at (a) $z/D = -1$, (b) $z/D = 0$, (c) $z/D = 1$, (d) $z/D = 2$, (e) $z/D = 3$, (f) $z/D = 4$, (g) $z/D = 5$, (h) $z/D = 6$, (i) $z/D = 7$, (j) $z/D = 8$, (k) $z/D = 9$, (l) $z/D = 10$, (m) $z/D = 12$, (n) $z/D = 16$ and (o) $z/D = 22$. 73

4.27 Mean y-velocity, $\langle v \rangle$, profiles for both non-spiral and spiral flow in model $D1$ at (a) $z/D = -1$, (b) $z/D = 0$, (c) $z/D = 1$, (d) $z/D = 2$, (e) $z/D = 3$, (f) $z/D = 4$, (g) $z/D = 5$, (h) $z/D = 6$, (i) $z/D = 7$, (j) $z/D = 8$, (k) $z/D = 9$, (l) $z/D = 10$, (m) $z/D = 12$, (n) $z/D = 16$ and (o)$z/D = 22$. Note that LES was also applied to this model. 74

4.28 Mean y-velocity, $\langle v \rangle$, profiles for both non-spiral and spiral flow in models $D2$, $D3$ and $D4$ at (a) $z/D = -1$, (b) $z/D = 0$, (c) $z/D = 1$, (d) $z/D = 2$, (e) $z/D = 3$, (f) $z/D = 4$, (g) $z/D = 5$, (h) $z/D = 6$, (i) $z/D = 7$, (j) $z/D = 8$, (k) $z/D = 9$, (l) $z/D = 10$, (m) $z/D = 12$, (n) $z/D = 16$ and (o)$z/D = 22$. 75

4.29 Turbulent kinetic energy, k (m^2/s^2), for both non-spiral and spiral flow in model $D1$ at (a) $z/D = -1$, (b) $z/D = 0$, (c) $z/D = 1$, (d) $z/D = 2$, (e) $z/D = 3$, (f) $z/D = 4$, (g) $z/D = 5$, (h) $z/D = 6$, (i) $z/D = 7$, (j) $z/D = 8$, (k) $z/D = 9$, (l) $z/D = 10$, (m) $z/D = 12$, (n) $z/D = 16$ and (o)$z/D = 22$. Note that LES was also applied to this model. 76

4.30 Turbulent kinetic energy, k (m^2/s^2), for both non-spiral and spiral flow in models $D2$, $D3$ and $D4$ at (a) $z/D = -1$, (b) $z/D = 0$, (c) $z/D = 1$, (d) $z/D = 2$, (e) $z/D = 3$, (f) $z/D = 4$, (g) $z/D = 5$, (h) $z/D = 6$, (i) $z/D = 7$, (j) $z/D = 8$, (k) $z/D = 9$, (l) $z/D = 10$, (m) $z/D = 12$, (n) $z/D = 16$ and (o)$z/D = 22$. 77

4.31 Circumferential average wall pressure (Pa) for both non-spiral and spiral flow in model $D1$. Note that LES was also applied to this model. 78

4.32 Circumferential average wall pressure (Pa) for both non-spiral and spiral flow in models $D2$, $D3$ and $D4$. 78

4.33 Circumferential average wall shear stress, τ (Pa), for both non-spiral and spiral flow in model $D1$. Note that LES was also applied to this model. 79
4.34 Circumferential average wall shear stress, τ (Pa), for both non-spiral and spiral flow in models $D2$, $D3$ and $D4$. 79
4.35 Bar chart of maximum turbulent kinetic energy for both non-spiral and spiral flow in all models for (a) $Re = 500$, (b) $Re = 1000$, (c) $Re = 1500$ and (d) 2000. 80
4.36 Contour plot of TKE, k (m^2/s^2), in model $A1$ for (a) non-spiral flow and (b) spiral flow. 81
4.37 Wall shear stress (Pa) at different phases of the wall in model $A1$ for both non-spiral and spiral flow. 81
4.38 Bar chart of maximum pressure drop for both non-spiral and spiral flow in all models for (a) $Re = 500$, (b) $Re = 1000$, (c) $Re = 1500$ and (d) 2000. 82
4.39 Bar chart of maximum wall shear stress for both non-spiral and spiral flow in all models for (a) $Re = 500$, (b) $Re = 1000$, (c) $Re = 1500$ and (d) 2000. 83

5.1 Inlet physiological 4th harmonic pulsatile velocity profiles, $\bar{w}$ (m/s), for a time cycle (a) at the centre of the tube, (b) at different locations between the wall and the centre, (c) bulk velocity profile and (d) during different phases of a time cycle while $A = 0.40$, $Re = 876$ and the Womersley parameter $\alpha = 17.3$. Reference phases at which results are obtained are also marked. 107
5.2 Outlet physiological 4th harmonic pulsatile pressure profiles, $\bar{p}$ (mmHg), for a time cycle while $A = 0.40$, $Re = 876$ and the Womersley parameter $\alpha = 17.3$. (1 mmHg= 133.32 Pa.) 107
5.3 Grid resolution study for phase-averaged streamwise velocity, $\langle\langle \bar{w} \rangle\rangle$ (m/s), in non-spiral flow during phase $P3$ at different indicated axial locations while $A = 0.67$, $Re = 741$ and the Womersley parameter $\alpha = 17.3$. 108

5.4 Grid resolution study for phase-averaged axial wall shear stress (Pa) in non-spiral flow during phase $P3$ while $A = 0.67$, $Re = 741$ and the Womersley parameter $\alpha = 17.3$. Phase averaging was done on the circumferential average WSS. 108

5.5 Time-step resolution study for phase-averaged streamwise velocity, $\langle\langle\bar{w}\rangle\rangle$ (m/s), in non-spiral flow during phase $P3$ at different indicated axial locations while $A = 0.67$, $Re = 741$ and the Womersley parameter $\alpha = 17.3$. 109

5.6 Time-step resolution study for phase-averaged axial wall shear stress (Pa) in non-spiral flow during phase $P3$ while $A = 0.67$, $Re = 741$ and the Womersley parameter $\alpha = 17.3$. Phase averaging was done on the circumferential average WSS. 109

5.7 Streamwise velocity, $\bar{w}$, in non-spiral flow during phase $P2$ of the first eight cycles i.e. (a) $t/T \approx 0.223$, (b) $t/T \approx 1.223$, (c) $t/T \approx 2.223$, (d) $t/T \approx 3.223$, (e) $t/T \approx 4.223$, (f) $t/T \approx 5.223$, (g) $t/T \approx 6.223$ and (h) $t/T \approx 7.223$ while $Re = 876$, $A = 0.40$ and the Womersley parameter $\alpha = 17.3$. 110

5.8 Time history of rms of centreline streamwise velocity fluctuations, $\langle w'' \rangle_{rms}$ (m/s), at different axial locations for both non-spiral and spiral pulsatile flow while $Re = 876$. The red coloured solid line denotes velocity fluctuations for non-spiral flow while the green coloured dashed line corresponds to velocity fluctuations for spiral flow. 111

5.9 Dynamic Smagorinsky constant, C_s, in non-spiral flow during phase $P3$ for (a) $Re = 438$, (b) $Re = 584$ and (c) $Re = 876$ while $A = 0.40$ and the Womersley parameter $\alpha = 17.3$. 112

5.10 Normalised SGS eddy viscosity, μ_{sgs}/μ, in non-spiral flow during phase $P3$ for (a) $Re = 438$, (b) $Re = 584$ and (c) $Re = 876$ while $A = 0.40$ and the Womersley parameter $\alpha = 17.3$. 112

5.11 Instantaneous y-vorticity, Ω_y $(1/s)$, in non-spiral flow at different phases of the last cycle (a) $P1$, (b) $P2$, (c) $P3$, (d) $P4$, (e) $P5$, (f) $P6$ and (g) $P7$ while $Re = 876$, $A = 0.40$ and the Womersley parameter $\alpha = 17.3$. 113

5.12 Instantaneous y-vorticity, $\Omega_y\ (1/s)$, in spiral flow at different phases of the last cycle (a) $P1$, (b) $P2$, (c) $P3$, (d) $P4$, (e) $P5$, (f) $P6$ and (g) $P7$ while $Re = 876$, $A = 0.40$ and the Womersley parameter $\alpha = 17.3$. 114

5.13 Instantaneous y-vorticity, $\Omega_y\ (1/s)$, in non-spiral flow during phase $P3$ for (a) $Re = 438$, (b) $Re = 584$ and (c) $Re = 876$ while $A = 0.40$ and the Womersley parameter $\alpha = 17.3$. 115

5.14 Instantaneous y-vorticity, $\Omega_y\ (1/s)$, in spiral flow during phase $P3$ for (a) $Re = 438$, (b) $Re = 584$ and (c) $Re = 876$ while $A = 0.40$ and the Womersley parameter $\alpha = 17.3$. 115

5.15 Instantaneous cross-sectional vectors appended on the contours of streamwise velocity, $\bar{w}\ (m/s)$, in non-spiral flow during phase $P3$ at (a) $z/D = 0$, (b) $z/D = 1$, (c) $z/D = 2$, (d) $z/D = 3$, (e) $z/D = 4$, (f) $z/D = 5$, (g) $z/D = 6$ and (h) $z/D = 8$ while $Re = 876$, $A = 0.40$ and the Womersley parameter $\alpha = 17.3$. 116

5.16 Instantaneous cross-sectional vectors appended on the contours of streamwise velocity, $\bar{w}$ (m/s), in spiral flow during phase $P3$ at (a) $z/D = 0$, (b) $z/D = 1$, (c) $z/D = 2$, (d) $z/D = 3$, (e) $z/D = 4$, (f) $z/D = 5$, (g) $z/D = 6$ and (h) $z/D = 8$ while $Re = 876$, $A = 0.40$ and the Womersley parameter $\alpha = 17.3$. 116

5.17 Instantaneous mid-plane streamlines in non-spiral flow during phase $P3$ for (a) $Re = 438$, (b) $Re = 584$ and (c) $Re = 876$ while $A = 0.40$ and the Womersley parameter $\alpha = 17.3$. 117

5.18 Instantaneous mid-plane streamlines in spiral flow during phase $P3$ for (a) $Re = 438$, (b) $Re = 584$ and (c) $Re = 876$ while $A = 0.40$ and the Womersley parameter $\alpha = 17.3$. 117

5.19 Instantaneous wall pressure, $\bar{p}$ (Pa), in both non-spiral and spiral flow for the different Reynolds numbers during different phases of the last cycle at the two indicated circumferential locations. Note that the corresponding k-ω results for $Re = 438$ are also appended. . 118

5.20 Instantaneous wall shear stress (Pa) in both non-spiral and spiral flow for the different Reynolds numbers during different phases of the last cycle at the two indicated circumferential locations. Note that the corresponding k-ω results for $Re = 438$ are also appended. . 119
5.21 Phase-averaged streamwise velocity, $\langle\langle\bar{w}\rangle\rangle$ (m/s), in both non-spiral (NSp) and spiral flow for the different Reynolds numbers during phase $P3$ at different axial locations. Note that the corresponding k-ω results for $Re = 438$ are also appended. 120
5.22 Phase-averaged wall shear stress (Pa) in both non-spiral and spiral flow for the different Reynolds numbers during phase $P3$ at the two indicated circumferential locations. Note that the corresponding k-ω results for $Re = 438$ are also appended. 120
5.23 rms of the streamwise velocity fluctuations, $\langle w'' \rangle_{rms}$ (m/s), in both non-spiral and spiral flow for the different Reynolds numbers during phase $P3$ at different axial locations. Note that the corresponding k-ω results for $Re = 438$ are also appended. 121
5.24 Turbulent kinetic energy, $\frac{1}{2}\langle u_j'' u_j'' \rangle$ (m^2/s^2), for Reynolds number $Re = 438$ in both non-spiral (NSp) and spiral flow during phase $P3$ at different axial locations. Note that the corresponding k-ω results are also appended. 121
5.25 Turbulent kinetic energy, $\frac{1}{2}\langle u_j'' u_j'' \rangle$ (m^2/s^2), for Reynolds number $Re = 584$ in both non-spiral (NSp) and spiral flow during phase $P3$ at different axial locations. 122
5.26 Turbulent kinetic energy, $\frac{1}{2}\langle u_j'' u_j'' \rangle$ (m^2/s^2), for Reynolds number $Re = 876$ in both non-spiral (NSp) and spiral flow during phase $P3$ at different axial locations. 122
5.27 rms of wall pressure fluctuations, $\langle p'' \rangle_{rms}$ (Pa), in both non-spiral and spiral flow for the different Reynolds numbers during phase $P3$ at the two indicated circumferential locations. Note that the corresponding k-ω results for $Re = 438$ are also appended. 123

5.28 Time history of centreline streamwise velocity, $\bar{w}$ (m/s), at different indicated axial locations for both non-spiral and spiral pulsatile flow while $Re = 876$. The red coloured solid line denotes $\bar{w}$ for non-spiral flow while the green coloured dashed line corresponds to $\bar{w}$ for spiral flow. 124

5.29 Time history of wall (0° circumferential location) pressure gradient, $\frac{\partial p}{\partial z}$, at different indicated axial locations for both non-spiral and spiral pulsatile flow while $Re = 876$. The red coloured solid line denotes $\frac{\partial p}{\partial z}$ for non-spiral flow while the green coloured dashed line corresponds to $\frac{\partial p}{\partial z}$ for spiral flow. 125

5.30 Time history of the centreline velocity fluctuations, (a) u''/u''_{max}, (b) v''/v''_{max} and (c) w''/w''_{max} at different axial locations for both non-spiral and spiral pulsatile flow while $Re = 876$. The red coloured solid line denotes velocity fluctuations for non-spiral flow while the green coloured dashed line corresponds to velocity fluctuations for spiral flow. 126

5.31 Time history of centreline turbulent kinetic energy (TKE), $\frac{1}{2}\langle u''_j u''_j \rangle$ (m^2/s^2), at different indicated axial locations for both non-spiral and spiral pulsatile flow while $Re = 876$. The red coloured solid line denotes TKE for non-spiral flow while the green coloured dashed line corresponds to TKE for spiral flow. 127

5.32 Time history of wall (0° circumferential location) pressure fluctuations, p'' (Pa), at different indicated axial locations for both non-spiral and spiral pulsatile flow while $Re = 876$. The red coloured solid line denotes p'' for non-spiral flow while the green coloured dashed line corresponds to p'' for spiral flow. 128

5.33 Energy spectra of the centreline streamwise velocity fluctuations, w'', at different axial locations normalised by centreline $\langle w'' \rangle_{rms}$ at the same locations, for both non-spiral and spiral pulsatile flow while $Re = 876$. The red and the green coloured lines correspond to the energy spectra of velocity fluctuations for non-spiral and spiral flow, respectively. 129

5.34 Energy spectra of the wall pressure fluctuations, p'', at different axial locations normalised by wall $\langle p'' \rangle_{rms}$ at the same locations, for both non-spiral and spiral pulsatile flow while $Re = 876$. The red and the green coloured line corresponds to the energy spectra of wall pressure fluctuations for non-spiral and spiral flow, respectively. 130

5.35 Effects of different percentages and lengths of stenosis: instantaneous wall pressure, $\bar{p}$ (Pa), in non-spiral flow during phases $P2$ and $P3$ for (i) 75% stenosis and length$= 2D$ (solid line), (ii) 91% stenosis and length$= 2D$ (dashed line) and (iii) 91% stenosis and length$= 4D$ (dash-dotted line) while $Re = 876$ and $A = 0.40$. The circumferential positions at which wall pressure was obtained are marked 131

5.36 Effects of different percentages and lengths of stenosis: instantaneous wall shear stress (Pa) in non-spiral flow during phases $P2$ and $P3$ for (i) 75% stenosis and length$= 2D$ (solid line), (ii) 91% stenosis and length$= 2D$ (dashed line) and (iii) 91% stenosis and length$= 4D$ (dash-dotted line) while $Re = 876$ and $A = 0.40$. The circumferential positions at which WSS was recorded are marked . . 131

5.37 Effects of different percentages and lengths of stenosis: turbulent kinetic energy (TKE), $\frac{1}{2}\langle u_j'' u_j'' \rangle$ (m^2/s^2), in non-spiral flow during phase $P3$ at different indicated axial locations for (i) 75% stenosis and length$= 2D$ (solid line), (ii) 91% stenosis and length$= 2D$ (dashed line) and (iii) 91% stenosis and length$= 4D$ (dash-dotted line) while $Re = 876$ and $A = 0.40$. 132

5.38 Effects of Womersley parameter and amplitude of pulsation: instantaneous wall pressure, $\bar{p}$ (Pa), in non-spiral flow during phases $P2$ and $P3$ for (i) Womersley parameter, $\alpha = 17.3$, $Re = 876$ and $A = 0.40$ (solid line), (ii) $\alpha = 17.3$, $Re = 741$ and $A = 0.67$ (dashed line) and (iii) $\alpha = 15.5$, $Re = 741$ and $A = 0.67$ (dash-dotted line) while the peak Reynolds number is same in all three cases, i.e. $Re_{pk} = 2400$. The circumferential positions at which WSS was recorded are marked 132

5.39 Effects of Womersley parameter and amplitude of pulsation: instantaneous wall shear stress (Pa) in non-spiral flow during phases $P2$ and $P3$ for (i) Womersley parameter, $\alpha = 17.3$, $Re = 876$ and $A = 0.40$ (solid line), (ii) $\alpha = 17.3$, $Re = 741$ and $A = 0.67$ (dashed line) and (iii) $\alpha = 15.5$, $Re = 741$ and $A = 0.67$ (dash-dotted line) while the peak Reynolds number is same in all three cases, i.e. $Re_{pk} = 2400$. The circumferential positions at which WSS was recorded are marked 133

5.40 Effects of Womersley parameter and amplitude of pulsation: turbulent kinetic energy (TKE), $\frac{1}{2}\langle u_j'' u_j'' \rangle$ (m^2/s^2), in non-spiral flow during phase $P3$ at different indicated axial locations for (i) Womersley parameter, $\alpha = 17.3$, $Re = 876$ and $A = 0.40$ (solid line), (ii) $\alpha = 17.3$, $Re = 741$ and $A = 0.67$ (dashed line) and (iii) $\alpha = 15.5$, $Re = 741$ and $A = 0.67$ (dash-dotted line) while the peak Reynolds number is same in all three cases, i.e. $Re_{pk} = 2400$. . 133

6.1 Three dimensional view of model artery having irregular stenosis: (a) the whole domain and (b) zoomed-in section on irregular stenosis. 150

6.2 Grid resolution study for phase-averaged streamwise velocity, $\langle\langle \bar{w} \rangle\rangle$ (m/s), in non-spiral blood flow during phase $P3$ at different indicated axial locations while $Re = 876$. 150

6.3 Grid resolution study for phase-averaged axial wall shear stress (Pa) in non-spiral blood flow during phase $P3$ while $Re = 876$. Phase averaging was done on the circumferential average WSS. 151

6.4 Dynamic Smagorinsky constant, C_s, in non-spiral blood flow during phase $P3$ for (a) $Re = 438$ and (b) $Re = 584$ and (c) $Re = 876$. 151

6.5 Normalised SGS eddy viscosity, μ_{sgs}/μ, in non-spiral blood flow during phase $P3$ for (a) $Re = 438$ and (b) $Re = 584$ and (c) $Re = 876$. 151

6.6 Instantaneous y-vorticity, Ω_y (1/s), in non-spiral flow during phase $P3$ for (a) $Re = 438$, (b) $Re = 584$ and (c) $Re = 876$. The corresponding Ω_y in non-spiral flow through the regular stenosis for $Re = 876$ is also appended in frame (d). 152

6.7 Instantaneous y-vorticity, Ω_y (1/s), in spiral flow during phase $P3$ for (a) $Re = 438$, (b) $Re = 584$ and (c) $Re = 876$. The corresponding Ω_y in spiral flow through the regular stenosis for $Re = 876$ is also appended in frame (d). 152

6.8 Instantaneous mid-plane streamlines in non-spiral blood flow during phase $P3$ for (a) $Re = 438$, (b) $Re = 584$ and (c) $Re = 876$. Note that the corresponding streamlines in non-spiral flow through the regular cosine-type stenosis for $Re = 876$ are also appended in frame (d). 153

6.9 Instantaneous mid-plane streamlines in spiral blood flow during phase $P3$ for (a) $Re = 438$, (b) $Re = 584$ and (c) $Re = 876$. The corresponding streamlines in spiral flow through the regular stenosis for $Re = 876$ are also appended in frame (d). 153

6.10 Instantaneous cross-sectional vectors appended on the contours of the streamwise velocity, $\bar{w}$, in non-spiral flow during phase $P3$ at (a) $z/D = 0$, (b) $z/D = 1$, (c) $z/D = 2$, (d) $z/D = 3$, (e) $z/D = 4$, (f) $z/D = 5$, (g) $z/D = 6$ and (h) $z/D = 8$ while $Re = 876$. 154

6.11 Instantaneous cross-sectional vectors appended on the contours of the streamwise velocity, $\bar{w}$, in spiral flow during phase $P3$ at (a) $z/D = 0$, (b) $z/D = 1$, (c) $z/D = 2$, (d) $z/D = 3$, (e) $z/D = 4$, (f) $z/D = 5$, (g) $z/D = 6$ and (h) $z/D = 8$ while $Re = 876$. 154

6.12 Instantaneous wall pressure, $\bar{p}$ (Pa), in both non-spiral (NSp) and spiral flow for the different Reynolds numbers, namely $Re = 438$, 584 and 876, during different phases of the last cycle at the two indicated circumferential locations. Note that the corresponding wall pressures for $Re = 876$ in non-spiral flow through the regular stenosis are also appended. 155

6.13 Instantaneous wall shear stress (Pa) for $Re = 438$ in both non-spiral and spiral flow during different phases of the last cycle at the two indicated circumferential locations. Note that the corresponding wall shear stresses for $Re = 438$ in non-spiral flow through the regular stenosis are also appended. 156

6.14 Instantaneous wall shear stress (Pa) for $Re = 584$ in both non-spiral and spiral flow during different phases of the last cycle at the two indicated circumferential locations. The corresponding wall shear stresses for $Re = 584$ in non-spiral flow through the regular stenosis are also appended. 157

6.15 Instantaneous wall shear stress (Pa) for $Re = 876$ in both non-spiral and spiral flow during different phases of the last cycle at the two indicated circumferential locations. The corresponding wall shear stresses for $Re = 876$ in non-spiral flow through the regular stenosis are also appended. 158

6.16 Phase-averaged streamwise velocity, $\langle\langle \bar{w} \rangle\rangle$ (m/s), in both non-spiral (NSp) and spiral flow for the different Reynolds numbers, namely $Re = 438$, 584 and 876, during phase $P3$ at different axial locations. Note that the corresponding $\langle\langle \bar{w} \rangle\rangle$ in non-spiral flow through the regular stenosis for $Re = 876$ are also appended. 159

6.17 Phase-averaged wall shear stress (Pa) in both non-spiral and spiral flow during phase $P3$ at the two indicated circumferential locations for (a) $Re = 438$, (b) $Re = 584$ and (c)$Re = 876$. Note that the corresponding wall shear stresses in non-spiral flow through the regular stenosis for $Re = 438$, 584 and 876 are also appended in frame (a), (b) and c respectively. 160

6.18 rms of the streamwise velocity fluctuations, $\langle w'' \rangle_{rms}$ (m/s), in both non-spiral (NSp) and spiral flow for the different Reynolds numbers, namely $Re = 438$, 584 and 876, during phase $P3$ at different axial locations. Note that the corresponding $\langle w'' \rangle_{rms}$ for $Re = 876$ in non-spiral flow through the regular stenosis are also appended. . . 161

6.19 Turbulent kinetic energy, $\frac{1}{2}\langle u_j'' u_j'' \rangle$ (m^2/s^2), for Reynolds number $Re = 438$ in both non-spiral (NSp) and spiral flow during phase $P3$ at different axial locations. The corresponding $\frac{1}{2}\langle u_j'' u_j'' \rangle$ in non-spiral flow through the regular stenosis for $Re = 438$ are also appended. 161

6.20 Turbulent kinetic energy, $\frac{1}{2}\langle u_j'' u_j'' \rangle$ (m^2/s^2), for Reynolds number $Re = 584$ in both non-spiral (NSp) and spiral flow during phase $P3$ at different axial locations. The corresponding $\frac{1}{2}\langle u_j'' u_j'' \rangle$ in non-spiral flow through the regular stenosis for $Re = 584$ are also appended. 162

6.21 Turbulent kinetic energy, $\frac{1}{2}\langle u_j'' u_j'' \rangle$ (m^2/s^2), for Reynolds number $Re = 876$ in both non-spiral (NSp) and spiral flow during phase $P3$ at different axial locations. The corresponding $\frac{1}{2}\langle u_j'' u_j'' \rangle$ in non-spiral flow through the regular stenosis for $Re = 876$ are also appended. 162

6.22 rms of wall pressure fluctuations, $\langle p'' \rangle_{rms}$ (Pa), in both non-spiral and spiral flow for the different Reynolds numbers, namely $Re = 438$, 584 and 876, during phase $P3$ at the two indicated circumferential locations. The corresponding $\langle p'' \rangle_{rms}$ for $Re = 876$ in non-spiral flow through the regular stenosis are also appended. . . . 163

6.23 Time history of the centreline velocity fluctuations, (a) u''/u''_{max}, (b) v''/v''_{max} and (c) w''/w''_{max} at different axial locations for both non-spiral and spiral pulsatile blood flow while $Re = 876$. The red coloured solid line denotes velocity fluctuations for non-spiral flow while the green coloured dashed line corresponds to velocity fluctuations for spiral flow. 164

6.24 Time history of centreline turbulent kinetic energy (TKE), $\frac{1}{2}\langle u_j'' u_j'' \rangle$ (m^2/s^2), at different indicated axial locations for both non-spiral (red coloured dashed line) and spiral (green coloured dash-dot-dot line) pulsatile blood flow while $Re = 876$. Note that the corresponding $\frac{1}{2}\langle u_j'' u_j'' \rangle$ for $Re = 876$ in non-spiral flow through the regular stenosis (blue coloured solid line) are also appended. 165

6.25 Energy spectra of centreline streamwise velocity fluctuations, w'', at different axial locations normalised by centreline $\langle w'' \rangle_{rms}$ at the same locations, for both non-spiral and spiral pulsatile flow while $Re = 876$. The red and the green coloured lines correspond to the energy spectra of velocity fluctuations for non-spiral and spiral flow, respectively. 166

6.26 Energy spectra of wall pressure fluctuations, p'', at different axial locations normalised by wall $\langle p'' \rangle_{rms}$ at the same locations, for both non-spiral and spiral pulsatile flow while $Re = 876$. The red and the green coloured line corresponds to the energy spectra of wall pressure fluctuations for non-spiral and spiral flow, respectively. . . 167

7.1 Three dimensional view of model artery having irregular stenosis with adjacent irregular aneurysm (a) the whole domain and (b) zoomed-in section on irregular stenosis with adjacent irregular aneurysm. 184

7.2 Inlet physiological 4$^{\text{th}}$ harmonic pulsatile velocity profiles, $\bar{w}$ (m/s), for a time cycle (a) at the centre of the tube, (b) at different locations between the wall and the centre, (c) bulk velocity profile and (d) during different phases of a time cycle while $A = 0.40$, $Re = 440$ and the Womersley parameter $\alpha = 6.92$. Reference phases at which results are obtained are also marked. 184

7.3 Outlet physiological 4$^{\text{th}}$ harmonic pulsatile pressure profiles, $\bar{p}$ (mmHg), for a time cycle while $A = 0.40$, $Re = 440$ and the Womersley parameter $\alpha = 6.92$. (1 mmHg= 133.32 Pa.) 185

7.4 Grid resolution study for phase-averaged streamwise velocity, $\langle\langle \bar{w} \rangle\rangle$ (m/s), in non-spiral blood flow during phase $P3$ at different indicated axial locations while $Re = 440$. 185

7.5 Grid resolution study for phase-averaged axial wall shear stress (Pa) in non-spiral blood flow during phase $P3$ while $Re = 440$. Phase averaging was done on the circumferential average WSS. 185

7.6 Dynamic Smagorinsky constant, C_s, in non-spiral blood flow during phase $P3$ for (a) $Re = 366$ and (b) $Re = 440$. 186

7.7 Normalised SGS eddy viscosity, μ_{sgs}/μ, in non-spiral blood flow during phase $P3$ for (a) $Re = 366$ and (b) $Re = 440$. 186

7.8 Contour plot of the instantaneous mid-plane streamwise velocity, $\bar{w}$ (m/s), for $Re = 440$ during phase $P2$ in (a) non-spiral and (b) spiral blood flow while $C = 1/6$. 187

7.9 Contour plot of the instantaneous mid-plane streamwise velocity, $\bar{w}$ (m/s), in non-spiral blood flow during phase $P3$ for (a) $Re = 366$ and (b) $Re = 440$ and (c) the corresponding $\bar{w}$ from k-ω Transitional model in non-spiral flow for $Re = 440$. 187

7.10 Contour plot of the instantaneous mid-plane streamwise velocity, $\bar{w}$ (m/s), in spiral blood flow during phase $P3$ for (a) $Re = 366$ while $C = 1/6$, (b) $Re = 440$ while $C = 1/6$ and (c) $Re = 440$ while $C = 1/4$. 187

7.11 Instantaneous cross-sectional vectors appended on the contours of the streamwise velocity, $\bar{w}$, in non-spiral flow during phase $P3$ at (a) $z/D = 0$, (b) $z/D = 1$, (c) $z/D = 2$, (d) $z/D = 3$, (e) $z/D = 4$, (f) $z/D = 5$, (g) $z/D = 6$, (h) $z/D = 7$, (i) $z/D = 8$, (j) $z/D = 9$, (k) $z/D = 10$ and (l) $z/D = 12$ while $Re = 440$. 188

7.12 Instantaneous cross-sectional vectors appended on the contours of the streamwise velocity, $\bar{w}$, in spiral flow during phase $P3$ at (a) $z/D = 0$, (b) $z/D = 1$, (c) $z/D = 2$, (d) $z/D = 3$, (e) $z/D = 4$, (f) $z/D = 5$, (g) $z/D = 6$, (h) $z/D = 7$, (i) $z/D = 8$, (j) $z/D = 9$, (k) $z/D = 10$ and (l) $z/D = 12$ while $Re = 440$. 189

7.13 The instantaneous mid-plane streamlines for $Re = 440$ during phase $P2$ in (a) non-spiral and (b) spiral blood flow while $C = 1/6$. 190

7.14 The instantaneous mid-plane streamlines in non-spiral blood flow during phase $P3$ for (a) $Re = 366$ and (b) $Re = 440$ and (c) the corresponding streamlines from k-ω Transitional model in non-spiral flow for $Re = 440$. 190

7.15 The instantaneous mid-plane streamlines in spiral blood flow during phase $P3$ for (a) $Re = 366$ while $C = 1/6$, (b) $Re = 440$ while $C = 1/6$ and (c) $Re = 440$ while $C = 1/4$. 190

7.16 The instantaneous wall pressure, $\bar{p}$ (Pa), in both non-spiral and spiral flow for Reynolds numbers $Re = 366$ (while $C = 1/6$) and $Re = 440$ (while $C = 1/6$ and $C = 1/4$) during different phases of the last cycle at the two indicated circumferential locations. The corresponding k-ω Transitional results in non-spiral flow for $Re = 440$ are also appended. 191

7.17 The instantaneous wall shear stress (Pa) for $Re = 366$ in both non-spiral and spiral ($C = 1/6$) flow during different phases of the last cycle at the two indicated circumferential locations. 192
7.18 The instantaneous wall shear stress (Pa) for $Re = 440$ in both non-spiral and spiral ($C = 1/6$ and $C = 1/4$) flow during different phases of the last cycle at the two indicated circumferential locations. Note that the corresponding k-ω Transitional results in non-spiral flow are also appended. 193
7.19 Phase-averaged streamwise velocity, $\langle\langle \bar{w} \rangle\rangle$ (m/s), in both non-spiral and spiral flow for Reynolds numbers $Re = 366$ (while $C = 1/6$) and $Re = 440$ (while $C = 1/6$ and $C = 1/4$) during phase $P3$ of the last cycle at different axial locations. Note that the corresponding k-ω Transitional results in non-spiral flow for $Re = 440$ are also appended. 194
7.20 Phase-averaged wall shear stress (Pa) in both non-spiral and spiral flow during phase $P3$ for (a) $Re = 366$ (while $C = 1/6$) and (b) $Re = 440$ (while $C = 1/6$ and $C = 1/4$) at the two indicated circumferential locations. The corresponding k-ω Transitional results in non-spiral flow for $Re = 440$ are also appended in (b). 194
7.21 rms of the streamwise velocity fluctuations, $\langle w'' \rangle_{rms}$ (m/s), in both non-spiral and spiral flow for Reynolds numbers $Re = 366$ (while $C = 1/6$) and $Re = 440$ (while $C = 1/6$ and $C = 1/4$) during phase $P3$ at different axial locations. Note the corresponding k-ω results in non-spiral flow for $Re = 440$ are also appended. 195
7.22 Turbulent kinetic energy (TKE), $\frac{1}{2}\langle u_j'' u_j'' \rangle$ (m^2/s^2), in both non-spiral and spiral ($C = 1/6$) flow for Reynolds numbers $Re = 366$ during phase $P3$ at different axial locations. 195
7.23 Turbulent kinetic energy (TKE), $\frac{1}{2}\langle u_j'' u_j'' \rangle$ (m^2/s^2), in both non-spiral and spiral ($C = 1/6$ and $C = 1/4$) flow for Reynolds numbers $Re = 440$ during phase $P3$ at different axial locations. Note the corresponding k-ω results in non-spiral flow for $Re = 440$ are also appended. 196

7.24 rms of wall pressure fluctuations, $\langle p'' \rangle_{rms}$ (Pa), in both non-spiral and spiral flow for Reynolds numbers $Re = 366$ (while $C = 1/6$) and $Re = 440$ (while $C = 1/6$ and $C = 1/4$) during phase $P3$ at the two indicated circumferential locations. The corresponding k-ω results in non-spiral flow for $Re = 440$ are also appended. 196

7.25 Time history of the centreline velocity fluctuations, (a) u''/u''_{max}, (b) v''/v''_{max} and (c) w''/w''_{max} at different axial locations for both non-spiral and spiral ($C = 1/6$) pulsatile blood flow while $Re = 440$. The red coloured solid line denotes velocity fluctuations for non-spiral flow while the green coloured dashed line corresponds to velocity fluctuations for spiral flow. 197

7.26 Time history of centreline turbulent kinetic energy (TKE), $\frac{1}{2}\langle u''_j u''_j \rangle$ (m^2/s^2), at different indicated axial locations for both non-spiral and spiral flow while $Re = 440$. The red coloured solid line denotes TKE for non-spiral flow while the green coloured dashed line and blue coloured dash-dot-dot line correspond to TKE for spiral flow corresponding to $C = 1/6$ and $C = 1/4$ respectively. 198

7.27 Energy spectra of centreline streamwise velocity fluctuations, w'', at different axial locations normalised by centreline $\langle w'' \rangle_{rms}$ at the same locations, for both non-spiral and spiral ($C = 1/6$) pulsatile flow while $Re_{pk} = 1200$. The red and the green coloured lines correspond to the energy spectra of velocity fluctuations for non-spiral and spiral flow, respectively. 199

List of Tables

4.1 Parameters of stenosed arteries with and without upstream curved section models. 38

Chapter 1

Introduction

Arterial stenosis is an abnormal condition in arteries having vascular disease named atherosclerosis, which alters the hemodynamics in the diseased arteries. Atherosclerosis, a progressive cardiovascular disease caused by the accumulated fatty materials like cholesterol and lipids beneath the intima (inner lining) of arterial wall, is one of the main causes of heart disease and stroke (Lusis [1]). A sudden increase of connective tissue occurs with the accumulation of the fatty materials and a thickened area called plaque is developed in the arterial wall. The arterial wall reshapes itself to accommodate the plaque, but the arterial cross-sectional area narrows eventually due to the increasingly complex pattern of the deposited plaque, which can potentially dangerously blocks blood flow in the circulatory system ([1]) mostly in aorta, coronary and carotid arteries. This local narrowing of arterial cross sectional area is known as arterial stenosis.

Severity of stenosis is determined by the percentage reduction in diameter or cross-sectional area of the stenosed vessel and therapeutic measures is taken if area reduction is greater than 75% as it is clinically important (Young [2];Ku [3]). Reynolds number found in human artery ranges normally between 1 and 4000 (Ku [3]). Blood viscosity is not constant at all flow rates. Blood exhibits non-Newtonian behaviour in the microcirculatory system, small branches and capillaries. Blood behaves like a Newtonian fluid in most arteries, however (Ku [3]).

Cyclic motion of the heart pumping makes the blood flow through arteries inherently pulsatile. Blood flow in the circulatory system is mostly pulsatile laminar. But blood flow through severely stenosed vessel can lead to periodic transition to turbulence in the post stenotic regime as a combined effect of flow pulsatility with strong shear layers, flow separation, recirculation, and reattachment generated by the stenotic flow. Accordingly, blood flow through arterial stenosis in critical ter-

ritories, e.g. one of the major vessels carrying blood to the brain, can result in a cerebral stroke as critical stenosis causes flow choking and non-recoverable head loss which in turn reduce flow rate (Young [2], Varghese et al. [4]). Higher velocities across the stenosis as the flow passes through the occlusion at increasing rate result in lower lateral pressure acting on the plaque and high shear stresses at the stenosis throat and low, oscillatory shear stress in the post stenotic area. The high shear stresses contribute to platelet build-up and cause thrombosis (blood clotting) by exposing the lipid plaque core to the blood flow, resulting in arguably plaque fissure, rupture and total occlusion of the vessel. Non-occlusive atherothrombosis is also clinically significant, especially in the extracranial carotid arteries as a source of stroke, as the accumulated thrombotic material is commonly unstable and a source of distal embolism (Ku and McCord [5], Wootton and Ku [6], Ku [3], Nichols and O'Rourke [7]). Low, oscillatory shear stresses in the post stenosis area have been considered as the major cause of progression of arterial wall thickening and atherosclerotic disease (Ku [3], Wootton and Ku [6]). The pressure drop across the plaque is increased if the velocity is increased by any increase in systematic pressure or further decrease in cross-sectional area of the vessel. Though the rupture of the plaque has long been ascribed to the local high Wall Shear Stress (WSS), pressure drop may be the main mechanical trigger for plaque rupture as the magnitude of WSS is extremely small compared to the overall loading of the plaque (Li et al. [8], Wootton and Ku [6]).

Stenosis in a coronary artery may induce heart attack as it restricts the blood flow. Blood clot in the flow, caused either by the stenosis-surface damage or by stagnant blood in the post-stenosis recirculation region, may choke the blood flow in cerebral and coronary artery. Also, it may be transported to the lung (Wootton and Ku [6]). The sites of low wall shear stresses such as cerebral and coronary artery are liable to accumulating lipids and hence developing plaque as low wall shear stress stimulates an atherogenic phenotype in the endothelial cells or vessels lining, Malek et al. [9]. Moreover, the pulsatility of the flow and the oscillating shear index are increasingly being implicated in the plaque formation as has been shown in 4D MRI (Magnetic Resonance Imaging) experiments, Frydrychowicz et al. [10]. Velocity/acceleration at/beyond the stenosis is also an important quantity as the quantification of arterial stenosis by both duplex ultrasound and quantitative flow MRI

techniques relies on it to deduce the the degree of underlying stenosis (Frydrychowicz et al. [10]).

Another abnormality of artery is aneurysm, which is localized, blood-filled balloon-like bulge in an artery due to weakness in the arterial wall. Aneurysm may rupture if it grows large. Blood velocity, wall pressure and wall shear stress can induce progression and rupture of aneurysm. Internal pressure can also influence the burst of aneurysm, causing severe pathological disorder, even death (Kumar and Naidu [11]). Blood flow through aneurysm may become transition-to-turbulent because of large recirculation zone inside the bulge.

In addition, the re-circulated blood inside aneurysm induces high shear stress, which is potentially harmful to the blood cells and arterial wall. Aneurysm may also pose risks of blood clotting and rupture of artery which may result in sudden death or severe disability (Lasheras [12]).

In addition to stenosis and aneurysm, one further compelling abnormal condition of artery is stenosis with adjacent aneurysm in the same arterial segment. Although severe stenoses with adjacent aneurysms are rare, they are more common in the posterior circulation (In et al. [13]). Flow physics of blood flow through such arterial stenosis with an adjacent aneurysm in the same arterial segment is unknown thus far.

A striking feature of blood-flow is its spiral or helical pattern, which could be due to twisting of the heart on its own axis and/or anatomy of the arterial tree (curved section, bifurcation), Stonebridge and Brophy [14], Stonebridge et al. [15]. Effects of spiral pattern of blood velocity is poorly understood, although they can be both beneficial and detrimental to artery. Spiral flow through stenoses generates lower laterally directed forces, arguably reduces near wall turbulence energy caused by stenosis and induces rotational stability (Stonebridge and Brophy [14], Stonebridge et al. [15; 16]), which are beneficial to circulatory system. On the other hand, oscillatory shear stress and strong circulation caused by the spiral flow in the post-stenosis region are harmful to the artery (Paul and Larman [17]).

Thus comprehending the complicated flow features of non-spiral and spiral blood flow through stenosis and stenosis with adjacent aneurysm is central to comprehending the possible causes that induce disease progression.

Chapter 2

Review of Previous Works

An overall review of previous studies pertaining to this thesis has been done in this chapter. Extensive reviews of experimental and computational studies on arterial stenosis are made in § 2.1 and § 2.2, respectively, which are followed by a brief review of the works on arterial aneurysm in § 2.3 and the previous studies related to spiral blood flow in arterial stenosis are reviewed in § 2.4. The objectives and outline of the thesis are presented at the end of this chapter.

2.1 Experimental Works on Stenosis

Most of the experimental works on the steady and pulsatile turbulent flow in model arterial stenosis or constricted tube investigated the impact of post stenotic turbulent flow on the blood cells and inner wall of the blood vessels. Some experimental researchers studied effects of the shear stress and turbulence on blood cells and arterial wall in the post stenotic region, while others studied the post-stenotic flow physics along with the effects of the various shapes and percentages of the stenosis on the flow downstream of the stenosis. There are also some experimental studies of spiral blood flow through stenosis.

2.1.1 Post-stenotic Flow Characteristics

Young and Tsai [18; 19] studied flow characteristics of steady and unsteady flow through axisymmetric and nonsymmetric stenosis models of different sizes. They found that the shape of the stenosis influences the flow characteristics e.g., pressure losses in the nonsymmetric models are considerably higher than the losses in the corresponding axisymmetric models. They also reported that, for the more

severely constricted models, the critical Reynolds number for unsteady or pulsatile flow is lower than that for steady flow. Highly disturbed flow after the stenosis was observed by Clark [20; 21] in his studies of both steady and pulsatile flow through nozzle type stenosis. He also pointed out that the higher the flow Reynolds number, the greater the intensity of disturbances of velocity. Cassanova and Giddens [22], on the other hand, focused on two aspects of the flow physics of post stenotic flows: the characterisation of flow disorder over a transitional Reynolds number ranging from 318 to 2540 and a pulsatile flow frequency parameter $\alpha = 15$ for mild and moderate degrees of sharp edged and smoothly configured occlusion; and the relationship between steady and pulsatile flow through such constrictions. They reported that the more abrupt, sharp edged stenoses generate a much greater flow disturbance at a given Reynolds number than the smoothly contoured configuration. Furthermore, for steady flow the visualisation studies and measurements indicate that, for the smoothly contoured stenosis, approximately 50% occulusion is required to cause substantial disturbances at the Reynolds numbers studied. For the pulsatile flow, however, the disturbances are generated with a mild 25% stenosis during the deceleration phase of a cycle. It is evident from this study, therefore, that the transition-to-turbulence in the post-stenosis region is strongly dependent on the flow pulsatility. This result is similar to that of Young and Tsai [19] for pulsatile flow.

Yongchareon and Young [23], motivated by the above mentioned studies, investigated the development of turbulence for both steady and pulsatile flow through the models of arterial stenoses. The results of their research can be summarised as follows: first, the critical Reynolds number for the development of turbulence in pulsatile flow through the stenosis depends on several factors, including the shape and size of the stenosis and the type of the inlet-flow waveform, which is similar to the findings reported by Young and Tsai [18; 19]; second, the turbulence develops at Reynolds numbers well below the critical value for an unobstructed tube; third, the critical Reynolds number reduces as the stenosis shape becomes more abrupt and the inlet flow frequency parameter increases; and, fourth, the axial location (critical length), at which turbulence was first observed, is a function of both stenosis shape and frequency parameter. Furthermore, the critical length tends to decrease as the frequency parameter increases, and the location of the most intense turbulent

fluctuations moves upstream if the Reynolds number increases beyond the critical value.

Khalifa and Giddens [24; 25] studied the evolution of post-stenotic flow disturbances of a sinusoidal type waveform using a laser Doppler anemometer (LDA) for the centreline velocity measurement of a Plexiglas (Perspex, PMMA) tube. The pulsatile frequency parameter and the peak Reynolds number were typical of the dog aorta and the nature post-stenotic flow disturbances were determined by employing ensemble averaging and Fourier transform techniques for the degrees of stenosis ranging from zero to severe. They have identified three types of flow disturbances: (i) a coherent structure associated with the initiation of each flow cycle, present in the mild stenosis; (ii) a periodic disturbance arising from the shear layer distal to the constriction; and (iii) a non-stationary turbulence generated after the stenosis. A similar study, detecting the vortex shedding and coherent structures under steady and pulsatile flow condition, was done by D'Luna et al. [26]. He used a pulsed RF directional Doppler system together with high resolution temporal auto regression spectral analysis for the study.

Additionally, flow disturbances in steady flow through axisymmetric stenoses of rigid tube using laser Doppler anemometry and a flow visualisation technique was investigated by Ahmed and Giddens [27; 28]. The degree of stenosis ranged from mild to severe and Reynolds numbers were of 500, 1000 and 2000. They reported that for the 75% stenosis the flow field is transitional-to-turbulent when $Re \geq 1000$ and for the 50% stenosis transition-to-turbulence takes place when $Re = 2000$ and the maximum centreline velocity occurs at the centre of the stenosis. They also found that the length of the re-circulation zone or the reattachment point reduces as the Reynolds number increases. These findings are very similar to that of Back and Roschke [29], who found three distinct regimes of flow re-attachment in the post-stenosis region. In the first regime, at low Reynolds numbers re-attachment is governed by the growth of the laminar shear layer and the re-attachment point moves downstream with increasing flow rate. In the second regime, as instabilities develop in this shear layer, the re-attachment point moves back towards the stenosis. In the third regime, which (for an 85% stenosis) exists above a flow Reynolds number of approximately 325, the shear layer is highly disturbed, the re-attachment point is near the stenosis and very slowly moves downstream with increasing flow

rate.

Ahmed and Giddens [30] also did a follow-up investigation to the above by studying the post-stenotic flow characteristics under sinusoidal pulsatile inflow conditions at a frequency parameter, $\alpha = 7.5$ and mean Reynolds number of 600. They concluded that a permanent region of post-stenotic flow separation does not exist even for the severest degree of stenosis, in contrast to results for steady flow. Turbulence was found only for 75% stenosis model and was generated only during a part of the cycle. By employing a two-component laser Doppler velocimeter (LDV), Ahmed [31] re-investigated the pulsatile flow through a smooth constriction fourteen years after his work with Giddens [30]. His findings for the post-stenotic turbulent flow physics are similar to those of Yongchareon and Young [23]. In a different kind of study, Back et al. [32] investigated effect of mild atherosclerosis on flow resistance in a coronary casting of man i.e., in an irregular stenosis with a 48% area occlusion. They reported that, for a Reynolds number greater than 200, flow resistance and hence pressure drop of the casting of the mild atherosclerosis (irregular stenosis) become gradually larger than the corresponding values from the axisymmetric model of the casting.

2.1.2 Pathophysiological Implications

High pressure drop and abnormal wall shear stress around the stenosis may weaken and even damage the internal arterial wall in the post-stenotic turbulent region. For example, the damage to the blood cell materials of a diseased artery could be caused by the presence of high wall shear stress in that artery. Additionally, the main diagnostic tool in the clinical practice for diagnosing the cardiovascular diseases is the qualitative interpretation of cardiovascular sounds and murmurs generated apparently by turbulence in blood flow in the diseased artery. This fact motivated many researchers to study sound generation, murmur characteristics, and transmission of energy of turbulence in diseased arteries for getting better understanding of hemodynamics in them.

Bruns [33] reported that the bulk of acoustic energy in murmurs is generated by the nearly periodic fluctuations in the wake of downstream of any appropriate obstacle. He also maintained that a significant amount of localised acoustic energy might

be generated in the physiological range of blood velocities. Yellin [34] studied the hydraulic noise of a bounded jet in a model with an intrafluid having less friction. Using spectral analyses he, however, proved that an insignificant amount of local turbulent pressure fluctuations was converted into sounds. To calculate the percentage of area reduction of a stenosis from the arterial sound created by turbulence, Lees and Dewey [35] offered a non-invasive diagnostic method (phonoangiography). They associated the local turbulence intensity with wall pressure fluctuations, the flow velocity and the arterial diameter, and these independent parameters provide enough information about the severity of stenosis.

As regards the effects of shear stress, Fry [36] found that the high shear stress produced by turbulence might be an important factor in causing endothelial cell degeneration in a atherosclerotic vessel. He also mentioned a critical value of wall shear stress $> 379 \pm 85$ (SD) dynes/cm^2 (or 37.9 ± 8.5(SD) Pa) contribute to endothelial cell damages in the artery. In addition, Sutera and Mehrjardi [37] showed that high wall shear stresses generated due to turbulent flow may lead to deformation and fragmentation of red blood cells. Additionally, Folts et al. [38] and Stein et al. [39] have pointed out that high wall shear stress could overstimulate platelet thrombosis which, in turn, expedite atherosclerosis. However, some researchers like Friedman et al. [40], Ku et al. [41] and Salam et al. [42], have reported that low shear stresses at the throat of the stenosis may stimulate the intimal thickening, resulting in remodelling of the stenosis. The most intimal thickening, in He and Ku's [43] view, occurs where the average wall shear stress is less than 10 dynes/cm^2 (or 1 Pa).

2.1.3 Turbulence Energy Spectra

Spectral analysis of turbulent flow quantities could be used to grasp how the turbulent fluctuations downstream of stenosis behave and interpret the sounds associated with pulsatile post-stenotic blood flows. Kim and Corcoran [44] reported turbulence spectra in the downstream of a stenosis using a hot-film anemometer technique. As can be seen from their findings, the turbulence spectra are quite different from the sound spectra measured at the centre of the tube for the same flow rate and orifice diameter. According to Clark [45; 46], the energy spectrum for the velocity and pressure fluctuations follow the $-5/3$ power slope – this confirms

the existence of a turbulent inertia subrange region, independent of the viscous effect. Non-dimensional power spectra of the maximum r.m.s. wall pressure showed no Reynolds number dependence and were almost independent of nozzle area ratio and shape. The spectrum from a pulsatile flow test was very similar to the corresponding spectrum from steady flow case.

Lu et al. [47] studied the intravascular pressure and velocity fluctuations in pulmonic arterial stenosis using a Laser Doppler Anemometer system. Spectral analysis of the simultaneously measured pressure and velocity fluctuations showed a region of $-5/3$ power slope in the flow energy spectra which break into $-10/3$ power slope at a 'break' frequency approximately $f_b = 100$ Hz. But, in a later study, Lu et al. [48] reported the differences between peak frequencies of the spectra of pressure fluctuations and the characteristic frequencies of the spectra of velocity fluctuations vary with positions downstream from the nozzle. It is possible for both spectra to have coincident characteristic frequencies only in the region where shear noise is so strong that it dominates the flow field over the contributions of all other noise sources. His other findings are: no universal spectrum for velocity exists within sections between the nozzle and 9 diameters downstream; the spectra of u and v velocity fluctuations at the same point are different, indicating non-isotropic turbulence.

Tobin and Chang [49] have investigated the scaling of wall pressure spectra downstream of axisymmetric stenoses thoroughly in steady tube flow. Their findings can be summarised as follows: first, the position of maximum r.m.s. wall pressure fluctuations is just upstream from the re-attachment point and at this position, the centreline flow velocity, even though the jet has been diverging, is roughly equal to the flow velocity within the stenosis; second, to characterise the frequency content of the spectra, they have defined a break or corner frequency, f_b, as the intersection of the two lines drawn parallel to the two major sloping portions of the recorded spectra. For fully developed turbulent pipe flow and Reynolds number between 1000 and 4000, they have evaluated a constant value for the Strouhal number, $Sr = \frac{f_b D}{u_j} \cong 0.578$, characterising the spectra taken at the position of maximum r.m.s. wall pressure. Here D is the tube diameter, u_j is the mean jet velocity. They have given a formula for the degree of stenosis in terms of this constant value as, $1 - \left(\frac{d}{D}\right)^2 = 1 - 0.578\left(\frac{f_b D}{U}\right)^{-1}$. Here d is the diameter of the orifice and U is the

cross-sectional mean velocity in the unobstructed part of the artery. Hence, the degree of stenosis can be predicted under steady flow conditions with a wall pressure spectrum at the position of maximum root mean square wall pressure and a knowledge of D and U; and third, they made a comparision of their wall pressure spectra with the corresponding turbulent pipe flow spectrum used by Lees and Dewey [35] and found significant mismatch in the slope of the spectra beyond the corner frequency. Additionally, Giddens et al. [50] did not find any such break frequency in their study of measurements of disordered blood flows distal to externally enforced, subtotal vascular stenoses in the descending thoracic aortas of dogs during open-chest surgery.

Jones and Fronek [51] analysed break frequencies downstream of a constrictions in an axisymmetric geometry under steady inflow conditions for the range of Reynolds numbers from 600 to 1500 and found a relationship $\frac{f_b d}{u_j} = Re^{0.72}(d/D)^{0.26}$ between the contraction ratio (d/D), break frequency f_b and the Reynolds number Re. The above relation can be expressed as $\frac{f_b D}{U} = Re^{0.72}(d/D)^{-2.74}$, with the help of continuity equation, $UD^2 = u_j d^2$. This expression can now be compared with the corresponding scaling of Lees and Dewey [35] and Tobin and Chang [49]. It is obvious from these studies that all three scalings are quite different. So further studies are needed to have a better understanding of the flow physics and scaling of spectra in the post-stenosis region.

2.2 Computational Investigations on Stenosis

Many computational fluid dynamics (CFD) researchers take great interest in getting better understanding of the post-stenotic flow field as it is clear from the experimental literature review that accurate depiction of the flow physics of post-stenotic blood flow help diagnose the arterial disease. With the state of art computing facilities, CFD plays an important role in getting accurate results and visualising the flow field properly. Reviews of relevant computational studies on steady and pulsatile flow through model arterial stenoses are presented below. Laminar flow studies are discussed first, which is followed by reviews of turbulent flow studies.

2.2.1 Laminar Flow

Lee and Fung [52] and Deshpande et al. [53] studied 2D steady laminar flow in arterial stenoses in 70s. Lee and Fung [52] developed the constriction in the model artery by using Gaussian normal distribution curve and Reynolds number range they studied is very low, from zero to 25. On the other hand, a cosine shape stenosis, which closely resembles the biological type stenosis, was formed by Deshpande et al. [53] for their model stenosis. Their results show that the maximum wall pressure drop and vorticity occur near the centre of the stenosis. For severe stenosis, Deshpande et al. [53] investigated the Reynolds number range from zero to 300. Deshpande et al. [53] also reported extended regions of flow recirculation and large values of wall shear stresses along the proximal wall of the stenoses.

Pulsatile laminar flows through the model arterial stenoses were investigated by Cheng et al. [54], Daly [55] and O'Brien and Ehrlich [56]. Cheng et al. [54] took a channel with square shape of stenosis for their pulsatile flow study. However, an axisymmetric cosine shape stenosis was developed by Daly [55] and O'Brien and Ehrlich [56]. A physiological pulsatile flow was used at the inlet in Daly's [55] study. On the other hand, a simple sinusoidal pulsatile flow was taken at the inlet by Cheng et al. [54] and O'Brien and Ehrlich [56]. Cheng et al. [54] and Daly [55] showed that the maximum pressure gradient and the shear stress drops occur at the centre of the stenosis. However, O'Brien and Ehrlich [56] reported that at each time-step the peak wall vorticity is found just prior to the stenosis throat and is proportional to the wall shear stress.

Much later on, by employing physiologically realistic pulsatile inlet conditions Cavalcanti [57] investigated hemodynamics of an artery in the early stages of the atherosclerosis or stenotic process with just 2% area reduction stenosis. He found that the flow velocity and the wall shear stress increase in the post-stenotic regime even for this very mild stenosis. Zendehbudi and Moayeri [58] have made a comparative study of physiological and simple pulsatile laminar flows through axisymmetric stenosed arteries and reported that for thorough understanding of pulsatile flow behaviour in stenosed arteries, the actual physiological flow should be simulated. Recently, a simulation of laminar physiological pulsatile blood flow in a model axisymmetric stenosis was carried out by Marques et al. [59]. They have shown that the effect of pulsatile flow is more significant near vessel wall, within the Stokes

layer. In this region, flow direction is changed due to a reversal of pressure gradient which is again due to the effect of viscous forces near the wall, with the changes in velocity being slightly delayed compared to the pressure gradient.

All the articles discussed above are on stenosis of regular shape. However there are few studies on irregular stenosis, though limited to two-dimensional study only. Following Back et al. [32], Johnston and Kilpatrick [60] and Andersson et al. [61] have studied steady flow through an irregular stenosis with 48% area occlusion for Reynolds numbers ranging from 10 to 1000. They found that the pressure drop across a stenosed artery is practically unaffected by surface irregularities at low Reynolds numbers, while an excess pressure drop up to 10% above that for a smooth stenosis is observed at higher Re. Pulsatile flow through stenoses was investigated by Yakhot et al. [62]. They observed that surface irregularities may affect the dynamics of the near-wall vortices that might be important for estimating the near-wall residence time of blood cells. Furthermore, Chakravarty et al. [63] and Sarifuddin et al. [64] have studied the effects of surface irregularities on unsteady pulsatile flow through distensible irregular arterial stenoses. They have demonstrated that the excess pressure drop across the cosine and smooth stenosis is neither caused by its smoothness nor by its higher degree of symmetry relative to the irregular stenosis but is rather an effect of area cover compared with the irregular stenosis.

Some relevant three-dimensional studies of laminar flow through stenoses are discussed below. Melaaen [65] investigated the steady flow in a constricted tubes and ducts for $Re = 200$. Additionally, analysis of the steady flow pattern for a stenosed coronary bypass for a Reynolds number of 250 was done by Bertolotti and Deplano [66]. However, Stroud et al. [67] studied the influence of stenosis morphology on pulsatile laminar flow through stenotic vessels for Reynolds number ranging from 200 to 1200. Dvinsky and Ojha [68] investigated the sinusoidal pulsatile laminar flow through an asymmetric stenosis. Furthermore, Long et al. [69] studied physiologically realistic pulsatile laminar flow through axisymmetric and asymmetric arterial stenoses for a Reynolds number of 300. Their results show that for severe stenoses, the stenosis influence length is shorter in asymmetrical models than in axisymmetrical cases. Long et al. [69] approximated the shape of the stenosis by two integrated Gaussian functions at each of the proximal and distal ends together with a straight segment in between, whereas Dvinsky and and Ojha [68]

developed a cosine shape asymmetric stenosis.

2.2.2 Turbulent Flow

As seen, computational studies reviewed above are laminar flow through stenosis. However, experimental findings demonstrate that flow through even moderately stenosed arteries is transitional-to-turbulent for high Reynolds number. Computational studies on the transition-to-turbulent flow through stenoses available in the literature are discussed below.

By employing the Reynolds-Average Navier-Stokes (RANS) approach, namely, the k-ω turbulence model, Ghalichi et al. [70], Varghese and Frankel [71], Lee et al. [72; 73] and Li et al. [74] have studied axisymmetric two-dimensional laminar to turbulent flow in stenosis. But Scotti and Piomelli [75] have found some limitations in the use of RANS turbulent models in modelling pulsatile flows where the inlet velocity profile/pressure gradient oscillates with time. They made a comparative study of results from experiment, DNS and LES and four different RANS models (one-equation Spalart-Allmaras [76], k-ϵ and k-ω^2 of Saffman and Wilcox [77], and k-ϵ-v^2 of Durbin [78]) in a channel flow driven by an oscillating pressure gradient. They observed that the RANS models give good agreement for the velocity results, but the predictions were unacceptable for the key turbulent results such as Reynolds shear stresses (important results from pathological aspect), turbulent kinetic energy and dissipation rate. Additionally, RANS models are incapable of simulating instantaneous pulsatile turbulent flows as the governing equations of motion are time-averaged. Moreover, Ryval et al. [79] have investigated three-dimensional pulsatile flow in stenosed tube by employing various k-ω models. They also concluded that if the fine details of transitional activities are of interest, then more computationally intensive large eddy or direct numerical simulations of turbulence may be unavoidable.

Mallinger and Drikakis [80; 81] have studied instabilities in three-dimensional pulsatile flow through stenosis. Their results demonstrate that the circumferential wall shear stress (WSS) drops just after the centre of the stenosis and then takes an oscillating form and the maximum longitudinal WSS occurs just before the centre of the stenosis. Three-dimensional instabilities and transition-to-turbulence of steady

and pulsatile flows through axisymmetric stenotic tube was studied by Sherwin and Blackburn [82; 83]. They applied Direct Numerical Simulation (DNS) based on the spectral method and took a simple sinusoidal pulse for pulsatile inlet velocity for the Reynolds number ranging from 250 to 800 in their studies.

In addition, by employing DNS, Varghses et al. [4; 84] have studied steady and pulsatile flow in axisymmetric and eccentric stenoses. Their findings demonstrate that, for pulsatile flow, transition-to-turbulence takes place even for a relatively low mean Reynolds number of 300. They observed highly oscillating wall shear stress in the post stenotic region due to occurrence of transition-to-turbulence flow there.

However, DNS is a right approach only for small Reynolds number flow and it may be computationally very expensive for the typical large Reynolds numbers found in circulatory system because in DNS all eddies (large or small scale) are resolved fully. In contrast, LES is suitable equally for small and large Reynolds number flows and it requires less mesh and time as in LES only the large scale eddies (turbulence energy-containing scales), are resolved in space and time while the smaller scale, sub-grid scale (SGS) eddies are modelled. In this thesis, mostly LES is applied due to its suitability for physiological flow simulation which is clear from the following studies.

Varghese et al. [85] and Tan et al. [86] made a comparison of LES of steady flow through stenosed pipe with other turbulence models. They suggested that LES can predict transitional stenotic flows more accurately than others. LES of transition to turbulence of pulsatile flow in a constricted channel was investigated by Mittal et al. [87; 88]. Their study is the extension of the study of Tutty [89] into three-dimension. They used semi-circular constriction in the upper wall of the channel, which is not a good representation of biological stenosis. Additionally, Molla [90], Paul et al. [91], Molla et al. [92] and Paul and Molla [93] also have investigated LES of various pulsatile flows through a three-dimensional channel with cosine type constriction on the upper wall. But channel is not a reasonable representation of artery. They have done spanwise average of flow variables in data processing, and hence, accurate depiction of flow field of pulsatile flow through arterial stenosis is not available from their studies. Recently, Gårdhagen et al. [94; 95] have studied wall shear stress (WSS) in steady and pulsating flow through stenotic pipe, which is a good representation of arterial stenosis, using LES. They used commercial soft-

ware ANSYS Fluent 6.3 and introduced a suitable amount of perturbations at the inlet to predict experimental data. Their results show that oscillatory WSS is present from the end of the stenosis to the exit. Furthermore, very recently, Barber and Simmons [96] have investigated LES of a femoral artery pulsatile flow in a rigid stenotic pipe. The inlet velocity profile they used varies only with time and they have shown only instantaneous vorticity and WSS at different phases of a cycle. No result on other important flow characteristics such as turbulent quantities and wall pressure is available from the above studies on LES of pulsatile flow through model arterial stenosis (see Gårdhagen et al. [95], Barber and Simmons [96]). Therefore, to get a good insight into the flow physics of transition-to-turbulence of pulsatile blood flow in arterial stenosis, further study is required.

2.3 Previous Works on Aneurysm

This thesis investigates flow in a stenosis with adjacent aneurysm in the same arterial segment (see In et al. [13]). No study on flow in a stenosis with adjacent aneurysm is available in the literature. So, a brief review of experimental and computational studies of aneurysm is given below.

2.3.1 Experimental Works

Scherer [97] observed, in his study of steady flow in rigid glass models of axisymmetrical spherical aneurysms, that the critical Reynolds number is $Re = 2900$ for the onset of turbulence inside the aneurysms and critical Reynolds number must depend on a dimension of the aneurysm itself since otherwise it would be possible to have identical flow conditions and identical Reynolds numbers upstream and downstream from aneurysms of greatly different size and shape, in which flow conditions are not at all similar. Egelhoff et al. [98] have investigated physiological pulsatile flow through asymmetric and axisymmetric aneurysms for peak Reynolds number ranging from 3308 to 5696 and Womersley number, $16.4 < \alpha < 21.2$. They have also reported turbulent flow inside the aneurysm.

Recently, Salsac et al. [99] have carried out experimental study on the wall shear stress in physiological pulsatile flow through a cosine shaped model aneurysm and

observed higher wall shear stresses in the systolic phase than in the diastolic phase. They also mentioned that the decrease in the average magnitude of the WSS becomes larger as the dilatation ratio increases and the number of re-circulation zones increases as the length of aneurysm increases. Additionally, Deplano et al. [100] reported that vortices within the balloon like abdominal aortic aneurysm (AAA) are highly dependent on the flow waveforms and vortices impacts can increase the local pressure on AAA walls and thus increase the wall shear stresses.

2.3.2 Computational Works

In early 80s, Wille [101] did a numerical study of pulsatile laminar flow in arterial aneurysm using the finite element method (FEM). Perltold et al. [102; 103] later studied the paths of the fluid particles in pulsatile flow through an axisymmetrical balloon like aneurysm for $Re = 100$ using FEM and observed that a large re-circulation zone occurs inside the aneurysm and the centre of this re-circulation changes with the time phase. Additionally, Kumar and Naidu [11] found that time-dependent re-circulation region in the concavity of the dilation are sensitive to the degree of dilation of the vessel. Furthermore, Kumar [104], in his numerical study of three-dimensional pulsatile flow through two asymmetric aneurysms using the finite volume method, observed that high wall shear stresses and high wall pressures are seen at the distal end of the aneurysm during the systolic phase and multiple re-circulation zones during the diastolic phase during which the magnitudes of the flow velocities are markedly low can trigger thrombus formation.

Some researchers have studied the relation between the hemodynamics and pathophysiological issues like rupture risk and thrombus formation in aneurysm. Utter and Rossmann [105], in their numerical study of aneurysm hemodynamics, have identified regions of extreme and alternating shear stress as sites potential for aneurysm rupture. Numerical simulations of the flow in three patient-specific intracranial aneurysm models, carried out by Rayz et al. [106], indicate that regions of thrombus formation correspond to slow flow and low wall shear stress regions. Additionally, Chatziprodromou et al. [107], in their study of hemodynamics and wall-remodelling of a growing cerebral aneurysm, have observed that fiber-related remodelling caused by very low shear stress is pivotal for the formation of fully

grown saccular aneurysm. Furthermore, Valencia et al. [108; 109] have reported that the abnormal (high and low) wall shear stresses are directly associated with the growth and rupture of the aneurysm.

All the numerical studies on aneurysm discussed above are restricted to laminar flow. Using the k-ω transitional variation of RANS model, Khanafer et al. [110] have done a numerical investigation of the turbulent pulsatile flow in an axisymmetric aortic aneurysm. Their results show that peak wall stress and peak deformation occur shortly after systolic peak flow velocity. Moreover, Molla [90] investigated physiological pulsatile flow through an asymmetric aneurysm in a channel using LES. He concluded that pressure drop occurs just at the end of the aneurysm and large re-circulation region is seen inside the aneurysm.

2.4 Spiral Blood Flow in Stenosis

An interesting feature of blood-flow is its spiral or helical characteristic. Blood-flow may exhibit spiral pattern as a normal physiological process i.e., because of the twisting of the heart on its own axis and/or because of the anatomy of the arterial tree such as the presence of bifurcation, tapered or curved section in an artery (see Stonebridge [14], Stonebridge et al. [15]). There is very little work available on spiral blood-flow through stenosis. Stonebridge et al. [16] investigated steady spiral flow in moderately stenosed (43.75% area reduction) conduit using MRI and CFD software STAR-CD. They reported that spiral flow through 75% cross-sectional area stenosed conduit produces 700% less near-wall turbulence. This result is ambiguous as the internal diameters of the non-stenosed and stenosed section of the conduit in their study are 8 mm and 6 mm, respectively, which is equivalent to 43.75% cross-sectional area reduction. They mentioned that near-wall turbulent kinetic energy in spiral and non-spiral flow are 0.025 m^2/s^2 and 0.16 m^2/s^2, respectively – this does not represent 700% less TKE in spiral flow rather approximately 84% less. Additionally, they characterised the turbulence kinetic energy by Reynolds stresses and did not specify the near-wall, i.e. the location of the near-wall. On the other hand, Paul and Larman [17] studied steady spiral blood flow through a rigid stenosed pipe with 75% area reduction stenosis for Reynold number 500 and 1000 using k-ω model and showed most of the results including the turbulent kinetic energy along

the centreline. They found spiral flow generates less turbulent kinetic energy (TKE) than non-spiral flow for $Re = 500$ and no difference between the spiral flow TKE and non-spiral flow TKE for $Re = 1000$. But maximum turbulence intensities occur in the shear layer rather than along the centreline (Deshpande and Giddens [111]). Moreover, their other results (centreline total pressure and wall shear stresses) show that differences between spiral and non-spiral flow exist mostly for $Re = 500$, not for $Re = 1000$. Hence, further thorough studies are required for getting a clear understanding of hemodynamics associated with spiral flow through stenosis.

2.5 Objectives of the Project

The LES technique has mostly been applied to turbulent flow modelling in engineering fields other than bio-fluid mechanics. It is only recently that LES has seen its excellent potential for studying the transition-to-turbulence of physiological flow in bio-fluid mechanics. The originality in this thesis is the study of the transition-to-turbulence of steady and unsteady physiological pulsatile spiral blood flow through three-dimensional models of a cosine-type arterial stenosis, physiological pulsatile non-spiral and spiral blood flow through three-dimensional models of an irregular stenosis and an irregular stenosis with an adjacent post-stenotic irregular aneurysm in the same arterial segment by applying mainly LES.

All the articles on spiral blood flow cited in § 2.4 are on steady spiral flow in a straight stenosed pipe without considering upstream curved section of the artery. It would be of great interest to study steady spiral flow in stenosed pipe with upstream curved section as spiral pattern may come from upstream curved segment.

Pressure was considered a constant quantity in the studies on pulsatile flow through either arterial stenosis or aneurysm reviewed above. Whereas, blood pressure is a waveform in a physiological flow (see McDonald [112], Nichols and O'Rourke [7] and Lam et al. [113]). So, LES of pulsatile non-spiral and spiral blood flow in a three-dimensional model of a cosine-type arterial stenosis using a pressure waveform at the outlet would help gain better insight into the transition-to-turbulence of the pulsatile flow and the effects of the spiral velocity on the pulsatile flow through a stenosis.

Although stenoses taken in most studies are cosine-type or smooth stenoses, but

in reality, they are of irregular shape (See Back et al. [32]). There are some studies on flow in irregular stenosis, limited to two-dimensional laminar, however, as discussed in the penultimate paragraph of § 2.2.1. Hence using the LES for modelling the physiological pulsatile non-spiral and spiral blood flow in a three-dimensional model of an irregular arterial stenosis with an outlet pressure waveform would provide more accurate understanding of the hemodynamics in an atherosclerotic artery.

Besides stenosis and aneurysm, another abnormal condition of artery is the presence of stenosis with an adjacent aneurysm in the same arterial segment. Although this condition is rare, but more common in the posterior circulation (see In et al. [13]). Study on (steady or pulsatile) flow through such an arterial stenosis with an adjacent aneurysm in the same arterial segment is not available so far. Therefore, it would be of paramount importance to study pulsatile non-spiral and spiral blood flow in such a model with an outlet pressure waveform using LES.

So, in the light of above potential for studies we set out the aims of the project, which are given below in bullet points, and the outlines of the thesis is presented in the next section sketching how these aims are achieved.

- To investigate the transition-to-turbulence phenomena of steady non-spiral and spiral blood flow through three-dimensional models of an axisymmetric cosine-type arterial stenosis with and without an upstream curved section of varying angles of curvature.

- To investigate the transition-to-turbulence of physiologically realistic pulsatile non-spiral and spiral blood flow in the model arterial stenosis without upstream curved section i.e., straight tube having an axisymmetric cosine-type constriction with a physiologically realistic pressure waveform at the outlet. And to investigate how the important results are influenced by different percentages and lengths of the stenosis. Also to study the effects of the Womersley number, α, and the amplitude of pulsation in the inflow velocity on the flow results.

- To investigate the physiological pulsatile non-spiral and spiral blood flow through a model of an irregular arterial stenosis with an outlet pressure waveform.

- Finally, to investigate how the physiological pulsatile non-spiral and spiral blood flow affect the flow transition in a model of an irregular arterial stenosis with an adjacent post-stenotic irregular aneurysm having a pressure waveform at the outlet. And to study how the results are influenced by the variation in the spiral velocity.

The walls of the arterial models were considered rigid in all the simulations in this thesis. As development of atherosclerosis in arteries leads to considerable reduction in the elastic property of the arterial wall, the assumption of rigid wall may not affect the simulation results in a big way (Zendehbudi and Moayeri [58]). Futhermore, many researchers take the view that the primary effect of wall deformability is on the shape of pressure and flow waveforms. Therefore, when the physiological waveform is simulated, the wall can be assumed rigid (Nerem [114]).

2.6 Thesis Outline

In Chapter 3, the governing equations for incompressible flow, two-equation turbulence models, namely k-ω standard transitional, k-ω-SST transitional models and Large Eddy Simulation (LES) technique are presented for investigating transition-to-turbulence of non-spiral and spiral blood flow in three-dimensional models of axisymmetric cosine-type arterial stenosis, irregular arterial stenosis and an irregular arterial stenosis with an adjacent aneurysm by using commercial Computational Fluid Dynamics (CFD) software, Fluent 6.3.

In Chapter 4, steady non-spiral and spiral blood flows through three-dimensional models of axisymmetric cosine-type arterial stenosis with and without an upstream curved section of varying angles of curvature are studied by applying mainly k-ω standard transitional model and LES technique. However, k-ω-SST is applied to straight stenosed tube and the axial velocity results are compared with the available experimental data and corresponding results from k-ω Standard Transitional model and its performance is assessed. A steady parabolic profile and a constant multiple (one-sixth) of the bulk velocity have been used at the inlet as the streamwise axial velocity and tangential velocity (for introducing a spiral effect at the inlet of the models), respectively. Reynolds numbers representative of those present in human

large artery are chosen in the study. In LES, only the large scale i.e., turbulence energy scale flows are resolved fully, while the unresolved smaller (sub-grid) scales SGS flows are modelled using the Germano-Lilly [115; 116] dynamic model. Spiral effects coming from the presence of an upstream curved section in the arterial stenosis and from the heart pumping on the downstream flow physics are examined.

In Chapter 5, physiological pulsatile non-spiral and spiral blood flows in straight tube having an axisymmetric cosine-type constriction (without upstream curved section) are investigated by using the LES technique with the Germano-Lilly [115; 116] dynamic subgrid model and k-ω standard transitional model. The physiological pulsation is generated at the inlet using the first four harmonics of the Fourier series of pressure pulse and a pressure waveform is used at the outlet. To introduce spiral velocity at the inlet, along with physiological pulsatile axial velocity, a constant multiple (one-sixth) of the bulk physiological pulsatile profile has been used as tangential velocity at the inlet. A grid resolution test is done and the effects of different time-steps on the simulated results are also investigated. The effects of different percentages and lengths of the stenosis on the results of wall pressure, wall shear stress (WSS) and turbulent kinetic energy are investigated. In addition to these, the effects of Womersley number, α and amplitude of pulsation in the inflow velocity on the flow results are studied as well. Moreover, comparison of the LES results of non-spiral flow with those of k-ω standard transitional model is shown in this chapter and the agreement found is good indeed. Furthermore, how the spiral blood flow affects the transition-to-turbulence process as compared to non-spiral blood flow for different Reynolds numbers is also studied.

In Chapter 6, transition of physiological pulsatile non-spiral and spiral blood flow through a model of irregular arterial stenosis for different Reynolds numbers is studied by applying LES technique with the Germano-Lilly [115; 116] dynamic subgrid model. A comparative study is also made between the corresponding results of Chapter 5 and Chapter 6 to understand how the irregular stenosis affects the downstream flow physics as compared to cosine-type regular stenosis.

In Chapter 7, non-spiral and spiral effects of physiological pulsatile blood flow in a model of irregular arterial stenosis with an adjacent post-stenotic irregular aneurysm in basilar artery is studied using the LES technique with the Germano-Lilly [115; 116] dynamic subgrid model and the results are compared. The effects of

different Reynolds numbers and and variation in spiral velocity are also examined. In addition, k-ω standard transitional model is applied to non-spiral physiological pulsatile blood flow and results are compared with corresponding results of LES to show reliability of the results.

In Chapter 8, the findings of the above investigations are summarised and some suggestions made for future research in this area.

Chapter 3

Numerical Methods

3.1 Governing Equations

Blood exhibits non-Newtonian effects only in small arteries and capillaries. Hence, blood flow in large arterial vessel may be modelled as a Newtonian fluid (Ku [3], Pedley [117] and Fung [118]). So the blood flow through the arterial stenosis can be described completely by the Navier-Stokes equations of motion. Blood in this study was assumed to be homogeneous, incompressible and Newtonian with a density of $\rho = 1060$ kg/m^3 and a constant dynamic viscosity of $\mu = 3.71 \times 10^{-3}$ Pa s. Therefore, the governing equations for a Newtonian and constant density blood flow can be written as the continuity equation,

$$\frac{\partial u_i}{\partial x_i} = 0, \tag{3.1}$$

and the momentum equations,

$$\frac{\partial u_i}{\partial t} + \frac{\partial u_i u_j}{\partial x_j} = -\frac{1}{\rho}\frac{\partial p}{\partial x_i} + \frac{\partial}{\partial x_j}\left[\nu\left(\frac{\partial u_i}{\partial x_j} + \frac{\partial u_j}{\partial x_i}\right)\right]. \tag{3.2}$$

Cartesian tensor notation is used in the above equations, where x_i is the coordinate system and u_i is the corresponding velocity components, p is the pressure, ρ is the density and ν is the kinematic viscosity of the fluid.

It should be noted that the above equations define both incompressible laminar and turbulent flow. Analytical solutions of the Navier-Stokes equations exist for only a few laminar flow cases, such as pipe and annulus flows or boundary layers. Turbulent flows are modelled by using various turbulence modelling schemes. In this study, two-equation k-ω Transitional models and LES, which are described

below in brief, are employed for turbulence analysis.

3.2 Standard k-ω Transitional Model

By using Reynolds decomposition, any flow property ϕ can be defined as the sum of a time-average component $\langle\phi\rangle$ and a time varying fluctuating component ϕ' i.e., $\phi = \langle\phi\rangle + \phi'$. Rules for time averages of the fluctuating properties $\phi = \langle\phi\rangle + \phi'$ and $\psi = \langle\psi\rangle + \psi'$ and their summation, derivatives and integrals can be summarised as follows:

$$\langle\phi'\rangle = \langle\psi'\rangle = 0; \qquad \langle\langle\phi\rangle\rangle = \langle\phi\rangle. \tag{3.3}$$

$$\langle\frac{\partial\phi}{\partial s}\rangle = \frac{\partial\langle\phi\rangle}{\partial s}; \qquad \langle\int\phi\,ds\rangle = \int\langle\phi\rangle\,ds. \tag{3.4}$$

$$\langle\phi+\psi\rangle = \langle\phi\rangle + \langle\psi\rangle; \qquad \langle\phi\psi\rangle = \langle\phi\rangle\langle\psi\rangle + \langle\phi'\psi'\rangle. \tag{3.5}$$

$$\langle\phi\langle\psi\rangle\rangle = \langle\phi\rangle\langle\psi\rangle; \qquad \langle\phi'\langle\psi\rangle\rangle = 0. \tag{3.6}$$

The above rules can be extended for div and $grad$ of a fluctuating vector quantity $\mathbf{a} = \langle\mathbf{a}\rangle + \mathbf{a}'$ and its combination with a fluctuating scalar $\phi = \langle\phi\rangle + \phi'$:

$$\langle div\,\mathbf{a}\rangle = div\,\langle\mathbf{a}\rangle; \qquad \langle div\,grad\,\phi\rangle = div\,grad\,\langle\phi\rangle. \tag{3.7}$$

$$\langle div(\phi\mathbf{a})\rangle = div(\langle\phi\rangle\langle\mathbf{a}\rangle) + div(\langle\phi'\mathbf{a}'\rangle). \tag{3.8}$$

Employing above rules (3.3)-(3.8) for time averaging, Reynolds time-averaged continuity and momentum equations can be written by

$$\frac{\partial\langle u_i\rangle}{\partial x_i} = 0, \tag{3.9}$$

$$\begin{aligned}\frac{\partial\langle u_i\rangle}{\partial t} + \frac{\partial\langle u_i\rangle\langle u_j\rangle}{\partial x_j} &= -\frac{1}{\rho}\frac{\partial\langle p\rangle}{\partial x_i} \\ &+ \frac{\partial}{\partial x_j}\left[\nu\left(\frac{\partial\langle u_i\rangle}{\partial x_j} + \frac{\partial\langle u_j\rangle}{\partial x_i}\right)\right] - \frac{1}{\rho}\frac{\partial\langle\rho u_i' u_j'\rangle}{\partial x_j},\end{aligned} \tag{3.10}$$

where $\langle u_i\rangle$ are the time-averaged velocities, $\langle p\rangle$ is the time-averaged pressure and

$\langle \rho u_i' u_j' \rangle$ are the time-averaged Reynolds stress tensors. In the k-ω two-equation turbulence model, Reynolds stress terms are approximated by using the Boussinesq hypothesis for incompressible flow as

$$-\langle \rho u_i' u_j' \rangle = \mu_T \left(\frac{\partial \langle u_i \rangle}{\partial x_j} + \frac{\partial \langle u_j \rangle}{\partial x_i} \right) - \frac{2}{3} \rho k \delta_{ij}, \tag{3.11}$$

where μ_T is the turbulent eddy-viscosity and k is the turbulent kinetic energy. The eddy-viscosity is modelled as

$$\mu_T = \frac{\rho k}{\omega}, \tag{3.12}$$

where ω is the specific dissipation rate. The following modelled transport equations (Wilcox [119]) are solved to obtain k and ω:

$$\begin{aligned} \frac{\partial k}{\partial t} + \frac{\partial k \langle u_j \rangle}{\partial x_j} &= -\frac{1}{\rho} \langle \rho u_i' u_j' \rangle \frac{\partial \langle u_i \rangle}{\partial x_j} - \beta^* k \omega \\ &\quad + \frac{\partial}{\partial x_j} \left[\frac{1}{\rho} \left(\mu + \sigma^* \mu_T \right) \frac{\partial k}{\partial x_j} \right], \end{aligned} \tag{3.13}$$

and

$$\begin{aligned} \frac{\partial \omega}{\partial t} + \frac{\partial \omega \langle u_j \rangle}{\partial x_j} &= -\alpha_1 \frac{\omega}{\rho k} \langle \rho u_i' u_j' \rangle \frac{\partial \langle u_i \rangle}{\partial x_j} \\ &\quad - \beta \omega^2 + \frac{\partial}{\partial x_j} \left[\frac{1}{\rho} \left(\mu + \sigma \mu_T \right) \frac{\partial \omega}{\partial x_j} \right], \end{aligned} \tag{3.14}$$

where $\sigma^* = 0.5$, $\beta^* = 0.072$, $\sigma = 0.5$, $\alpha_1 = 1.0$ and $\beta = 0.072$.

Equations (3.11)-(3.14) describe the standard k-ω model. The transitional variant of the standard k-ω model is used in the study because flow under investigation is not fully turbulent in the entire domain or throughout the pulse. Some modifications are applied to the standard k-ω model to obtain the transitional model. The low-Re correction factor is applied to the eddy-viscosity, seemed as the most important modification,

$$\mu_T = \alpha^* \frac{\rho k}{\omega}, \tag{3.15}$$

which affects the entire closure as it appears in the momentum and turbulence equa-

tions. The low-Re correction factor is obtained from

$$\alpha^* = \alpha^*_\infty \left(\frac{\alpha^*_0 + Re_t/R_k}{1 + Re_t/R_k} \right), \tag{3.16}$$

where $Re_t = \rho k/\mu\omega$, $R_k = 6$, $\alpha^*_0 = \beta_i/3$, $\beta_i = 0.072$ and $\alpha^* = \alpha^*_\infty = 1$. The coefficient on the dissipation term in the k equation takes the form:

$$\beta^* = \beta^*_\infty \left[\frac{4/15 + (Re_t/R_\beta)^4}{1 + (Re_t/R_\beta)^4} \right], \tag{3.17}$$

where $R_\beta = 8$ and $\beta^*_\infty = 0.09$. The production coefficient in the ω equation becomes

$$\alpha_1 = \frac{\alpha_\infty}{\alpha^*} \left(\frac{\alpha_0 + Re_t/R_\omega}{1 + Re_t/R_\omega} \right), \tag{3.18}$$

where $R_\omega = 2.95$, $\alpha_\infty = 0.52$ and $\alpha_0 = 1/9$.

3.3 Shear-Stress Transport (SST) k-ω (or k-ω-SST) model

SST k-ω, denoted by k-ω-SST, model was developed by Menter [120]. This model acts like the standard k-ω model in the near-wall region and becomes the standard k-ϵ model in the far field. The transport equation for k and ω are:

$$\begin{aligned} \frac{\partial k}{\partial t} + \frac{\partial k \langle u_j \rangle}{\partial x_j} &= -\frac{1}{\rho} \langle \rho u_i' u_j' \rangle \frac{\partial \langle u_i \rangle}{\partial x_j} \\ &- \beta^* k\omega + \frac{\partial}{\partial x_j} \left[\frac{1}{\rho} \left(\mu + \sigma^* \mu_T \right) \frac{\partial k}{\partial x_j} \right], \end{aligned} \tag{3.19}$$

and

$$\begin{aligned} \frac{\partial \omega}{\partial t} + \frac{\partial \omega \langle u_j \rangle}{\partial x_j} &= -\alpha_1 \frac{\omega}{\rho k} \langle \rho u_i' u_j' \rangle \frac{\partial \langle u_i \rangle}{\partial x_j} \\ &- \beta \omega^2 + \frac{\partial}{\partial x_j} \left[\frac{1}{\rho} \left(\mu + \sigma \mu_T \right) \frac{\partial \omega}{\partial x_j} \right] \\ &+ 2 \left(1 - F_1 \right) \sigma_{\omega,2} \frac{1}{\omega} \frac{\partial k}{\partial x_j} \frac{\partial \omega}{\partial x_j}, \end{aligned} \tag{3.20}$$

where

$$\sigma^* = F_1/\sigma_{k,1} + (1 - F_1)/\sigma_{k,2}, \tag{3.21}$$

and

$$\sigma = F_1/\sigma_{\omega,1} + (1 - F_1)/\sigma_{\omega,2}. \tag{3.22}$$

Turbulent eddy-viscosity, μ_T, is obtained from:

$$\mu_T = \frac{\rho k}{\omega} \frac{1}{max\left[\frac{1}{\alpha^*}, \frac{SF_2}{a_1\omega}\right]}, \tag{3.23}$$

where S is the strain rate magnitude and α^* is defined in Equation (3.16).

F_1 and F_2 are the blending functions and defined by

$$F_1 = \tanh\left(\Phi_1^4\right), \tag{3.24}$$

and

$$F_2 = \tanh\left(\Phi_2^2\right), \tag{3.25}$$

where

$$\Phi_1 = min\left[max\left(\frac{\sqrt{k}}{0.09\omega y_1}, \frac{500\mu}{y_1^2\omega\rho}\right), \frac{4\rho\sigma_{\omega,2}k}{D_\omega^+ y_1^2}\right], \tag{3.26}$$

$$\Phi_2 = max\left(2\frac{\sqrt{k}}{0.09\omega y_1}, \frac{500\mu}{y_1^2\omega\rho}\right), \tag{3.27}$$

$$D_\omega^+ = max\left[2\rho\sigma_{\omega,2}\frac{1}{\omega}\frac{\partial k}{\partial x_j}\frac{\partial \omega}{\partial x_j}, 10^{-10}\right], \tag{3.28}$$

y_1 is the distance to the nearest wall and D_ω^+ is the positive portion of the cross-diffusion term in Equation (3.20). The blending function, F_1, is unity near the walls, thus Equation (3.20) results in the standard ω equation. The blending function is zero in the far field and thus corresponds to the standard ϵ equation there. Instead of a having a constant β in Equation (3.20), β_i is defined by

$$\beta_i = F_1\beta_{i,1} + (1 - F_1)\beta_{i,2}. \tag{3.29}$$

The model constants are $\sigma_{k,1} = 1.176$, $\sigma_{\omega,1} = 2.0$,$\sigma_{k,2} = 1.0$, $\sigma_{\omega,2} = 1.168$,

$a_1 = 0.31$, $\beta_{i,1} = 0.075$ and $\beta_{i,2} = 0.0828$.

3.4 Large Eddy Simulation

3.4.1 Filtered Governing Equations

Sub-grid scale (SGS), smaller than the filter width used in the computations, eddies are effectively filtered out through a filtering operation in LES. If $g(\mathbf{x})$ is a generic variable, its corresponding filtered variable, also known as the resolvable component of $g(\mathbf{x})$, is denoted by $\bar{g}(\mathbf{x})$. It is defined as the convolution of $g(\mathbf{x})$ with a filter function G, that establishes the scale of the resolved eddies, as (Leonard [121])

$$\bar{g}(\mathbf{x}) = \int_{\mathcal{D}} g(\mathbf{x}')G(\mathbf{x}, \mathbf{x}')\, d\mathbf{x}', \tag{3.30}$$

where $\mathcal{D}$ is the blood domain. Filter function used is defined as

$$G\left(\mathbf{x}, \mathbf{x}'\right) = \begin{cases} \frac{1}{\mathbf{dV}} & \text{if} \quad \mathbf{x}' \in \mathbf{dV} \\ 0 & \quad \mathbf{x}' \text{ otherwise}, \end{cases} \tag{3.31}$$

where $\mathbf{dV}$ is the volume of a computational cell. The finite-volume discretisation itself implicitly performs filtering operation:

$$\bar{g}(\mathbf{x}) = \frac{1}{\mathbf{dV}} \int_{\mathbf{dV}} g(\mathbf{x}')\, d\mathbf{x}', \mathbf{x}' \in \mathbf{dV}. \tag{3.32}$$

The governing equations for LES are obtained by applying the above spatial filter function (3.31) to the Navier-Stokes equations of motion (3.1)-(3.2). The filtered continuity and momentum equations are:

$$\frac{\partial \bar{u}_i}{\partial x_i} = 0, \tag{3.33}$$

$$\frac{\partial \bar{u}_i}{\partial t} + \frac{\partial \bar{u}_i \bar{u}_j}{\partial x_j} = -\frac{1}{\rho}\frac{\partial \bar{p}}{\partial x_i} + \frac{\partial}{\partial x_j}\left[\nu\left(\frac{\partial \bar{u}_i}{\partial x_j} + \frac{\partial \bar{u}_j}{\partial x_i}\right)\right] - \frac{\partial \tau_{ij}}{\partial x_j}, \tag{3.34}$$

where the effects of the subgrid-scale stress tensor,

$$\tau_{ij} = \overline{u_i u_j} - \bar{u_i}\bar{u_j}, \tag{3.35}$$

are modelled using the dynamic Smagorinsky-Lilly model ([122; 115; 116; 123]) and are discussed below.

3.4.2 Smagorinsky-Lilly Subgrid-scale Model

The model was first developed by Smagorinsky [122] and is based on the eddy viscosity formulation as

$$\tau_{ij} - \frac{1}{3}\delta_{ij}\tau_{kk} = -2\nu_{sgs}\bar{S}_{ij}, \tag{3.36}$$

where ν_{sgs} is the subgrid kinetic eddy-viscosity (related to the subgrid dynamic eddy viscosity, μ_{sgs}, as $\rho\nu_{sgs} = \mu_{sgs}$), τ_{kk}, very small for incompressible flow and thus neglected (Erlebacher et al. [124]), is the isotropic part of the SGS stress tensor, δ_{ij} is the Kronecker delta and $\bar{S}_{ij}$ is the rate-of-strain tensor for the resolved scale which is defined by

$$\bar{S_{ij}} = \tfrac{1}{2}\left(\frac{\partial \bar{u_i}}{\partial x_j} + \frac{\partial \bar{u_j}}{\partial x_i}\right). \tag{3.37}$$

In the Smagorinsky-Lilly model, the turbulent eddy-viscosity, ν_{sgs} is modelled as

$$\nu_{sgs} = L_s^2|\bar{S}|, \tag{3.38}$$

where L_s is the mixing length and and $|\bar{S}| = \sqrt{2\bar{S}_{ij}\bar{S}_{ij}}$ is the magnitude of the large scale strain rate tensor. The mixing length L_s is calculated using the following equation

$$L_s = min\left(\kappa d, C_s\triangle\right), \tag{3.39}$$

where κ is the von Kármán constant, which is a dimensionless number in a turbulent flow describing the logarithmic velocity profile near a boundary with a no-slip condition, d is the distance to the closest wall, C_s is the Smagorinsky constant and $\triangle$ is the cubic root of the volume of the computational cell. Hence the

Smagorinsky-Lilly model takes the form

$$\tau_{ij} - \frac{1}{3}\delta_{ij}\tau_{kk} = -2L_s^2|\bar{S}|\bar{S}_{ij}. \tag{3.40}$$

A universal value for Smagorinsky constant C_s is not suitable for transition-to-turbulent flow as C_s varies at different locations inside the full flow domain. Hence C_s is computed dynamically ([115; 116; 123]) using the information obtained from the resolved scales of motion.

3.4.3 Dynamic Smagorinsky-Lilly Subgrid-scale Model

The dynamic subgrid model was first proposed by Germano et al. [115]. In this model, the Smagorinsky constant is computed as a function of time and position. Following Germano et al. [115], a $test$-filter having larger filter width than the original filter, ($\tilde{\triangle} > \triangle$), is applied to the filtered Navier-Stokes Equations. (3.33)-(3.34), leading to the subgrid-scale stress tensor, T_{ij}, similar to τ_{ij} of (3.35) as

$$T_{ij} = \widetilde{\overline{u_i u_j}} - \tilde{\bar{u}}_i\tilde{\bar{u}}_j. \tag{3.41}$$

The relationship between the two stress tensors, τ_{ij} and T_{ij}, can be expressed by the following Germano identity,

$$L_{ij} = T_{ij} - \tilde{\tau_{ij}} \tag{3.42}$$

Assuming the similar functional form to the Samgorinsky model, the deviatoric part of T_{ij} yields

$$T_{ij} - \frac{1}{3}\delta_{ij}T_{kk} = -2(C_s\tilde{\triangle})^2|\tilde{\bar{S}}|\tilde{\bar{S}}_{ij}, \tag{3.43}$$

with the test-scale shears defined similarly to those of the grid scale.

The elements of L_{ij} in Equation (3.42) are the resolved components of the stress tensor associated with the test and grid scales of motion. When $L_s = C_s\triangle$ in Equation (3.39), the right hand side of Equation (3.42) can be calculated explicitly by subtracting (3.40) from (3.43),

$$L_{ij}^a = L_{ij} - \frac{1}{3}\delta_{ij}L_{kk} = 2C_s^2M_{ij}, \tag{3.44}$$

where

$$M_{ij} = -\tilde{\triangle}^2 |\tilde{\bar{S}}| \tilde{\bar{S}}_{ij} + \triangle^2 \widetilde{|\bar{S}| \bar{S}_{ij}}. \tag{3.45}$$

A least square approach is employed, as Lilly [116] suggested, to evaluate the values of C_s^*,

$$C_s^2 = C_s^* = \frac{1}{2} \frac{L_{ij}^a M_{ij}}{M_{ij}^2}. \tag{3.46}$$

The Smagorinsky coefficient C_s is calculated iteratively. To avoid numerical instability, the Smagorinsky coefficient C_s is clipped at zero when it is negative and 0.23 when it exceeds this value ([125]).

3.5 Boundary Conditions

The following boundary conditions have been applied to solve the governing time-averaged Equations (3.9-3.10) and the filtered Equations (3.33-3.34). Furthermore, in the k-ω Transitional models turbulence is specified by percentage of turbulence intensity and hydraulic diameter which is the diameter of the tube.

3.5.1 Velocity Inlet

Flow velocity at the inlet, which influences the transition-to-turbulent of the stenotic flow, is defined by employing velocity inlet boundary condition. It will be described in the relevant chapters.

3.5.2 Wall

A no-slip condition can generally be applied if the domain boundary coincides with a rigid impermeable surface. This no-slip boundary condition is used for the pipe surface, which is defined as

$$\bar{u}_i(\mathbf{x}; t)|_{\Gamma} = 0. \tag{3.47}$$

The prescription for a no-slip condition in the proximity of the wall for LES of a turbulent flow is not straight forward. LES match up with DNS in the vicinity of the wall as all important energy levels containing scales of LES must include all

viscous scales in the sublayer. Acceptable standard results are ensured by using fine grid resolution near the wall, needed to capture the viscous scales in the sublayer. For all cases in this study, the first grid point off the wall lies in the region $y^{+}\approx 1$.

3.5.3 Pressure Outlet

In the pressure outlet boundary condition, only the static pressure at the outlet is specified either by a fixed pressure quantity (for steady flow) or by a pressure wave (for pulsatile flow) and all other quantities are extrapolated from the interior solution. An overall mass balance correction is performed at this boundary and the diffusion fluxes in the direction normal to the exit plane are assumed to be zero, however gradients may exist in the cross-stream direction. Outlet static pressure (wave) will be described in the relevant chapter.

Convergence difficulties arising from reverse flow at the outlet during solution process are minimised by specifying a realistic backflow condition. When backflow occurs during iteration, the use of a pressure outlet boundary condition instead of an outflow condition gives a better convergence rate.

3.6 Overview of Numerical Procedures

An outline of the solution procedure used this study is laid out in this section. The commercial cell-centred finite volume fully implicit and second order accurate in both space and time code, Fluent 6.3, with its turbulent models namely the two-equation k-ω Transitional model and LES with Smagorinsky-Lilly dynamic subgrid model was employed to solve the incompressible governing equations for both steady and physiological pulsatile non-spiral and spiral blood flow through models of arterial stenosis and aneurysm. Fluent with above mentioned turbulent models has previously been exploited to investigate pulsatile and steady flow in arterial stenosis by Ryval et al. [79], Varghese et al. [85], Paul and Larman [17], Barber and Simmons [96] and Gårdhagen et al. [94; 95].

Pressure-based fully implicit solver was chosen for this study. Finite-volume approach is used to discretise the governing equations to construct a system of linear equations. For the k-ω Transitional model, the diffusive and convective terms

of the momentum equations and the equations of turbulent kinetic energy (k) and specific dissipation rate (ω) were discretised by using second-order upwind scheme. However, in LES, a second-order-accurate bounded central differencing scheme is used to discretise the diffusive and convective terms of the momentum equations. And the pressure at a cell face was computed using second-order scheme for both LES and k-ω Transitional model. Three-point backward difference scheme is used to discretise time derivatives. A uniform time step was applied in the simulation and stability of the solution is ensured.

A segregated pressure correction algorithm, SIMPLEC (SIMPLE-Consistent) (Vandoormaal and Raithby [126]) for the k-ω Transitional model and PISO (Pressure-Implicit with Splitting of Operators) (Issa [127]) for LES, is employed to couple pressure with the velocity components and results are stored at the cell centres as Fluent uses co-located scheme. To prevent unphysical checker-boarding of pressure, the Poisson like pressure-correction equation is discretised by using a procedure similar to Rhie and Chow [128] pressure smoothing approach. The pressure correction equation is solved by using the algebraic multigrid (AMG) method. Splitting error, introduced by segregated solution process, is controlled by using an iterative-time advancement scheme.

A point implicit (Gauss-Seidel) solver in conjunction with algebraic multigrid (AMG) method is used to solve the discretised system of linear equations. For all the computations, convergence is assumed to have achieved when the residuals become less than 10^{-5} at each time-step.

3.7 Data Processing and Flow Statistics

Data processing for steady flow and unsteady pulsatile flow is done by using a time-averaging and a phase-averaging technique, respectively, on the solutions obtained from LES model. For a generic flow filtered variable, $\bar{g}$, the time averaged mean over the total number of time-step N_t is computed as

$$\langle \bar{g} \rangle (x, y, z) = \frac{1}{N_t} \sum_{i=1}^{N_t} \bar{g}(x, y, z, t_i), \tag{3.48}$$

where t_1 is the time at which averaging process is initiated. In steady flow, the random turbulent fluctuations, deviation from the time averaged mean, is defined as

$$g'(x,y,z,t) = \bar{g}(x,y,z,t) - \langle\bar{g}\rangle(x,y,z). \tag{3.49}$$

A phase-averaging technique (Varghese et al. [84], Lieber and Giddens [129], Scotti and Piomelli [75] and Mittal et al. [88]) is employed to differentiate the pulsatile fluctuations from the random turbulent fluctuations. The phase-averaged mean over a period $T_f = NT$, where N is the number of time-period cycles over which phase-averaging is performed and T is the time period of each pulsatile cycle, can be calculated as

$$\langle\langle\bar{g}\rangle\rangle(x,y,z,t) = \frac{1}{N}\sum_{n=0}^{N-1}\bar{g}(x,y,z,t+nT). \tag{3.50}$$

The pulsatile phase-average turbulent fluctuations are defined as

$$g''(x,y,z,t) = \bar{g}(x,y,z,t) - \langle\langle\bar{g}\rangle\rangle(x,y,z,t). \tag{3.51}$$

Hence, the root mean square (rms) values of the pulsatile turbulent fluctuations are computed as

$$\langle g''\rangle_{rms} = \sqrt{\langle\langle g''^2\rangle\rangle}. \tag{3.52}$$

The energy spectra, E, of the pulsatile turbulent fluctuations are defined as

$$E = \sum_{j=1}^{L} g''^2 e^{-2i\pi(j-1)(k-1)}\,, \qquad k = 1,2,\cdots,L, \tag{3.53}$$

where L is the number of time-steps. The energy spectra of the pulsatile turbulent fluctuations and the vortex shedding frequency from the sampling frequency are computed by using MATLAB (MATLAB 7.6 [130]). The algorithm for finding the energy spectra is as follows

- Load the data sets of g'' and L and compute g''^2 for the energy spectra.
- Use MATLAB FFT (Fast Fourier Transform) algorithm on g''^2 and save the data as X.

- Use MATLAB Nyquist frequency algorithm on L and save the data as the vortex shedding frequency f_s.
- Lastly, compute the energy spectra, E, taking the absolute value of X.

Chapter 4

A Computational Study on Spiral Blood Flow in Stenosed Arteries with and without an Upstream Curved Section

4.1 Introduction

Computational study of spiral blood flow in arterial stenosis is relatively new. Among all the investigations of spiral blood flow, only two studies, namely Stonebridge et al. [16] and Paul and Larman [17], involve turbulence analysis of the flow in stenosed artery. As pointed out in § 2.4 of Chapter 2, Stonebridge et al. [16] used an ambiguous approach to study spiral flow through stenosis and their findings are open to doubt. On the other hand, Paul and Larman [17] showed turbulent kinetic energy only on the central line for $Re = 500$ and 1000. But maximum turbulence occurs in the shear layer, not along the central line. Apart from the twisting of the heart on its own axis, spiral pattern in blood flow may also be generated due to the presence of a curved section in the upstream. Above mentioned two studies were only on a straight stenosed tube. Therefore, to get a good insight of the transition-to-turbulence of spiral blood flow through arterial stenosis, more numerical investigations are needed.

In this chapter, transition of steady spiral blood flow through models of arterial stenosis with and without an upstream curved section is studied by applying two-equation standard k-ω transitional turbulence model and LES technique. Straight

tubes having axisymmetric cosine-type stenosis with and without upstream curved segment of varying angles are taken as the computational domains. A parabolic profile for axial velocity was introduced at the inlet. And for generating spiral effect at the inlet, one-sixth of the bulk velocity was taken as the tangential velocity, as suggested by Stonebridge et al. [15; 16] that spiral velocity is one-sixth of the forward velocity within the artery. At the outlet, a constant static pressure of 80 mmHg (or 10665.6 Pa) was imposed. In this study, the focus is on the effects of spiral pattern on the flow physics in the downstream region of the stenosis.

As discussed in Chapter 2, the filtering operation in LES divides the flow field up into large scale eddies and small scale (Sub-grid scale or SGS) eddies. The turbulence energy containing large scale eddies are resolved directly while the unresolved small scale eddies are modelled using Smagorinsky-Lilly dynamic subgrid model (Germano [115], Lilly [116] and Kim [123]), as described in Chapter 3. The commercial code Fluent 6.3 is validated for axial velocity profiles in the non-spiral blood flow in a model arterial stenosis for Reynolds numbers $Re = 1000$ and 2000 against available corresponding experimental data of Ahmed and Giddens [28; 27]. The performance of k-ω-SST transitional model in comparison with standard k-ω transitional model is also assessed by comparing the axial velocity profiles obtained from using them against the available corresponding experimental data. In addition, it is also examined how much inlet turbulence intensity can be introduced in LES and k-ω transitional model to control transition and hence benchmark against experimental data.

The layout of this chapter is as follows: a description of the model geometries and mesh distribution is given in § 4.2, inflow boundary condition is presented in § 4.3, validation with experiment and results and discussion are presented in § 4.4 and § 4.5, respectively, and finally a general conclusion of this chapter is drawn in § 4.6.

4.2 Flow Models and Meshing

Solid models of stenosed arteries with and without upstream curved section of varying angles were built using GAMBIT 2.4 (Fluent Inc.) and are shown in Figure 4.1. Diameter of the unstenosed section of the arterial models is $D = 0.02m$ and the

angle of curvature for the upstream curved sections are: $60°$, $90°$ and $120°$. Axial direction is along z-coordinate axis. For the straight tube (without upstream curved section), stenosis is centred at $z = 0$. Lengths of the stenosis, upstream and downstream section of the model arteries are $2D$, $3D$ and $22D$, respectively, as measured from the stenosis throat. Vessels with curved upstream section are further extended to $10D$ in the upstream as shown in Figure 4.1. Degree of a stenosis is generally measured by a percentage reduction in diameter or cross-sectional area at the throat of the stenosis. For our study throughout the thesis 75% stenosis by area reduction, corresponding to a 50% diameter reduction was used as it is clinically significant when the area reduction is greater than 75% (Young [2] and Ku [3]). Furthermore, a 75% stenosis has also been used in many previous experimental and computational studies.

The stenosis is formed using the following cosine-type relation

$$\frac{r_0\left(z\right)}{R} = \begin{cases} 1 - \frac{\delta_c}{2}\left(1 + \cos\frac{z\pi}{D}\right), & -D \leq z \leq D \\ 1, & \text{elsewhere} \end{cases} \tag{4.1}$$

where r_0 and R are the cross-sectional radius and radius of the unaffected section of models, respectively. The parameter δ_c determines the cross-sectional area reduction of the stenosis and it is fixed at $\frac{1}{2}$, giving a 75% reduction of the cross-sectional area at the centre of the stenosis. The cosine-type realistically shaped constriction/stenosis developed in the model arteries using above the relation (4.1) provides a quite reasonable representation of an arterial stenosis, see Ahmed and Giddens [27].

Meshing of the flow domains was done using the meshing software GAMBIT 2.4 (Fluent Inc.). As no-slip condition is applied to the wall, a boundary layer is developed inside the wall to increase the resolution in the sublayer. A gradient scheme is also applied along the axial direction of the models to ensure the finest mesh at the centre and immediate downstream of the stenosis because high level of vortices and turbulent fluctuations occur in these regions. And in the further downstream region of the stenosis a gradually coarsening mesh help keep computational cost to a minimal.

Table 4.1: Parameters of stenosed arteries with and without upstream curved section models.

Model	θ (angle of curvature)	Re
$A1$	$0°$	500
$A2$	$60°$	500
$A3$	$90°$	500
$A4$	$120°$	500
$B1$	$0°$	1000
$B2$	$60°$	1000
$B3$	$90°$	1000
$B4$	$120°$	1000
$C1$	$0°$	1500
$C2$	$60°$	1500
$C3$	$90°$	1500
$C4$	$120°$	1500
$D1$	$0°$	2000
$D2$	$60°$	2000
$D3$	$90°$	2000
$D4$	$120°$	2000

4.3 Inflow Boundary Condition

A parabolic velocity profile along the axial direction:

$$w(x,y) = 2\bar{V}\left[1 - \left(\frac{r}{R}\right)^2\right], \tag{4.2}$$

where $\bar{V}$ is the bulk axial velocity which depends on the blood flow Reynolds number defined as $Re = \frac{\rho \bar{V} D}{\mu}$, is imposed at the inlet of the models. And for introducing spiral property, a tangential velocity profile:

$$v_t(x,y) = \frac{\bar{V}}{6}\left(\frac{r}{R}\right), \tag{4.3}$$

is applied at the inlet. These inlet boundary conditions were coded in C-language using the User Defined Function (UDF) interface of Fluent and linked with the solver. In this chapter, each model is investigated for four Reynolds numbers namely $Re = 500$, 1000, 1500 and 2000. The parameters of the models are presented in

Table 4.1 and models will be referred by their names in the following sections of the chapter.

Inlet turbulence characteristics are defined by inlet turbulence intensities and diameter of the model. For the k-ω models, inlet turbulence intensity of 3.8%, 1.5%, 1.0% and 0.7% are found to give acceptable results for $Re = 500$, 1000, 1500 and 2000, respectively, as it is clear from the experimental validation for two Reynolds number in § 4.4. LES is applied to only model $D1$ for both non-spiral and spiral blood flow and model $B1$ for non-spiral blood flow. Three different inlet turbulent intensities: 0% i.e., no inlet perturbation, 1% and 5% are considered for experimental validation. The inlet perturbations in LES were generated using the vortex method ([125]) and the magnitude of these artificial intensities adjust downstream from the inlet. A time-step size of 1.0×10^{-3} s is taken for temporal advancement in LES. Instantaneous axial velocity at several points on the centreline is recorded for each time-step and sampling for time statistics is initiated when the initial transients has vanished. A total time-steps of 15000 are used to get statistical convergence when the time averaged values has levelled off. Results presented in this chapter are mainly of k-ω model unless it is mentioned otherwise.

4.4 Validation with Experiment

Before discussing the main results, it would be interesting to see how the simulation results obtained from using different turbulence models match available experimental results of Ahmed and Giddens [27; 28]. Figures 4.2 and 4.3 show a comparison of axial velocity profiles at various locations downstream of the stenosis models $B1$ and $D1$, respectively, for non-spiral flow, i.e. straight tube with 75% cross-sectional area reduction stenosis for Reynolds numbers $Re = 1000$ and 2000, respectively. Velocity profiles in models $B1$ and $D1$ obtained by using k-ω models with inlet intensity 1.5% and 0.7%, respectively, closely follow corresponding experimental data, though they over-predict in the further downstream region. For the k-ω models, any inlet intensity lower than above intensities for a corresponding geometric model gives unconvincing velocity profiles as it is clear from Figures 4.2 and 4.3. It is to note from the above figures that the standard k-ω transitional and k-ω-SST transitional models give almost the same results, i.e., none of the two k-ω models

matches experimental data better than the other. So, the standard k-ω transitional model will be used in this thesis in preference to the k-ω-SST transitional model.

Three distinct inlet perturbations: 0%, 1% and 5% were introduced in LES for both geometric models $B1$ and $D1$. It appears from the above figures that LES with 0% inlet intensity agrees better with the experimental results than the other two inlet intensities for model $B1$. However, for model $D1$, LES with 5% inlet intensity matches experimental data better. Therefore for model $D1$, 5% inlet intensity will be used in this study. Furthermore, performance of LES is obviously better than the k-ω transitional model as it can be seen that the blunt turbulent velocity profiles in the downstream region from experimental data matches only LES results. In spite of small disagreements with experimental results of Ahmed and Giddens [27; 28], which are also present in the studies of Ryval et al. [79] and Gårdhagen et al. [95], overall agreement of the present simulation results with experimental results is very good.

4.5 Results and Discussion

Although all the geometric models are studied for spiral blood flow, results from models $D1$, $D2$, $D3$ and $D4$ are presented in detail while the findings from all the models are summarised in bar charts at the end. As the focus is on the effects of spiral pattern on the flow field in the downstream of the stenosis, results in the curved section of all the models having upstream section are ignored to compare the results in the remaining section with corresponding results in the stenosed straight tube without upstream curved section.

Grid resolution tests are done for spiral flow in two models namely $D1$ and $D3$ by applying LES and standard k-ω transitional model, respectively, to ensure simulation results are independent of grid arrangements employed. The test results are shown in Figures 4.4 and 4.5 for axial velocity profiles at different locations along the axial directions. In Figure 4.4 for model $D1$, Grid 1 corresponds to a total of $\approx 500,000$ control volumes which is increased by 40% for Grid 2 to get $\approx 700,000$ control volumes. Grid 3 consists of huge control volumes i.e., $\approx 1,260,000$ which is further an increase of 80% on Grid 2. However, in Figure 4.5 for model $D3$, Grid 1, Grid 2 and Grid 3 consist of $\approx 750,000$, $950,000$ and $1,500,000$ control

volumes, respectively, keeping almost the same ratio of control volumes as in model $D1$. The grid resolution studies in Figures 4.4 and 4.5 clearly show that resolution of Grid 2 is good enough to get high level accuracy in the simulation while keeping the computational cost to a minimum.

4.5.1 Flow Visualization

To see how the flow field in the downstream of the stenosis in non-spiral flow differs from that in the spiral flow, cross-sectional streamlines are appended on the contour plot of axial velocity at various locations along the flow directions in Figures 4.6-4.13 for models $D1$, $D2$, $D3$ and $D4$. As a result of an adverse pressure gradient in the downstream region of the stenosis, reverse flow occurs near the wall, causing recirculation of blood there. Figure 4.6 demonstrates that the re-circulation region for non-spiral flow in model $D1$ is between $2D$ (frame e) and $4D$ (frame g). The reverse flow or negative axial velocity is stretched from $2D$ (frame e) to $4D$ (frame g) in Figure 4.6, which makes the blood there to recirculate near the wall. While in Figure 4.7 for spiral flow in the same model, the re-circulation region is larger and lies between $2D$ (frame e) and $5D$ (frame h) as the reverse flow near the wall is stretched up to $5D$. Also the twisting pattern of the spiral flow in this region is much stronger than that found in the further downstream region. In the further downstream region, the spiral property tries to stabilise the flow. The "twisted" pattern found in the downstream of spiral flow in model $D1$ as seen in Figure 4.7 is similar to the "corkscrew" pattern found in the MRI measurements of the blood flow in a thrombosed artery by Frydrychowicz et al. [10].

However, the length of the recirculation zone for non-spiral and spiral flow in model $D3$ is same and lies between $2D$ (frame e) and $5D$ (frame h), as it is clear from Figures 4.8 and 4.9. It is to note that unlike spiral flow in model $D1$ as in Figure 4.7, no spiral pattern is seen in the upstream region and at the throat of the stenosis for either non-spiral or spiral flow in model $D3$. But for spiral flow in model $D3$ as in Figure 4.9, a rotational pattern is visible in the further downstream region. Moreover, two distinct recirculations of secondary flow can be observed for both non-spiral and spiral flow in model $D3$ at $-3D$ (frame a) in the upstream of the stenosis due to the presence of a curved section there. For both spiral and non-

spiral flow in models $D1$ and $D3$, the velocity vectors move towards the centre at the throat of the stenosis where the axial velocity is maximum, forming a narrow jet from throat of the stenosis. At the onset of turbulence at $2D$ (frame e), direction of the vectors reverses from their previous direction at $1D$ (frame d) where they start to break away from the centre as it is clear from Figures 4.6, 4.7, 4.8 and 4.9.

No spiral pattern is seen anywhere in the flow domain for either non-spiral or spiral flow in models $D2$ and $D4$ from Figures 4.10, 4.11, 4.12 and 4.13, respectively. For both non-spiral and spiral flow in these two models $D2$ and $D4$, velocity vectors between $1D$ (frame d) and $5D$ (frame h) downstream of the stenosis, which is the region of most turbulence activities, move towards a ring formed in the cross-sections where axial velocity changes from positive to negative near the wall and elsewhere in the flow domain the vectors move from wall to wall. These large recirculation zones for both non-spiral flow and spiral flow in the models are clinically harmful as these may cause potential damage to blood cells and intima of the stenosed artery (Paul and Larman [17], Molla [90]).

Furthermore, it can also be seen from the pathlines for spiral flow in model $D2$ as presented in Figure 4.14 that the flow enters the stenosis without any spiral pattern. The absence of spiral pattern in the immediate upstream of the stenosis and at the throat of the stenosis for spiral flow in models $D2$, $D3$ and $D4$ may be due to the constraints imposed in the simulations such as rigid wall of the models and steady flow. But in reality, the arterial wall is distensible and the arerial blood flow is unsteady pulsatile due to the heart pumping.

The effects of spiral pattern are more clear from the contour plot of tangential velocity in Figures 4.15-4.22 for both non-spiral and spiral flow in models $D1$, $D2$, $D3$ and $D4$. Among all the contour plots of tangential velocity, it is of rotational pattern at the upstream region and the throat of the stenosis only in Figure 4.16 i.e., for spiral flow in model $D1$. Fig. 4.15 shows that maximum and minimum tangential velocity for non-spiral flow in model $D1$ occurs at $1D$ (frame d) i.e. at the post-lip of the stenosis. However, maximum and minimum tangential velocity for spiral flow in the same model $D1$ occur at the throat of the stenosis and $4D$ (frame g) downstream, respectively, as seen from Figure 4.16. Figures 4.17-4.22 demonstrate that, for both non-spiral and spiral flow in other models namely $D2$, $D3$ and $D4$, tangential velocity has its maximum and minimum at the throat of the steno-

sis where it forms two crescent-like shapes of positive and negative values. Unlike contour plots of tangential velocity for spiral flow in model $D1$, no rotational pattern at the upstream or at the throat of the stenosis is seen for spiral flow in models $D2$, $D3$ and $D4$ (see Figures 4.18, 4.20 and 4.22), which is again an indication of the loss of spiral pattern before the stenosis in the models with an upstream curved section as discussed in the above paragraph. As discussed above, this may be due to the rigid wall of the models and/or the treatment of blood flow as steady flow in the simulations. For all the cases, a ring of negative tangential velocity can be observed around the centre of the cross-sections in the recirculation zones, which takes a semicircular shape in the further downstream region.

4.5.2 Flow Velocity

The mean axial velocity, $\langle w \rangle$, profiles for both non-spiral and spiral flow at different locations in the models $D1$ and $D2$, $D3$ and $D4$ are presented in Figures 4.23 and 4.24, respectively. Note that the corresponding LES results in model $D1$ are also appended in Figure 4.23. As blood enters the stenosis, it accelerates through the constriction, generating a plug-shaped velocity profile within the stenosis and a flow separation region immediately downstream of the stenosis. No substantial effect of spiral flow on the axial velocity is observed from the above figures. However, the axial velocity in model $D1$ increases for spiral flow near the wall and decreases around the centre between $2D$ (frame d) and $4D$ (frame f) which can be seen from the LES results. In the further downstream region, i.e. after $8D$ (frame j), it is almost same for all models. Magnitude of the axial velocity around the centre is maximum in model $D1$ in the immediate downstream region and it falls slightly from this maximum value in model $D3$. While it is minimum in models $D2$ and $D4$. Though the axial velocity is almost same in models $D2$ and $D4$, it decreases in model $D4$ around the mid-region between the wall and the centre in the downstream between $3D$ (frame e) and $4D$ (frame f). All these differences in the axial velocity profiles in the different models are due to the effect of an upstream curved segment of varying angles of curvature.

Figure 4.25 and 4.26 show the mean x-velocity, $\langle u \rangle$, profiles at different locations in models $D1$ and $D2$, $D3$ and $D4$, respectively. The LES results for the mean

x-velocity differ significantly from the corresponding k-ω model results, which can be seen from Figure 4.25. Also in model $D1$, the spiral effect on $\langle u \rangle$ is distinctly visible, especially up to $9D$ (frame k) as the $\langle u \rangle$ profiles in non-spiral flow vary in magnitude and pattern from those in spiral flow. However, in other models, the effect of spiral flow is not significant on $\langle u \rangle$, as it is clear from Figure 4.26. The magnitudes of $\langle u \rangle$ are almost same in models $D1$ and $D3$ at all corresponding locations, however, they are maximum in model $D2$ and of opposite pattern in model $D4$ which can be attributed to the existence of an upstream curved segment of different angles of curvature. The mean y-velocity profiles, $\langle v \rangle$, in models $D1$ and $D2$, $D3$ and $D4$ are shown in Figures 4.27 and 4.28, respectively, to see the influence of spiral flow and an upstream curved section on $\langle v \rangle$. As seen in $\langle u \rangle$ profiles, the LES results for $\langle v \rangle$ do not match the corresponding k-ω model results, which is clear from Figure 4.27. Due to the effect of spiral velocity introduced at the inlet, the $\langle v \rangle$ profiles for spiral flow at different locations differ from the corresponding results for non-spiral flow in model $D1$, which can also be seen from this figure, especially from LES results. But $\langle v \rangle$ profiles for spiral and non-spiral flow are almost same in other models at all corresponding locations, as can be seen from Figure 4.28. However, the effect of an upstream curved section on $\langle v \rangle$ is distinctly visible from the figure. At some places in the downstream region up to $5D$ (frame g), $\langle v \rangle$ is maximum in model $D4$ which is follwed by its corresponding value in models $D3$ and $D2$. In the further downstream region, the $\langle v \rangle$ profiles are almost same in all models.

4.5.3 Turbulent Kinetic Energy (TKE)

The effects of spiral flow and un pstream curved segment on the turbulent kinetic energy (TKE) at different locations in the flow domain in models $D1$ and $D2$, $D3$ and $D4$ are presented in Figures 4.29 and 4.30, respectively. The LES results in Figure 4.29 clearly show that in model $D1$ at some places between $2D$ (frame d) to $5D$ (frame g) i.e., in the core turbulence region, the TKE increases greatly for spiral flow though it may decrease along the centreline as shown by Paul and Larman [17]. Also the TKE in model $D2$ increases at some places when a spiral effect is introduced at the inlet of the model as can be seen from Figure 4.30(d-f). No influence

of spiral flow or an upstream curved segment on the TKE in other models can be seen from Figure 4.30. It remains same in the other models at the corresponding locations, however, the TKE is high in the post-stenotic region between $2D$ (frame d) and $6D$ (frame h). The high TKE in the post-stenotic region for spiral flow in modelS $D1$ and $D2$ has even more serious detrimental effect on the human circulatory system because large TKE damages the red blood cell materials and activates the platelets in the blood leading to many pathological diseases (Ku [3]).

4.5.4 Wall Pressure and Shear Stress

Figures 4.31 and 4.32 present the circumferential average wall pressure in models $D1$ and $D2$, $D3$ and $D4$, respectively. And the circumferential average wall shear stress (WSS) in models $D1$ and $D2$, $D3$ and $D4$ are shown in Figures 4.33 and 4.34, respectively. Note that the corresponding LES results for both non-spiral and spiral flow in model $D1$ are also shown in Figures 4.31 and 4.33. The spiral flow does not affect the wall pressure and WSS in model $D1$, $D2$, $D3$ and $D4$ as it is clear from the above figures. The large velocities at the throat of the stenosis cause a steep drop in pressure at the stenosis throat in each model. Figures 4.31 and 4.32 show that the pressure drop around the stenosis throat is greater in models $D1$ and $D3$ than other two models $D2$ and $D4$. The Pressure drop is maximum in model $D3$ and it is same and minimum in models $D2$ and $D4$. The LES results in Figure 4.31 shows that the pressure in model $D1$ recovers earlier than other models after its drop. This high Bernoulli-type pressure drop at the stenosis throat can cause local collapse of the stenosis in severe stenoses (Wootton and Ku [6]). Consequently, choking can restrict the flow rate and generated compressive loading may rupture the plaque, a precipitating event in most heart attacks and stroke (Wootton and Ku [6], Li et al. [8]).

The WSS increases to an extremely high magnitude just prior to the throat of the stenosis in each model because of high velocity at the throat as can be seen in Figures 4.33 and 4.34. It drops just after the throat where it is almost zero and takes an oscillatory form in the post-stenotic region. Like the pressure drop, the WSS increase just before the throat is maximum (31 Pa) and almost same in models $D1$ and $D3$ while in models $D2$ and $D4$, the WSS is of same value and its rise before

the throat is (25 Pa) less than that in other two models. This high increase in the WSS just before the throat has many pathological significances. Malek et al. [9] reported that shear stress higher than 70 dynes/cm^2 (or 7 Pa) may induce thrombosis. According to Fry [36], high WSS ($> 379 \pm 85$ (SD) dynes/cm^2 or 37.9 ± 8.5 (SD) Pa) around the throat may damage endothelial cells and fissure plaque. And it may also overstimulate platelet thrombosis (Ku [3]), leading to total occlusion (Folts et al. [38]). Additionally, high shear stress ($\geq$ 100 dynes/cm^2 or 10 Pa) is also responsible for deformation of the red blood cells (Sutera and Mehrjardi [37]). Moreover, the abnormal oscillatory shear stress found in the downstream of the stenosis in all the models may cause potential damage to the red blood cells and the inner lining of a post-stenotic blood vessel (Paul and Molla [93]).

4.5.5 Summary of the other models

Bar charts in Figure 4.35 summarises the effects of spiral flow and upstream curved segments on maximum (derived from the whole domain) TKE in all the models. Spiral flow has no significant effect on the maximum TKE as it is clear from the Figure 4.35. The maximum TKE increases slightly for spiral flow in models $A1$, $B1$, $B3$, $C2$, $D1$ and $D2$, while for spiral flow in models $A2$, $A3$, $A4$, $B2$, $B4$, $C4$ and $D4$, it decreases a little and its change in the remaining models is very insignificant. Particularly, for spiral flow, a maximum increase of $\approx 6\%$, $\approx 2\%$, $\approx 3\%$ and $\approx 5\%$ in the maximum TKE for $Re = 500$ in straight stenosed tube, $Re = 1000$ in straight stenosed tube, $Re = 1500$ in 60° curved upstream model and $Re = 2000$ in 60° curved upstream model, respectively, can be observed. And a maximum decrease of $\approx 7\%$, $\approx 3\%$, $\approx 2\%$ and $\approx 2\%$ in the maximum TKE for $Re = 500$ in 60° curved upstream model, $Re = 1000$ in 60° curved upstream model, $Re = 1500$ in 120° curved upstream model and $Re = 2000$ in 120° curved upstream model, respectively, can also be found for spiral flow.

The influence of an upstream curved segment on the maximum TKE can be seen for all the investigated Reynolds numbers. For Reynolds numbers $Re = 1000, 1500$ and 2000, the maximum TKE increases most in the model with 120° curved upstream segment which is followed by the maximum TKE in 60°, 90° and 0° curved upstream segment model consecutively; but for $Re = 500$, the maximum TKE de-

creases most in 120° curved upstream segment model. It is interesting to note that the maximum TKE in 90° curved upstream segment model drops compared with 60° curved upstream segment model, especially for $Re = 1500$ and $Re = 2000$. Further investigations involving more models with a curved upstream segment close to (less than and greater than) 90° curved upstream segment and different efficient numerical approach such as LES for the simulations are needed to comprehend this sudden drop of the maximum TKE in 90° curved upstream segment model. The maximum TKE rises by 18%, 18% and 19% in 120° curved upstream model compared with its minimum value in straight stenosed tube for $Re = 1000$, 1500 and 2000, respectively; however, for $Re = 500$, it rises by 34% in 60° curved upstream model compared with its minimum value in 120° curved upstream model. As mentioned earlier, this extreme rise in TKE in curved models may potentially harm the red blood cells and activate the platelets in the blood, resulting in many pathological diseases (Ku [3]).

Additionally, contour plot of TKE for both non-spiral and spiral flow in model $A1$ in Figure 4.36 also shows that (maximum) TKE increases for spiral flow (frame b), though it decreases along the centreline for spiral flow as reported by Paul and Larman [17]. Therefore, taking only the centreline data for TKE would provide an incomplete description of the spiralling effects.

As to the effect of spiral flow on WSS, WSS at different phases of the wall in model $A1$ in Figure 4.37 for both non-spiral and spiral flow further clarifies that the influence of spiral flow on WSS is negligible. Furthermore, it can be observed that the effect of spiral flow on the maximum pressure drop (Figure 4.38) and the maximum WSS (Figure 4.39) in any model for all the Reynolds numbers is very insignificant. However, the effect of upstream curved segment on the maximum pressure drop and the maximum WSS is clearly seen. The maximum pressure drop increases by $\approx 7\%$ in 120° curved upstream model compared with its minimum value in straight stenosed tube for all the investigated Reynolds numbers. On the other hand, the maximum WSS increases by $\approx 3\%$, $\approx 1.5\%$, $\approx 3\%$ and $\approx 4\%$ in 120° curved upstream model compared with its minimum value in straight stenosed tube for $Re = 500$, 1000, 1500 and 2000, respectively. Thus, the stenosis in an artery with a curved upstream segment increases the risk of potential rapture of the plaque and thrombosis formation, as discussed in § 4.5.4, compared with a straight

stenosed artery.

4.6 Conclusion

The standard k-ω transitional model and LES were applied to study the effects of steady spiral blood flow in 75% area reduction arterial stenosis models without and with upstream curved segments of 60°, 90° and 120° angle of curvature for Reynolds numbers $Re = 500$, 1000, 1500 and 2000. LES results for non-spiral flow in the straight stenosed tube for Reynolds numbers $Re = 1000$ and 2000 with appropriate inlet perturbation match the corresponding experimental data closely. Spiral blood flow increases the recirculation zone in the straight stenosed tube which is potentially harmful as it can induce blood clot, a potential source of stroke.

The effect of spiral velocity on any flow property in the models with an upstream curved segment for the investigated Reynolds numbers is insignificant. In the models with an upstream curved segment, spiral pattern is lost before the stenosis, which may be due to the rigid wall of the models taken in the simulations and/or assumption of steady flow of blood in the simulations. Contrary to the reports of Paul and Larman [17] and Stonebridge et al. [16], the influence of spiral blood flow increases the TKE in the straight stenosed tube for the investigated Reynolds numbers, whereas it does not affect WSS or wall pressure. Although spiral pattern has many beneficial effects on hemodynamics in unstenosed arteries as reported by Stonebridge et al. [15], its detrimental effects are observed in stenosed arteries.

As for the effects of upstream curved segment, the results in the straight stenosed tube at different locations are almost same as the corresponding results in the model with 90° curved upstream segment at corresponding locations and greater than the corresponding data in the other two models. In addition, the other two models, i.e. 60° and 120° curved upstream models give almost same results at corresponding locations. However, the effect of curved upstream segment on the maximum TKE is prominent as the maximum TKE increases significantly in 120° curved upstream model from its minimum value in straight stenosed tube for $Re = 1000$, 1500 and 2000 and it decreases dramatically in 120° curved upstream model from its maximum value in 60° curved upstream model for $Re = 500$. Additionally, the maximum pressure drop and the maximum WSS increase in 120° curved upstream

model from their corresponding minimum values in straight stenosed tube for all the Reynolds numbers.

Blood flow is physiologically pulsatile. The study in this chapter was simplified by considering steady flow in the arterial stenosis models. A thorough numerical investigation of physiologically pulsatile spiral blood flow in a straight stenosed tube will be done as a natural extension of this chapter.

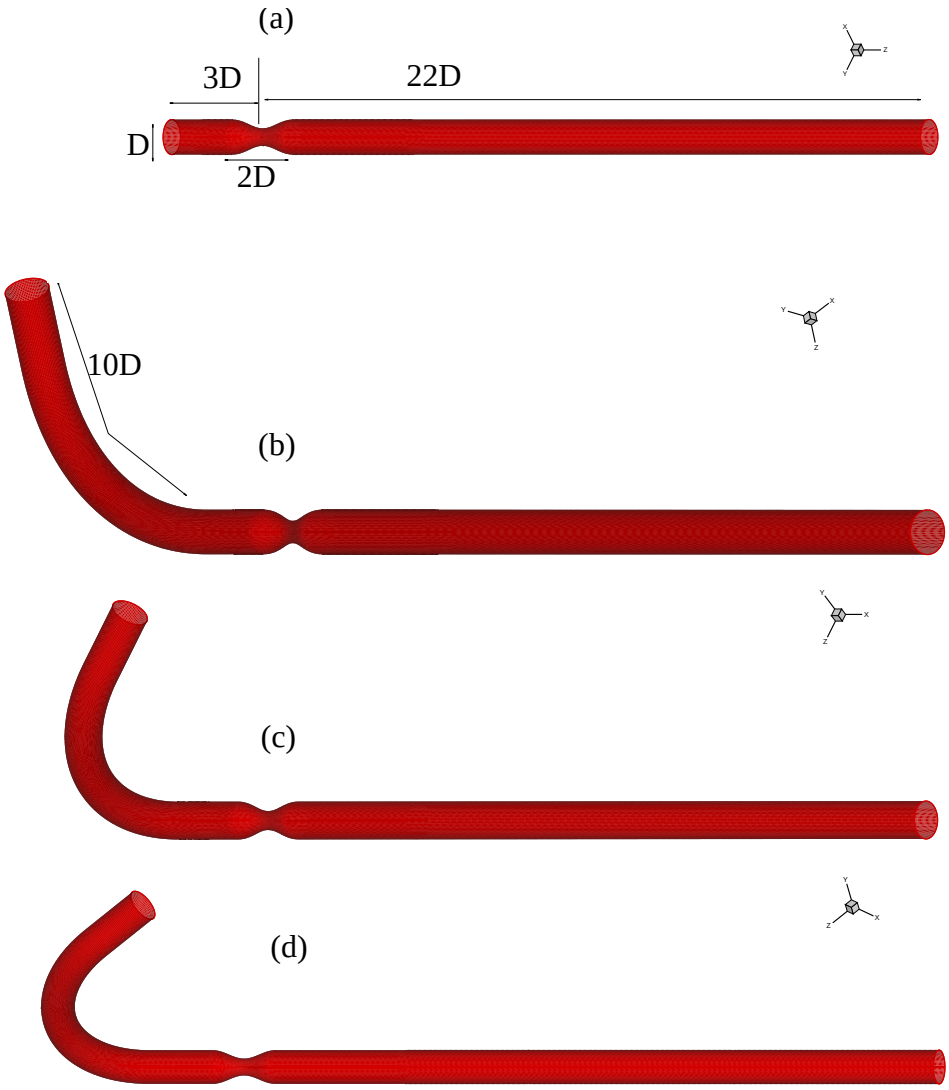

Figure 4.1: Three dimensional view of model arteries without and with an upstream curved section of varying angles of curvature. Angles of curvature in frame (a), (b), (c) and (d), are $0°$, $60°$, $90°$ and $120°$, respectively.

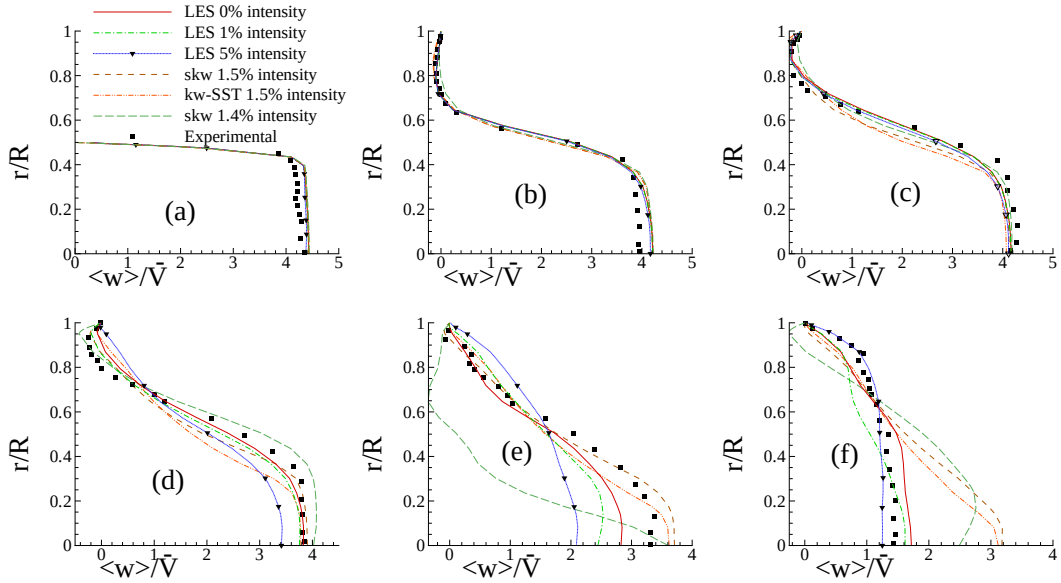

Figure 4.2: Axial velocity comparison with the experimental data of Ahmed and Giddens [28] for non-spiral flow in model $B1$ at (a) $z/D = 0$, (b) $z/D = 1$, (c) $z/D = 2.5$, (d)$z/D = 4$, (e) $z/D = 5$ and (f) $z/D = 6$.

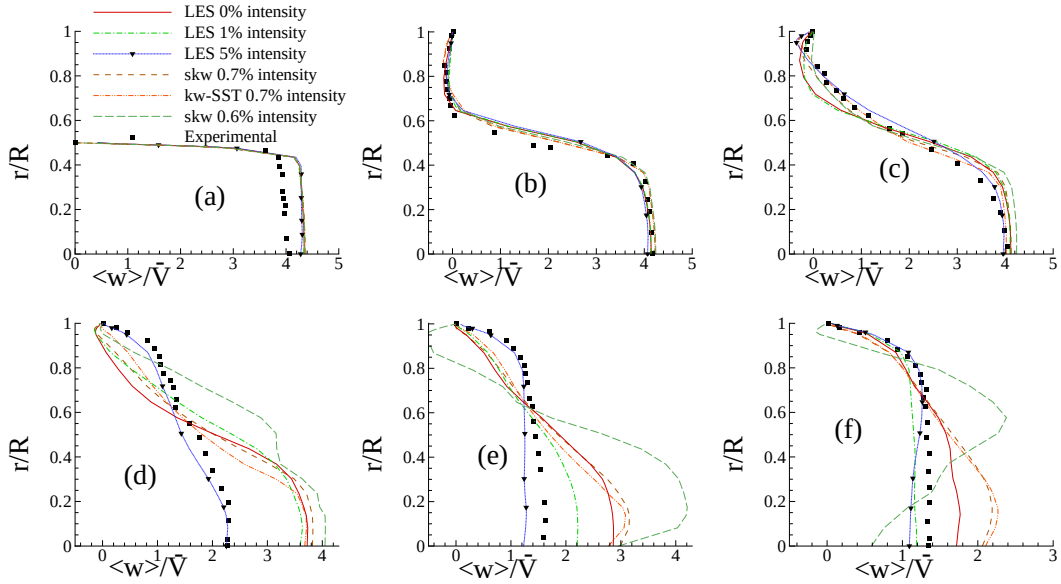

Figure 4.3: Axial velocity comparison with the experimental data of Ahmed and Giddens [27] for non-spiral flow in model $D1$ at (a) $z/D = 0$, (b) $z/D = 1$, (c) $z/D = 2.5$, (d)$z/D = 4$, (e) $z/D = 5$ and (f) $z/D = 6$.

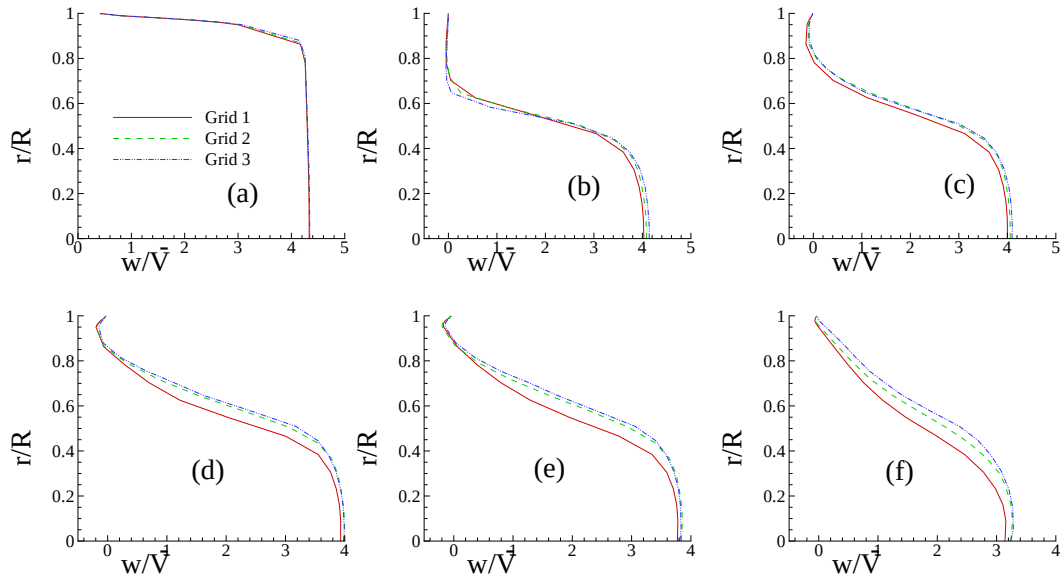

Figure 4.4: Grid resolution study for LES of spiral flow in model $D1$ showing axial velocity at (a) $z/D = 0$, (b) $z/D = 1$, (c) $z/D = 2.5$, (d)$z/D = 4$, (e) $z/D = 5$ and (f) $z/D = 6$.

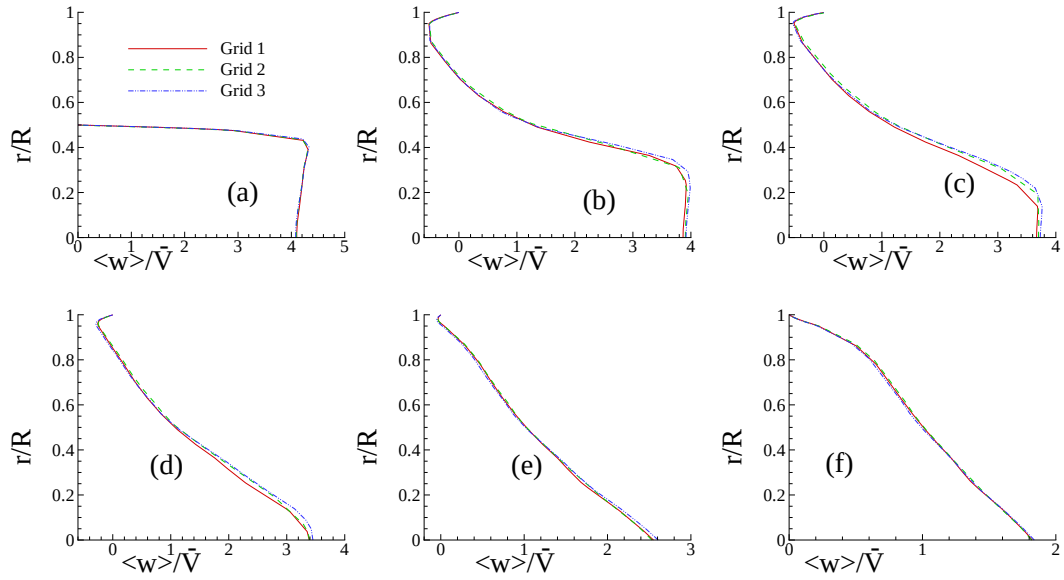

Figure 4.5: Grid resolution study for spiral flow in model $D3$ with $k-\omega$ Transitional approach showing axial velocity at (a) $z/D = 0$, (b) $z/D = 1$, (c) $z/D = 2.5$, (d)$z/D = 4$, (e) $z/D = 5$ and (f) $z/D = 6$.

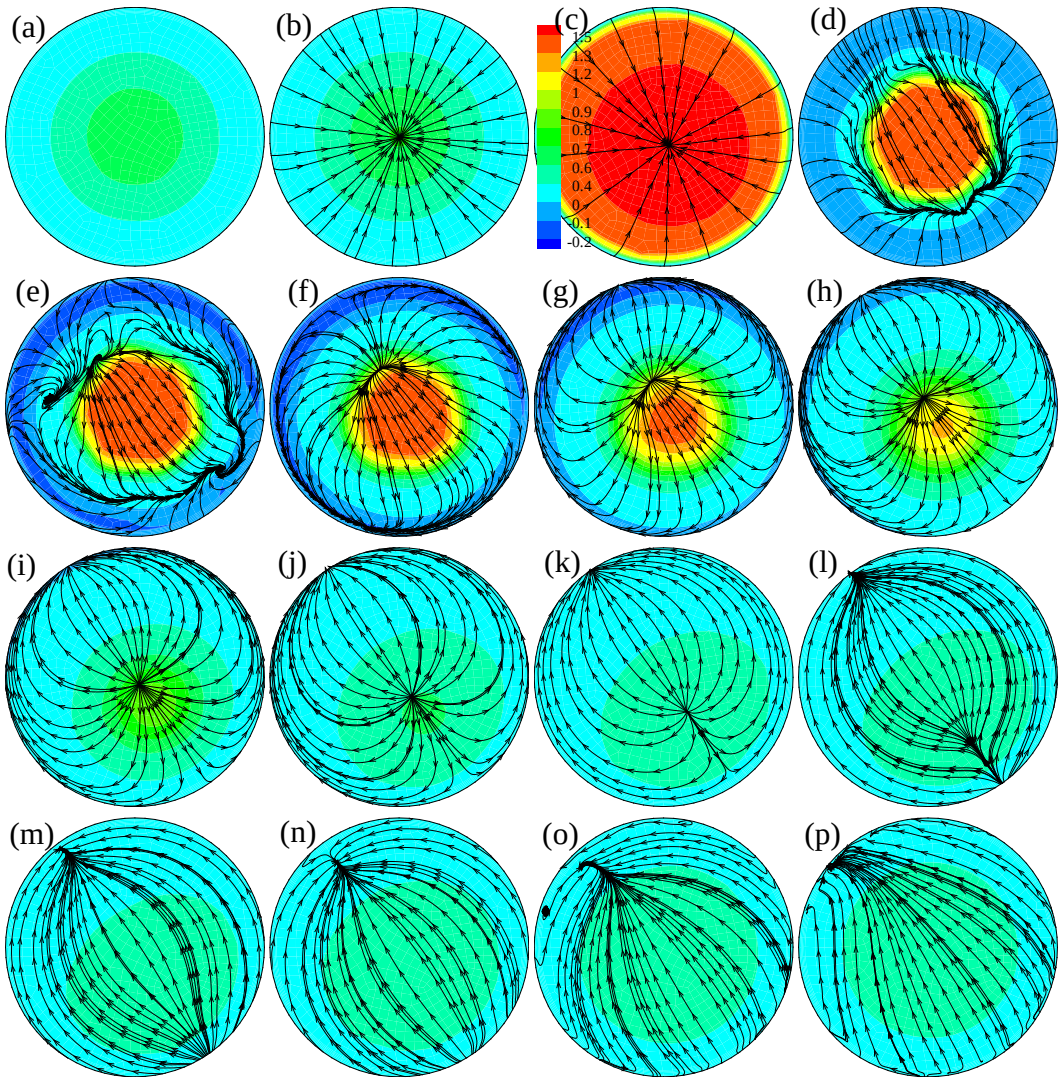

Figure 4.6: Cross-sectional streamlines appended on the axial velocity contour for non-spiral flow in model $D1$ at (a) $z/D = -3$, (b) $z/D = -1$, (c) $z/D = 0$, (d) $z/D = 1$, (e) $z/D = 2$, (f) $z/D = 3$, (g) $z/D = 4$, (h) $z/D = 5$, (i) $z/D = 6$, (j) $z/D = 7$, (k) $z/D = 8$, (l) $z/D = 9$, (m) $z/D = 10$, (n) $z/D = 12$, (o) $z/D = 16$ and (p) $z/D = 22$.

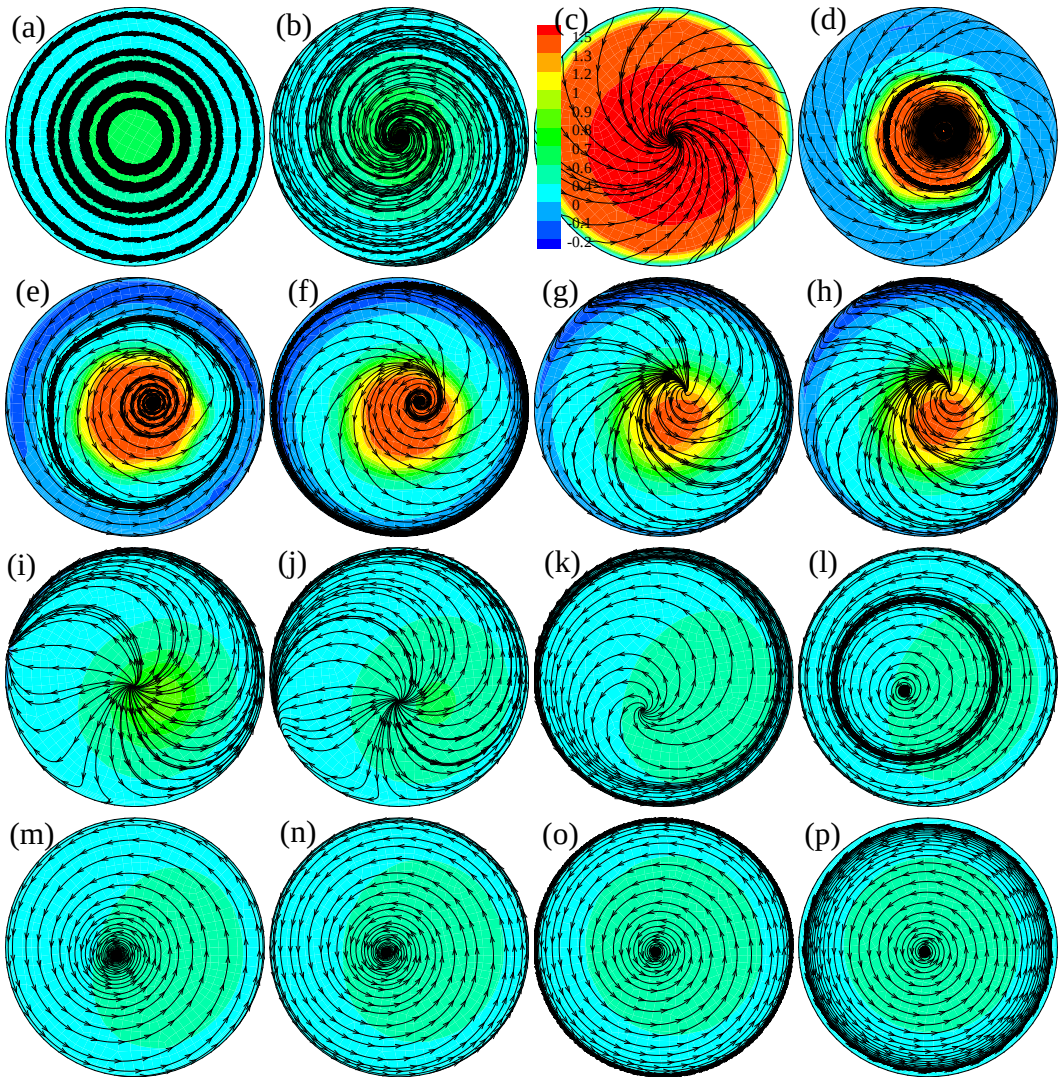

Figure 4.7: Cross-sectional streamlines appended on the axial velocity contour for spiral flow in model $D1$ at (a) $z/D = -3$, (b) $z/D = -1$, (c) $z/D = 0$, (d) $z/D = 1$, (e) $z/D = 2$, (f) $z/D = 3$, (g) $z/D = 4$, (h) $z/D = 5$, (i) $z/D = 6$, (j) $z/D = 7$, (k) $z/D = 8$, (l) $z/D = 9$, (m) $z/D = 10$, (n) $z/D = 12$, (o) $z/D = 16$ and (p) $z/D = 22$.

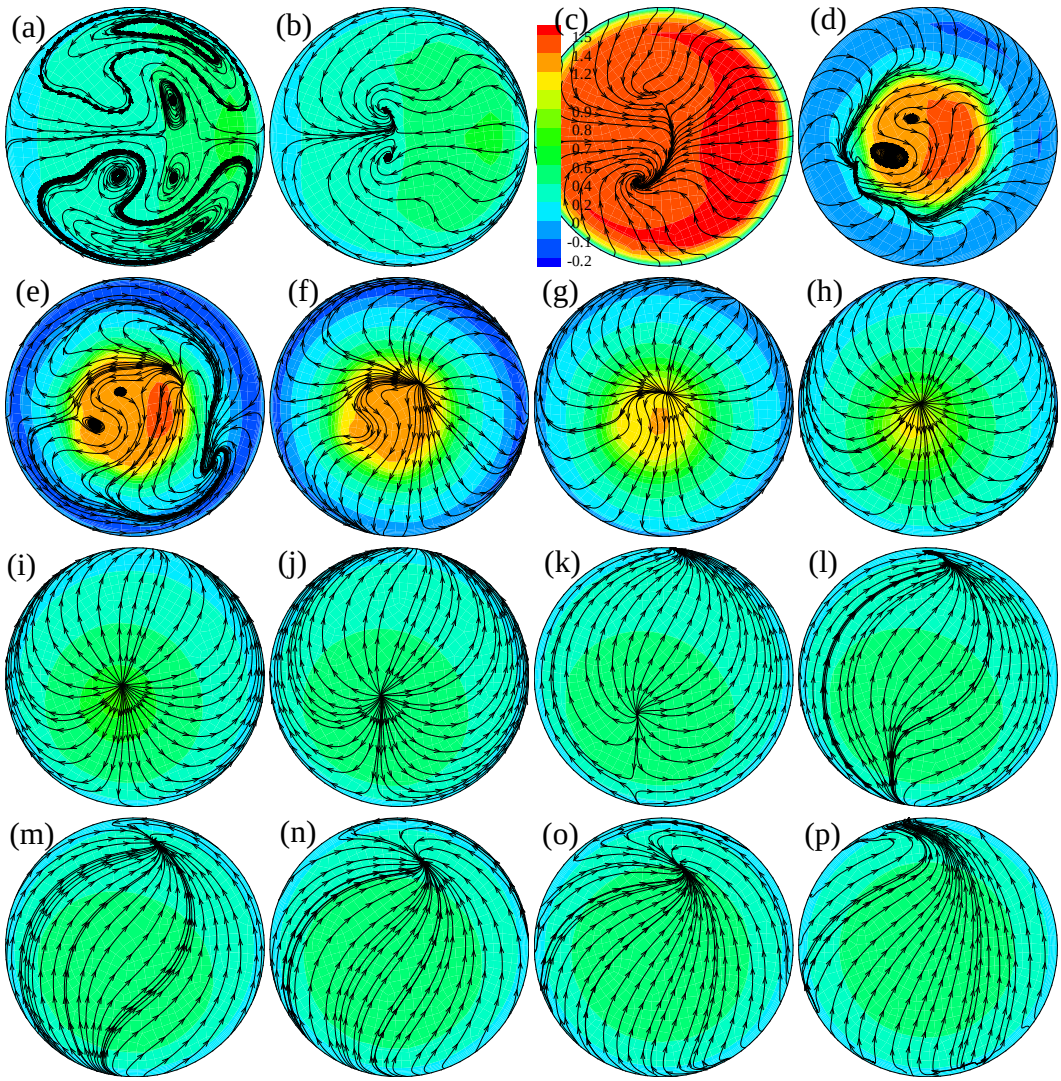

Figure 4.8: Cross-sectional streamlines appended on the axial velocity contour for non-spiral flow in model $D3$ at (a) $z/D = -3$, (b) $z/D = -1$, (c) $z/D = 0$, (d) $z/D = 1$, (e) $z/D = 2$, (f) $z/D = 3$, (g) $z/D = 4$, (h) $z/D = 5$, (i) $z/D = 6$, (j) $z/D = 7$, (k) $z/D = 8$, (l) $z/D = 9$, (m) $z/D = 10$, (n) $z/D = 12$, (o) $z/D = 16$ and (p) $z/D = 22$.

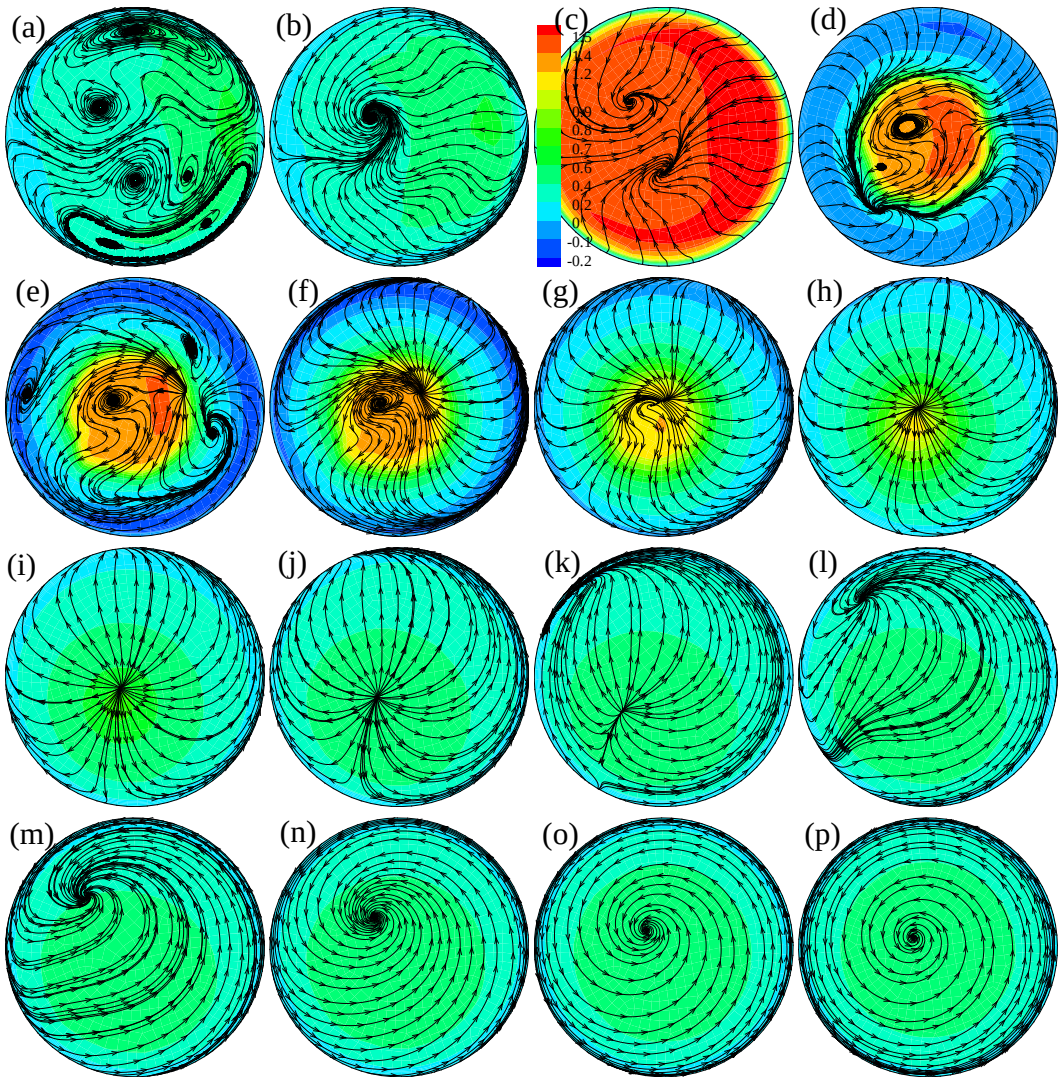

Figure 4.9: Cross-sectional streamlines appended on the axial velocity contour for spiral flow in model $D3$ at (a) $z/D = -3$, (b) $z/D = -1$, (c) $z/D = 0$, (d) $z/D = 1$, (e) $z/D = 2$, (f) $z/D = 3$, (g) $z/D = 4$, (h) $z/D = 5$, (i) $z/D = 6$, (j) $z/D = 7$, (k) $z/D = 8$, (l) $z/D = 9$, (m) $z/D = 10$, (n) $z/D = 12$, (o) $z/D = 16$ and (p) $z/D = 22$.

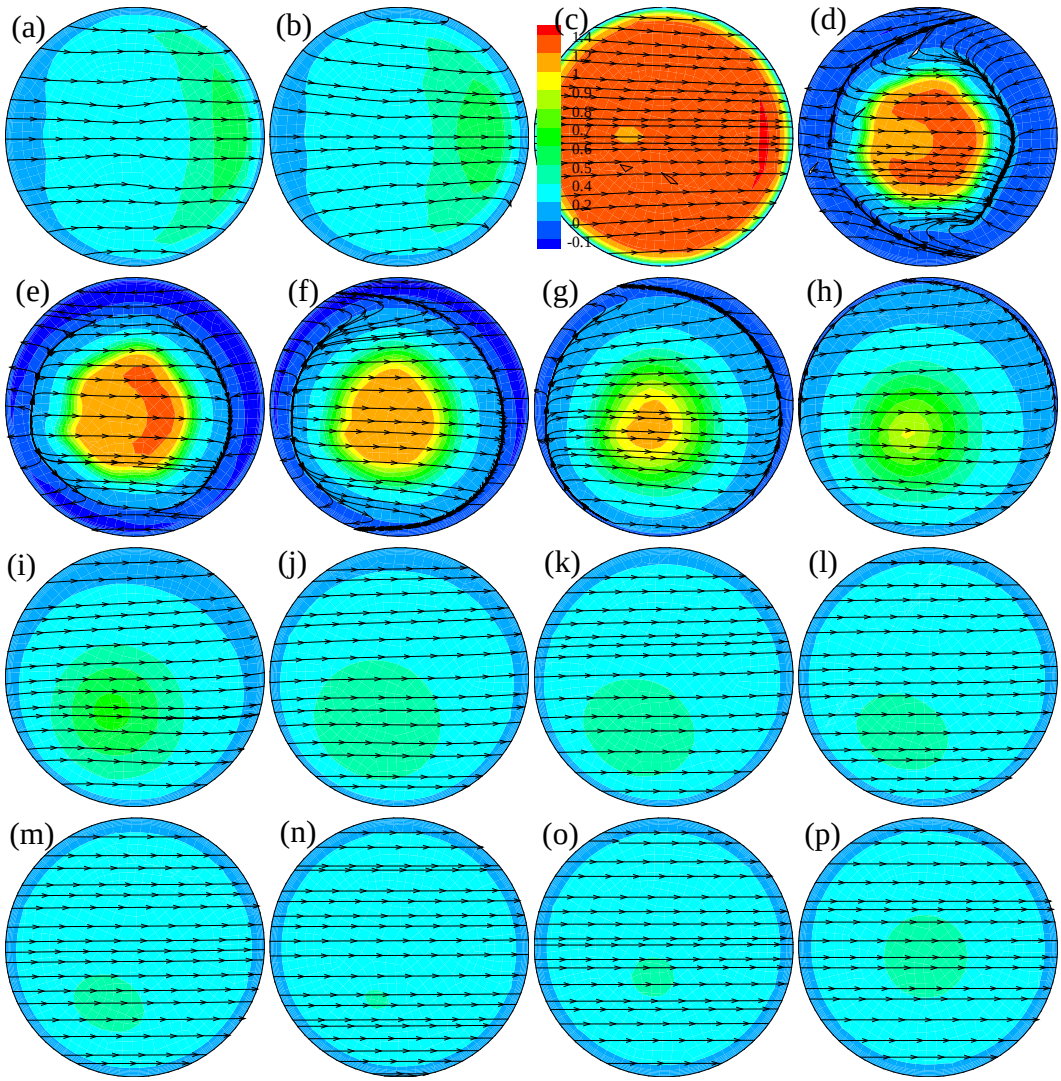

Figure 4.10: Cross-sectional streamlines appended on the axial velocity contour for non-spiral flow in model $D2$ at (a) $z/D = -3$, (b) $z/D = -1$, (c) $z/D = 0$, (d) $z/D = 1$, (e) $z/D = 2$, (f) $z/D = 3$, (g) $z/D = 4$, (h) $z/D = 5$, (i) $z/D = 6$, (j) $z/D = 7$, (k) $z/D = 8$, (l) $z/D = 9$, (m) $z/D = 10$, (n) $z/D = 12$, (o) $z/D = 16$ and (p) $z/D = 22$.

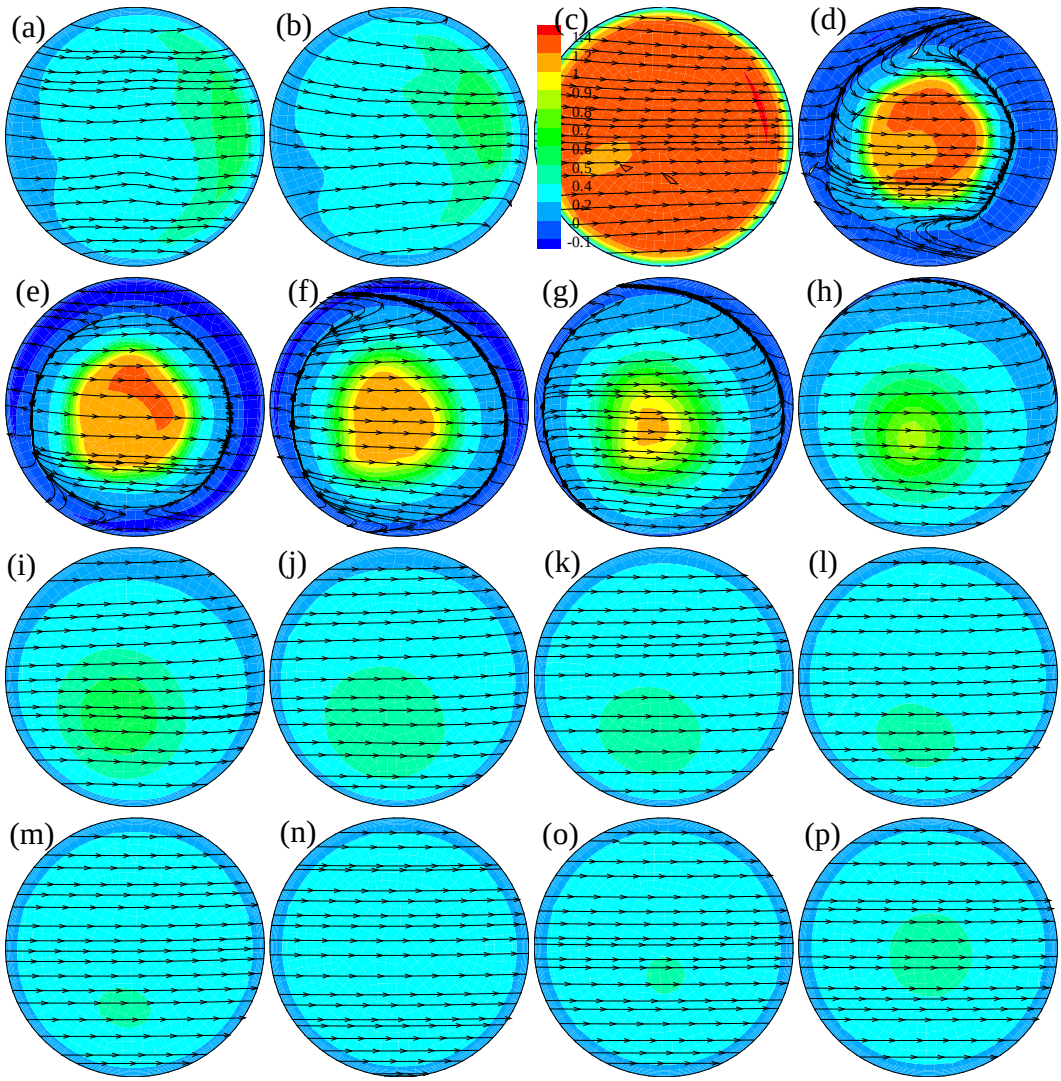

Figure 4.11: Cross-sectional streamlines appended on the axial velocity contour for spiral flow in model $D2$ at (a) $z/D = -3$, (b) $z/D = -1$, (c) $z/D = 0$, (d) $z/D = 1$, (e) $z/D = 2$, (f) $z/D = 3$, (g) $z/D = 4$, (h) $z/D = 5$, (i) $z/D = 6$, (j) $z/D = 7$, (k) $z/D = 8$, (l) $z/D = 9$, (m) $z/D = 10$, (n) $z/D = 12$, (o) $z/D = 16$ and (p) $z/D = 22$.

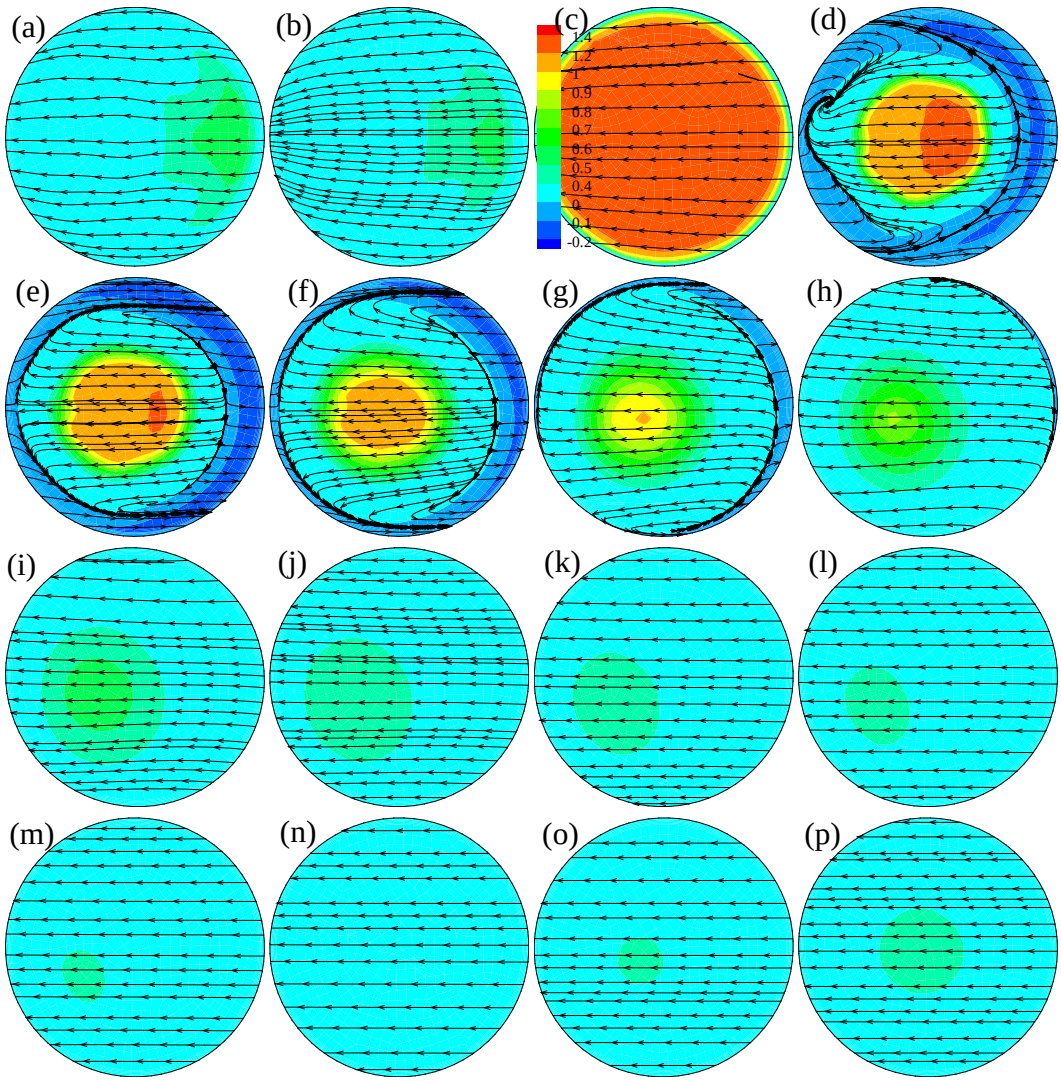

Figure 4.12: Cross-sectional streamlines appended on the axial velocity contour for non-spiral flow in model $D4$ at (a) $z/D = -3$, (b) $z/D = -1$, (c) $z/D = 0$, (d) $z/D = 1$, (e) $z/D = 2$, (f) $z/D = 3$, (g) $z/D = 4$, (h) $z/D = 5$, (i) $z/D = 6$, (j) $z/D = 7$, (k) $z/D = 8$, (l) $z/D = 9$, (m) $z/D = 10$, (n) $z/D = 12$, (o) $z/D = 16$ and (p) $z/D = 22$.

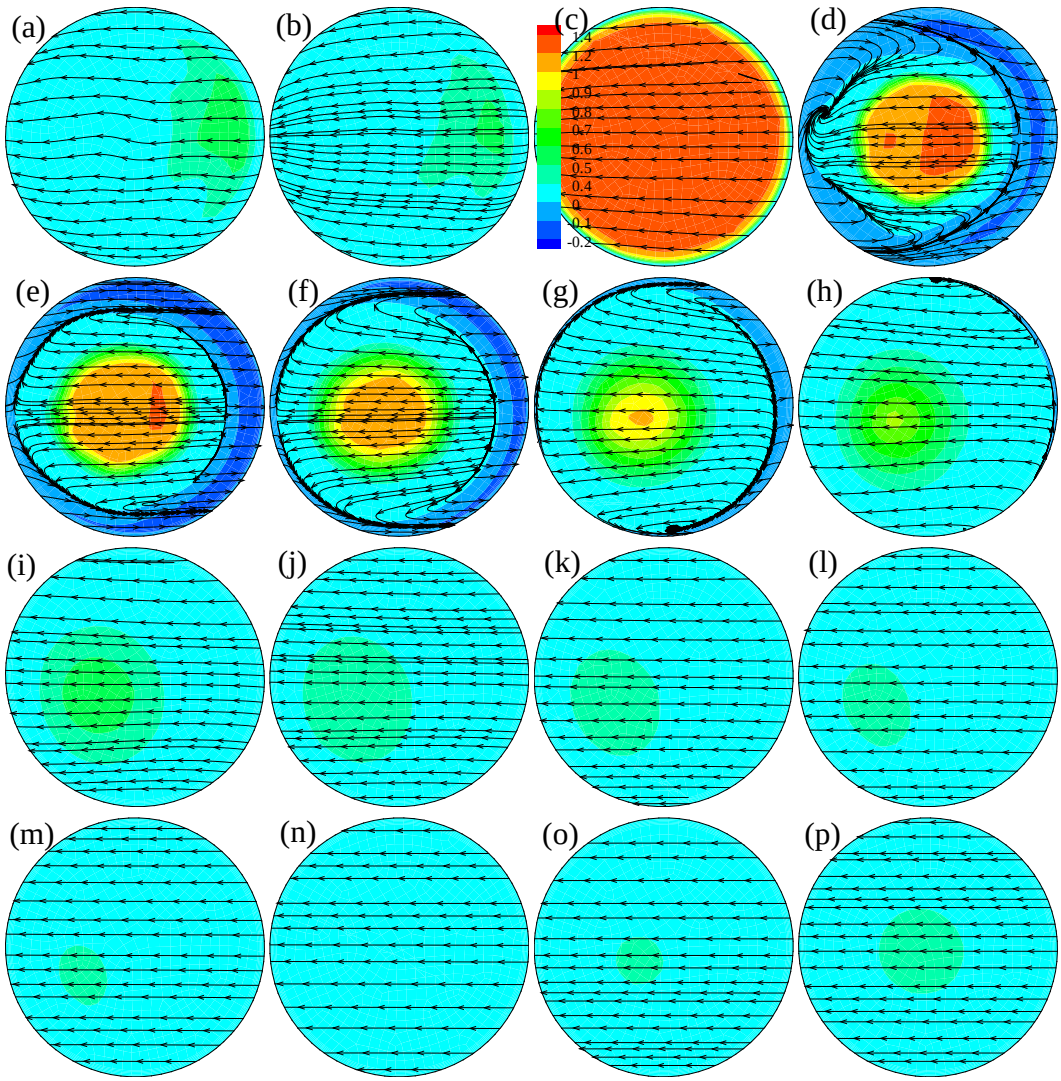

Figure 4.13: Cross-sectional streamlines appended on the axial velocity contour for spiral flow in model $D4$ at (a) $z/D = -3$, (b) $z/D = -1$, (c) $z/D = 0$, (d) $z/D = 1$, (e) $z/D = 2$, (f) $z/D = 3$, (g) $z/D = 4$, (h) $z/D = 5$, (i) $z/D = 6$, (j) $z/D = 7$, (k) $z/D = 8$, (l) $z/D = 9$, (m) $z/D = 10$, (n) $z/D = 12$, (o) $z/D = 16$ and (p) $z/D = 22$.

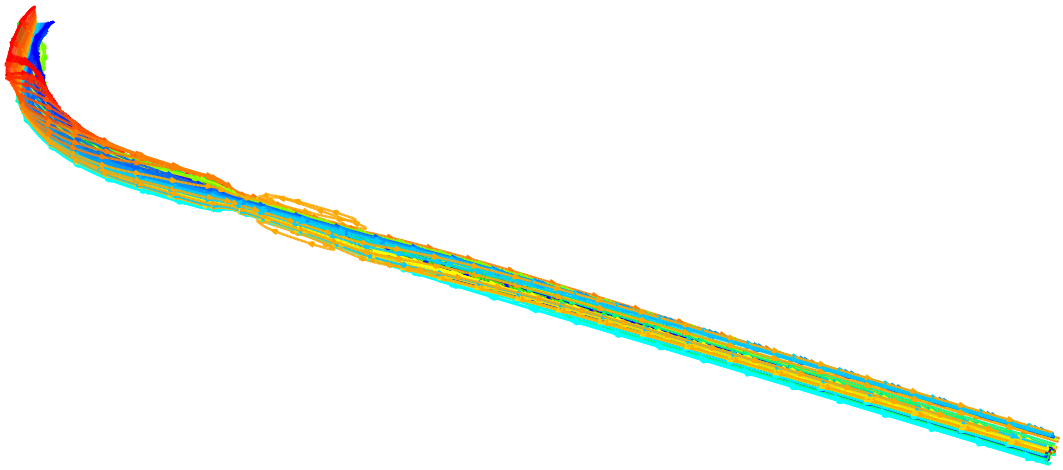

Figure 4.14: Pathlines, coloured by the particle ID, for spiral flow in model $D2$

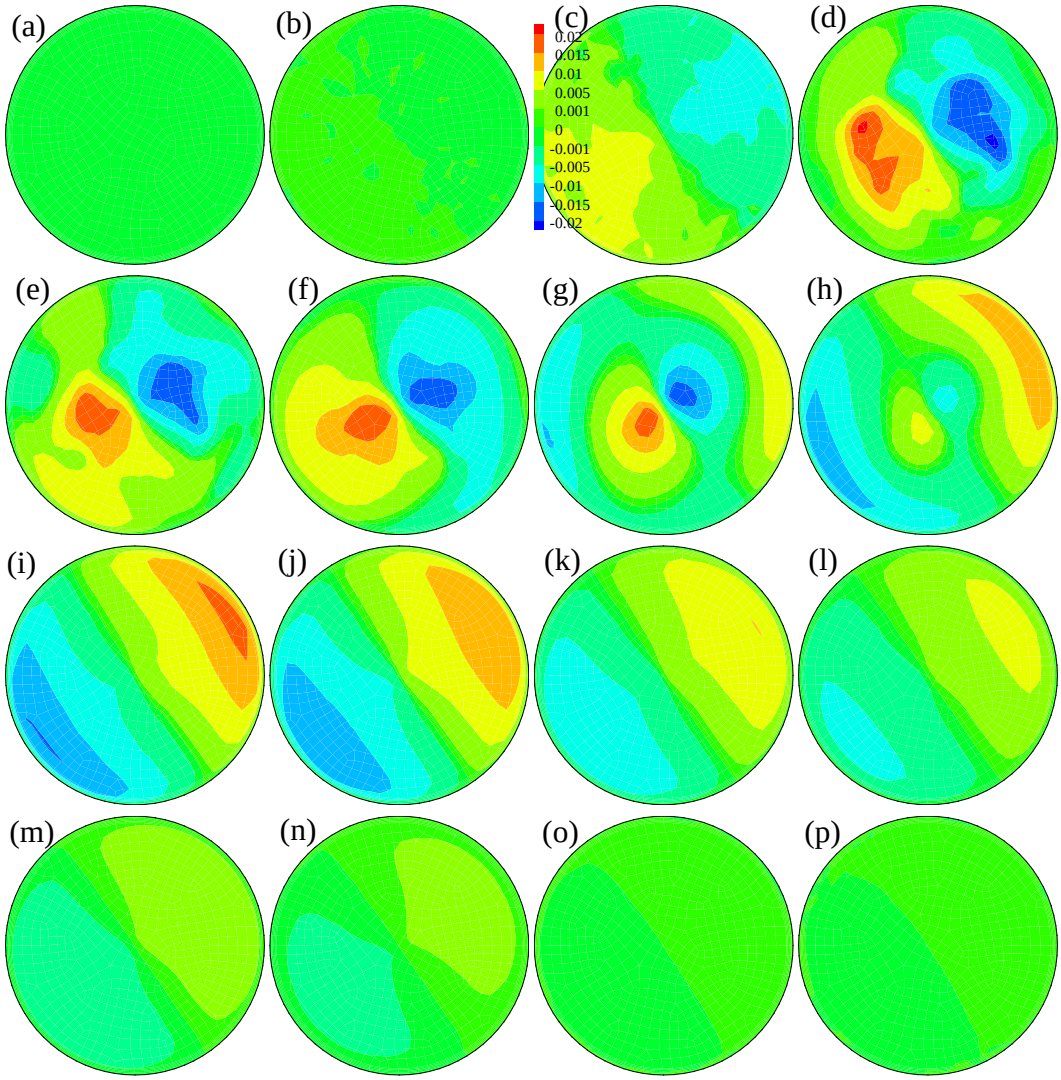

Figure 4.15: contour plots of tangential velocity for non-spiral flow in model $D1$ at (a) $z/D = -3$, (b) $z/D = -1$, (c) $z/D = 0$, (d) $z/D = 1$, (e) $z/D = 2$, (f) $z/D = 3$, (g) $z/D = 4$, (h) $z/D = 5$, (i) $z/D = 6$, (j) $z/D = 7$, (k) $z/D = 8$, (l) $z/D = 9$, (m) $z/D = 10$, (n) $z/D = 12$, (o) $z/D = 16$ and (p) $z/D = 22$.

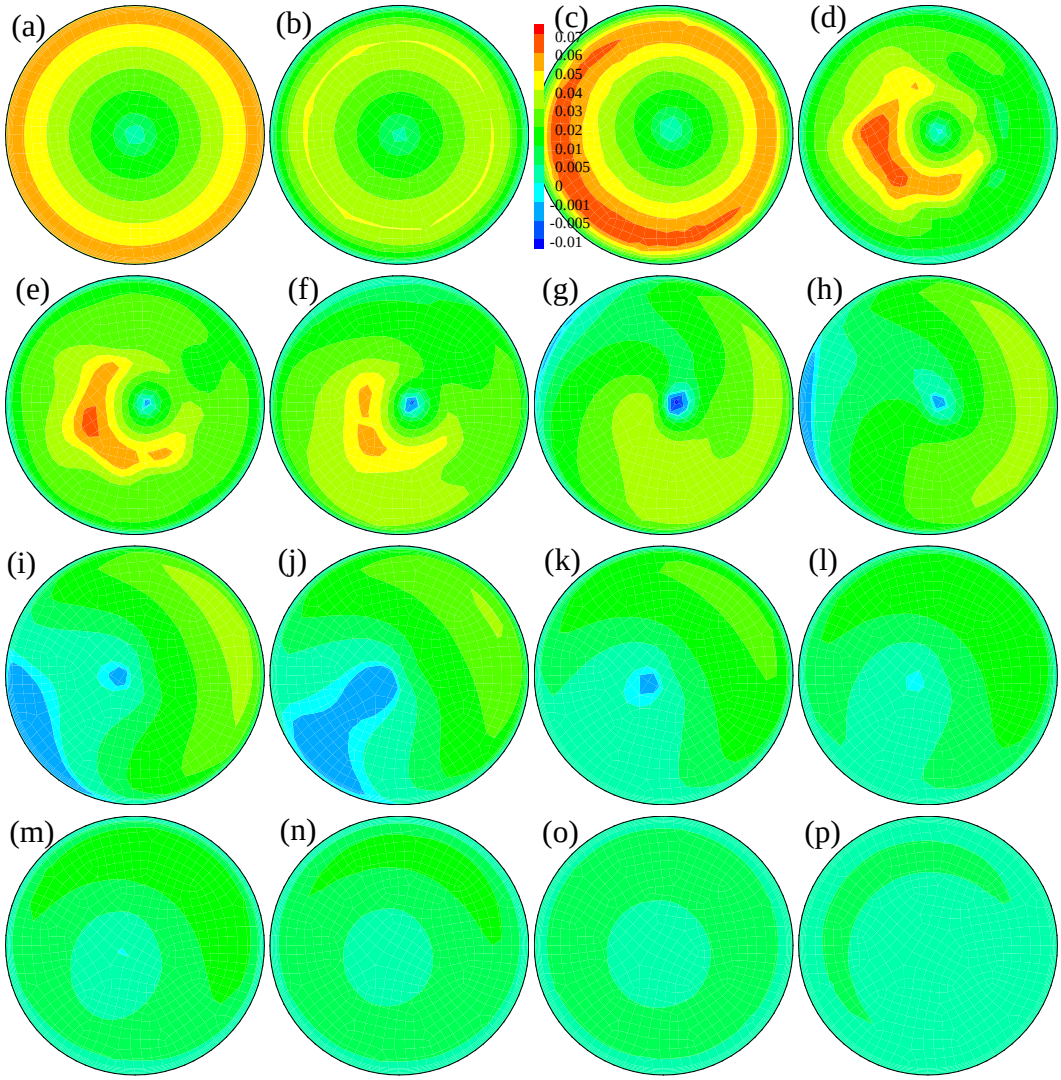

Figure 4.16: contour plots of tangential velocity for spiral flow in model $D1$ at (a) $z/D = -3$, (b) $z/D = -1$, (c) $z/D = 0$, (d) $z/D = 1$, (e) $z/D = 2$, (f) $z/D = 3$, (g) $z/D = 4$, (h) $z/D = 5$, (i) $z/D = 6$, (j) $z/D = 7$, (k) $z/D = 8$, (l) $z/D = 9$, (m) $z/D = 10$, (n) $z/D = 12$, (o) $z/D = 16$ and (p) $z/D = 22$.

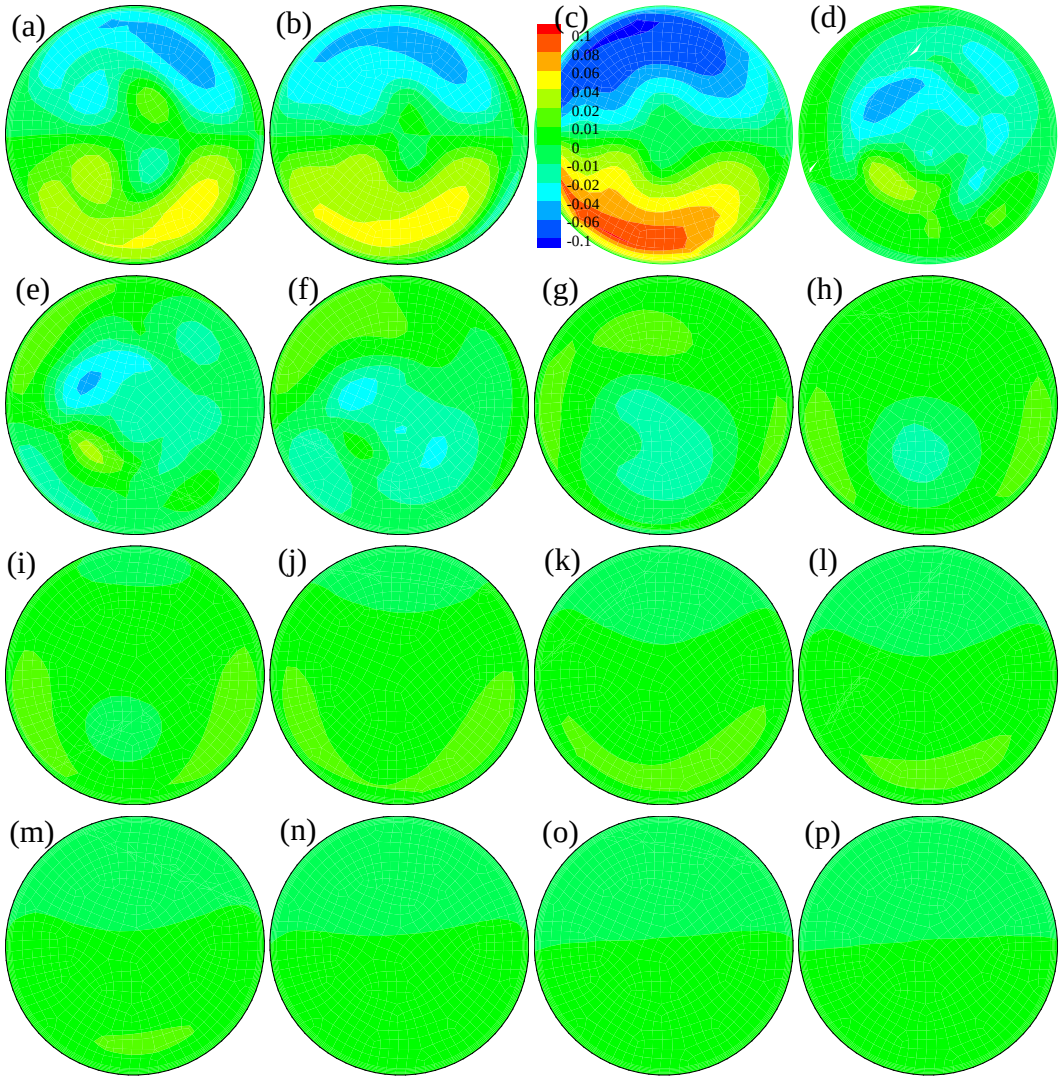

Figure 4.17: Contour plots of tangential velocity for non-spiral flow in model $D2$ at (a) $z/D = -3$, (b) $z/D = -1$, (c) $z/D = 0$, (d) $z/D = 1$, (e) $z/D = 2$, (f) $z/D = 3$, (g) $z/D = 4$, (h) $z/D = 5$, (i) $z/D = 6$, (j) $z/D = 7$, (k) $z/D = 8$, (l) $z/D = 9$, (m) $z/D = 10$, (n) $z/D = 12$, (o) $z/D = 16$ and (p) $z/D = 22$.

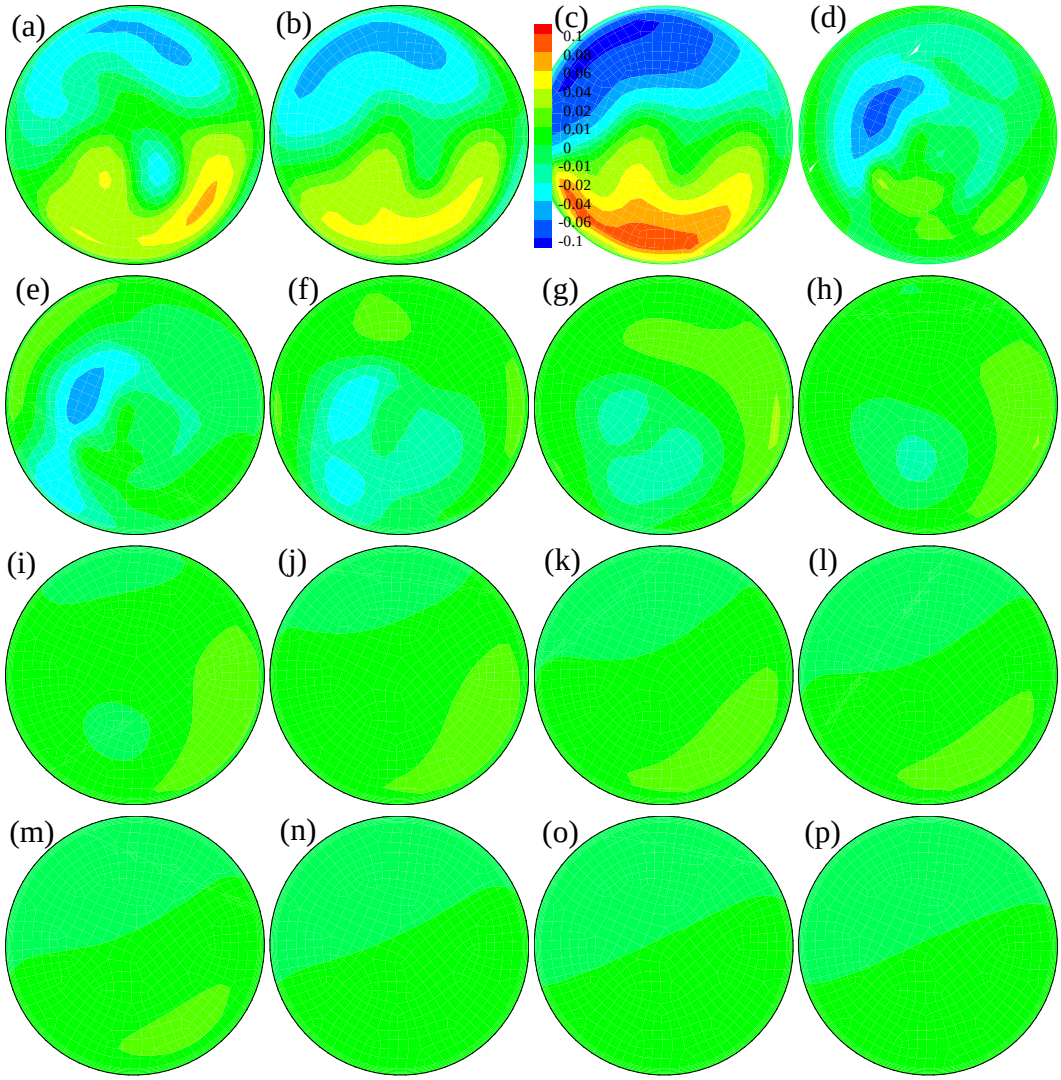

Figure 4.18: contour plots of tangential velocity for spiral flow in model $D2$ at (a) $z/D = -3$, (b) $z/D = -1$, (c) $z/D = 0$, (d) $z/D = 1$, (e) $z/D = 2$, (f) $z/D = 3$, (g) $z/D = 4$, (h) $z/D = 5$, (i) $z/D = 6$, (j) $z/D = 7$, (k) $z/D = 8$, (l) $z/D = 9$, (m) $z/D = 10$, (n) $z/D = 12$, (o) $z/D = 16$ and (p) $z/D = 22$.

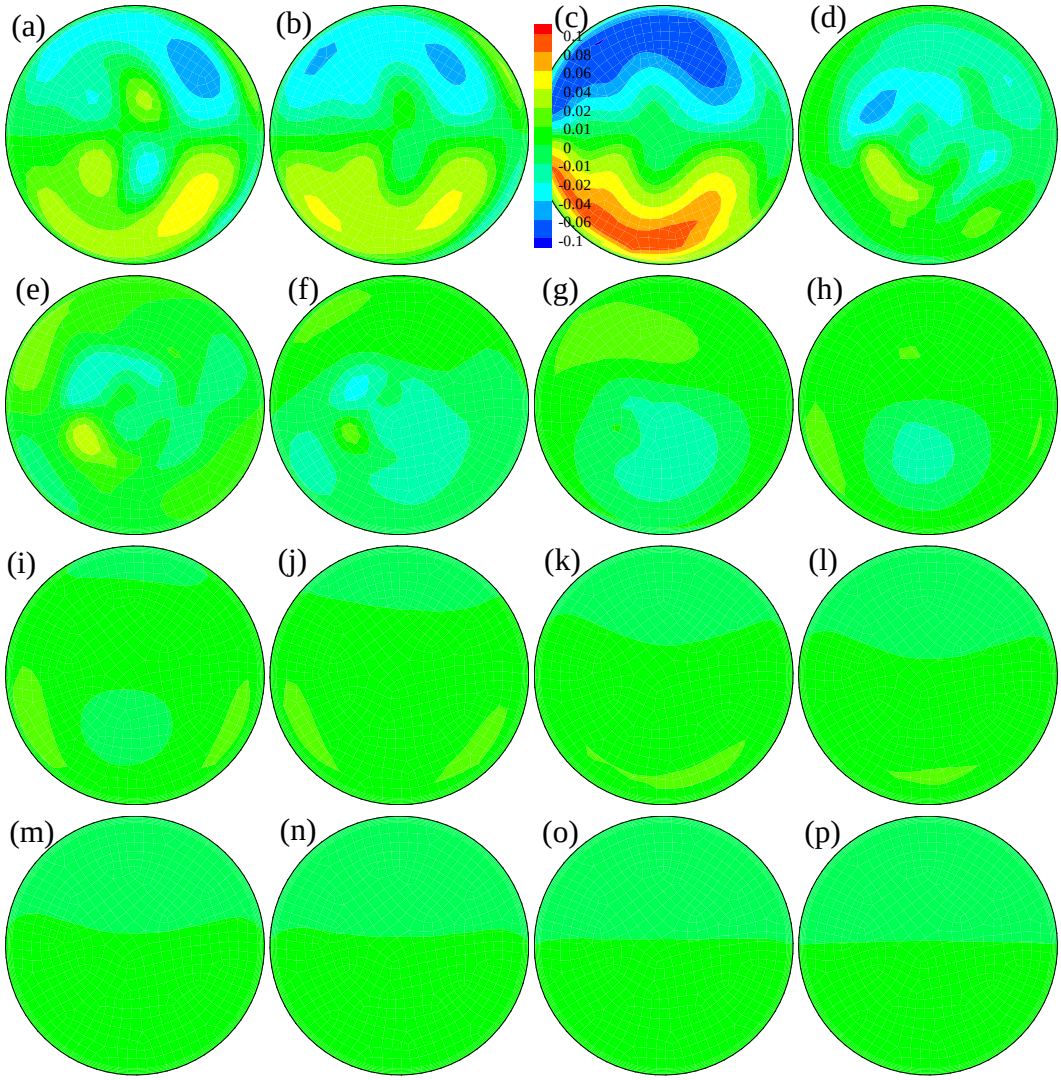

Figure 4.19: Contour plots of tangential velocity for non-spiral flow in model $D3$ at (a) $z/D = -3$, (b) $z/D = -1$, (c) $z/D = 0$, (d) $z/D = 1$, (e) $z/D = 2$, (f) $z/D = 3$, (g) $z/D = 4$, (h) $z/D = 5$, (i) $z/D = 6$, (j) $z/D = 7$, (k) $z/D = 8$, (l) $z/D = 9$, (m) $z/D = 10$, (n) $z/D = 12$, (o) $z/D = 16$ and (p) $z/D = 22$.

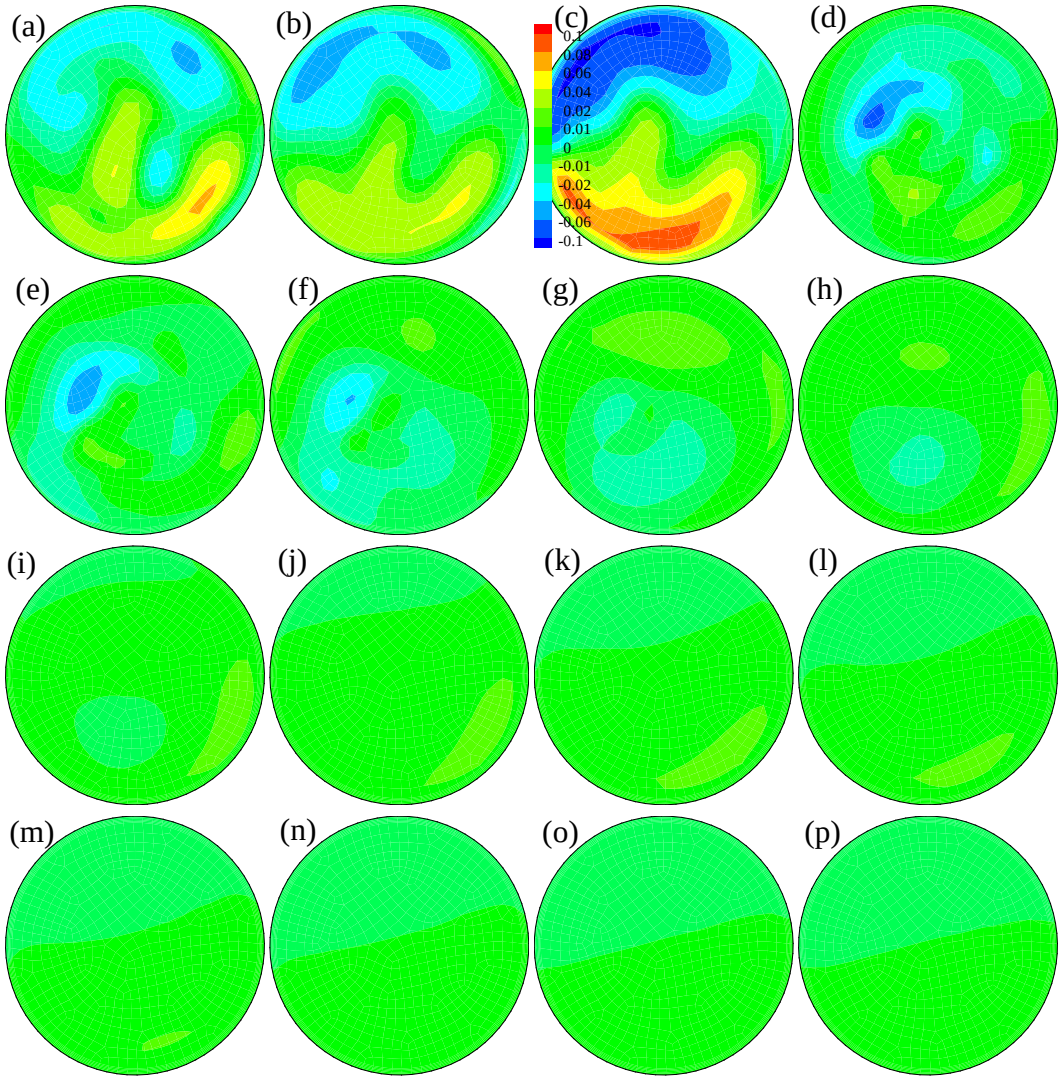

Figure 4.20: contour plots of tangential velocity for spiral flow in model $D3$ at (a) $z/D = -3$, (b) $z/D = -1$, (c) $z/D = 0$, (d) $z/D = 1$, (e) $z/D = 2$, (f) $z/D = 3$, (g) $z/D = 4$, (h) $z/D = 5$, (i) $z/D = 6$, (j) $z/D = 7$, (k) $z/D = 8$, (l) $z/D = 9$, (m) $z/D = 10$, (n) $z/D = 12$, (o) $z/D = 16$ and (p) $z/D = 22$.

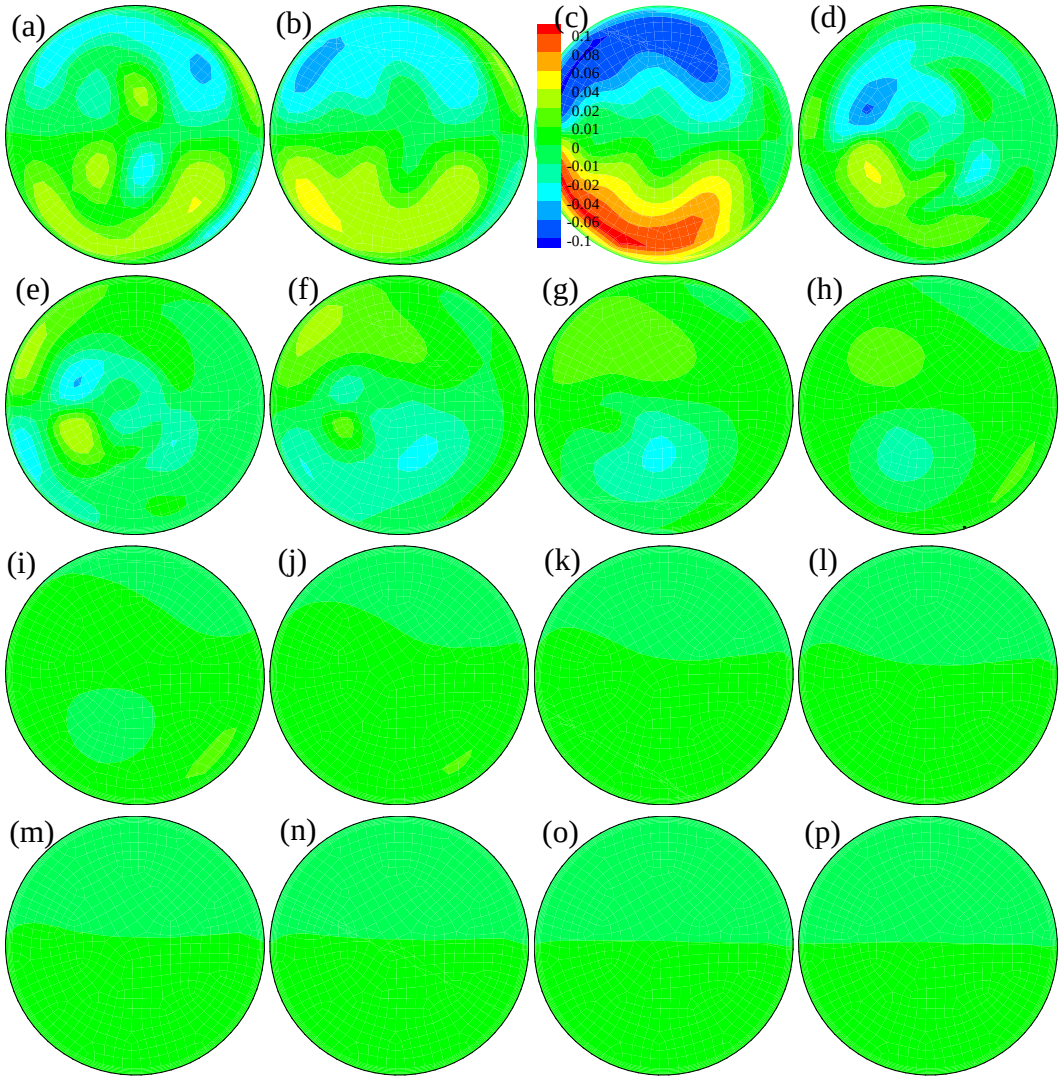

Figure 4.21: Contour plots of tangential velocity for non-spiral flow in model $D4$ at (a) $z/D = -3$, (b) $z/D = -1$, (c) $z/D = 0$, (d) $z/D = 1$, (e) $z/D = 2$, (f) $z/D = 3$, (g) $z/D = 4$, (h) $z/D = 5$, (i) $z/D = 6$, (j) $z/D = 7$, (k) $z/D = 8$, (l) $z/D = 9$, (m) $z/D = 10$, (n) $z/D = 12$, (o) $z/D = 16$ and (p) $z/D = 22$.

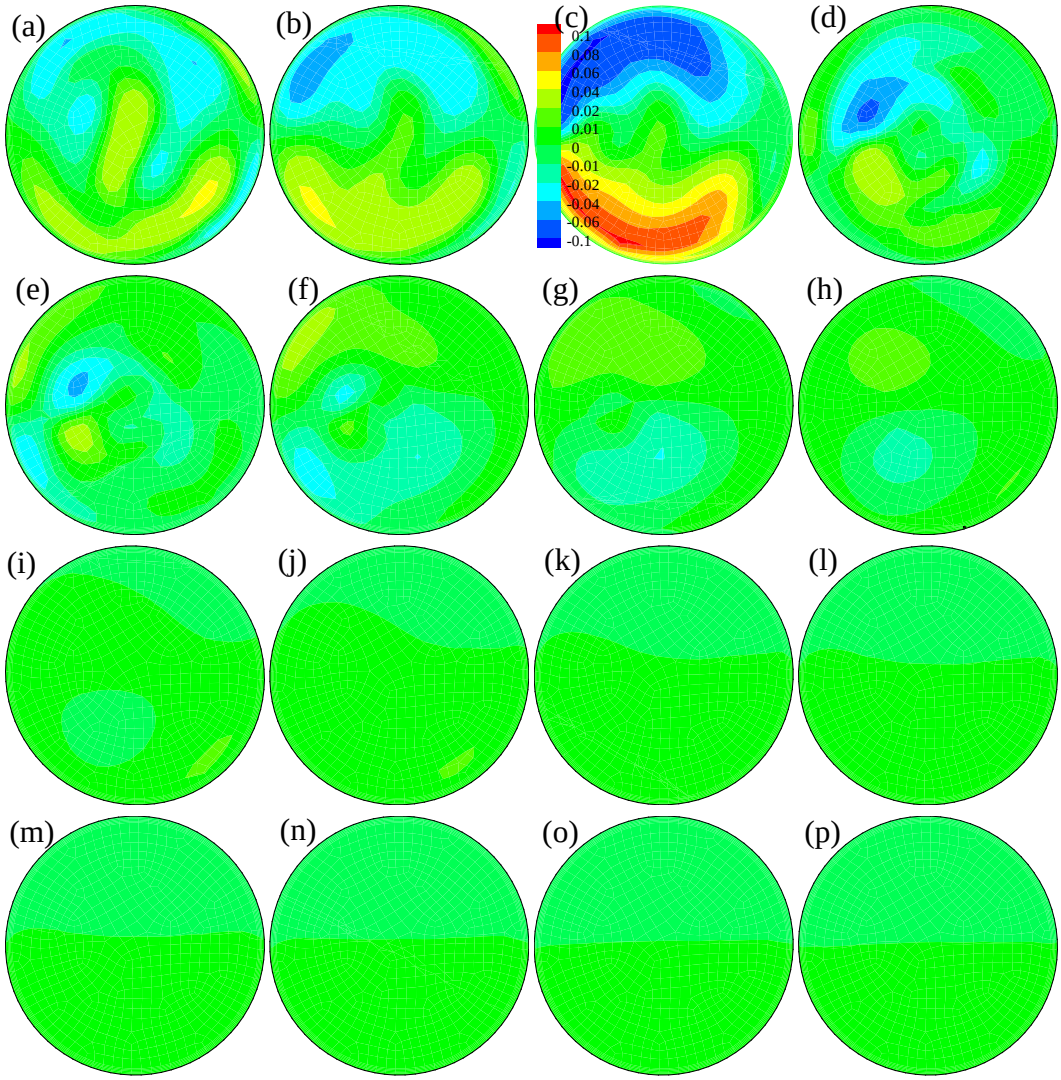

Figure 4.22: contour plots of tangential velocity for spiral flow in model $D4$ at (a) $z/D = -3$, (b) $z/D = -1$, (c) $z/D = 0$, (d) $z/D = 1$, (e) $z/D = 2$, (f) $z/D = 3$, (g) $z/D = 4$, (h) $z/D = 5$, (i) $z/D = 6$, (j) $z/D = 7$, (k) $z/D = 8$, (l) $z/D = 9$, (m) $z/D = 10$, (n) $z/D = 12$, (o) $z/D = 16$ and (p) $z/D = 22$.

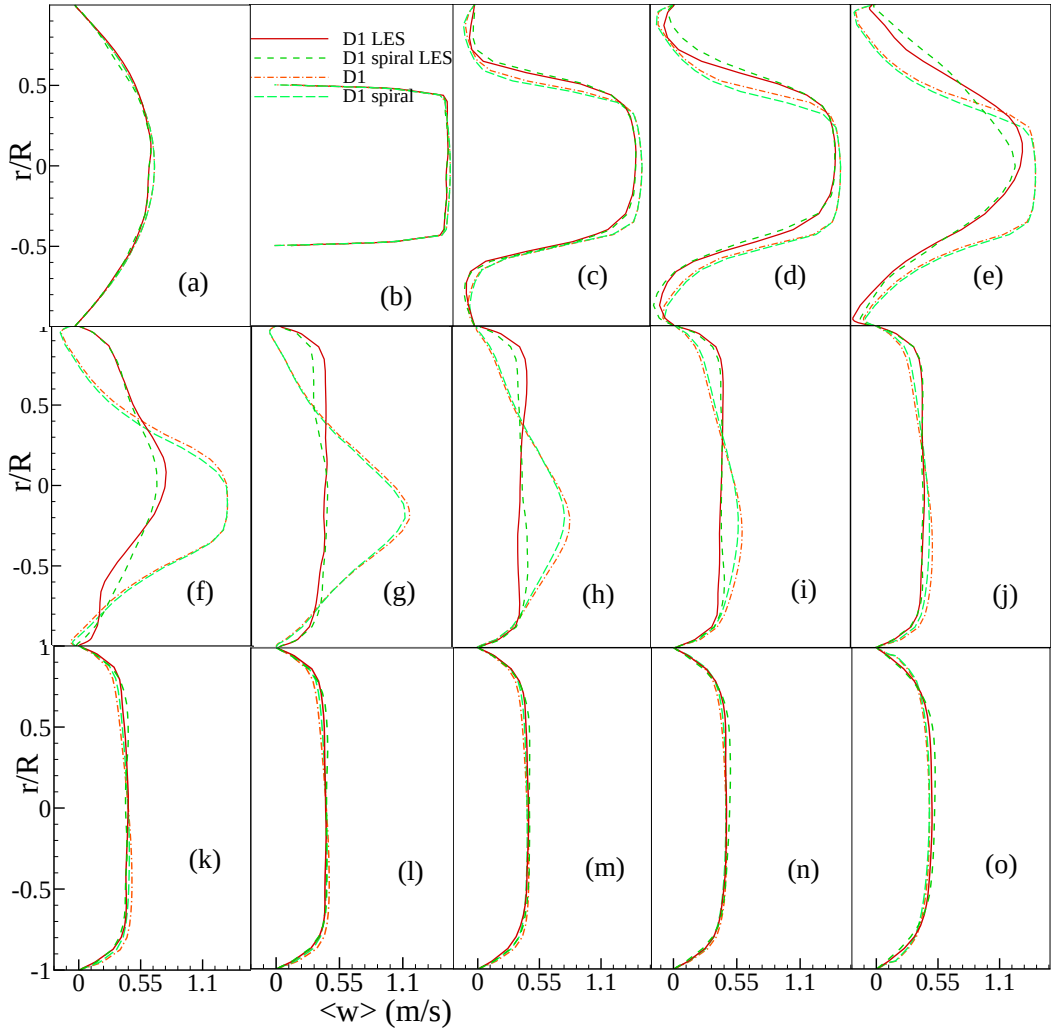

Figure 4.23: Mean axial velocity, $\langle w \rangle$, profiles for both non-spiral and spiral flow in model $D1$ at (a) $z/D = -1$, (b) $z/D = 0$, (c) $z/D = 1$, (d) $z/D = 2$, (e) $z/D = 3$, (f) $z/D = 4$, (g) $z/D = 5$, (h) $z/D = 6$, (i) $z/D = 7$, (j) $z/D = 8$, (k) $z/D = 9$, (l) $z/D = 10$, (m) $z/D = 12$, (n) $z/D = 16$ and (o) $z/D = 22$. Note that LES was also applied to this model.

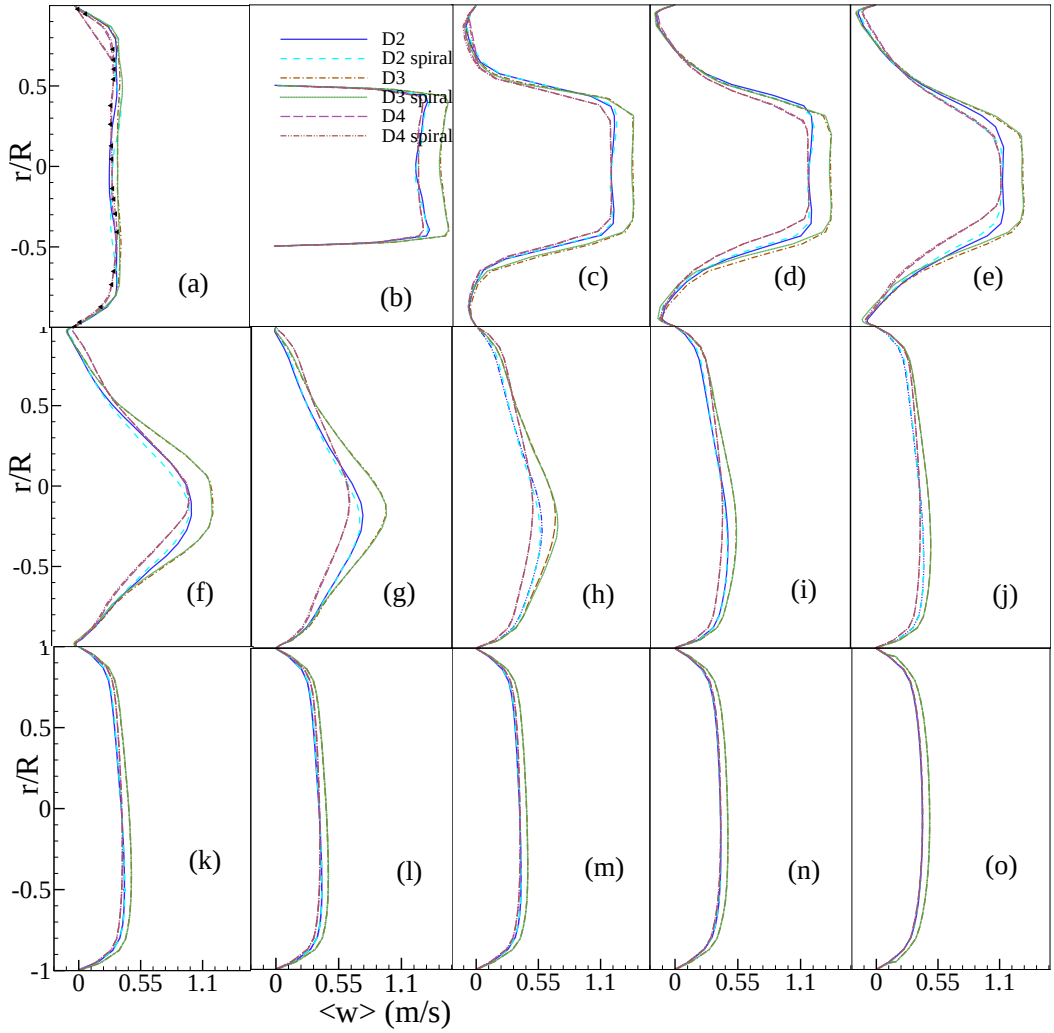

Figure 4.24: Mean axial velocity, $\langle w \rangle$, profiles for both non-spiral and spiral flow in models $D2$, $D3$ and $D4$ at (a) $z/D = -1$, (b) $z/D = 0$, (c) $z/D = 1$, (d) $z/D = 2$, (e) $z/D = 3$, (f) $z/D = 4$, (g) $z/D = 5$, (h) $z/D = 6$, (i) $z/D = 7$, (j) $z/D = 8$, (k) $z/D = 9$, (l) $z/D = 10$, (m) $z/D = 12$, (n) $z/D = 16$ and (o) $z/D = 22$.

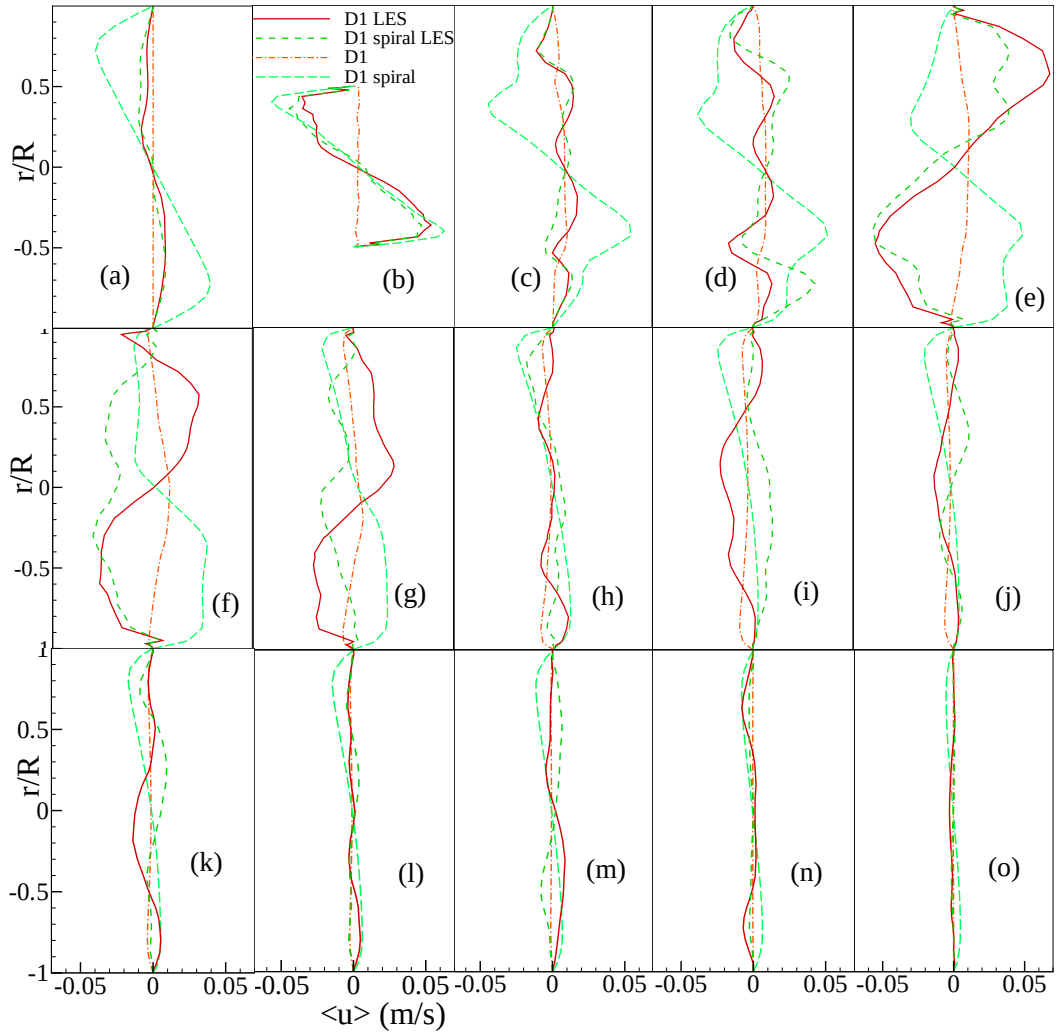

Figure 4.25: Mean x-velocity, $\langle u \rangle$, profiles for both non-spiral and spiral flow in model $D1$ at (a) $z/D = -1$, (b) $z/D = 0$, (c) $z/D = 1$, (d) $z/D = 2$, (e) $z/D = 3$, (f) $z/D = 4$, (g) $z/D = 5$, (h) $z/D = 6$, (i) $z/D = 7$, (j) $z/D = 8$, (k) $z/D = 9$, (l) $z/D = 10$, (m) $z/D = 12$, (n) $z/D = 16$ and (o) $z/D = 22$. Note that LES was also applied to this model.

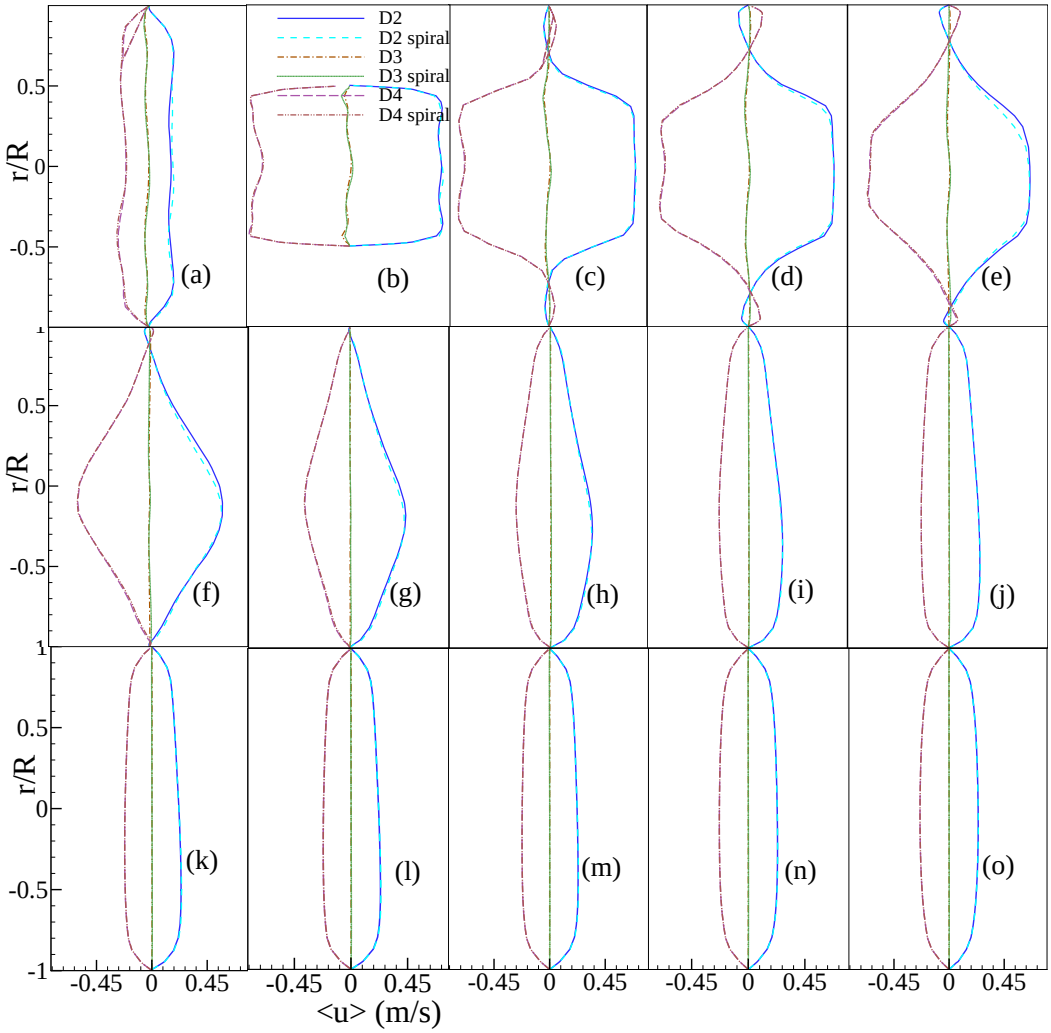

Figure 4.26: Mean x-velocity, $\langle u \rangle$, profiles for both non-spiral and spiral flow in models $D2$, $D3$ and $D4$ at (a) $z/D = -1$, (b) $z/D = 0$, (c) $z/D = 1$, (d) $z/D = 2$, (e) $z/D = 3$, (f) $z/D = 4$, (g) $z/D = 5$, (h) $z/D = 6$, (i) $z/D = 7$, (j) $z/D = 8$, (k) $z/D = 9$, (l) $z/D = 10$, (m) $z/D = 12$, (n) $z/D = 16$ and (o) $z/D = 22$.

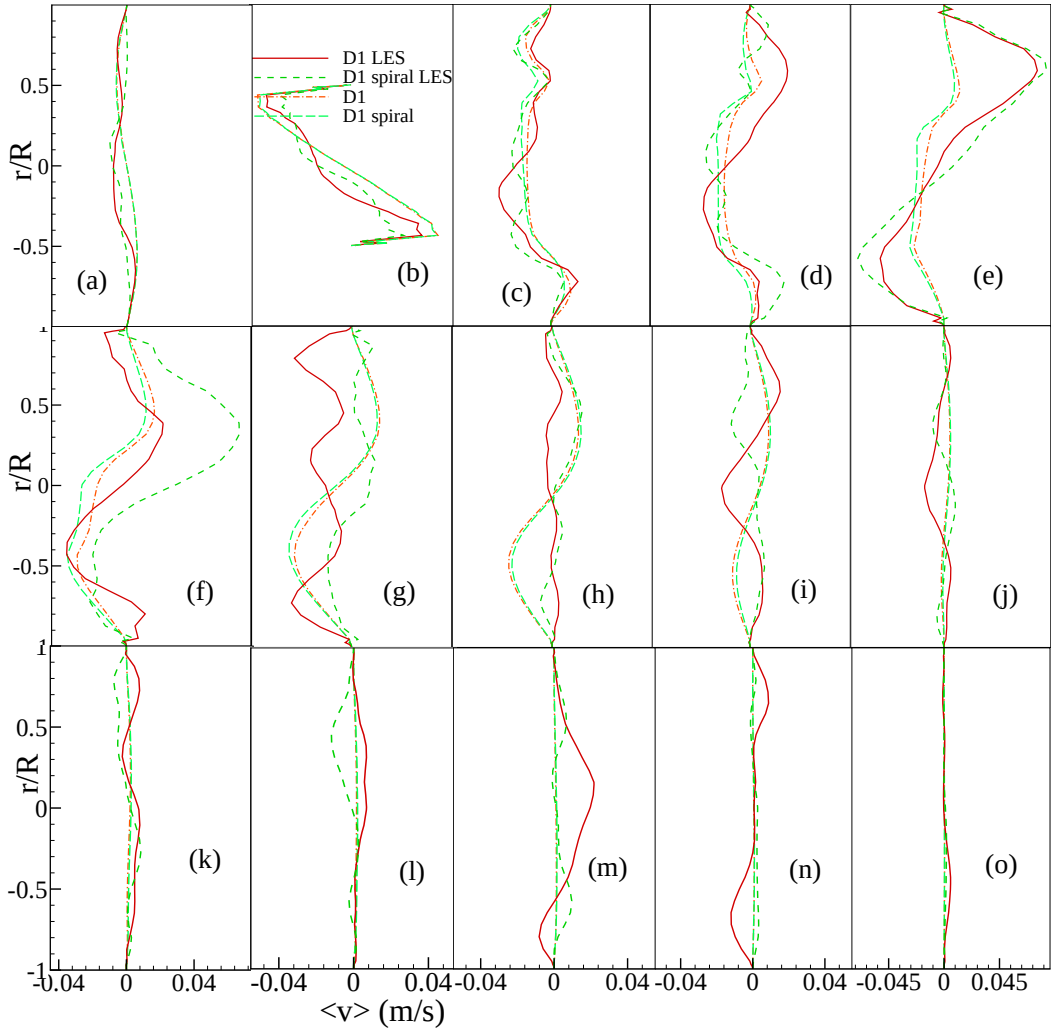

Figure 4.27: Mean y-velocity, $\langle v \rangle$, profiles for both non-spiral and spiral flow in model $D1$ at (a) $z/D = -1$, (b) $z/D = 0$, (c) $z/D = 1$, (d) $z/D = 2$, (e) $z/D = 3$, (f) $z/D = 4$, (g) $z/D = 5$, (h) $z/D = 6$, (i) $z/D = 7$, (j) $z/D = 8$, (k) $z/D = 9$, (l) $z/D = 10$, (m) $z/D = 12$, (n) $z/D = 16$ and (o)$z/D = 22$. Note that LES was also applied to this model.

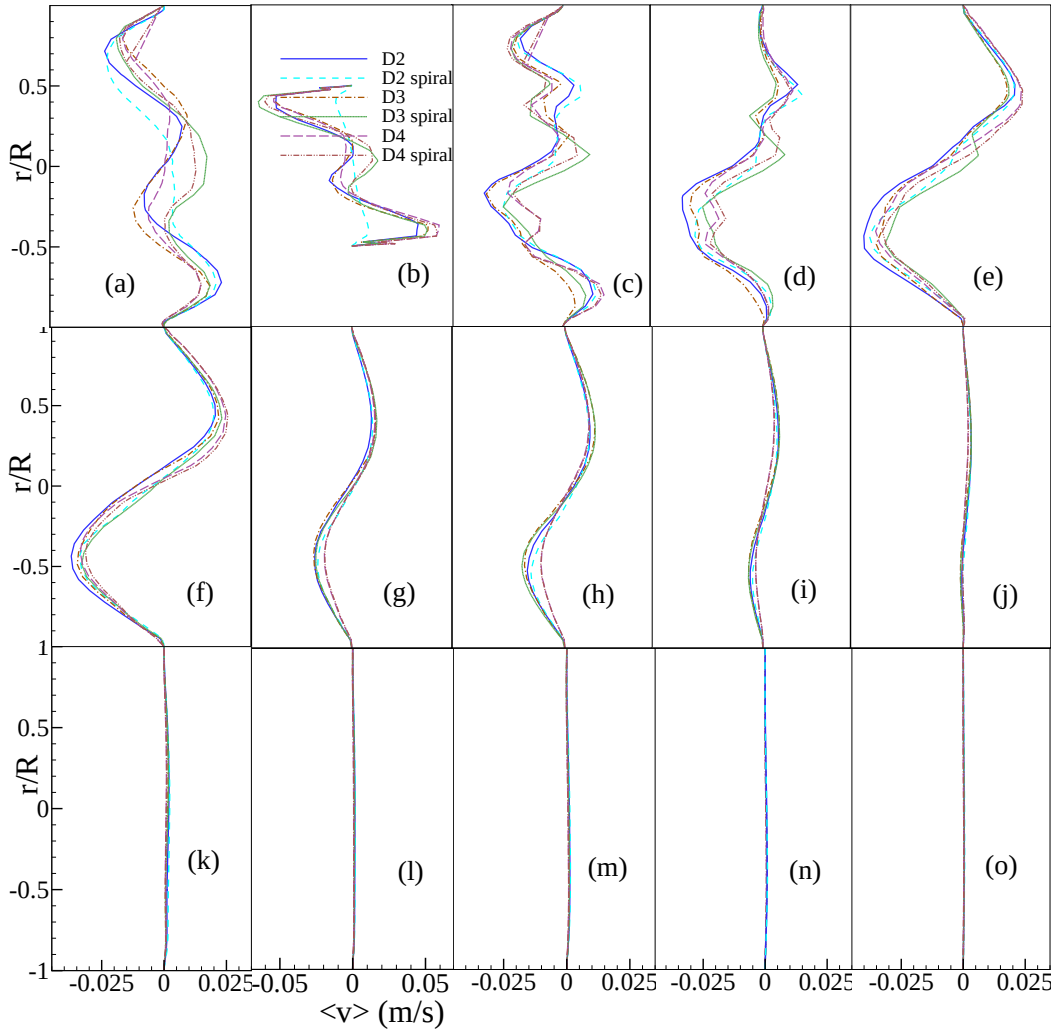

Figure 4.28: Mean y-velocity, $\langle v \rangle$, profiles for both non-spiral and spiral flow in models $D2$, $D3$ and $D4$ at (a) $z/D = -1$, (b) $z/D = 0$, (c) $z/D = 1$, (d) $z/D = 2$, (e) $z/D = 3$, (f) $z/D = 4$, (g) $z/D = 5$, (h) $z/D = 6$, (i) $z/D = 7$, (j) $z/D = 8$, (k) $z/D = 9$, (l) $z/D = 10$, (m) $z/D = 12$, (n) $z/D = 16$ and (o)$z/D = 22$.

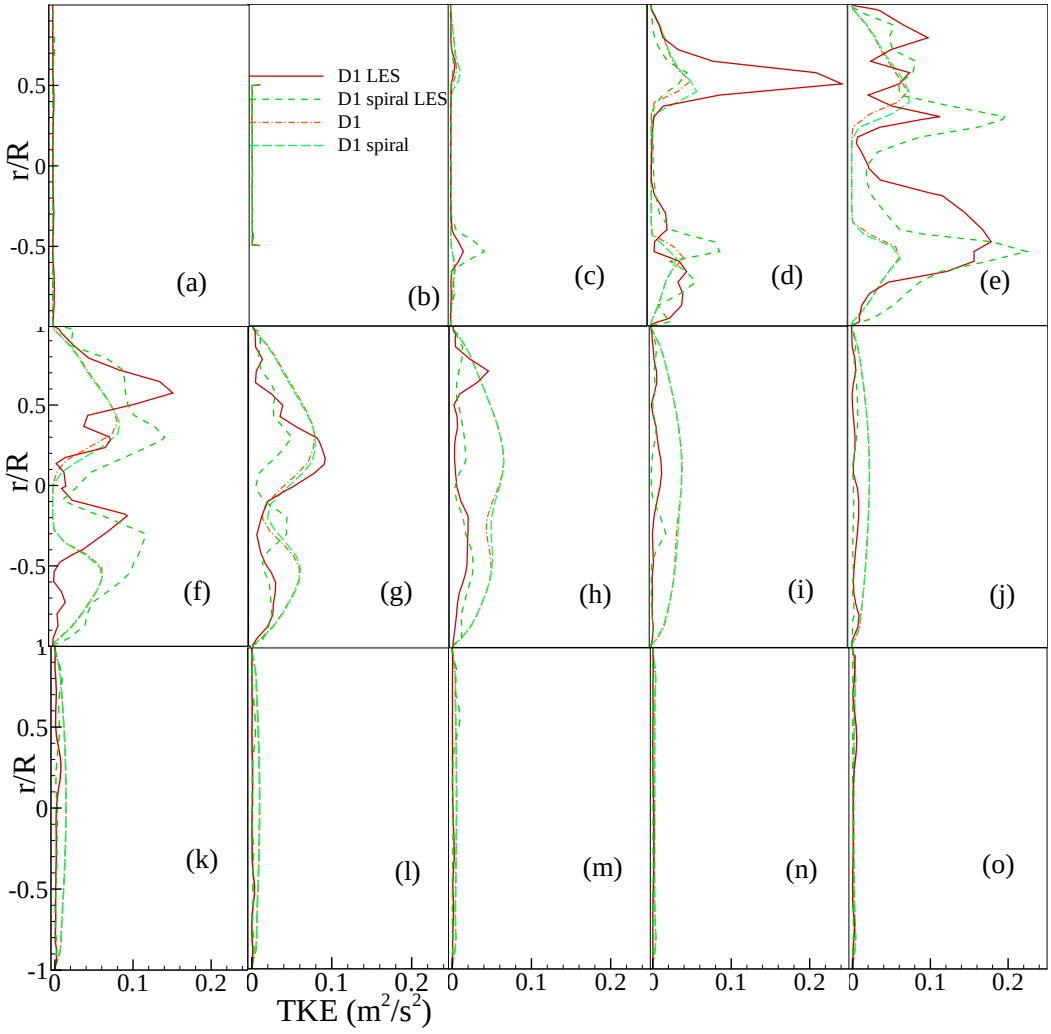

Figure 4.29: Turbulent kinetic energy, k (m^2/s^2), for both non-spiral and spiral flow in model $D1$ at (a) $z/D = -1$, (b) $z/D = 0$, (c) $z/D = 1$, (d) $z/D = 2$, (e) $z/D = 3$, (f) $z/D = 4$, (g) $z/D = 5$, (h) $z/D = 6$, (i) $z/D = 7$, (j) $z/D = 8$, (k) $z/D = 9$, (l) $z/D = 10$, (m) $z/D = 12$, (n) $z/D = 16$ and (o)$z/D = 22$. Note that LES was also applied to this model.

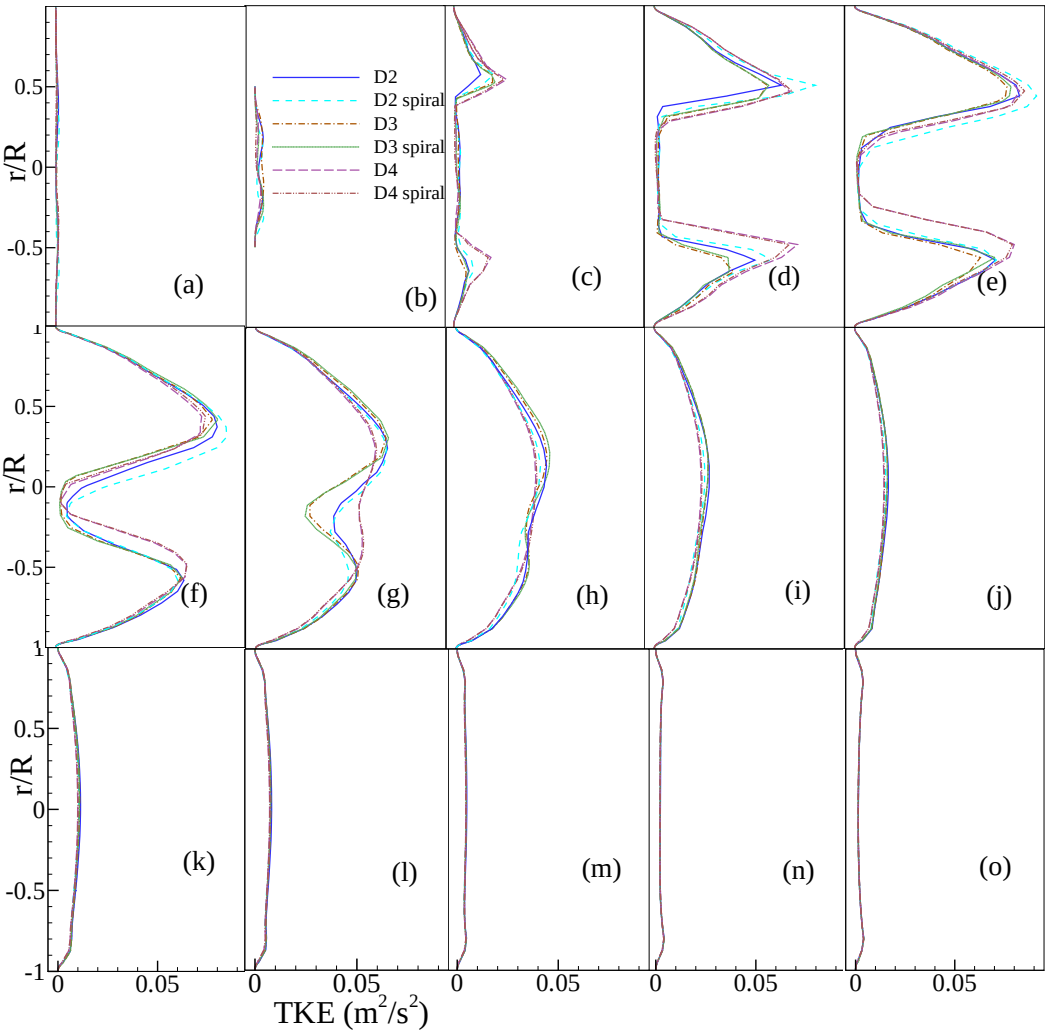

Figure 4.30: Turbulent kinetic energy, k (m^2/s^2), for both non-spiral and spiral flow in models $D2$, $D3$ and $D4$ at (a) $z/D = -1$, (b) $z/D = 0$, (c) $z/D = 1$, (d) $z/D = 2$, (e) $z/D = 3$, (f) $z/D = 4$, (g) $z/D = 5$, (h) $z/D = 6$, (i) $z/D = 7$, (j) $z/D = 8$, (k) $z/D = 9$, (l) $z/D = 10$, (m) $z/D = 12$, (n) $z/D = 16$ and (o)$z/D = 22$.

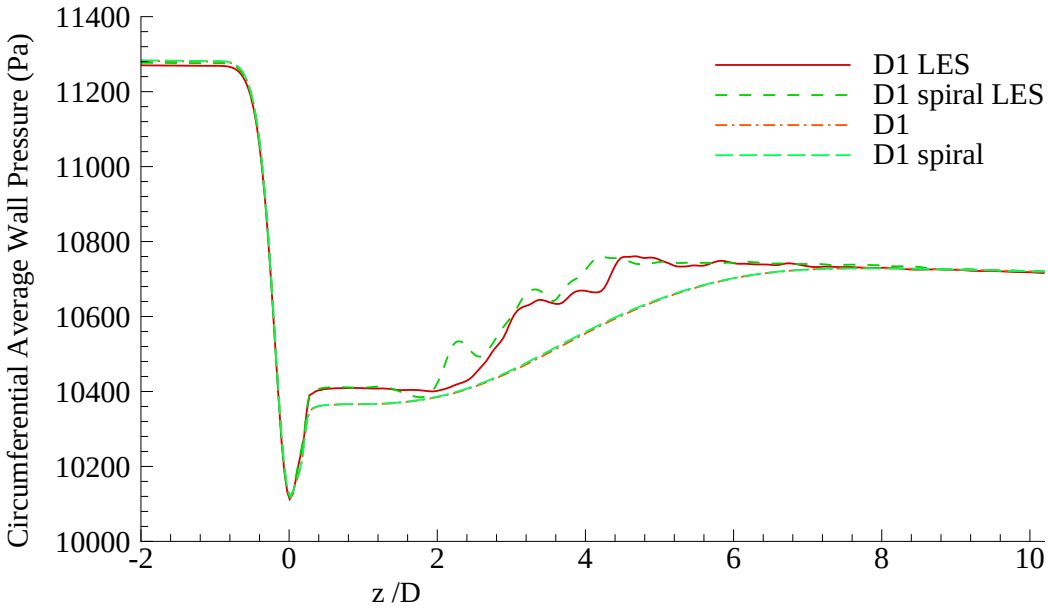

Figure 4.31: Circumferential average wall pressure (Pa) for both non-spiral and spiral flow in model $D1$. Note that LES was also applied to this model.

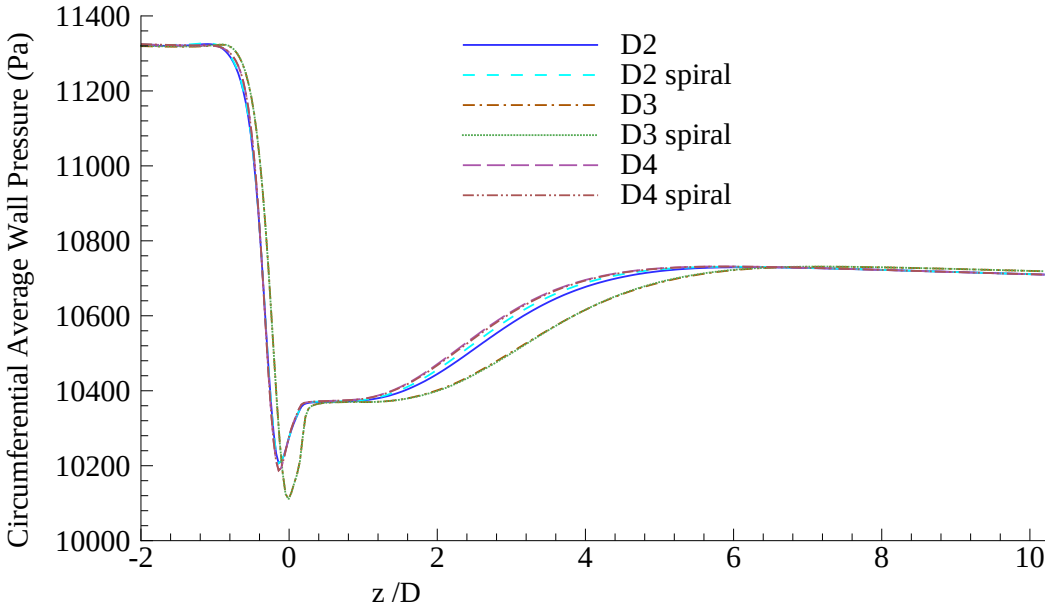

Figure 4.32: Circumferential average wall pressure (Pa) for both non-spiral and spiral flow in models $D2$, $D3$ and $D4$.

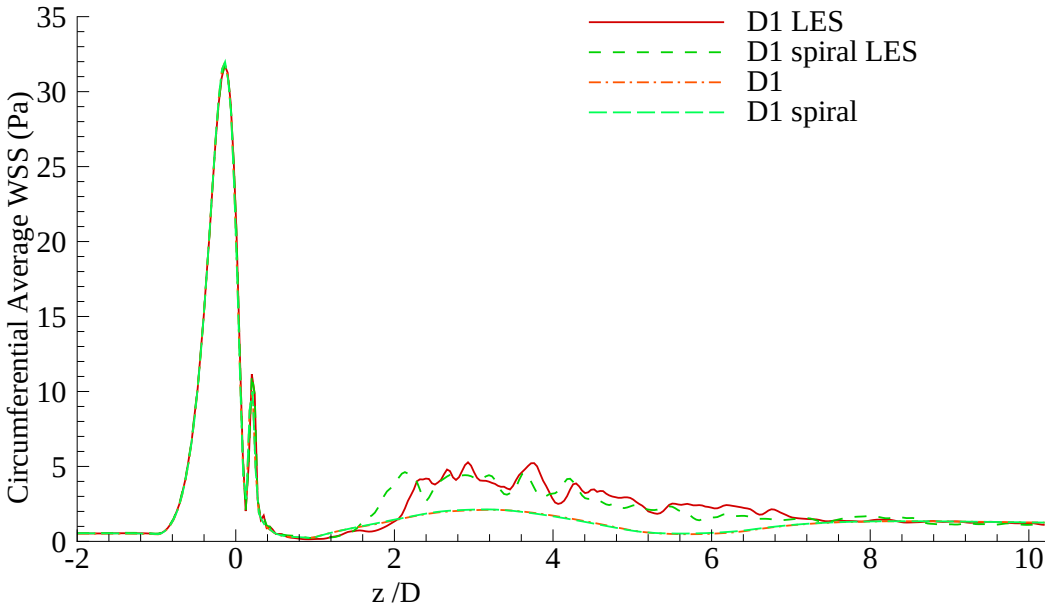

Figure 4.33: Circumferential average wall shear stress, τ (Pa), for both non-spiral and spiral flow in model $D1$. Note that LES was also applied to this model.

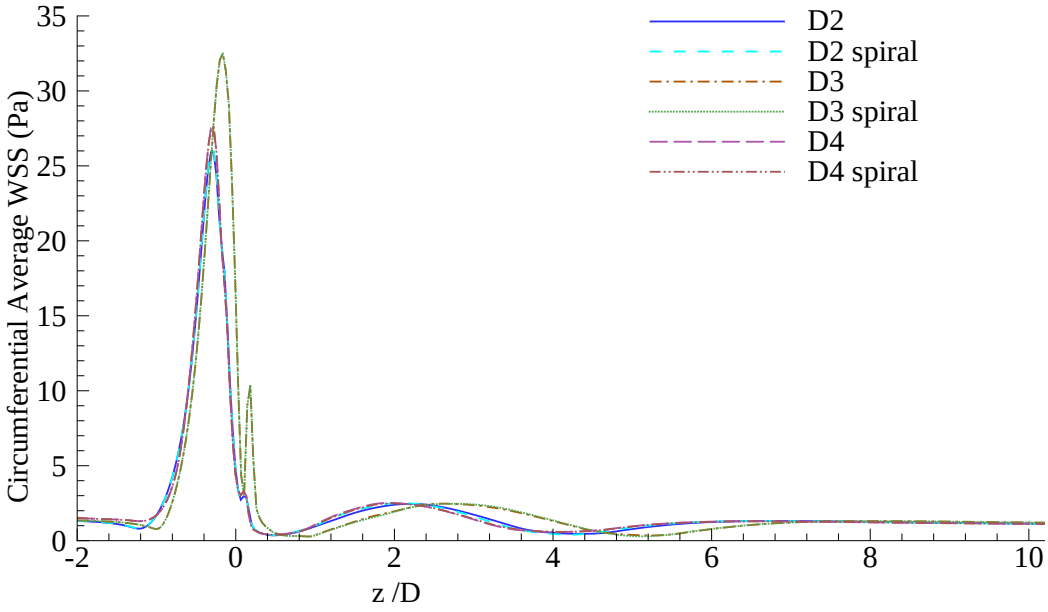

Figure 4.34: Circumferential average wall shear stress, τ (Pa), for both non-spiral and spiral flow in models $D2$, $D3$ and $D4$.

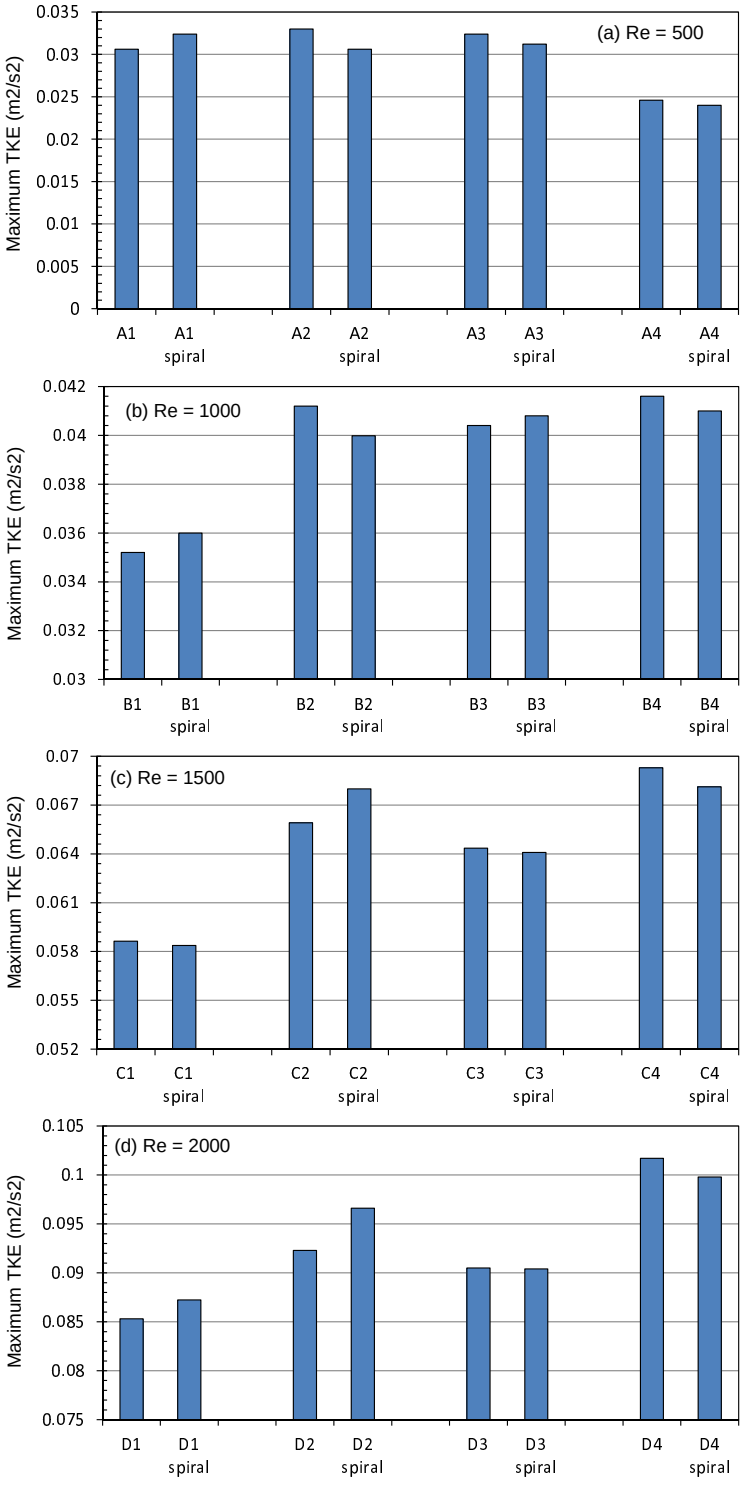

Figure 4.35: Bar chart of maximum turbulent kinetic energy for both non-spiral and spiral flow in all models for (a) $Re = 500$, (b) $Re = 1000$, (c) $Re = 1500$ and (d) 2000.

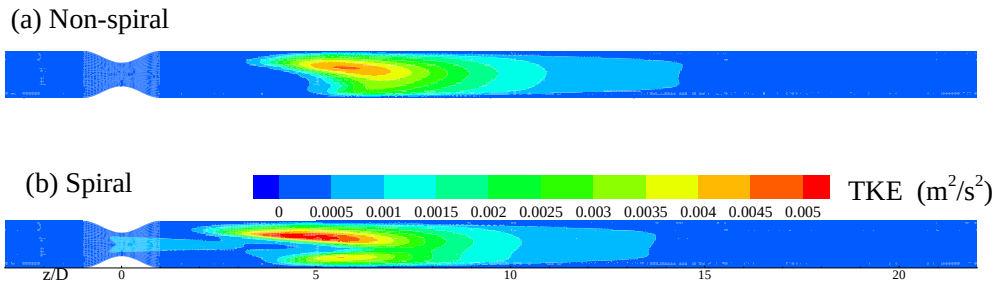

Figure 4.36: Contour plot of TKE, k (m^2/s^2), in model $A1$ for (a) non-spiral flow and (b) spiral flow.

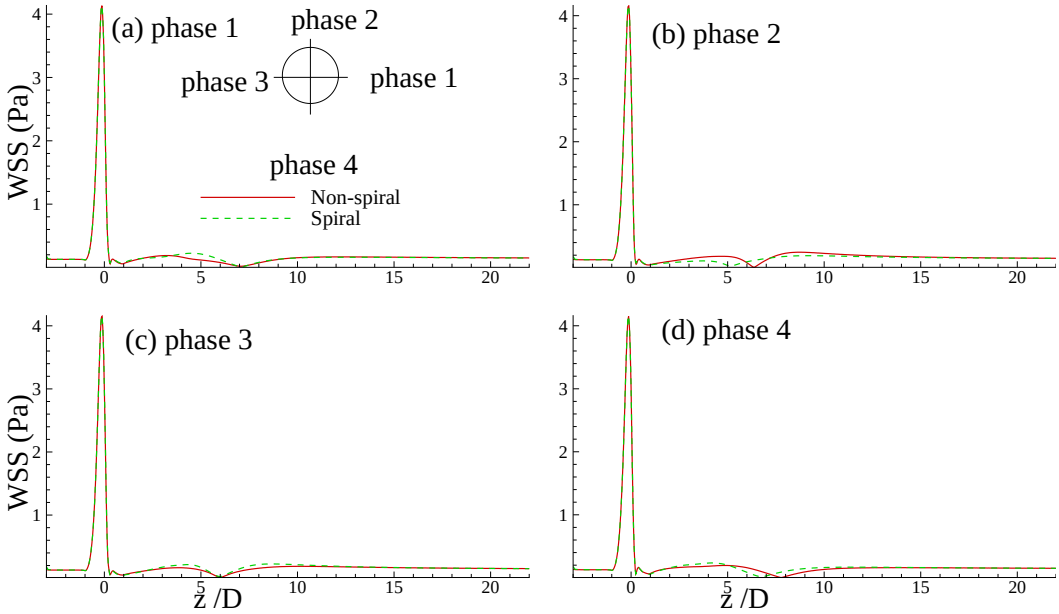

Figure 4.37: Wall shear stress (Pa) at different phases of the wall in model $A1$ for both non-spiral and spiral flow.

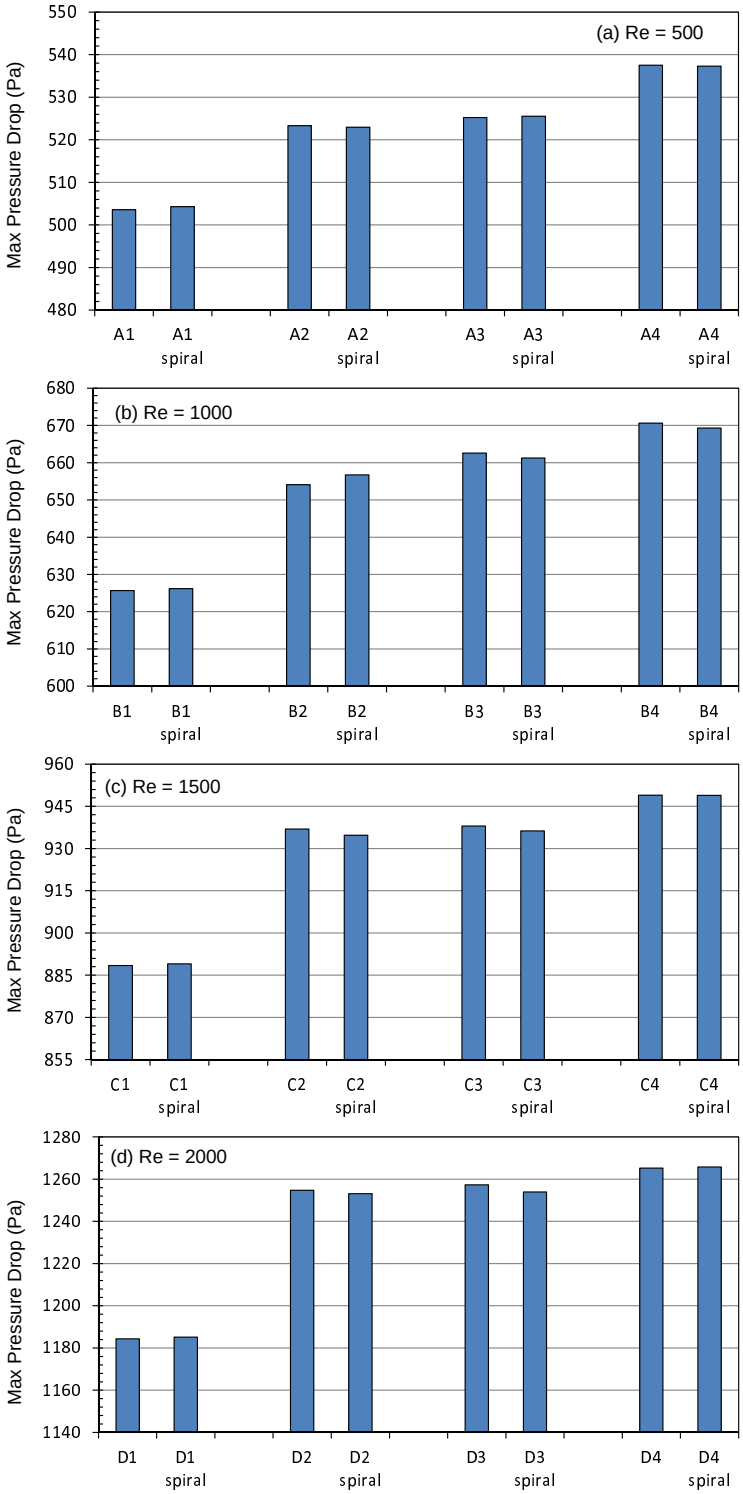

Figure 4.38: Bar chart of maximum pressure drop for both non-spiral and spiral flow in all models for (a) $Re = 500$, (b) $Re = 1000$, (c) $Re = 1500$ and (d) 2000.

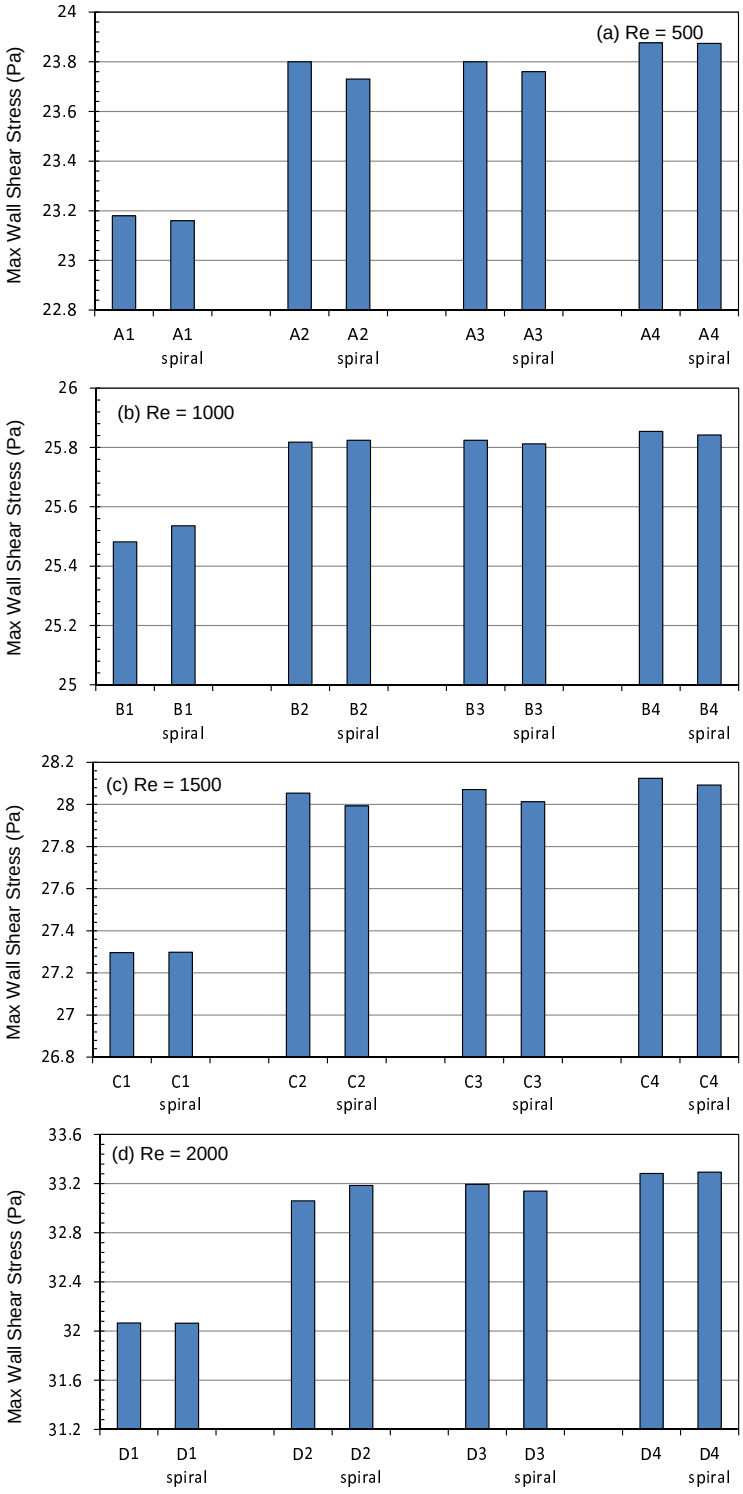

Figure 4.39: Bar chart of maximum wall shear stress for both non-spiral and spiral flow in all models for (a) $Re = 500$, (b) $Re = 1000$, (c) $Re = 1500$ and (d) 2000.

Chapter 5

Simulation of Physiological Pulsatile Non-spiral and Spiral Blood Flow in a Regular Arterial Stenosis

5.1 Introduction

LES of physiological pulsatile flow through arterial stenosis is relatively new. Notable studies on LES of pulsatile flow in models of stenosed artery include studies of Paul and Molla [93], Gårdhagen et al. [95] and Barber and Simmons [96]. The limitations of the available studies were highlighted in the last paragraph of § 2.2.2 in Chapter 2. On the other hand, only steady spiral blood flow through a straight stenosed tube was investigated by applying LES and two-equation k-ω Transitional turbulence model in the previous Chapter. Therefore, LES of physiological pulsatile non-spiral and spiral blood flow through straight stenosed tube would be performed to get better insight of the transition-to-turbulence phenomena of the flows through stenosis and the effects of spiral blood flow on the flow properties in the downstream of the stenosis. Two-equation k-ω Transitional model was also applied to pulsatile non-spiral flow to assess its ability to model the transient pulsatile flow. For LES, the Smagorinsky-Lilly dynamic subgrid model (Germano [115], Lilly [116] and Kim [123]) was used.

Following Womersley [131] solution, physiological pulsatile velocity profile was introduced at the inlet using the first four harmonics of the Fourier series of the pressure pulse. To create spiral effect, one-sixth of pulsatile bulk velocity was taken as tangential velocity at the inlet according to Stonebridge et al. [15; 16].

At the outlet, a physiological pulsatile pressure profile was generated according to Nichols and O'Rourke [7].

Transition-to-turbulence of pulsatile non-spiral and spiral blood flow in the downstream of the stenosis is investigated in terms of various numerical quantities such as velocity, streamlines, velocity vectors, vortices, wall pressure and shear stresses, turbulent kinetic energy, pressure gradient, velocity and pressure fluctuations and their energy spectra etc. Relevant pathophysiological implications of these results are also discussed. Influence of stenosis percentage and length on the flow results in non-spiral pulsatile flow is investigated in this Chapter. Additionally, the effects of Womersley parameter, α, and amplitude of pulsation in the inflow velocity on the non-spiral flow results are examined as well.

5.2 Problem Formulation

The model geometry was a straight stenosed tube with a 75% area reduction cosine type regular stenosis of length $2D$ as shown in Figure 4.1(a) of Chapter 4. The governing equations are described in Chapter 3. For studying the effects of percentage and length of stenosis on the flow results, stenoses with 91% area reduction corresponding to 70% diameter reduction and lengths $2D$ and $4D$ were also considered in the investigation. The inlet and outlet boundary conditions used in this chapter are presented in the following sub-section.

5.2.1 Physiological Inlet and Outlet Conditions and Computational Parameters

The time-dependent physiological pulsatile velocity profile was introduced at the inlet. It is generated by adding steady profile with the unsteady pulsatile profile, which can be obtained from the analytic solution of one-dimensional form of the Navier-Stokes equation in the streamwise direction taking a time-periodic pressure gradient $Be^{i(\eta t)}$, where B is a complex constant and η is the angular frequency of pulsation (Womersley [131], Chandran [132] and Nichols and O'Rourke [7]). The angular frequency, η, is defined as $\eta = \frac{2\pi}{T}$, with $T = 0.6$ s being the period of the pulsation used in this study corresponding to 100 heartbeats per minute (Barber and

Simmons [96]). The Navier-Stokes equation in the streamwise direction becomes

$$\frac{\partial^2 \bar{w}}{\partial r^2} + \frac{1}{r}\frac{\partial \bar{w}}{\partial r} - \frac{1}{\nu}\frac{\partial \bar{w}}{\partial t} = -\frac{B}{\mu}e^{i\eta t}, \quad -R \leq r \leq R. \tag{5.1}$$

Here r is the coordinate in the radial direction. As the considered pressure gradient is periodic in time, the solution of Equation (5.1) can be written as the sum of a series of terms in the following form:

$$\bar{w}(r,t) = \sum_{n=1}^{N_h} \frac{M_n R^2}{\mu \alpha^2} M_0' \sin(n\eta t + \phi_n + \epsilon_0). \tag{5.2}$$

Here $R = 0.01$ m is the radius of the straight tube. The constant N_h is the total number of harmonics of the pulsatile flow. M_n and ϕ_n are the coefficient and the phase angle, respectively, of n^{th} harmonic of the velocity profile; and α is the non-dimensional unsteady Reynolds number or the Womersley parameter which is defined as $\alpha = R\sqrt{\frac{\rho\eta}{\mu}}$, ratio of oscillatory inertial force to viscous force. As the blood in the investigations was assumed to be Newtonian with a density of $\rho = 1060$ kg/m^3 and a constant dynamic viscosity of $\mu = 3.71 \times 10^{-3}$ Pa s, hence the Womersley number, α, was taken as 17.3. It is to note that laminar profile departs from quasi-steadiness when $\alpha \geq 3$ (Varghese et al. [84]). The parameters M_0' and ϵ_0 are defined by the following equations

$$M_0' = \sqrt{1 + h_0^2 - 2h_0\cos(\delta_0)}, \tag{5.3}$$

and

$$\tan(\epsilon_0) = \frac{h_0 \sin(\delta_0)}{1 - h_0\cos(\delta_0)}, \tag{5.4}$$

where $h_0 = \frac{M_0\left(\frac{r}{R}\right)}{M_0}$ and $\delta_0 = \theta_0 - \theta_0\left(\frac{r}{R}\right)$. Again the moduli M_0 and $M_0\left(\frac{r}{R}\right)$ and phases θ_0 and $\theta_0\left(\frac{r}{R}\right)$ are expressed in terms of Bessel function of order zero with complex argument as follows

$$J_0\left(\alpha\frac{r}{R}i^{\frac{3}{2}}\right) = M_0\left(\frac{r}{R}\right)e^{i\theta_0\left(\frac{r}{R}\right)}, \tag{5.5}$$

$$J_0\left(\alpha i^{\frac{3}{2}}\right) = M_0 e^{i\theta_0}. \tag{5.6}$$

For any real variable ζ, McLachlan [133] gave tables for $M_0(\zeta)$ and $\theta_0(\zeta)$ and also defined them in terms of $ber(\zeta)$ and $bei(\zeta)$ by the following

$$J_0\left(\zeta i^{\frac{3}{2}}\right) = M_0(\zeta)e^{i\theta_0(\zeta)} = ber(\zeta) + i\, bei(\zeta), \tag{5.7}$$

where

$$ber\,(\zeta) = 1 - \frac{\left(\frac{1}{2}\zeta\right)^4}{(2!)^2} + \frac{\left(\frac{1}{2}\zeta\right)^8}{(4!)^2} - \frac{\left(\frac{1}{2}\zeta\right)^{12}}{(6!)^2} + \ldots, \tag{5.8}$$

and

$$bei\,(\zeta) = \left(\frac{1}{2}\zeta\right)^2 - \frac{\left(\frac{1}{2}\zeta\right)^6}{(3!)^2} + \frac{\left(\frac{1}{2}\zeta\right)^{10}}{(5!)^2} - \frac{\left(\frac{1}{2}\zeta\right)^{14}}{(7!)^2} + \ldots. \tag{5.9}$$

Therefore, $M_0(\zeta)$ and $\theta_0(\zeta)$ can be written as

$$M_0(\zeta) = \sqrt{ber(\zeta)^2 + bei(\zeta)^2}, \tag{5.10}$$

and

$$\theta_0(\zeta) = \arctan\frac{bei(\zeta)}{ber(\zeta)}, \tag{5.11}$$

respectively. By adding the steady velocity profile to Equation (5.2), the physiological pulsatile velocity profile may be written as

$$\bar{w}(x,y,t) = 2\bar{V}\left(\left[1 - \left(\frac{r}{R}\right)^2\right] + A\sum_{n=1}^{N_h}\frac{M_nR^2}{\mu\alpha^2}M_0'\sin(n\eta t + \phi_n + \epsilon_0)\right), \tag{5.12}$$

and following the expression for flow rate given by Womersley [131], the physiological pulsatile bulk velocity profile becomes

$$\bar{W}(t) = \bar{V}\left(1 + A\sum_{n=1}^{N_h}\frac{M_nR^2}{\mu\alpha^2}M_{10}'\sin(n\eta t + \phi_n + \epsilon_{10})\right), \tag{5.13}$$

where A is the amplitude of pulsation and for $\alpha \leq 10$, the values of $\frac{M_{10}'}{\alpha^2}$ and ϵ_{10} can be obtained from the table provided in [131]. For $\alpha > 10$, Womersley [131] gave the following expressions:

$$\frac{M_{10}'}{\alpha^2} \doteq \frac{1}{\alpha^2} - \frac{\sqrt{2}}{\alpha^3} + \frac{1}{\alpha^4}, \tag{5.14}$$

$$\epsilon_{10} \doteq \frac{\sqrt{2}}{\alpha} + \frac{1}{\alpha^2} + \frac{19}{24\sqrt{2}\alpha^3}. \tag{5.15}$$

To introduce spiral velocity, one-sixth of the pulsatile bulk velocity from Equation (5.13) was taken as the tangential velocity at the inlet, i.e.

$$v_t(x, y, t) = \bar{W}(t)\left(\frac{Cr}{R}\right), \tag{5.16}$$

where $C = \frac{1}{6}$. Four harmonics ($N_h = 4$) were taken in this study. The Reynolds numbers investigated, based on the diameter of unstenosed section of the tube, D, and steady inlet bulk velocity, $\bar{V}$, were $Re = 438$, 584 and 876 with peak Reynolds numbers, $Re_{pk} = 1200$, 1600 and 2400, respectively, corresponding to a value of $A = 0.40$ in Equation (5.12). To investigate the effects of Womersley number, α, and amplitude of pulsation, A, on the non-spiral flow results, other values of $\alpha = 15.5$ and $A = 0.67$, with $Re_{pk} = 2400$ corresponding to $Re = 741$, were also taken in the investigation. The resulting physiological pulsatile inlet velocity profiles, derived from Equations (5.12)-(5.13), are shown in Figure 5.1 for $\alpha = 17.3$, $Re = 876$ and $A = 0.40$. The velocity profile at the centre of the inlet plane and seven phases in the pulsatile cycle at which results were obtained are shown in frame (a), while velocity profiles at $\frac{r}{R} = 0.5$, 0.8 and 0.95 are shown in frame (b). Frames (c) and (d) present bulk velocity profile and velocity profiles along a diametric line at different phases of a time cycle, respectively. It is interesting to note that due to pulsation, back flow occurs close to the wall during the late decelerating systolic phase, i.e. at $P4$ ($t/T = 0.4$).

A physiological 4$^{\text{th}}$ harmonic pulsatile pressure profile (Nichols and O'Rourke [7]), shown in Figure 5.2, which can be defined by the following expression was taken at the outlet.

$$\bar{p} = P + \sum_{n=1}^{N_h} P_n \cos(n\eta t + \varphi_n), \tag{5.17}$$

where P is the steady pressure at the outlet; P_n and φ_n are the coefficient and the phase angle, respectively, of n^{th} harmonic of the pressure profile. To link with the solver, these inlet and outlet boundary conditions were coded in C-language using the User Defined Function (UDF) interface of Fluent.

5.3 Grid Independence and Simulation Details

A mesh of comprising of $\approx 700,000$ control volumes was taken for the simulation of pulsatile non-spiral and spiral blood flow through the model. Grid independence test was conducted in LES of non-spiral flow for $Re = 741$, $A = 0.67$, $\alpha = 17.3$ and time-step, $\delta t = 10^{-3}$ s by taking three grids, namely Grid 1, Grid 2 and Grid 3. Grid 1 corresponds to a total of $\approx 500,000$ control volumes which is increased by 40% for Grid 2 to get $\approx 700,000$ control volumes. Grid 3 consists of huge control volumes i.e., $\approx 1,260,000$ which is further an increase of 80% on Grid 2. Results of the test are presented in Figures 5.3 and 5.4 in terms of phase-averaged streamwise velocity, $\langle\langle\bar{w}\rangle\rangle$ (m/s), at different axial positions and wall shear stress (Pa), respectively, during phase $P3$. Note that the phase averaging of WSS was done on the circumferential average WSS. The results show a good agreement and the resolution of Grid 2 is seemed to be adequate for the simulation, though the phase-averaged streamwise velocity in Figure 5.3 in the further downstream region (frame e-g) is slightly sensitive to the choice of grid –which is quite normal in LES. Both the resolved scale and the SGS eddies are different, depending on the mesh resolution. Therefore, LES results will show some dependence on the grid resolution until the LES grid resolution becomes fine enough to qualify as a DNS resolution (Mittal et al. [88]; Paul and Molla [93]).

Time-step independence test was also carried out for Grid 2 by taking two different time-steps of $\delta t = 10^{-3}$ s and 1.5×10^{-3} s while keeping the other parameters same as in the grid resolution study and the results are compared in Figures 5.5 and 5.6 in terms of phase-averaged streamwise velocity,$\langle\langle\bar{w}\rangle\rangle$ (m/s), at different axial positions and wall shear stress (Pa), respectively, during phase $P3$. The results are quite independent of the time-step used which is clear from the above two figures. However, the phase-averaged streamwise velocity in Figure 5.5 in the further downstream region (frame d-f) is sensitive slightly as seen previously in the case of grid resolution test. These sensitivities are reasonable as one fixed grid configuration was used. Time-step in the simulation of turbulent flow, however, depends on the grid size (Choi and Moin [134]). The smallest time-step of 10^{-3} s was chosen in all the investigations of this thesis to achieve stable solutions.

In the present study of pulsatile non-spiral and spiral blood flow through 75%

area reduction cosine-type stenosis, Reynolds numbers considered are $Re = 438$, 584 and 876. LES was applied for all cases and two-equation standard k-ω transitional model was also applied in non-spiral flow for $Re = 438$ to assess its suitability for modelling pulsatile turbulence flow. In this study and all other subsequent studies in this thesis, eight initial cycles were run and phase-averaged statistics, as defined in § 3.7, were collected over the last 12 time period cycles, following the initial eight cycles. The phase-averaged statistics results are presented during phase $P3$, i.e. during decelerating systolic phase when turbulence generation by pulsatility is greatest (Ku [3]).

Cycle-to-cycle development of instantaneous streamwise velocity, $\bar{w}$, in non-spiral flow for $Re = 876$ in the initial eight cycles during phase $P2$, as shown in Figure 5.7, shows that flow has developed well by this time and initial transients have disappeared from the computational domain. Figure 5.8 shows the root mean square (rms) of centreline streamwise velocity fluctuations, $\langle w'' \rangle_{rms}$ (m/s), over the last three cycles at different axial locations for both non-spiral and spiral pulsatile flow while $Re = 876$. It can be observed from the figure that the rms velocity in both non-spiral and spiral flow has reached time-periodic state in the considered 12 cycles for the calculation of phase-averaged statistics.

5.4 Results and Discussion

First, the contribution of the dynamic SGS model constant C_s and eddy viscosity are presented in § 5.4.1. This is followed by the results of the instantaneous and phase-averaged flow physics in § 5.4.2 and § 5.4.3 consecutively. The results of the thorough investigations of the turbulent flow characteristics are summarised in § 5.4.4 and § 5.4.5. Effects of percentage and length of stenosis are discussed in § 5.4.6 and finally, effects of Womersley number and amplitude of pulsation flow are given in § 5.4.7.

5.4.1 Contribution of the SGS Model

Figure 5.9 depicts the contour plots of dynamic Smagorinsky constant, C_s, in non-spiral flow during phase $P3$ in the $z - x$ mid-plane for $Re = 438$, 584 and 876.

The effects of Reynolds number on C_s is clear from the figure, i.e. the value of C_s increases with Reynolds number. It is worth noting that the maximum value of C_s occurs in the post-stenotic region where the flow may become turbulent. However, the value of C_s in the upstream of the stenosis is very small and therefore negligible as the flow is laminar there.

The contour plots of the corresponding normalised SGS eddy viscosity, μ_{sgs}/μ, is presented in Figure 5.10. The maximum eddy viscosity is ≈ 0.3 for $Re = 438$ (frame a), whereas it is ≈ 0.5 for $Re = 584$ (frame b) and 876 (frame c). Though the maximum eddy viscosity is same for $Re = 584$ and 876, but the difference between the two plots is obvious as the maximum eddy viscosity occurs at more locations in frame (c) than in frame (b). This observation suggests that the SGS model add up to 50% extra dissipation into the flow, depending up on the Reynolds number; and less energy dissipated through the SGS for low Reynolds number, as expected. Like C_s, the SGS dissipation is maximum in the downstream region where the flow transients to turbulence. The values of C_s and μ_{sgs}/μ in the respective contour plots in spiral flow remain almost same as those in non-spiral flow.

5.4.2 Instantaneous Flow Field

The y-vorticity, $\Omega_y = (\frac{\partial \bar{w}}{\partial x} - \frac{\partial \bar{u}}{\partial z})$ (1/s), in non-spiral and spiral flow at different phases over the last pulsatile cycle for $Re = 876$, as presented in Figures 5.11 and 5.12, respectively, shows how and where the transition-to-turbulence takes place in both flows. In both figures, two vortices, one anti-clockwise (red) and the other clockwise (blue), are generated at the post-stenotic region near the wall as the shear layers separate from the stenosis throat during phase $P1$ (frame a). As the phase increases, the vortex pair roll down further downstream in frame (b) and (c). With the adverse pressure gradient, the unstable jet and shear layers break down at $z \approx 4D$ and $z \approx 3D$ in non-spiral and spiral flow, respectively, apparently causing the flow to experience transition to turbulence between $z = 4D$ and $6D$ in the non-spiral case, and between $z = 3D$ and $5D$ in the spiral case during phases $P1$, $P2$ and $P3$ (frame a, b and c). Due to jet breakdown and increased mixing in the transition-to-turbulence region, flow reattachment occurs in non-spiral and spiral flow by $z \approx 6D$ and $z \approx 5D$, respectively, during the above first three phases. No

vortex-ring is found beyond phase $P3$ (frame d-g). Furthermore, the vortex pair in frames (a-c) in non-spiral flow look very similar to that in spiral flow, i.e. no effect of spiral velocity on vorticity development can be observed.

The effects of Reynolds number on the development of y-vortices in both non-spiral and spiral flow during phase $P3$ for $Re = 438$, 584 and 876 are shown in Figures 5.13(a-c) and 5.14(a-c), respectively. In both non-spiral and spiral flow, vortices pattern generated in the post-stenotic region are quite similar in look, however, the vortex-rings move further downstream as the Reynolds number is increased. In addition, for Reynolds numbers $Re = 438$ and 584, the shear layers break down at $z \approx 4D$ in both non-spiral and spiral flow. However, for Reynolds number 876, the shear layers breakdown earlier (at $z \approx 3D$) in spiral flow than in non-spiral flow (at $z \approx 4D$).

Further flow characteristics can be observed through velocity vectors and streamlines. Figures 5.15 and 5.16 show in-plane velocity vectors appended on the streamwise velocity, $\bar{w}$ (m/s), contours for $Re = 876$ during phase $P3$ in non-spiral and spiral flow, respectively, at different axial locations. In both flows, the stenotic jet is maximum at $z = 2D$ (frame c) and cross-sectional velocities directing fluid toward the vessel wall. In non-spiral flow (Figure 5.15), the jet is relatively stable and flow is laminar at $z \approx 3D$ (frame d); however, at $z \approx 4D$ (frame e), the jet breaks down and flow is re-circulated and becomes transitional. On the other hand, in spiral flow (Figure 5.16), the jet breaks down at $z \approx 3D$ (frame d), with flow being re-circulating and transitional. The reattachment of the flow in non-spiral and spiral flow takes place at $z \approx 6D$ (Figure 5.15(g)) and $z \approx 5D$ (Figure 5.16(f)), respectively, as can be seen from the in-plane vectors. Additionally, though spiral pattern in spiral flow (Figure 5.16) is visible at the throat and post-lip of the stenosis (frames a-b), it is lost in the further downstream region (frames c-h) due to the occurrence of strong turbulence activities there. From pathological point of view, the strong re-circulations found in non-spiral (Figure 5.15(e-g)) and spiral (Figure 5.16(d-f)) flow is detrimental to blood cells and intima of the stenosed artery as pointed out earlier in Chapter 4.

The instantaneous $z - x$ mid-plane streamlines in non-spiral and spiral flow during phase $P3$ for (a)$Re = 438$, (b)$Re = 584$ and (c)$Re = 876$ are shown in Figures 5.17 and 5.18, respectively. The corresponding streamlines in non-spiral

and spiral flow are of similar pattern and no significant difference can be found between these two figures. As a result of reverse flow near the wall, large recirculation regions are created around the post post-lip of the stenosis. Blood residence time in these recirculation regions is increased as these are the sites of low shear stress, which in turn increases the chances of heart attack and stroke (Molla [90]). Furthermore, the recirculation region in both non-spiral and spiral flow increases slightly with Reynolds number which can be observed from the Figures 5.17 and 5.18, respectively.

5.4.2.1 Instantaneous Wall Pressure and Shear Stress

Figure 5.19 depicts the instantaneous wall pressure, $\bar{p}$ (Pa), in both non-spiral and spiral flow during different phases of the last pulsatile cycle for $Re = 438$, 584 and 876 at two circumferential locations (0° and 90°) of the wall. Note that the corresponding wall pressures obtained from the k-ω model in non-spiral flow for $Re = 438$ are also appended. It is clear from the figure that the effect of spiral velocity on pressure drop is negligible. However, due to spiral flow, some variations in the oscillating part of the pressure within $2 \leq z/D \leq 6$ can be observed, especially for higher Reynolds number. It is interesting to note that k-ω results are in good agreement with the corresponding LES results. No significant difference can be observed between the profiles plotted at 0° circumferential location and those plotted at 90° circumferential location. A Bernouilli-type pressure drop occurs at the stenosis throat and in the immediate post-stenotic region where the streamwise velocity is extremely high and this pressure drop increases as the Reynolds number is increased. In addition, the pressure drop is extremely large during phases $P1$ (late accelerating systole), $P2$ (systolic peak) and $P3$ (early decelerating systole) compared with the pressure drop during late decelerating systolic phase $P4$ or other diastolic phases; and it is maximum during psae $P1$, which is ≈ 685 Pa for $Re = 876$. In the pathophysiological context, this extremely large pressure drop is potentially harmful as this can cause local collapse of the stenosis, which in turn results in flow-choking and compressive stress, capable of buckling the structure. The oscillations in compressive loading may lead to rupture of the plaque cap, a precipitating event in most heart attacks and strokes (Wootton and Ku [6]; Li et al. [8]). An extremely large pressure drop at the stenosis throat was also found in the steady

case in Chapter 4 which was discussed there with the relevant clinical implications.

The corresponding wall shear stress in both non-spiral and spiral flow is shown in Figure 5.20. No significant influence of spiral velocity on wall shear stress is observed; wall shear stress in spiral flow for the investigated Reynolds numbers match that in non-spiral flow in the critical region of stenosis, i.e. around the throat and immediate post-stenotic region during all the phases, though they vary slightly in the further downstream region ($z \geq 2D$). Additionally, it should be noted that shear stress obtained from k-ω model match well the corresponding LES results, as seen previously in the results of wall pressure. For all the Reynolds numbers, shear stress rises sharply just before the stenosis throat during all the phases due to the extremely high velocities at the throat, it then takes oscillatory form in the downstream region with some smaller peaks than that around the throat. During late decelerating systolic phase $P4$, the second peak is bigger than the first one around the throat except for the case of spiral velocity with $Re = 876$ in which the peak around $z \approx 3.5D$ is bigger than the first peak. It is interesting to note that during phase $P3$ for $Re = 876$, the second peak at $z = 2D$ is also quite large. The oscillatory pattern of shear stress, which is prominent between $2D \leq z \leq 6D$ from phase $P4$ to the end of the pulsatile cycle, is responsible for arterial disease progression as this has detrimental effect on red blood cells and inner lining of the blood vessel (Ku [3]; Paul and Molla [93]).

It is clear from the figure that the wall shear stress is dependent on Reynolds number, i.e. it increases with Reynolds number. Shear stress reaches maximum value during phase $P2$ (frame c-d) just before the throat for all the investigated Reynolds numbers; and this maximum shear stress is closely followed by its value during $P1$ (frame a-b) and $P3$ (frame e-f). For $Re = 876$, the wall shear stresses are ≈ 20 Pa, ≈ 20 Pa and ≈ 16 Pa during $P1$, $P2$ and $P3$, respectively. According to Malek et al. [9], as mentioned in the previous chapter, shear stress > 7 Pa may induce thrombosis. On the other hand, Sutera and Mehrjardi [37] reported that higher shear stress (≥ 10 Pa) cause deformation of the red blood cells. Hence, it is clear from the figure that shear stress for the Reynold number $Re = 876$ reaches the harmful level during all phases except the last phase $P7$; however, for $Re = 584$, it reaches the clinically dangerous level only during phases $P1$, $P2$ and $P3$ and it remains in the normal range during all the phases for $Re = 438$.

5.4.3 Phase-averaged Flow Characteristics

The phase-averaged streamwise velocity obtained at different axial locations during phase $P3$ in both non-spiral (NSp) and spiral flow is shown in Figure 5.21(a-l) for different Reynolds numbers along with the corresponding k-ω results. The profile, which resembles fully developed Poiseuille flow at the pre-lip of the stenosis, becomes plug-shaped jet at the throat of the stenosis and in the immediate post-stenotic region (frames b-d) as the flow passes through the stenosis with extremely high velocity. The negative values of the velocity found near the wall in frames (c-d) correspond to the occurrence of the permanent re-circulation region observed in Figures 5.17 and 5.18. The effect of Reynolds number on the streamwise velocity is distinctive in the figure. The influence of spiral flow is seen only in the turbulent region, from $z = 3D$ to $6D$ (frames e-h), where the velocity profiles corresponding to both the non-spiral and spiral flow begins to lose their jet-like character and tend to uniformity. In this region, the profiles corresponding to spiral flow differ from non-spiral flow profiles; and specifically for $Re = 438$ and 584, the streamwise velocity in spiral flow increases slightly at some places from its value in non-spiral flow, whereas it decreases in spiral flow at some places for $Re = 876$. It should be noted that in the turbulent region, the phase-averaged velocity profiles obtained from k-ω model do not match the corresponding LES profiles because k-ω model provides time-averaged information instead of time-accurate or instantaneous information. The blunt-type profiles seen after $z = 6D$ are common to turbulent flow and in the far downstream region (frame l), the profiles regain the upstream parabolic shape – an indication of laminar flow field.

Though the instantaneous wall shear stress during different phases was shown in Figure 5.20 and discussed in detail in § 5.4.2.1, it is interesting to notice how the phase-averaged wall shear stress behaves around the throat of the stenosis and in the downstream region. Figure 5.22 shows the phase-averaged wall shear stress at two circumferential locations (0° and 90°) during phase $P3$ for the investigated Reynolds numbers in both non-spiral and spiral flow. The pattern and magnitudes of phase-averaged wall shear stress are largely same as those of the instantaneous wall shear stress in Figure 5.20(e-f), however, the highly oscillatory pattern that was found in the downstream region in the instantaneous shear stress has almost disappeared in the phase-averaged shear stress. As the oscillatory nature of WSS in the

downstream region disappears due to phase-averaging, hence to get the real picture of WSS, the instantaneous results should be considered. As seen in Figure 5.20(e-f), the phase-averaged shear stress increases sharply just before the throat of the stenosis; and this extreme rise is follow by smaller peaks in the downstream region. This finding is quite similar to the WSS results of Mittal et al. [88] and Varghese et al. [84]. It is to note that phase-averaged shear stresses for $Re = 438$ obtained from k-ω model are in excellent agreement with the corresponding LES results.

5.4.4 Turbulent Characteristics

A quantitative measure of turbulence can be obtained from the root mean square (rms) of velocity fluctuations. Profiles of the root mean square (rms) of the streamwise velocity fluctuations, $\langle w'' \rangle_{rms}$ (m/s), as defined in § 3.7, recorded at different axial locations are shown in Figure 5.23 for the Reynolds numbers $Re = 438$, 584 and 876 in both non-spiral (NSp) and spiral flow during phase $P3$. Figures 5.24, 5.25 and 5.26 present the turbulent kinetic energy (TKE), $\frac{1}{2}\langle u_j'' u_j'' \rangle$ (m^2/s^2), for Reynolds number $Re = 438$, 584 and 876, respectively, in both non-spiral (NSp) and spiral flow during phase $P3$ at different axial locations. The values of both $\langle w'' \rangle_{rms}$ and TKE at the post-lip of the stenosis and the immediate post-stenotic region are very small as the flow is still laminar in this region and the transition-to-turbulence is yet to start; they are extremely large in the downstream region, from $z = 3D$ to $6D$, where transition-to-turbulence takes place with jet breakdown and they gradually decrease after $z = 6D$, indicating a relaminarised flow field in the further downstream region. The influence of spiral flow on both $\langle w'' \rangle_{rms}$ and TKE can be observed for all the investigated Reynolds numbers; the values of both $\langle w'' \rangle_{rms}$ and TKE rises extremely at some axial locations in spiral flows from their corresponding values in non-spiral flows – this finding is in direct contradiction to the claims of Paul and Larman [17] and Stonebridge et al. [16]. Both groups studied steady spiral flow through arterial stenosis and claimed that spiral flow decreases TKE. But blood flow is unsteady and pulsatile. Also, our TKE results in steady spiral flow in Chapter 4 contradicted the above claim made by Paul and Larman [17] and Stonebridge et al. [16]. The limitations of their studies were highlighted in Chapter 4 and discussed in detail in § 2.4 of Chapter 2.

The effect of Reynold number on both the rms of the streamwise velocity fluctuations and the turbulent kinetic energy is clearly visible from the figure; both $\langle w'' \rangle_{rms}$ and TKE generally increase with Reynolds number though this rule is broken at some axial locations . For example, $\langle w'' \rangle_{rms}$ for $Re = 876$ at $z = 3D$ and $4D$ is smaller than its corresponding value for $Re = 584$ at those positions and TKE for $Re = 876$ in non-spiral flow at $z = 4D$ decreases from its corresponding value for $Re = 584$ in non-spiral and spiral flow at that location. The clinical impact of extreme velocity fluctuations or high level of TKE found in the transition-to-turbulence region in both non-spiral and spiral flow is severe as they may damage blood cells and the tissues inside a blood vessel (Ku [3]; Paul and Molla [93]).

Figure 5.27 depicts the rms of wall pressure fluctuations, $\langle p'' \rangle_{rms}$ (Pa), in both non-spiral and spiral flow for the investigated Reynolds numbers during phase $P3$ at two circumferential locations (0° and 90°). In both non-spiral and spiral flow for $Re = 876$, $\langle p'' \rangle_{rms}$ rises at around $z = 2D$ and in the downstream region of $3D \leq z \leq 7D$ and maximum $\langle p'' \rangle_{rms}$ in non-spiral flow occurs at around $z = 5D$, whereas in spiral flow, $\langle p'' \rangle_{rms}$ is maximum at around $z = 2D$. For $Re = 584$, $\langle p'' \rangle_{rms}$ rises only in the downstream region of $3D \leq z \leq 5.5D$ and maximum $\langle p'' \rangle_{rms}$ in spiral flow is larger than that in non-spiral flow. However, the change in $\langle p'' \rangle_{rms}$ along the axial direction is very small for $Re = 438$. Furthermore, the high level of SGS eddy viscosity, which was also found at the immediate downstream region at around $z = 2D$ and in the downstream region from $z = 3D$ to $6D$, shows its strong correlation with the high level of $\langle p'' \rangle_{rms}$, TKE or $\langle w'' \rangle_{rms}$. In the pathophysiological context, the high level of $\langle p'' \rangle_{rms}$ is potentially harmful as it may affect the arterial wall, resulting in post-stenotic dilation and arterial murmurs, which is a key diagnostic condition of arterial stenosis through bio-acoustic techniques (Ask et al. [135]).

The corresponding k-ω turbulent results in non-spiral flow for $Re = 438$ are also appended in the above figures. It is to note that k-ω turbulent results in Figures 5.23, 5.24 and 5.27 are in disagreement with the corresponding LES turbulent results – shows the inability of k-ω model to simulate transition to turbulence of pulsatile blood flow because the model is not capable of giving instantaneous or time-accurate results, instead, it gives time-averaged results arising from the time-averaged governing equations of motion (Scotti and Piomelli [75]). Both the pulsatile nature of the blood flow and the relatively low Reynolds number make

URANS turbulence models such as k-ω and k-ϵ models, which are designed primarily for simulating well-developed high-Reynolds-number turbulent flows, unsuited for these arterial flows. On the other hand, LES can provide time-accurate information about a wide range of dynamically important scales in the flow. Hence the various turbulence results in a pulsatile flow can be accurately calculated from the LES time-accurate results – which is not possible by using URANS (Mittal et al. [88]) results.

5.4.4.1 Cycle-to-cycle variations

Cycle-to-cycle variations of important flow quantities reveal further information about transition to turbulence of physiological pulsatile non-spiral and spiral blood flow. In this section, cycle-to-cycle variations of centreline streamwise velocity, wall pressure gradient, centreline velocity fluctuations, centreline TKE and wall pressure fluctuations in both non-spiral and spiral flow for $Re = 876$ are presented. Figure 5.28 shows that the centreline streamwise velocity, $\bar{w}$ (m/s), in both non-spiral and spiral flow increases at the throat of the stenosis from its upstream value due to presence stenosis and remain almost undisturbed in every pulsatile cycle even at $z = 2D$ and the flow becomes completely chaotic in the downstream region of $3D \leq z \leq 9D$, where the jet starts to break and mixing of the fluid takes place; however, the flow tries to regain its upstream pattern in the further downstream region. The magnitude of the flow velocity in the disturbed region is different at every cycle and axial location and its cycle-to-cycle variation is non-periodic; it drops gradually in the downstream region to its upstream value as the flow passes along the artery. It should be noted that the effects of spiral flow on the streamwise velocity can be seen only in the turbulent region as the spiral flow causes the streamwise velocity at different locations in this region to be in disagreement with its corresponding value in non-spiral flow, however they match well elsewhere.

Figure 5.29 illustrates cycle-to-cycle variation of the wall pressure gradient obtained at 0° circumferential locations in both non-spiral and spiral flow at different axial locations. The extremely oscillating wall pressure gradient observed in the downstream region of $3D \leq z \leq 7D$ is closely associated with arterial murmurs that was discussed in the previous section. In addition, the wall pressure gradient in non-spiral flow differs from that in spiral flow in this oscillating region as seen in

the case of streamwise velocity.

Cycle-to-cycle variations of the cross-stream velocity fluctuations, u''/u''_{max} and v''/v''_{max}, and the streamwise velocity fluctuations, w''/w''_{max}, at different axial locations on the centreline in both non-spiral and spiral flow are shown in Figure 5.30. The fluctuations in all the velocities before $z = 3D$ are negligible as the flatness of them even at $z = 2D$ can be seen clearly in the figure. The magnitudes of the velocity fluctuations increase after $z = 2D$; and the velocity fluctuations in spiral flow are large in the region of $3D \leq z \leq 5D$, whereas in non-spiral flow, extreme velocity fluctuations can be found within $3D \leq z \leq 6D$. As seen in the streamwise velocity in Figure 5.28, the velocity fluctuations are non-periodic. The fluctuating quantities in both non-spiral and spiral flow decrease in the further downstream region and become almost flat as the effect of the stenosis vanishes there and relaminarisation takes place. Furthermore, Figure 5.31 illustrates the effect of spiral flow on TKE, $\frac{1}{2}\langle u''_j u''_j \rangle$ (m^2/s^2), over last three pulsatile cycles considered for turbulence calculation at various axial locations on the centreline. TKE in spiral flow increases significantly during various phases of the cycle at some locations on the centreline, especially within $2D \leq z \leq 5D$, from its corresponding magnitude in non-spiral flow.

Again, the non-periodic wall pressure fluctuations, p'' (Pa), in both non-spiral and spiral flow as shown in Figure 5.32, which are large in the downstream region of $2D \leq z \leq 6D$, are strongly correlated with the arterial murmurs created due to arterial stenosis. The effects of spiral flow on the wall pressure fluctuations are prominent at some phases of the pulsatile cycle, especially during systolic and early diastolic phase in the downstream region of $2D \leq z \leq 6D$.

5.4.5 Turbulent Energy Spectra

Additional information about the nature of random turbulent fluctuations in both non-spiral and spiral flow seen in the post-stenotic region can be obtained from the turbulent energy spectra presented in Figures 5.33 and 5.34 for $Re = 876$. Following the convention used by Cassanova and Giddens [22], Khalifa and Giddens [25] and Varghese et al. [84], the normalised energy spectra, $E_{g''g''} = (E(f)w_p) \,/\, (2\pi D_m)$, (where g is a generic fluctuating variable for either streamwise velocity, w or pres-

sure, p) and the Strouhal number, $Sr = 2\pi f D_m/w_p$, have been defined and plotted in the above two figures. $D_m = 0.5D$ is the minimum stenosis diameter, f is the frequency of the fluctuation and w_p is peak cross-sectional average velocity at the stenosis throat. For the energy spectra of the centreline streamwise velocity fluctuations, w'', in both non-spiral and spiral flow in Figure 5.33, $E(f)$ is the frequency spectrum of the normalised centreline streamwise velocity fluctuations, $(w''/\langle w''\rangle_{rms})^2$, whereas for the for the energy spectra of the wall pressure fluctuations, p'', in Figure 5.34, $E(f)$ is frequency spectrum of the normalised wall pressure fluctuations, $(p''/\langle p''\rangle_{rms})^2$. Cassanova and Giddens [22] postulated that D_m and w_p are effective scaling parameters for the spectra as the peak stenotic jet velocity causes the transition to start in the downstream region. The FFT (Fast Fourier Transform) scheme was employed to compute the frequency spectra, $E(f)$.

The lines corresponding to $(Sr)^{-5/3}$ and $(Sr)^{-7}$, describing the inertial subrange (or the broadband frequency region), where energy transfers from the large eddies to smaller ones with very small energy dissipation, and the viscous dissipation range, respectively, are shown in Figure 5.33 (Tennekes and Lumley [136]; Hinze [137]; Wilcox [119]; Varghese et al. [84]). In addition, another line corresponding to $(Sr)^{-10/3}$ is also shown in the figure. Gross et al. [138] and Lu et al. [47] observed that *in vivo* velocity spectra of $-5/3$ power slope break into $-10/3$ power slope at a frequency closely connected with arterial murmurs. The inertial subrange region in both non-spiral and spiral flow is very small at $z = 1D$ and $z = 2D$ (frames a-b) as the flow is relatively undisturbed. But in the transition-to-turbulence region of $3D \leq z \leq 5D$ (frame c-e), the inertial subrange region is large and $-5/3$ power slopes break into $-10/3$ power slope at higher frequencies. The viscous dissipation range is almost absent in this region. These results agree quite well with the experimental findings of Gross et al. [138] and Lu et al. [47]. In both non-spiral and spiral flow, the inertial subrange region decays gradually in the further downstream region of $z \geq 6D$ (frame f-i) and the spectra roll off to viscous dissipation range at lower frequencies as the turbulence intensity becomes weaker and relaminarisation takes place. It is interesting to note that at $z = 5D$ and $6D$, the inertial subrange in the velocity spectra in spiral flow has larger range of frequencies than that in non-spiral flow (frame e-f), however at $z = 4D$, the velocity spectra in non-spiral flow has larger range of frequencies constituting the

inertial subrange than that in spiral flow; and $-10/3$ power slope is almost absent in non-spiral flow at this location (frame d). Additionally, in the region $z \geq 8D$, the velocity spectra of $-10/3$ power slope in spiral flow break into -7 power slope, i.e. the viscous dissipation range at lower frequencies compared with the corresponding break frequencies in non-spiral flow; and the viscous dissipation range in spiral flow is smaller than that in non-spiral flow as the spectra in spiral flow immediately changes from -7 power slope to another slope inclining towards horizontal line (frame g-i).

Figure 5.34 depicts the normalised energy spectra of normalised pressure fluctuations, $E_{p''p''}$, along with lines corresponding to $(Sr)^{-5/3}$, $(Sr)^{-7/3}$ and $(Sr)^{-7}$. Note that unlike velocity spectra, $-10/3$ power slope is absent in wall pressure spectra (Paul and Molla [93]). In frames (a-b), the inertial subrange (or broadband) region is very small as it was seen in frames 5.33(a-b) of velocity spectra. In $3D \leq z \leq 5D$ (frames c-e), a relatively large range of frequencies fall under the broadband range; and the broad band region becomes small again at $z = 6D$ (frame f) as the turbulent intensity is relatively low here. It is to note that the viscous dissipation range is observed clearly only at $z = 2D$ (frame b), $z = 3D$ (frame c) and $z = 5D$ (frame e); and it is almost absent elsewhere. The energy spectra of pressure fluctuations roll off from $-5/3$ power slope to $-7/3$ power slope at frequencies which transfer the energy from pressure fluctuations spectra to the sound spectra, a potential source of arterial stenosis murmurs (Paul and Molla [93]). As to the effect of spiral flow on energy spectra of wall pressure fluctuations, no significant change in the spectra breaking into a power slope of interest due to spiral flow can be observed.

5.4.6 Effects of Percentage and Length of the Stenosis

It is interesting to see how the increase in the percentage of area reduction of the stenosis and the length of the stenosis affect the important results of pulsatile non-spiral blood flow in the stenosis for $Re = 876$. Figure 5.35 shows instantaneous wall pressure (Pa) for non-spiral flow in 75%, 91% and 91% area reduction stenosis with length$= 2D$, $2D$ and $4D$, respectively, at 0° and 90° circumferential locations during phase $P2$ and $P3$ while $Re = 876$ and $A = 0.40$. Pressure drop

increases with stenosis percentage; the maximum pressure drops for 91% stenosis with length$= 2D$ during phase $P2$ and $P3$ are ≈ 5206 Pa and ≈ 3769 Pa, respectively, whereas for 75% stenosis with length$= 2D$, the maximum pressure drops are ≈ 661 Pa and ≈ 426 Pa during phase $P2$ and $P3$, respectively. That is, the maximum pressure drops increase by $\approx 688\%$ and $\approx 785\%$ during phase $P2$ and $P3$, respectively, in 91% stenosis compared with its corresponding value in 75% stenosis. It is clear from the figure that the effect of the length of stenosis on pressure drop is very insignificant. The maximum pressure drop increases by $\approx 0.5\%$ in stenosis with $4D$ length during phase $P2$ compared with its corresponding value in stenosis with $2D$ length, whereas during phase $P3$, the maximum pressure drop decreases by $\approx 1.6\%$ in stenosis with $4D$ length compared with its corresponding value in stenosis with $2D$ length. Additionally, when the stenosis percentage is increased, pressure rises in the further downstream region to regain its normal undisturbed value after dropping at the stenosis throat. These extreme pressure drops has severe clinical consequences including flow-choking and rupture as discussed in § 5.4.2.1. Therefore, 91% area reduction is a very severe stenosis case which calls for an immediate therapeutic measure.

The corresponding instantaneous wall shear stress (WSS) (Pa) is presented in Figure 5.36. The maximum WSS increases when the stenosis percentage is increased, however it decreases if the length of the stenosis is increased as can be observed from the figure. In addition, shear stress becomes increasingly oscillatory in the downstream region of $3D \leq z \leq 6D$ with the increase in area reduction in stenosis. The maximum WSS in 91% stenosis with length$= 2D$ are ≈ 116 Pa and ≈ 93.3 Pa during phase $P2$ and $P3$, respectively; and in 91% stenosis with length$= 4D$, it is ≈ 81 Pa and ≈ 65 Pa during phase $P2$ and $P3$, respectively, whereas in 75% stenosis with length$= 2D$, the maximum WSS are ≈ 20 Pa and ≈ 16 Pa during phase $P2$ and $P3$, respectively. Hence, the maximum WSS in 91% stenosis rise by $\approx 480\%$ and $\approx 481\%$ during phase $P2$ and $P3$, respectively, compared with its corresponding value in 75% stenosis; and the the maximum WSS decreases by $\approx 30\%$ in stenosis with length$= 4D$ during phase $P2$ and $P3$ both compared with its corresponding value in stenosis with length$= 2D$. The pathophysiological impacts of these extremely high WSS were discussed in § 5.4.2.1. In addition to those implications, high WSS ($> 37.9 \pm 8.5$ (SD) Pa) can cause endothe-

lial cells damage (Fry [36]) as well.

Figure 5.37 shows that the TKE, $\frac{1}{2}\langle u_j'' u_j'' \rangle$ (m^2/s^2), like the maximum pressure drop and the maximum WSS, increases with the area reduction in stenosis. Moreover, TKE also rises sharply when the length of the stenosis is increased fixing the stenosis percentage. The maximum TKE found in the figure for 75% stenosis with length$= 2D$, 91% stenosis with length$= 2D$ and 91% stenosis with length$= 4D$ are 0.023 m^2/s^2 (frame e), 0.37 m^2/s^2 (frame e) and 0.496 m^2/s^2 (frame d), respectively; i.e. the maximum TKE increases by $\approx 1509\%$ in 91% stenosis compared with its corresponding value in 75% stenosis and it increases by $\approx 34\%$ in the stenosis with length$= 4D$ compared with its corresponding value in the stenosis with length$= 2D$. The physiological consequences of extremely high TKE was discussed earlier and will not be repeated here. It is clear from the above discussion that the 91% area reduction stenosis has devastating effects on cardiovascular health and therapeutic measure, therefore, should be taken immediately in this case.

5.4.7 Effects of amplitude of pulsation and Womersley number

The effect of the amplitude of pulsation, A, and the Womersley parameter, α, on the instantaneous wall pressure in non-spiral flow during phase $P2$ and $P3$ at 0° and 90° circumferential location of the vessel wall is illustrated in Figure 5.38 for (i) $Re = 876$, $A = 0.40$ and $\alpha = 17.3$, (ii) $Re = 741$, $A = 0.67$ and $\alpha = 17.3$ and (iii) $Re = 741$, $A = 0.67$ and $\alpha = 15.5$ while the peak Reynolds number is same in all three cases, i.e. $Re_{pk} = 2400$. The maximum pressure drop rises by $\approx 17\%$ during phase $P2$ if the amplitude of pulsation is increased from $A = 0.40$ to 0.67 and it remains almost same during phase $P3$ for both amplitudes of pulsation. However, when the Womersley number is decreased from $\alpha = 17.3$ to 15.5, the maximum pressure drop falls by $\approx 2\%$ during phase $P2$ and it grows by $\approx 2\%$ during phase $P3$. Additionally, the pressure drop occurs over a relatively larger region in the small Womersley number case.

Figure 5.39 shows the corresponding instantaneous WSS. Like the maximum pressure drop, the maximum WSS increases by $\approx 15\%$ during phase $P2$ if the amplitude of pulsation is increased from $A = 0.40$ to 0.67. And if the Womersley number is decreased from $\alpha = 17.3$ to 15.5, the maximum WSS decreases too

during phase $P2$, though insignificantly (by $\approx 1\%$). However, during phase $P3$, the maximum WSS is insensitive to the change either in the amplitude of pulsation or in the Womersley number, though differences can be observed in the smaller peaks downstream of the stenosis.

For higher amplitude of pulsation, $A = 0.67$, transition-to-turbulence takes place within $3D \leq z \leq 5D$, whereas for $A = 0.40$, it takes place in the further downstream region, $4D \leq z \leq 6D$, as it can be seen from the TKE results in Figure 5.39. Though the maximum TKE decreases by $\approx 45\%$ when the amplitude of pulsation is increased from $A = 0.40$ to 0.67, TKE rises sharply at some places in the transition region in $A = 0.67$ case from its corresponding value at those locations in the case of $A = 0.40$ (frame c-e). Furthermore, when the Womersley number is reduced from $\alpha = 17.3$ to 15.5 keeping the Reynolds number and the amplitude of pulsation fixed, the maximum TKE increases by $\approx 36\%$. Additionally, the transition-to-turbulence occurs in the further downstream region, $4D \leq z \leq 6D$, in the low Womersley number case.

5.5 Conclusion

The physiological pulsatile non-spiral and spiral blood flow in a straight stenosed tube having 75% area reduction stenosis has been studied for $Re = 438$, 584 and 876 by employing Large Eddy Simulation with Smagorinsky-Lilly dynamic subgrid model (Germano [115], Lilly [116] and Kim [123]). A maximum of 50% extra energy dissipation into the flow through the SGS model for $Re = 876$ found in the intense turbulence region justifies using LES in the study. The SGS contribution increases with Reynolds number as the turbulence intensity in the downstream of the stenosis rises if the Reynolds number is increased. The two-equation Standard k-ω Transitional model was also applied to non-spiral flow through the model for $Re = 438$ to assess its suitability for pulsatile flow simulation. Some of the results obtained from k-ω model, especially the wall pressure and WSS are in good agreement with the corresponding LES results; the turbulent results, however, differ from the corresponding LES results which is expected because the k-ω model gives time-averaged results rather than instantaneous results. Grid resolution and time-step resolution seem to have been achieved through a quite good agreement in

phase-averaged results for different grid resolutions and time-steps. The number of pulsatile cycles taken for the phase-averaged statistics seems to be enough for the rms velocity to reach a time-periodic state by that time.

Extremely large pressure drop in both non-spiral and spiral flow occurs at the throat of the stenosis during phases $P1$, $P2$ and $P3$ compared with other phases which can lead to flow-choking and even rupture of the plaque in pulsatile flow. Additionally, the sharp rise of the WSS just before the stenosis throat, that is also extremely high during phases $P1$, $P2$ and $P3$, has many pathological consequences including thrombosis and deformation of red blood cells. The effect of spiral flow on both the maximum pressure drop and maximum WSS which occur around the throat of the stenosis is found to be insignificant as it was seen in Chapter 4. However, spiral flow affects the wall pressure and WSS slightly in the downstream region where they take the oscillatory pattern, i.e. within $2 \leq z/D \leq 6$.

All the results in both non-spiral and spiral flow are heavily dependent on the flow Reynolds number, e.g. the maximum pressure drop, the maximum shear stress, TKE, the rms of turbulent fluctuations, etc. increase with Reynolds number. In spiral flow, the transition-to-turbulence takes place in the downstream region ($3 \leq z/D \leq 5$) of the stenosis, whereas it occurs in the further downstream region ($4 \leq z/D \leq 6$) in non-spiral flow. The TKE in pulsatile spiral flow rises extremely at some places and phases compared with its corresponding value in pulsatile non-spiral flow – similar results were seen in Chapter 4. This result contradicts the claim made in similar studies (Paul and Larman [17]; Stonebridge et al. [16]) that spiral flow decreases turbulent kinetic energy. The drawbacks of the claim made in those studies were discussed in detail in § 2.4. The clinical impacts of the high level of turbulent fluctuations observed in the post-stenotic region in both non-spiral ($4 \leq z/D \leq 6$) and spiral ($3 \leq z/D \leq 5$) flow are profound as it may activate the blood platelets and also harm the blood cell materials, leading to many pathological diseases (Ku [3]; Paul and Molla [93]).

Additionally, the change of power slope of energy spectra for velocity and pressure fluctuations from $-5/3$ to $-10/3$ and $-7/3$, respectively, at the break frequencies which are closely connected with the arterial murmurs is clearly found in the transition-to-turbulence region in both non-spiral and spiral flow. The distinct viscous dissipation range corresponding to -7 power slope is also observed in the

further downstream region where the turbulent intensity becomes weaker and relaminarisation occurs. The velocity spectra of $-5/3$ power slope in spiral flow has larger range of frequencies at $z = 5D$ and $6D$ than that in non-spiral flow at those locations, while at $z = 4D$, the opposite is found, i.e. the broadband frequency region in non-spiral flow is larger than that in spiral flow. Furthermore, in the region $z \geq 8D$, the velocity spectra in spiral flow roll off into the viscous dissipation range at lower frequencies compared with the corresponding break frequencies in non-spiral flow; and the viscous dissipation range in spiral flow has smaller range of frequencies than that in non-spiral flow. On the other hand, as for the effect of spiral flow on the wall pressure spectra, no significant difference between non-spiral and spiral flow in the spectra rolling off into a power slope of interest can be found.

As to the effects of the area reduction of stenosis, the important results, such as the maximum pressure drop, the maximum WSS and the TKE increase dramatically when the area reduction of the stenosis is increased from 75% to 91%. On the other hand, the increase in the length of the stenosis cause the maximum WSS to drop significantly and the maximum TKE to rise sharply; but the change in the maximum pressure drop due to the increase in the stenosis length is insignificant.

Furthermore, the increase in the amplitude of pulsation causes both the maximum pressure drop and the maximum WSS to rise significantly under the inlet peak flow condition, i.e. during phase $P2$; whereas during phase $P3$, the maximum pressure drop and the maximum WSS remain almost unaffected by the increase in the amplitude of pulsation. While the increased amplitude of pulsation decrease the maximum TKE, it is nevertheless responsible for the sharp rise in TKE found at some places in the transition-to-turbulence region.

The Womersley number has a very weak influence on the maximum pressure drop and the maximum WSS as they fall slightly during phase $P2$ only when the Womersley number is decreased from $\alpha = 17.3$ to 15.5. However, the decrease in the Womersley number causes the maximum TKE to rise extremely.

The stenosis used in the studies done so far is cosine-type regular stenosis. However, *in vivo* arterial stenoses are of irregular shape (Back et al. [32]). In Chapter 6, pulsatile non-spiral and spiral blood flow through irregular stenosis will be investigated by using LES.

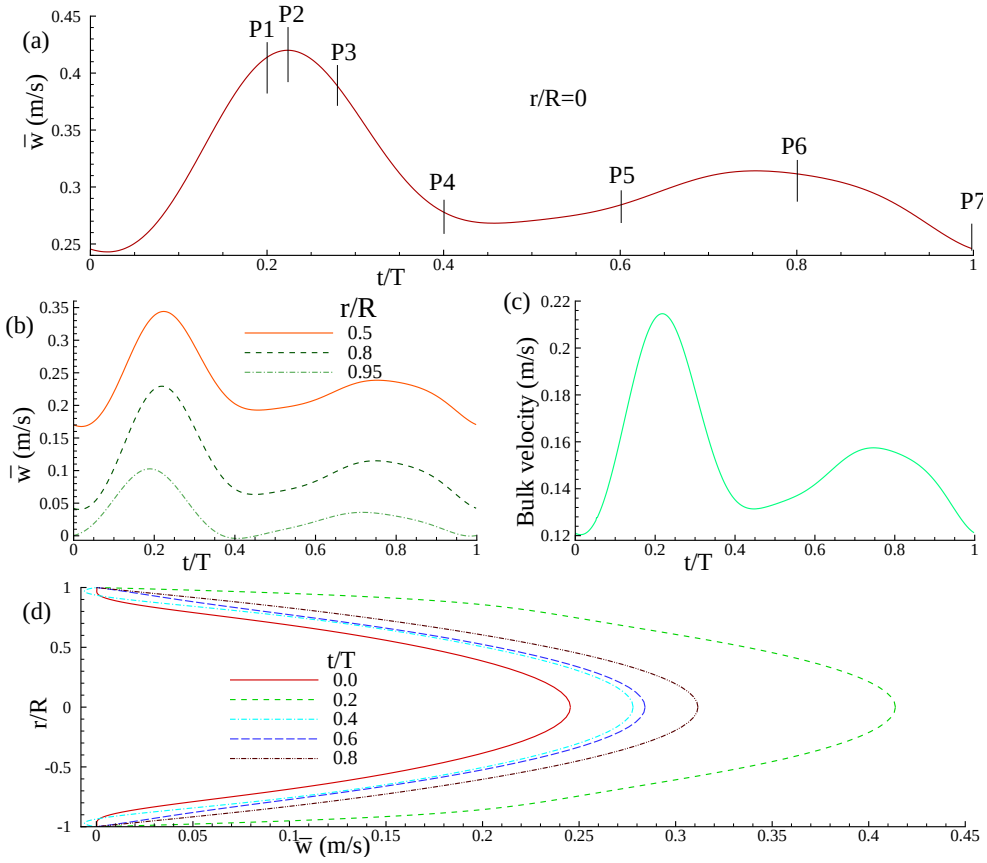

Figure 5.1: Inlet physiological 4$^{\text{th}}$ harmonic pulsatile velocity profiles, $\bar{w}$ (m/s), for a time cycle (a) at the centre of the tube, (b) at different locations between the wall and the centre, (c) bulk velocity profile and (d) during different phases of a time cycle while $A = 0.40$, $Re = 876$ and the Womersley parameter $\alpha = 17.3$. Reference phases at which results are obtained are also marked.

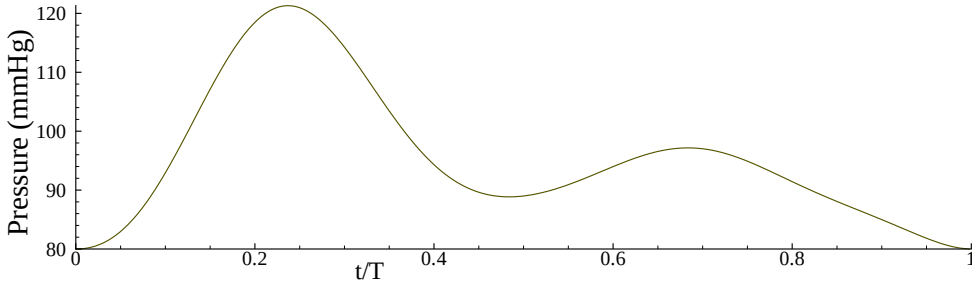

Figure 5.2: Outlet physiological 4$^{\text{th}}$ harmonic pulsatile pressure profiles, $\bar{p}$ (mmHg), for a time cycle while $A = 0.40$, $Re = 876$ and the Womersley parameter $\alpha = 17.3$. (1 mmHg$=$ 133.32 Pa.)

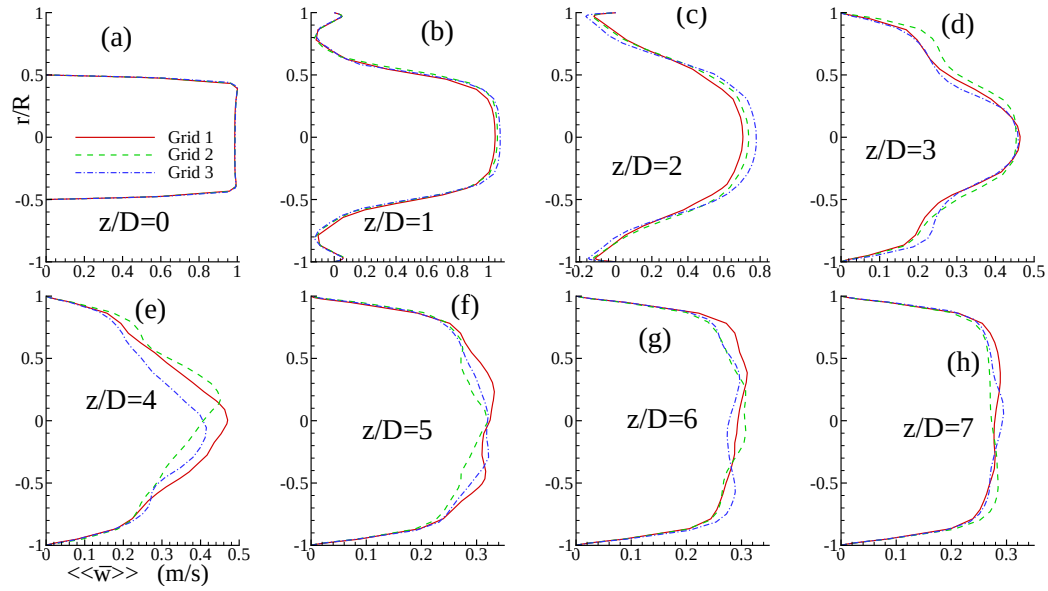

Figure 5.3: Grid resolution study for phase-averaged streamwise velocity, $\langle\langle\bar{w}\rangle\rangle$ (m/s), in non-spiral flow during phase $P3$ at different indicated axial locations while $A = 0.67$, $Re = 741$ and the Womersley parameter $\alpha = 17.3$.

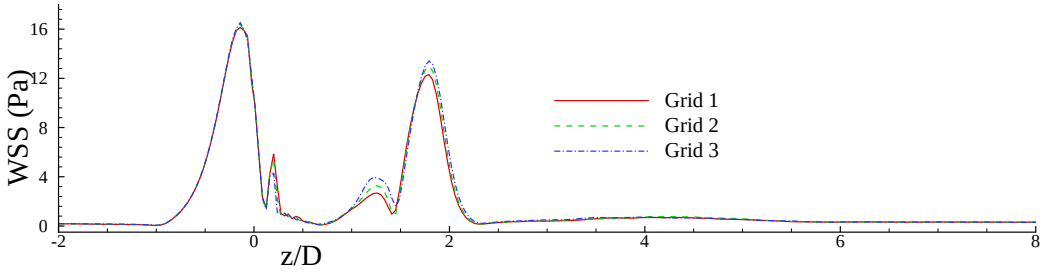

Figure 5.4: Grid resolution study for phase-averaged axial wall shear stress (Pa) in non-spiral flow during phase $P3$ while $A = 0.67$, $Re = 741$ and the Womersley parameter $\alpha = 17.3$. Phase averaging was done on the circumferential average WSS.

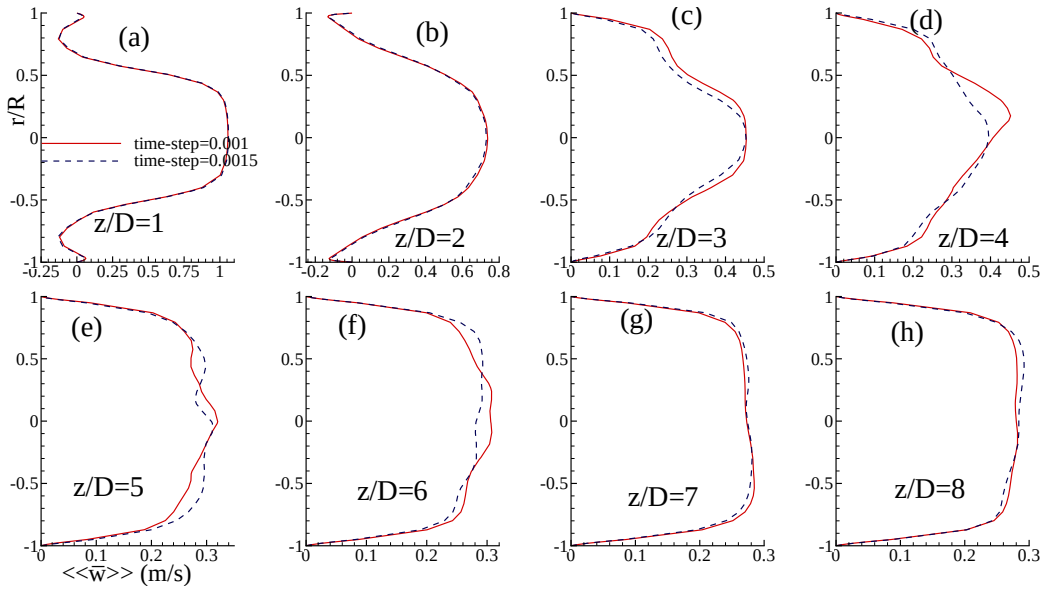

Figure 5.5: Time-step resolution study for phase-averaged streamwise velocity, $\langle\langle\bar{w}\rangle\rangle$ (m/s), in non-spiral flow during phase $P3$ at different indicated axial locations while $A = 0.67$, $Re = 741$ and the Womersley parameter $\alpha = 17.3$.

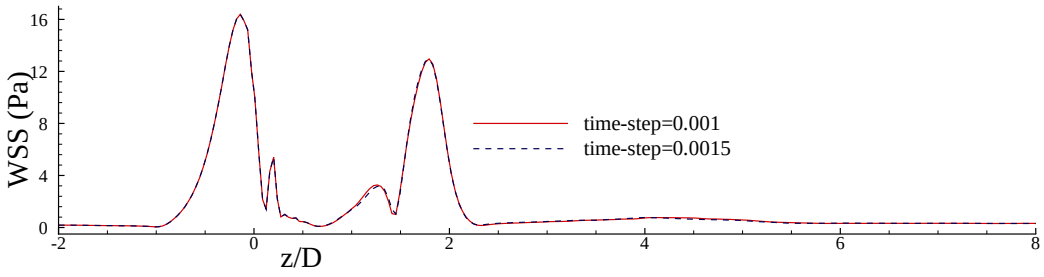

Figure 5.6: Time-step resolution study for phase-averaged axial wall shear stress (Pa) in non-spiral flow during phase $P3$ while $A = 0.67$, $Re = 741$ and the Womersley parameter $\alpha = 17.3$. Phase averaging was done on the circumferential average WSS.

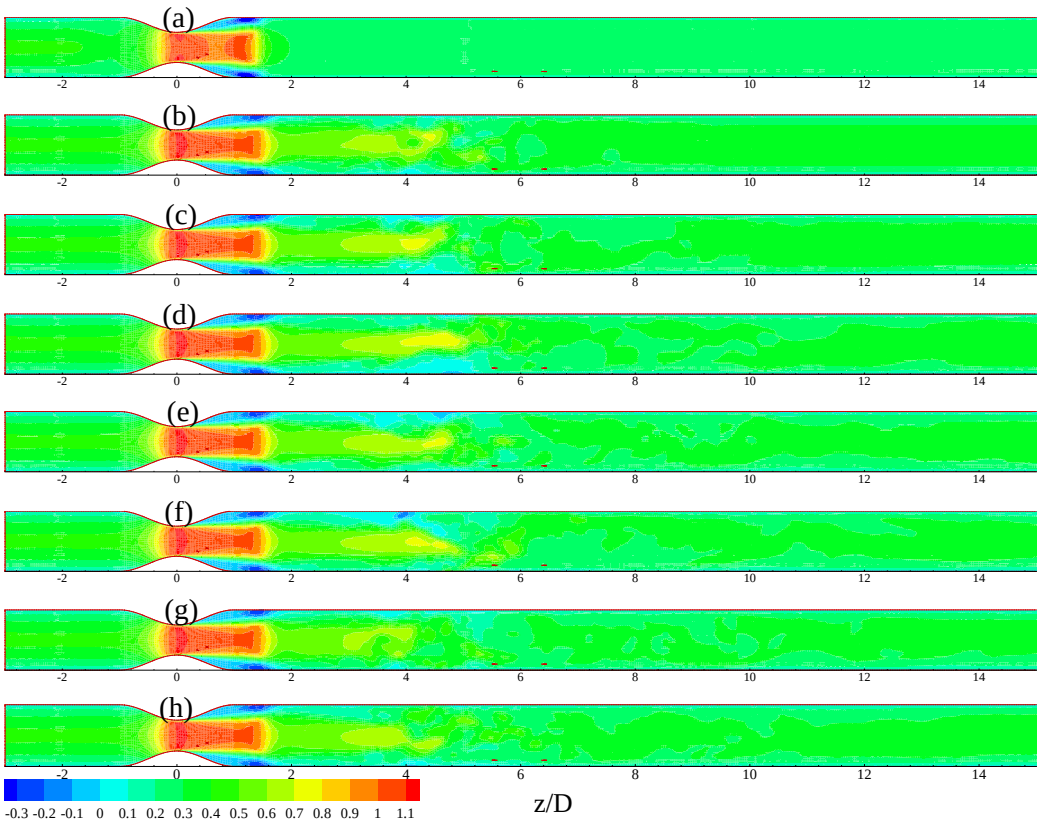

Figure 5.7: Streamwise velocity, $\bar{w}$, in non-spiral flow during phase $P2$ of the first eight cycles i.e. (a) $t/T \approx 0.223$, (b) $t/T \approx 1.223$, (c) $t/T \approx 2.223$, (d) $t/T \approx 3.223$, (e) $t/T \approx 4.223$, (f) $t/T \approx 5.223$, (g) $t/T \approx 6.223$ and (h) $t/T \approx 7.223$ while $Re = 876$, $A = 0.40$ and the Womersley parameter $\alpha = 17.3$.

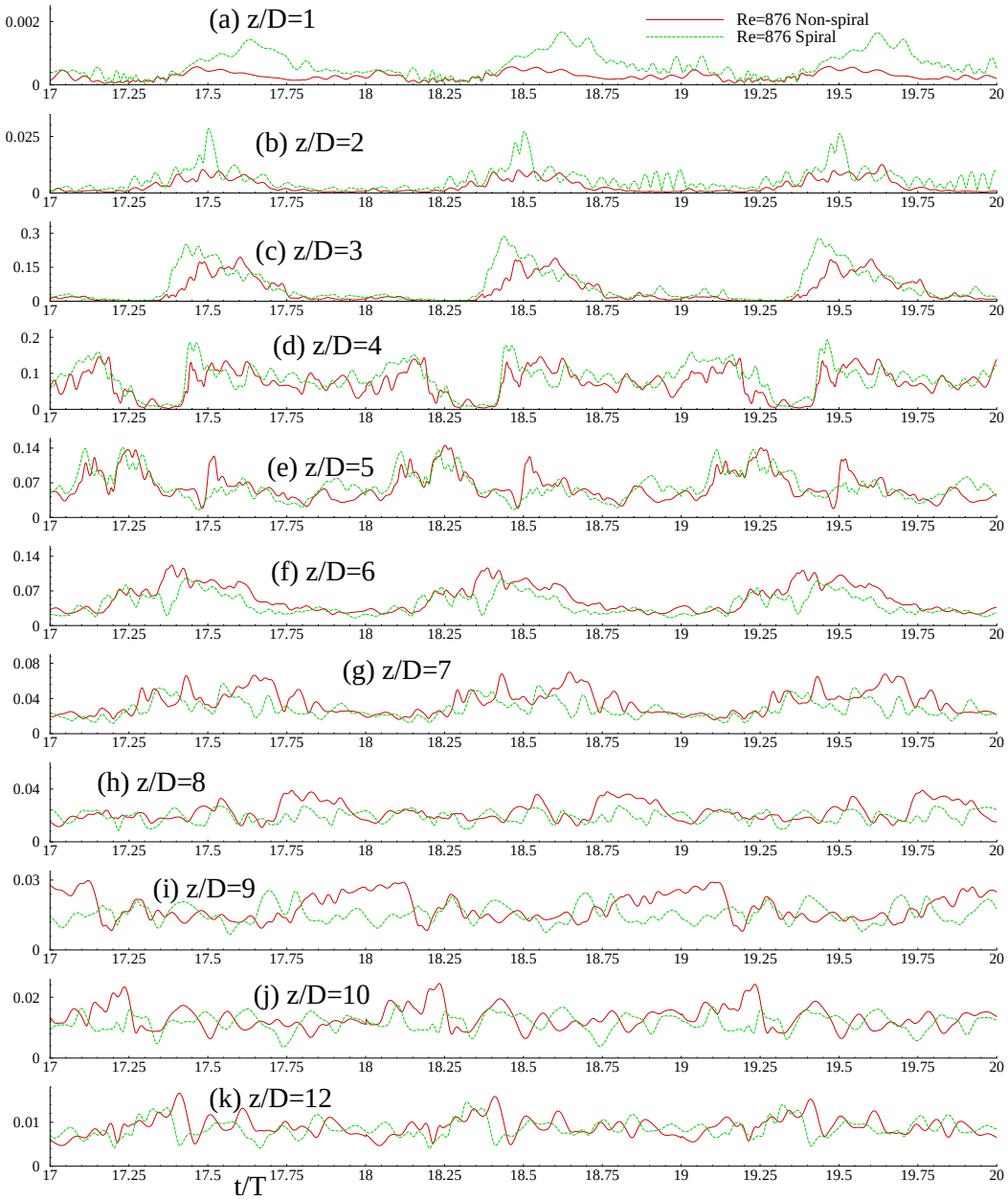

Figure 5.8: Time history of rms of centreline streamwise velocity fluctuations, $\langle w'' \rangle_{rms}$ (m/s), at different axial locations for both non-spiral and spiral pulsatile flow while $Re = 876$. The red coloured solid line denotes velocity fluctuations for non-spiral flow while the green coloured dashed line corresponds to velocity fluctuations for spiral flow.

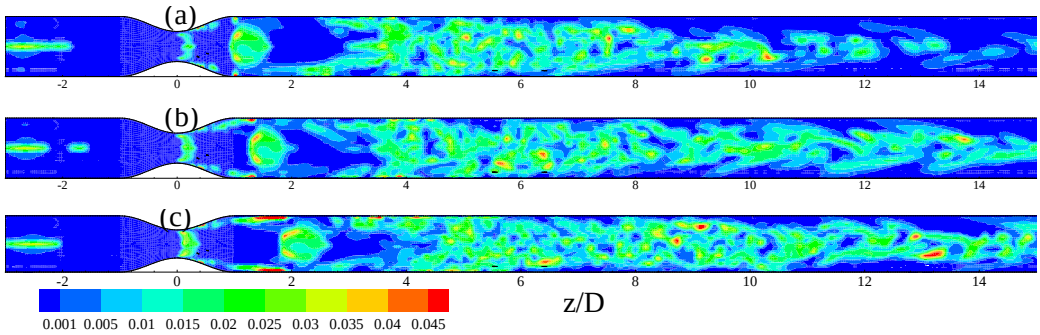

Figure 5.9: Dynamic Smagorinsky constant, C_s, in non-spiral flow during phase $P3$ for (a) $Re = 438$, (b) $Re = 584$ and (c) $Re = 876$ while $A = 0.40$ and the Womersley parameter $\alpha = 17.3$.

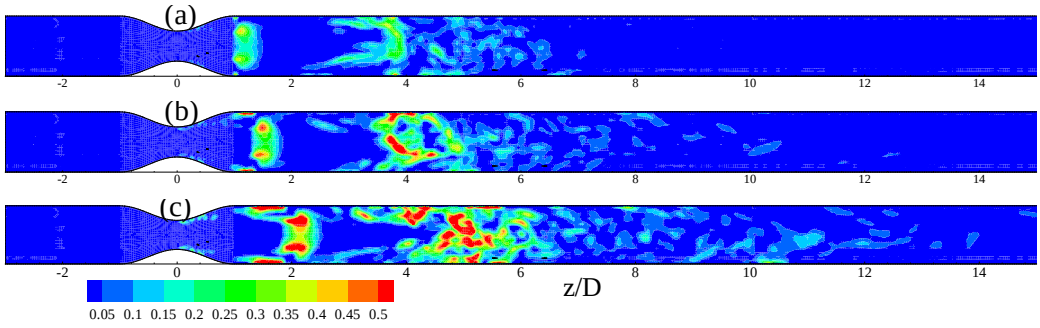

Figure 5.10: Normalised SGS eddy viscosity, μ_{sgs}/μ, in non-spiral flow during phase $P3$ for (a) $Re = 438$, (b) $Re = 584$ and (c) $Re = 876$ while $A = 0.40$ and the Womersley parameter $\alpha = 17.3$.

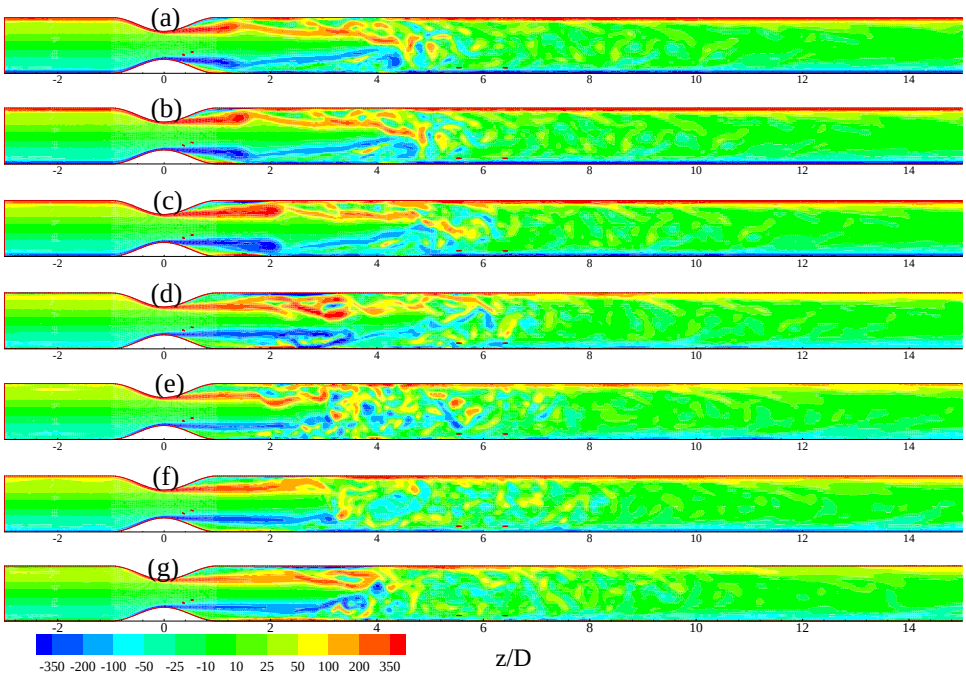

Figure 5.11: Instantaneous y-vorticity, Ω_y $(1/s)$, in non-spiral flow at different phases of the last cycle (a) $P1$, (b) $P2$, (c) $P3$, (d) $P4$, (e) $P5$, (f) $P6$ and (g) $P7$ while $Re = 876$, $A = 0.40$ and the Womersley parameter $\alpha = 17.3$.

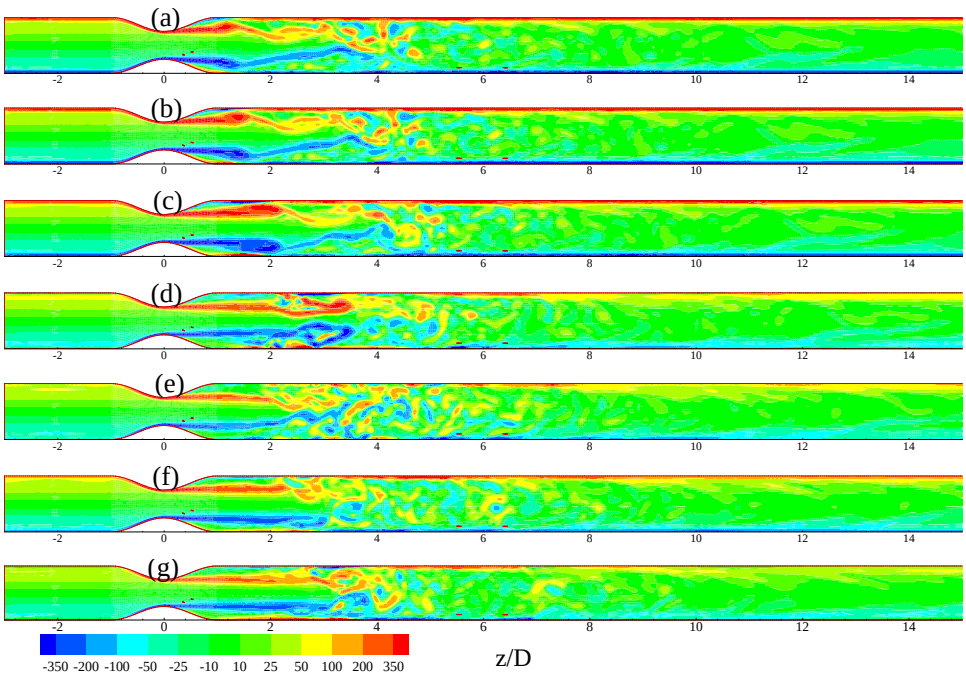

Figure 5.12: Instantaneous y-vorticity, Ω_y $(1/s)$, in spiral flow at different phases of the last cycle (a) $P1$, (b) $P2$, (c) $P3$, (d) $P4$, (e) $P5$, (f) $P6$ and (g) $P7$ while $Re = 876$, $A = 0.40$ and the Womersley parameter $\alpha = 17.3$.

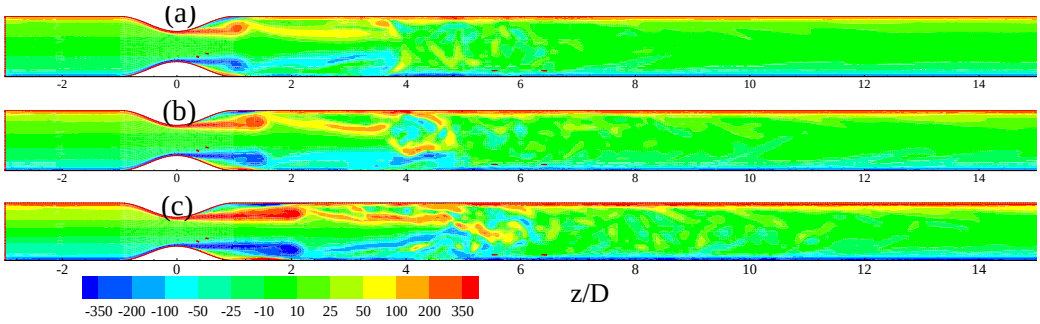

Figure 5.13: Instantaneous y-vorticity, Ω_y $(1/s)$, in non-spiral flow during phase $P3$ for (a) $Re = 438$, (b) $Re = 584$ and (c) $Re = 876$ while $A = 0.40$ and the Womersley parameter $\alpha = 17.3$.

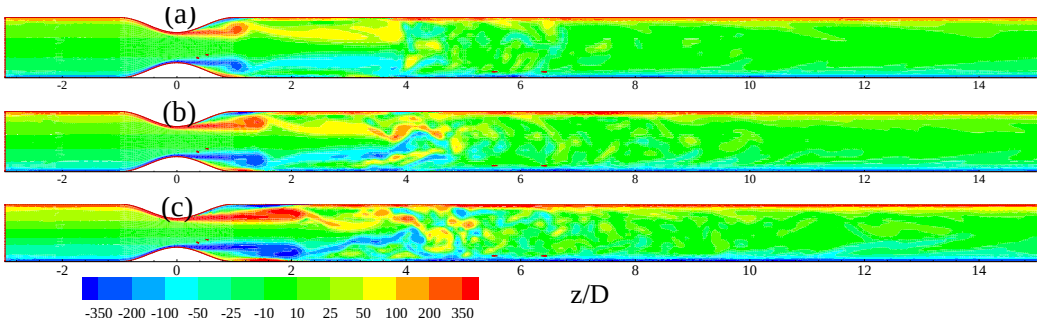

Figure 5.14: Instantaneous y-vorticity, Ω_y $(1/s)$, in spiral flow during phase $P3$ for (a) $Re = 438$, (b) $Re = 584$ and (c) $Re = 876$ while $A = 0.40$ and the Womersley parameter $\alpha = 17.3$.

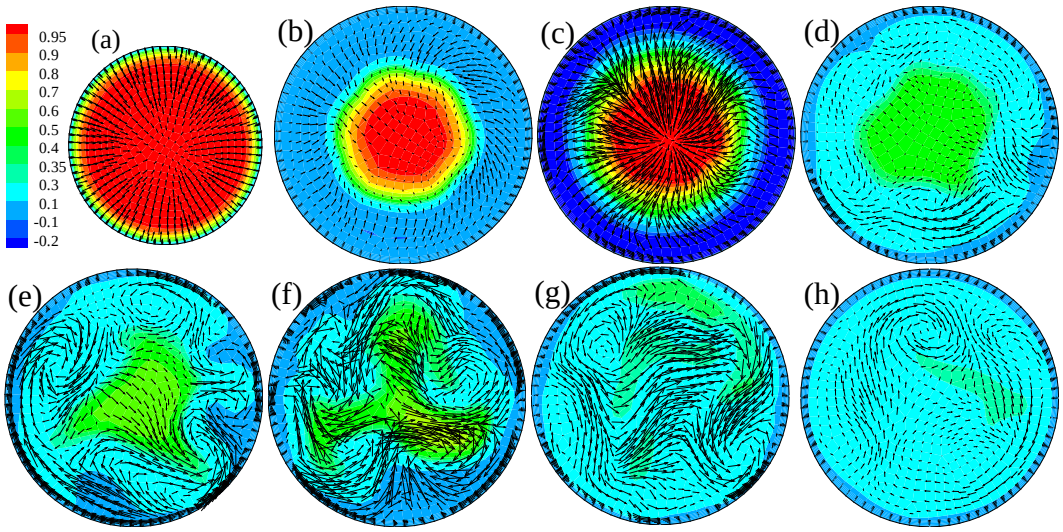

Figure 5.15: Instantaneous cross-sectional vectors appended on the contours of streamwise velocity, $\bar{w}$ (m/s), in non-spiral flow during phase $P3$ at (a) $z/D = 0$, (b) $z/D = 1$, (c) $z/D = 2$, (d) $z/D = 3$, (e) $z/D = 4$, (f) $z/D = 5$, (g) $z/D = 6$ and (h) $z/D = 8$ while $Re = 876$, $A = 0.40$ and the Womersley parameter $\alpha = 17.3$.

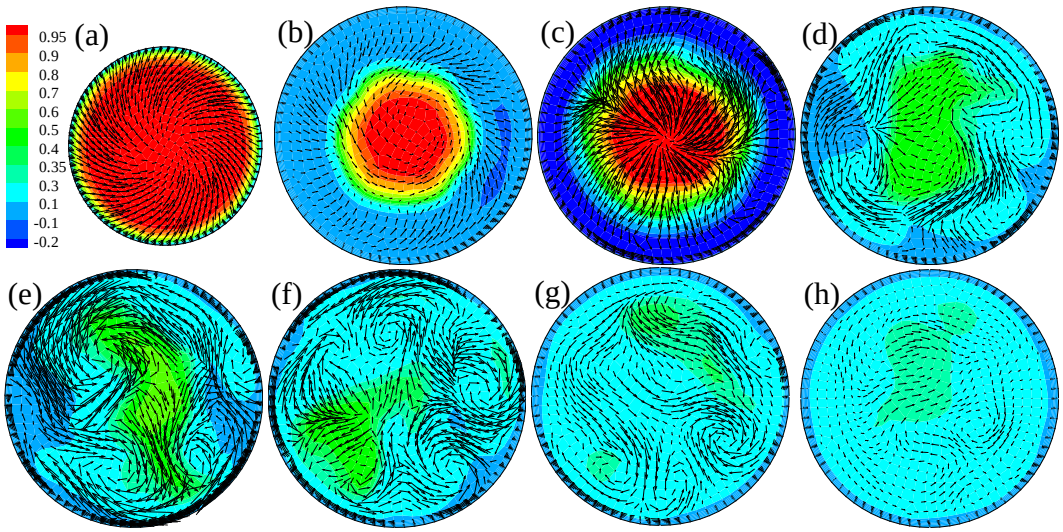

Figure 5.16: Instantaneous cross-sectional vectors appended on the contours of streamwise velocity, $\bar{w}$ (m/s), in spiral flow during phase $P3$ at (a) $z/D = 0$, (b) $z/D = 1$, (c) $z/D = 2$, (d) $z/D = 3$, (e) $z/D = 4$, (f) $z/D = 5$, (g) $z/D = 6$ and (h) $z/D = 8$ while $Re = 876$, $A = 0.40$ and the Womersley parameter $\alpha = 17.3$.

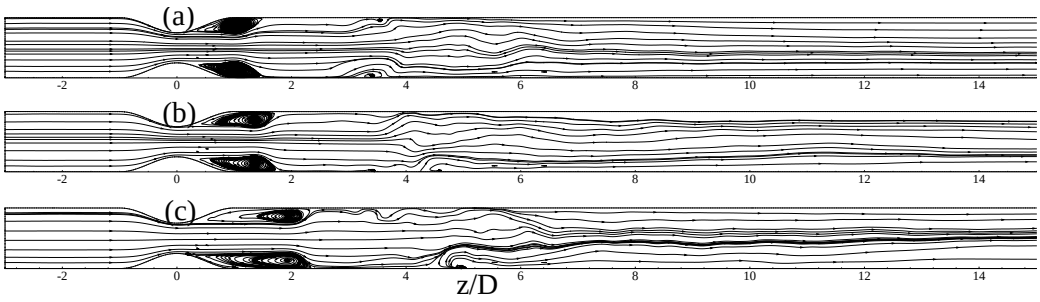

Figure 5.17: Instantaneous mid-plane streamlines in non-spiral flow during phase $P3$ for (a) $Re = 438$, (b) $Re = 584$ and (c) $Re = 876$ while $A = 0.40$ and the Womersley parameter $\alpha = 17.3$.

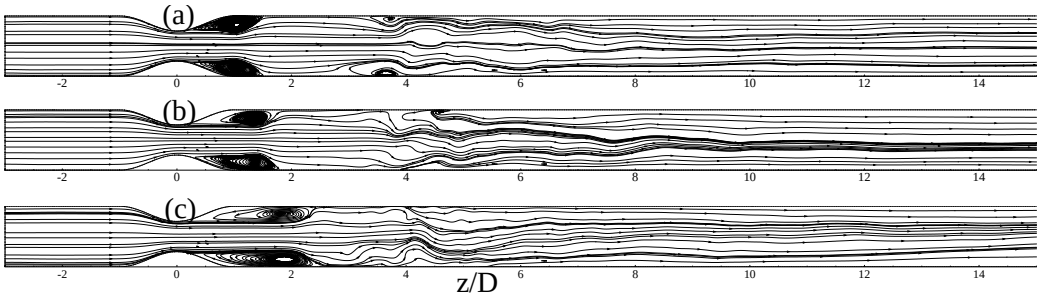

Figure 5.18: Instantaneous mid-plane streamlines in spiral flow during phase $P3$ for (a) $Re = 438$, (b) $Re = 584$ and (c) $Re = 876$ while $A = 0.40$ and the Womersley parameter $\alpha = 17.3$.

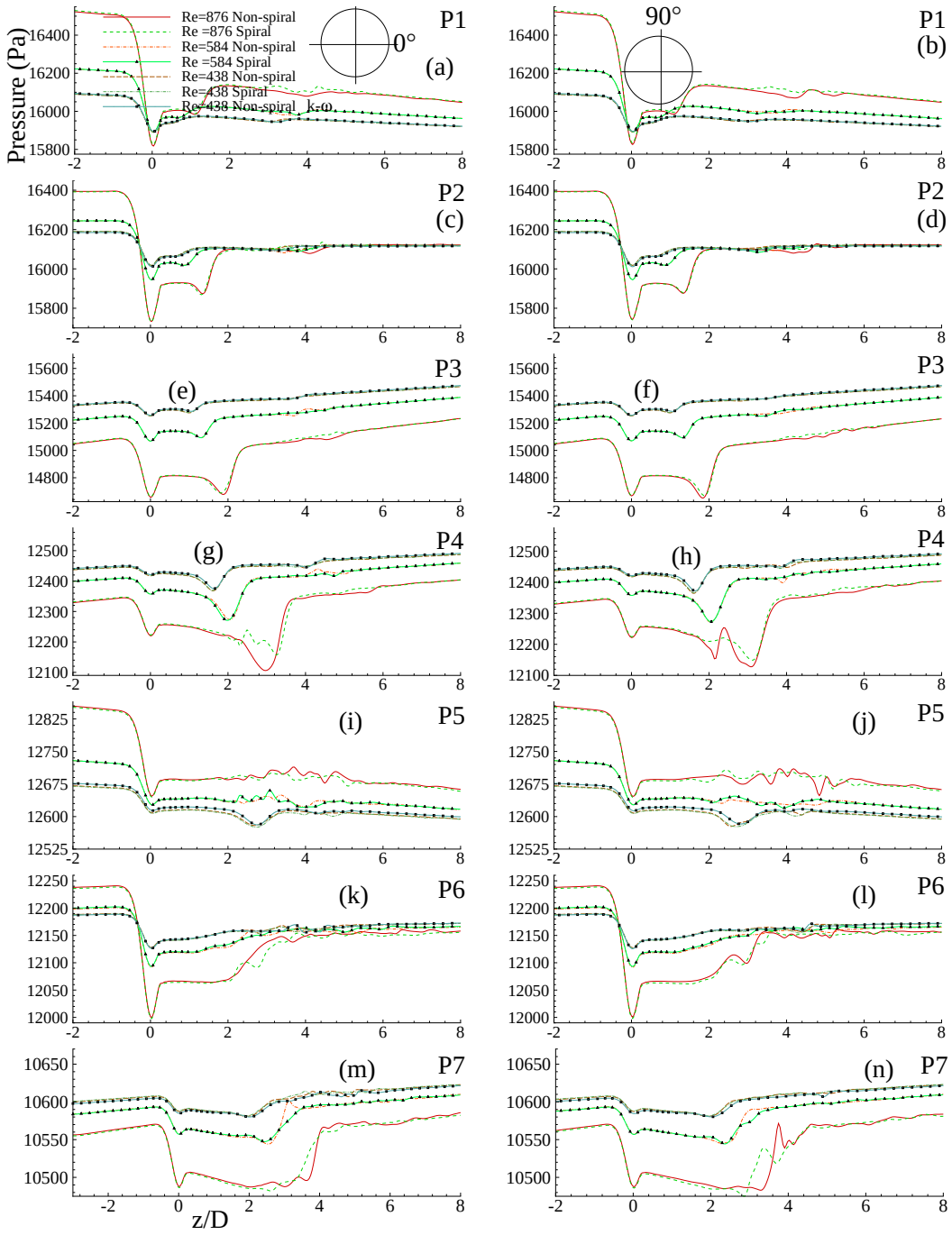

Figure 5.19: Instantaneous wall pressure, $\bar{p}$ (Pa), in both non-spiral and spiral flow for the different Reynolds numbers during different phases of the last cycle at the two indicated circumferential locations. Note that the corresponding k-ω results for $Re = 438$ are also appended.

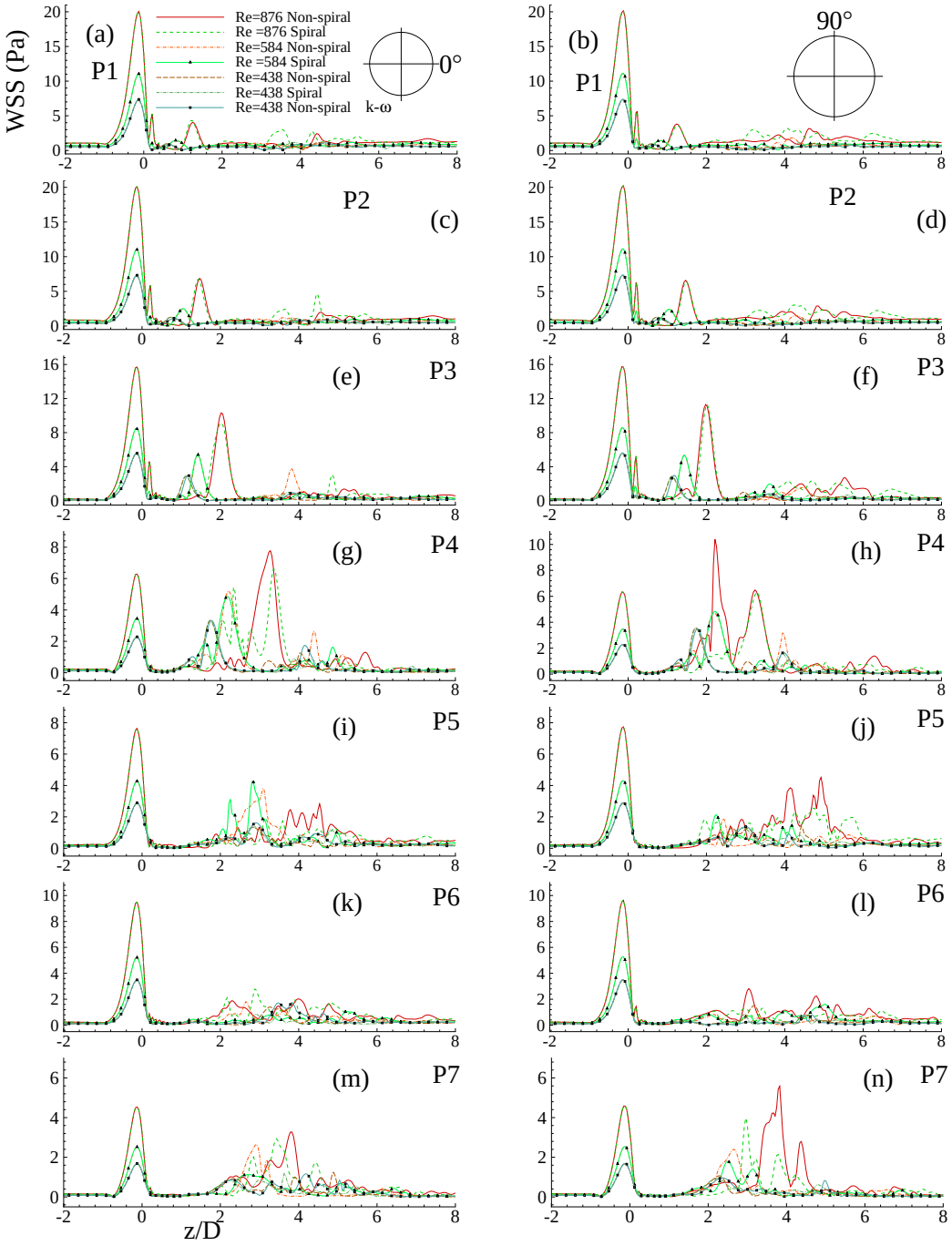

Figure 5.20: Instantaneous wall shear stress (Pa) in both non-spiral and spiral flow for the different Reynolds numbers during different phases of the last cycle at the two indicated circumferential locations. Note that the corresponding k-ω results for $Re = 438$ are also appended.

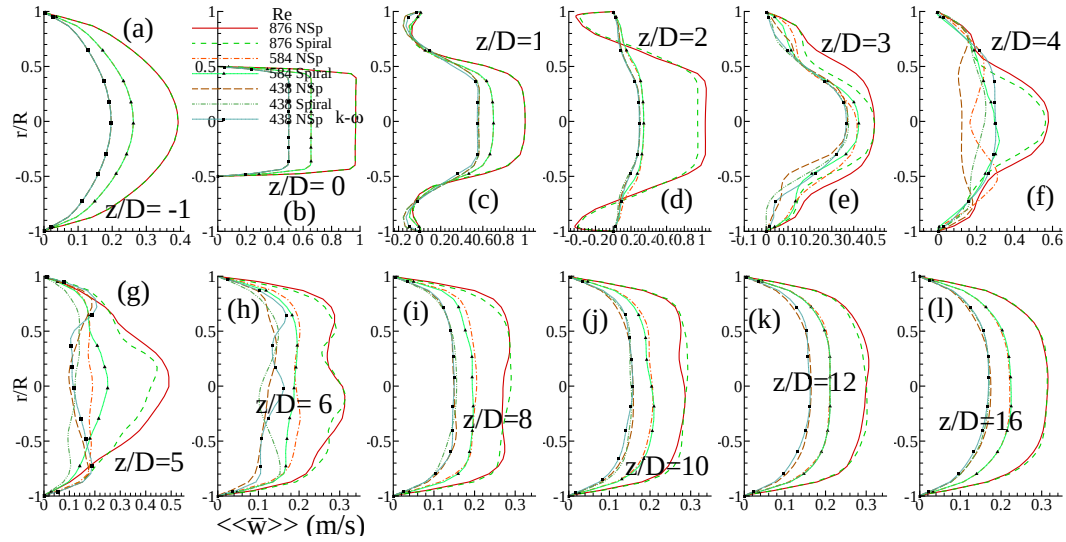

Figure 5.21: Phase-averaged streamwise velocity, $\langle\langle\bar{w}\rangle\rangle$ (m/s), in both non-spiral (NSp) and spiral flow for the different Reynolds numbers during phase $P3$ at different axial locations. Note that the corresponding k-ω results for $Re = 438$ are also appended.

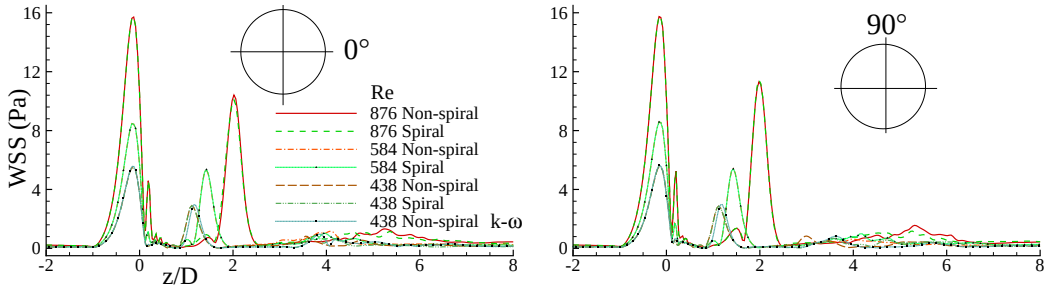

Figure 5.22: Phase-averaged wall shear stress (Pa) in both non-spiral and spiral flow for the different Reynolds numbers during phase $P3$ at the two indicated circumferential locations. Note that the corresponding k-ω results for $Re = 438$ are also appended.

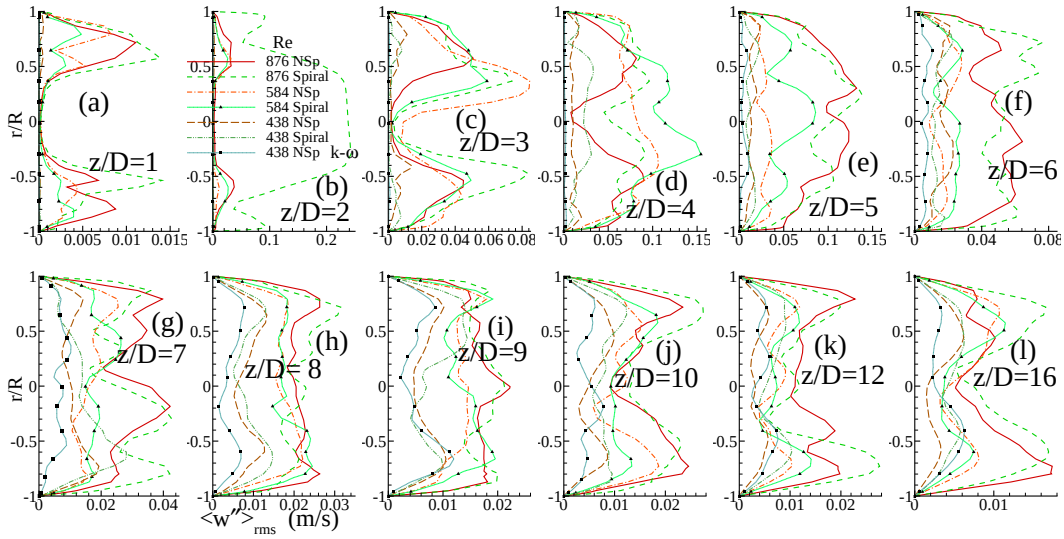

Figure 5.23: rms of the streamwise velocity fluctuations, $\langle w'' \rangle_{rms}$ (m/s), in both non-spiral and spiral flow for the different Reynolds numbers during phase $P3$ at different axial locations. Note that the corresponding k-ω results for $Re = 438$ are also appended.

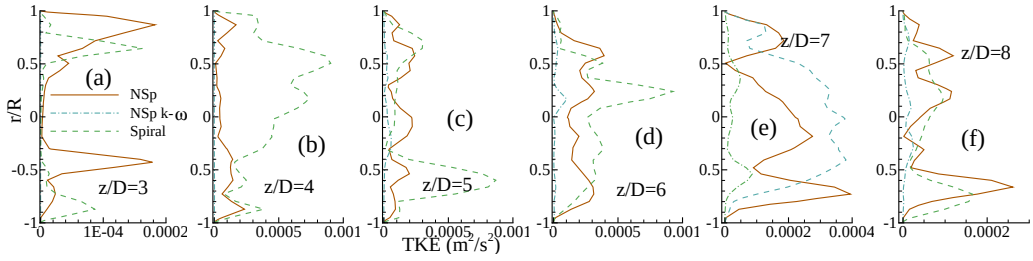

Figure 5.24: Turbulent kinetic energy, $\frac{1}{2}\langle u_j'' u_j'' \rangle$ (m^2/s^2), for Reynolds number $Re = 438$ in both non-spiral (NSp) and spiral flow during phase $P3$ at different axial locations. Note that the corresponding k-ω results are also appended.

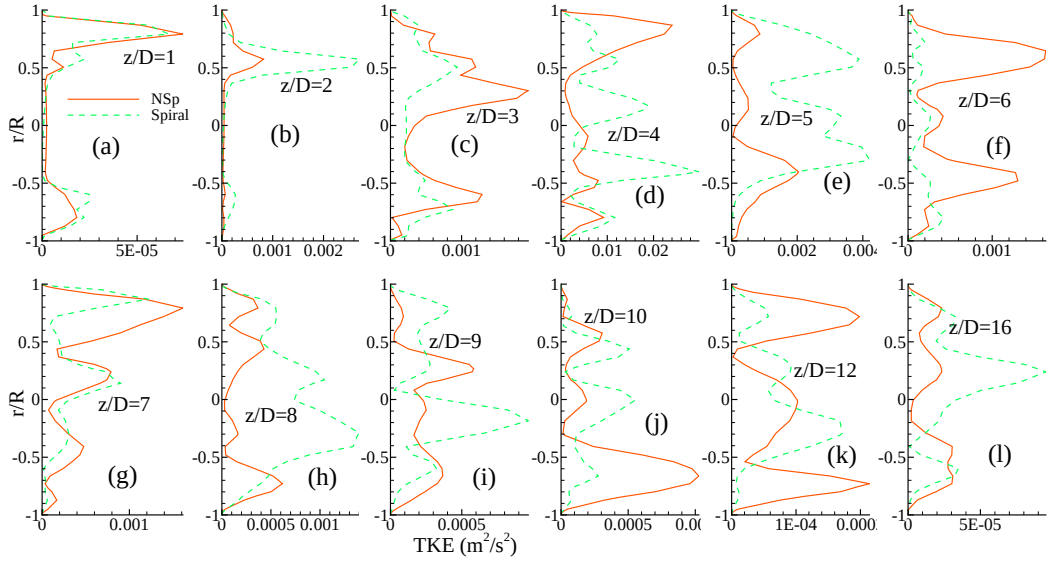

Figure 5.25: Turbulent kinetic energy, $\frac{1}{2}\langle u_j'' u_j'' \rangle$ (m^2/s^2), for Reynolds number $Re = 584$ in both non-spiral (NSp) and spiral flow during phase $P3$ at different axial locations.

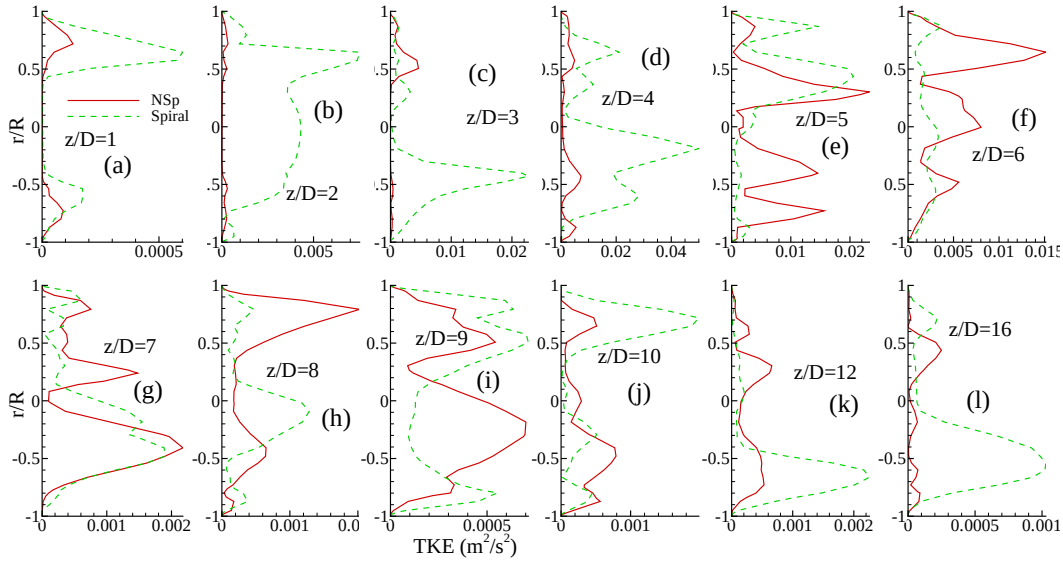

Figure 5.26: Turbulent kinetic energy, $\frac{1}{2}\langle u_j'' u_j'' \rangle$ (m^2/s^2), for Reynolds number $Re = 876$ in both non-spiral (NSp) and spiral flow during phase $P3$ at different axial locations.

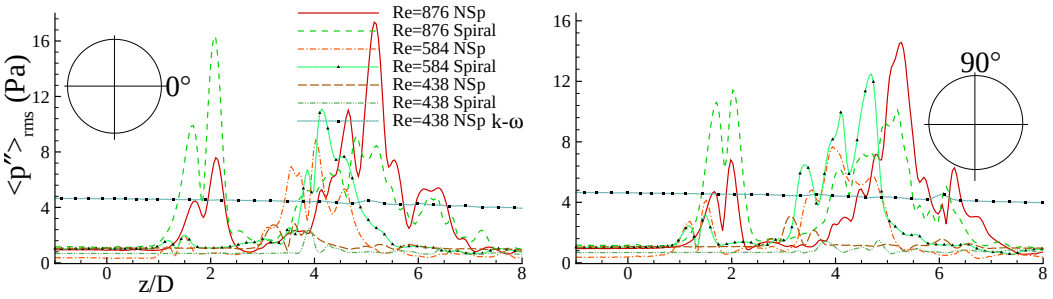

Figure 5.27: rms of wall pressure fluctuations, $\langle p'' \rangle_{rms}$ (Pa), in both non-spiral and spiral flow for the different Reynolds numbers during phase $P3$ at the two indicated circumferential locations. Note that the corresponding k-ω results for $Re = 438$ are also appended.

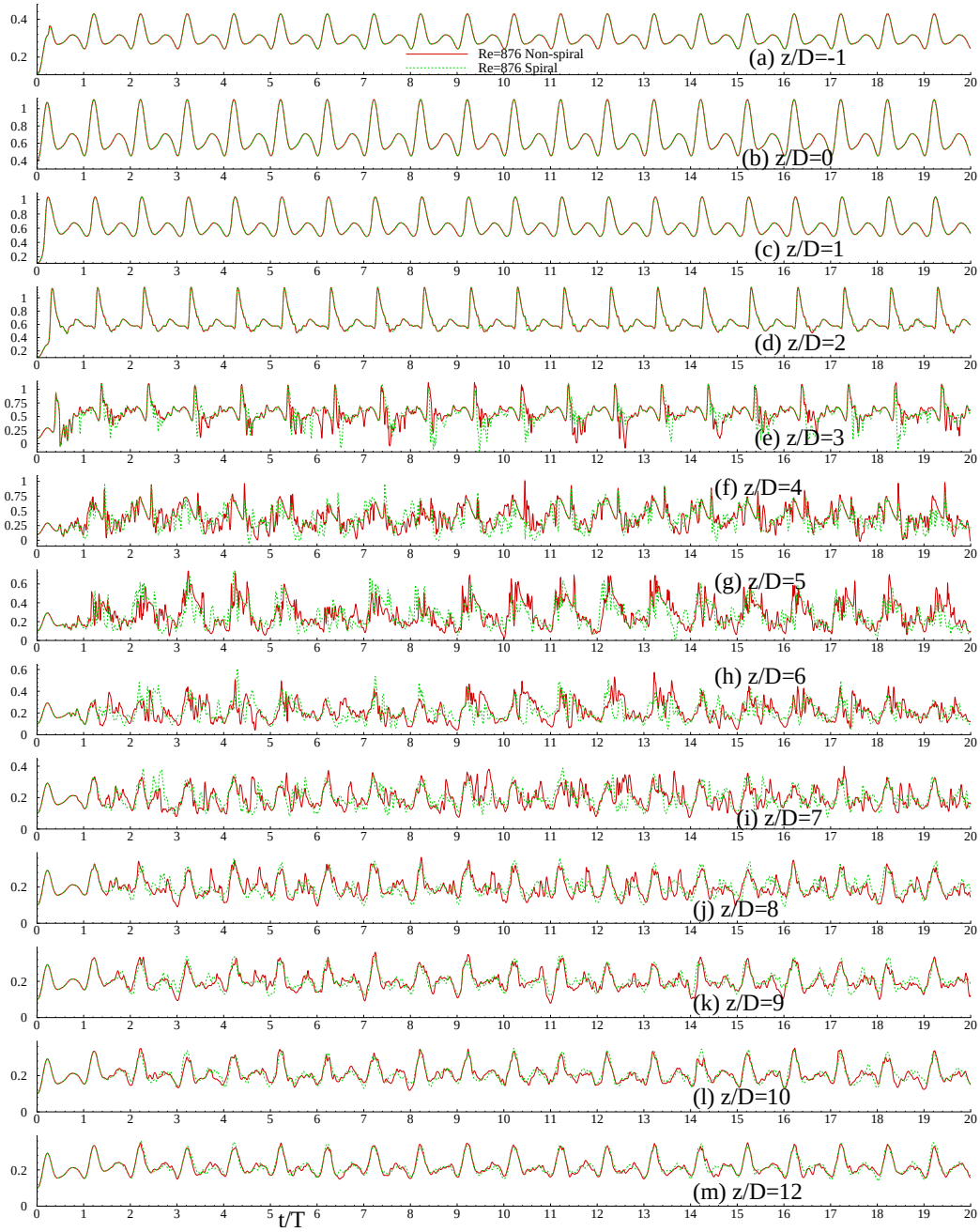

Figure 5.28: Time history of centreline streamwise velocity, $\bar{w}$ (m/s), at different indicated axial locations for both non-spiral and spiral pulsatile flow while $Re = 876$. The red coloured solid line denotes $\bar{w}$ for non-spiral flow while the green coloured dashed line corresponds to $\bar{w}$ for spiral flow.

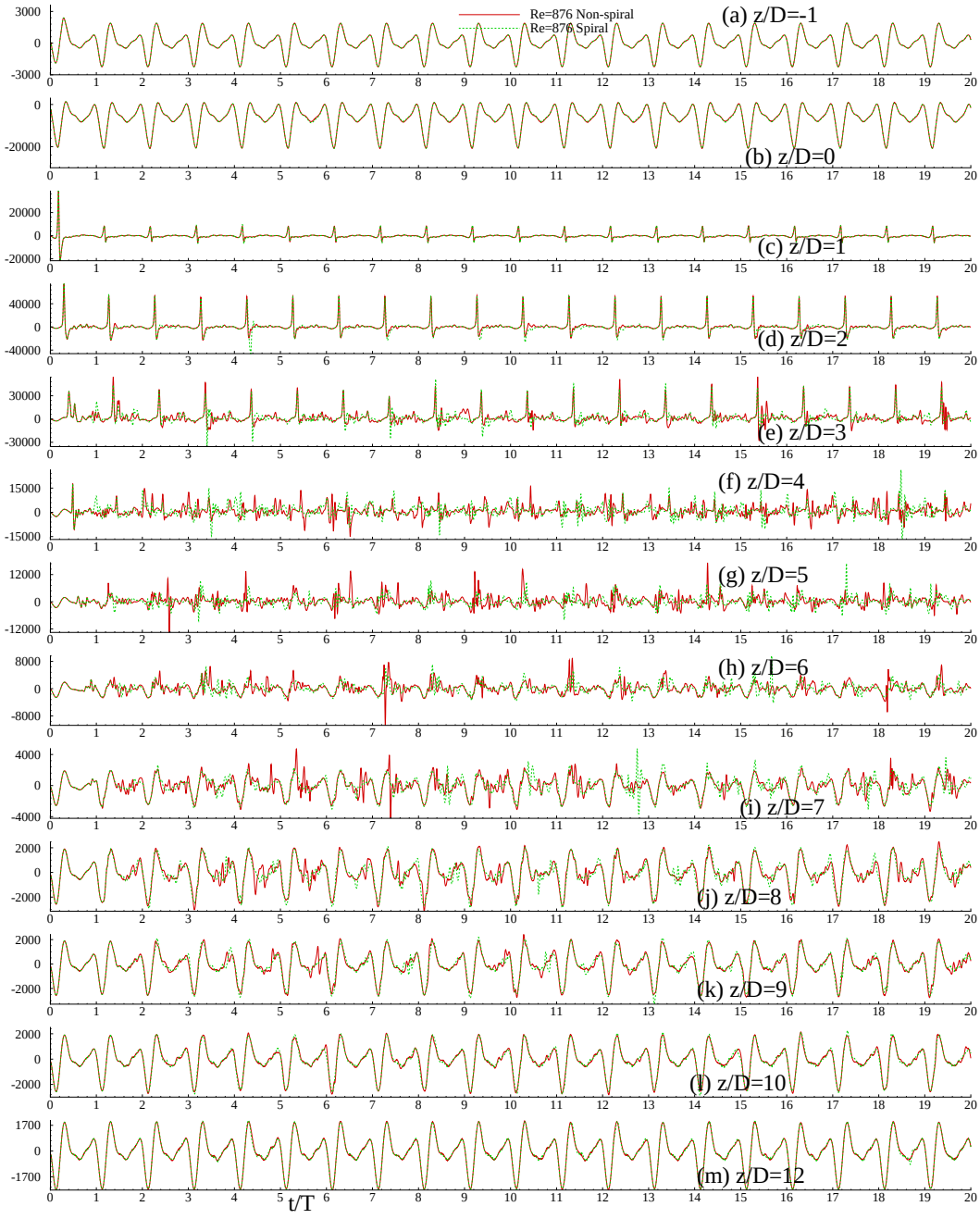

Figure 5.29: Time history of wall (0° circumferential location) pressure gradient, $\frac{\partial p}{\partial z}$, at different indicated axial locations for both non-spiral and spiral pulsatile flow while $Re = 876$. The red coloured solid line denotes $\frac{\partial p}{\partial z}$ for non-spiral flow while the green coloured dashed line corresponds to $\frac{\partial p}{\partial z}$ for spiral flow.

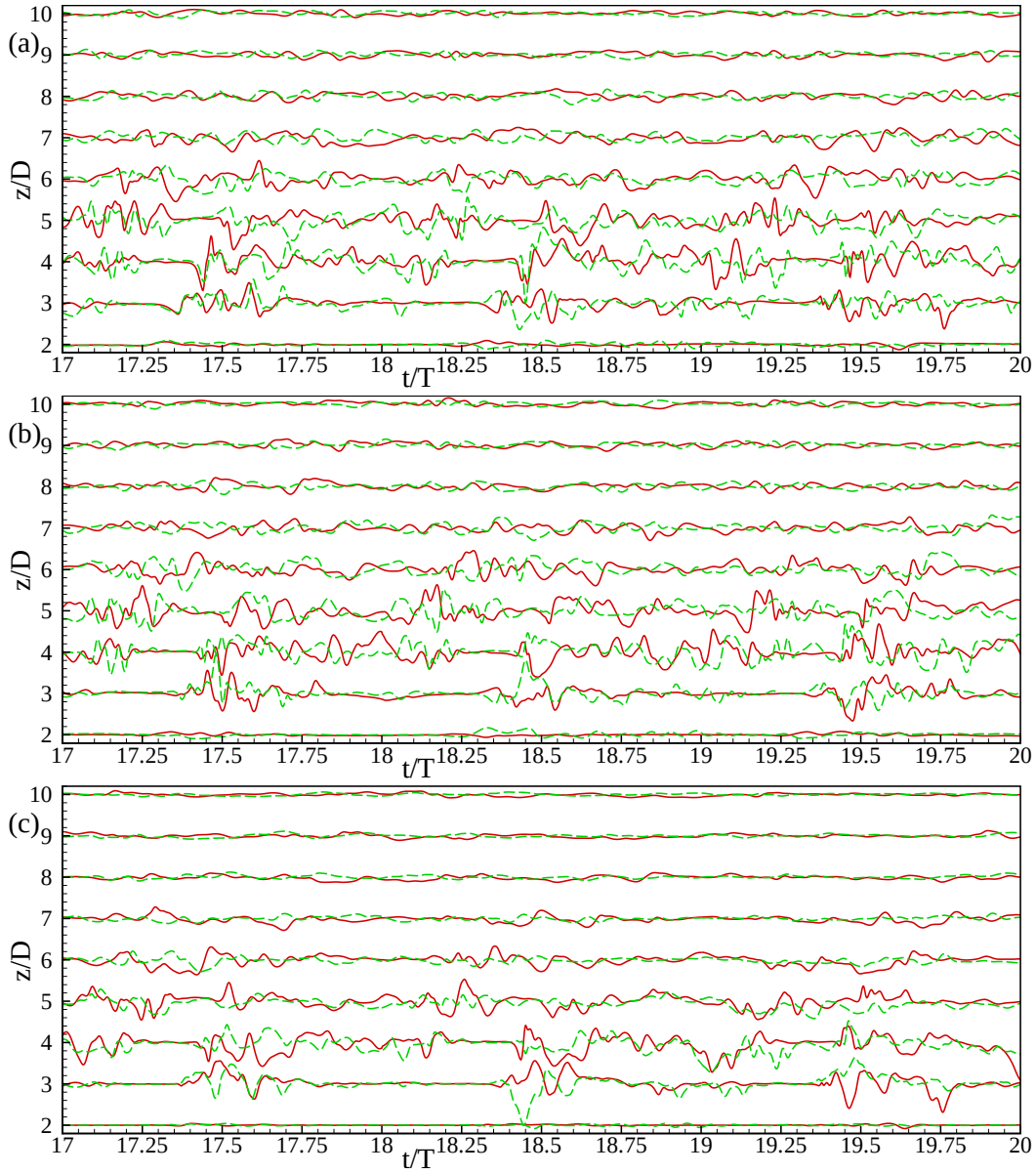

Figure 5.30: Time history of the centreline velocity fluctuations, (a) u''/u''_{max}, (b) v''/v''_{max} and (c) w''/w''_{max} at different axial locations for both non-spiral and spiral pulsatile flow while $Re = 876$. The red coloured solid line denotes velocity fluctuations for non-spiral flow while the green coloured dashed line corresponds to velocity fluctuations for spiral flow.

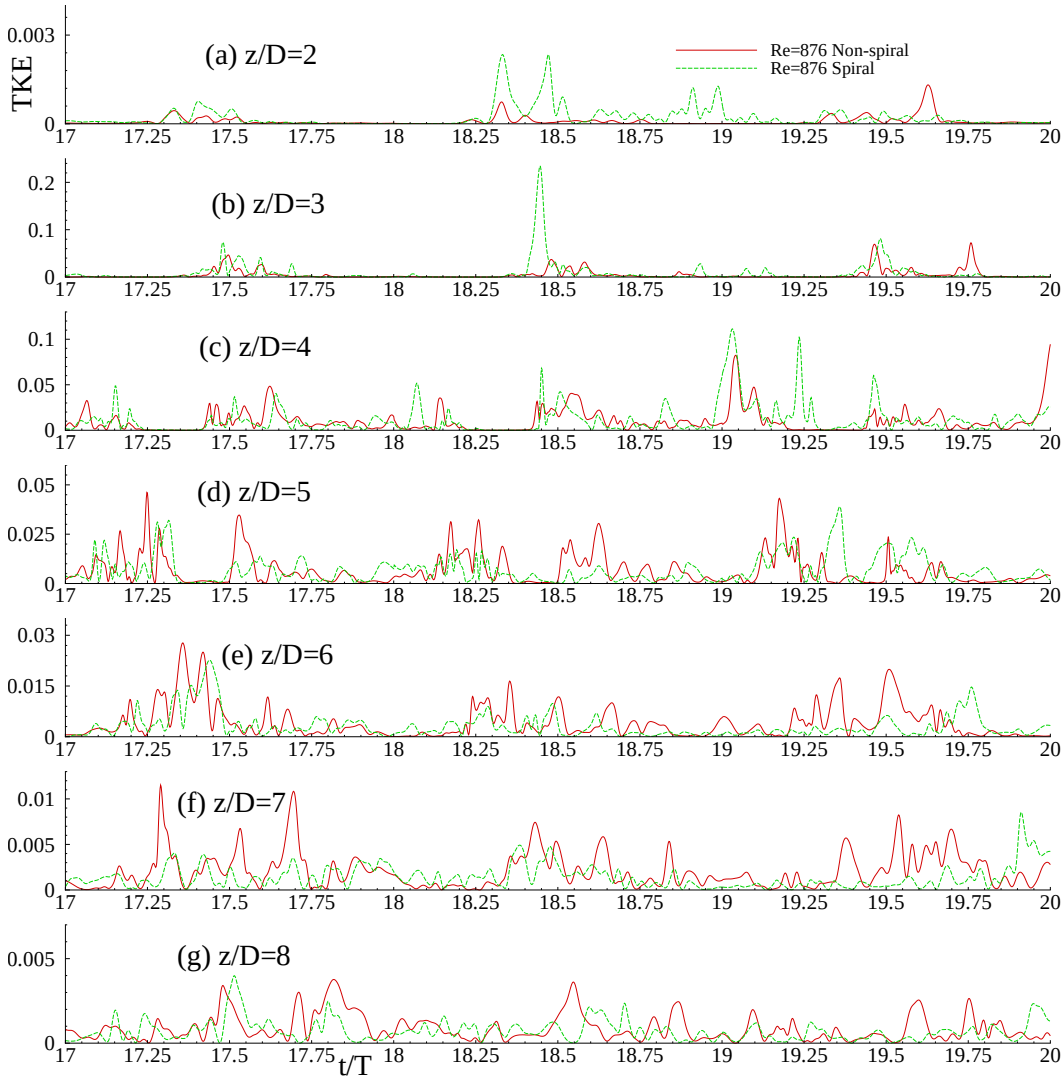

Figure 5.31: Time history of centreline turbulent kinetic energy (TKE), $\frac{1}{2}\langle u_j'' u_j'' \rangle$ (m^2/s^2), at different indicated axial locations for both non-spiral and spiral pulsatile flow while $Re = 876$. The red coloured solid line denotes TKE for non-spiral flow while the green coloured dashed line corresponds to TKE for spiral flow.

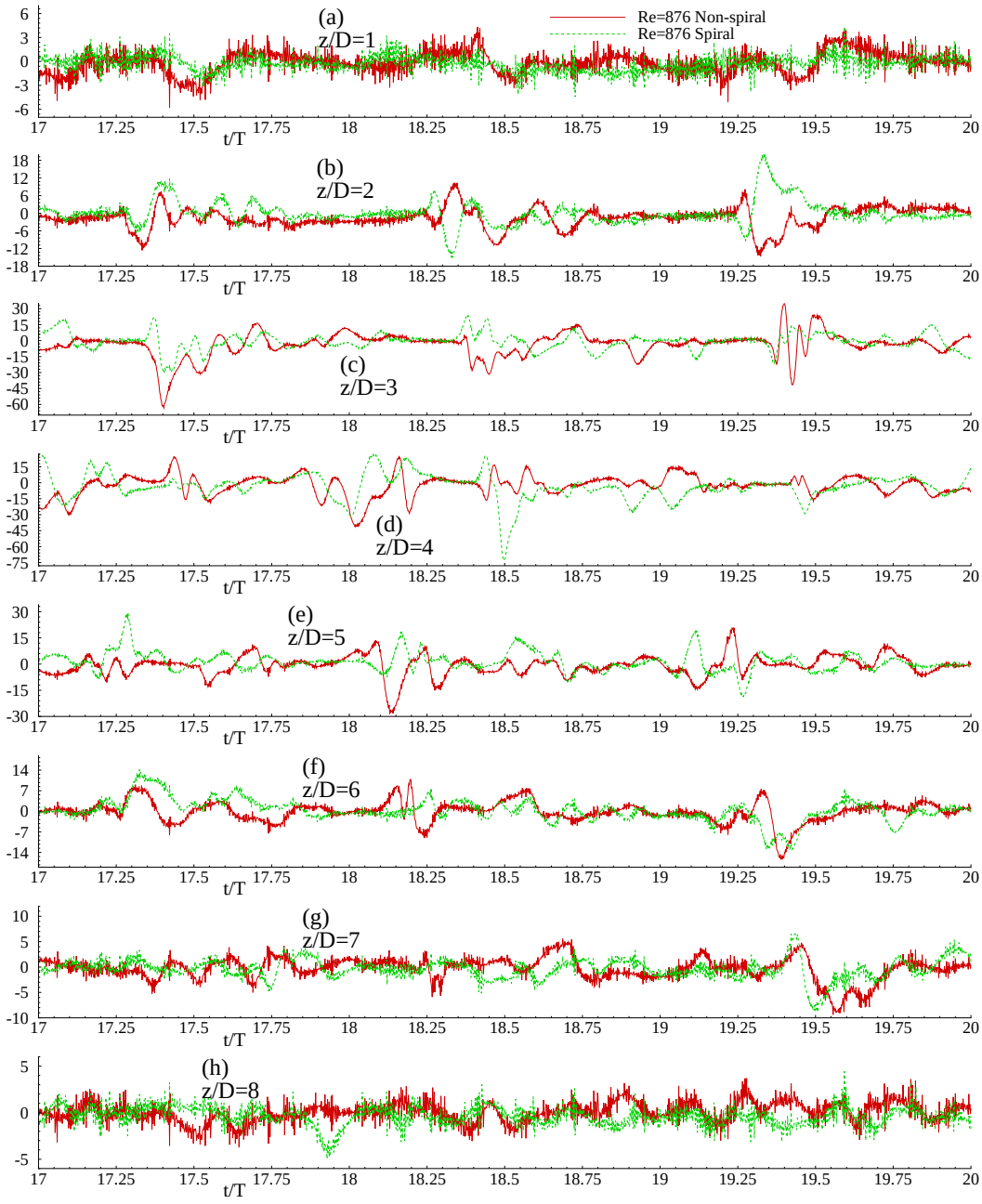

Figure 5.32: Time history of wall (0° circumferential location) pressure fluctuations, p'' (Pa), at different indicated axial locations for both non-spiral and spiral pulsatile flow while $Re = 876$. The red coloured solid line denotes p'' for non-spiral flow while the green coloured dashed line corresponds to p'' for spiral flow.

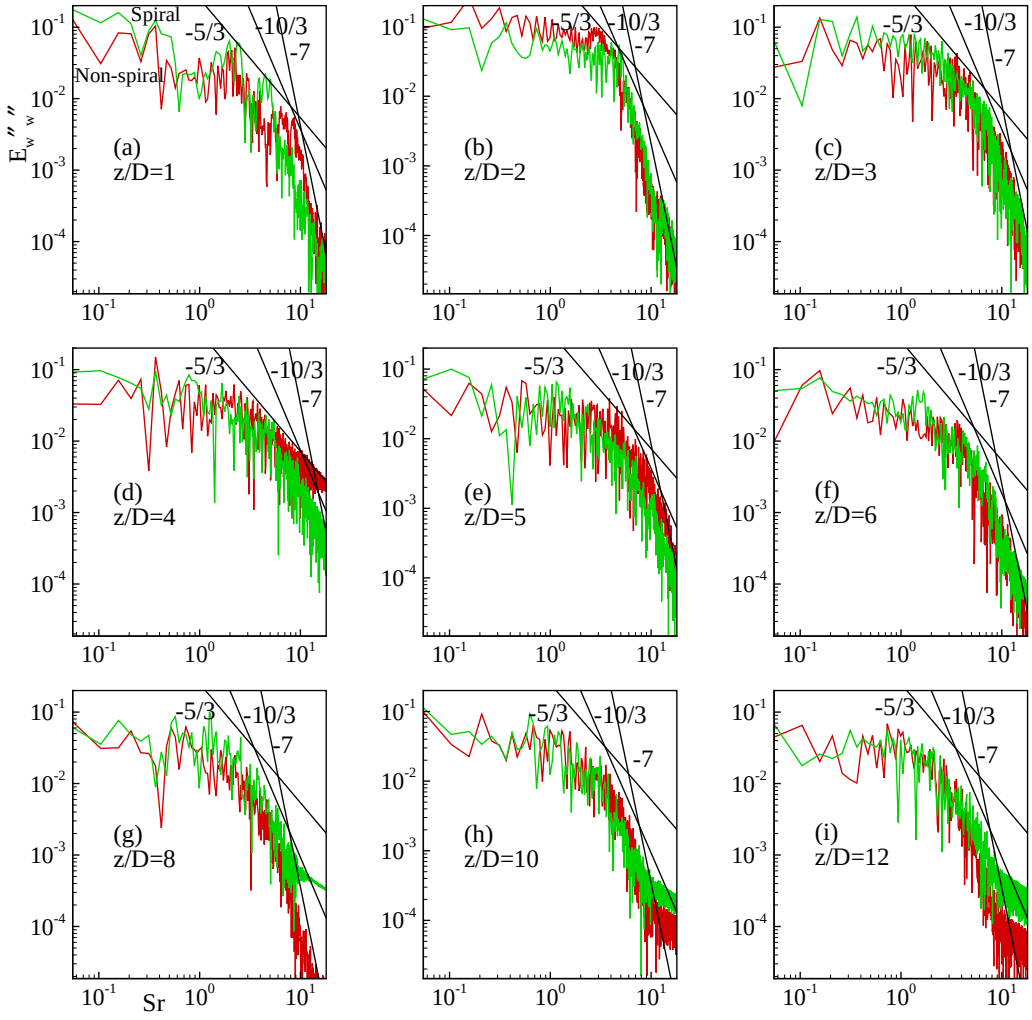

Figure 5.33: Energy spectra of the centreline streamwise velocity fluctuations, w'', at different axial locations normalised by centreline $\langle w'' \rangle_{rms}$ at the same locations, for both non-spiral and spiral pulsatile flow while $Re = 876$. The red and the green coloured lines correspond to the energy spectra of velocity fluctuations for non-spiral and spiral flow, respectively.

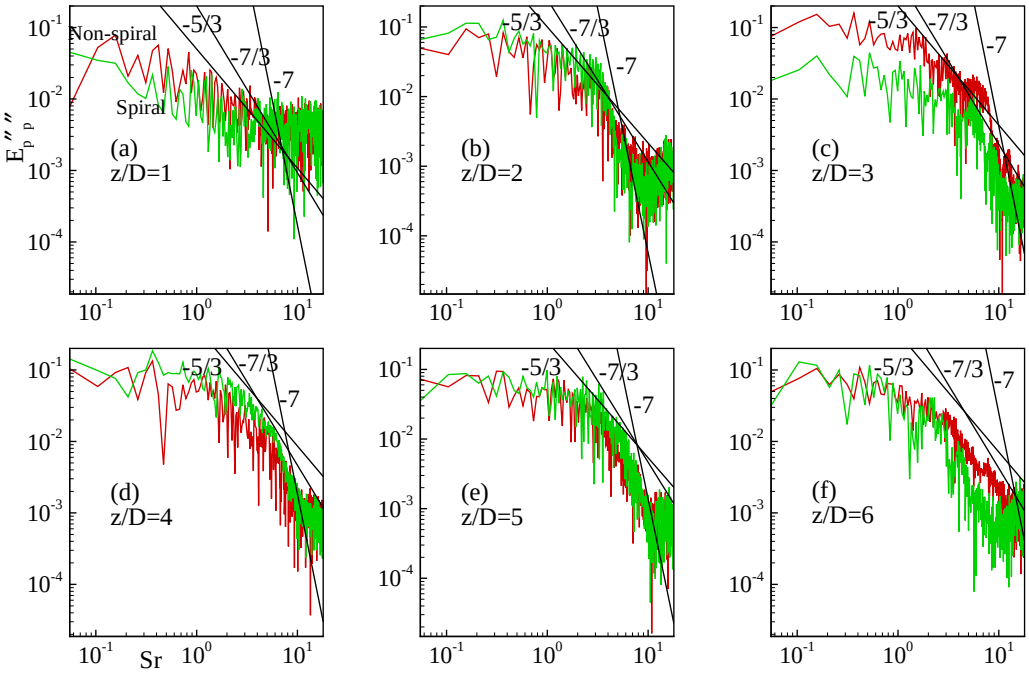

Figure 5.34: Energy spectra of the wall pressure fluctuations, p'', at different axial locations normalised by wall $\langle p'' \rangle_{rms}$ at the same locations, for both non-spiral and spiral pulsatile flow while $Re = 876$. The red and the green coloured line corresponds to the energy spectra of wall pressure fluctuations for non-spiral and spiral flow, respectively.

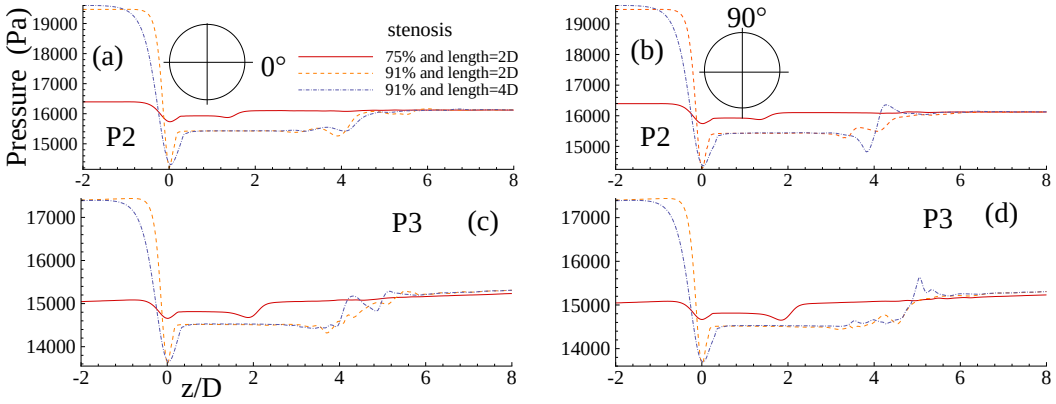

Figure 5.35: Effects of different percentages and lengths of stenosis: instantaneous wall pressure, $\bar{p}$ (Pa), in non-spiral flow during phases $P2$ and $P3$ for (i) 75% stenosis and length$=2D$ (solid line), (ii) 91% stenosis and length$=2D$ (dashed line) and (iii) 91% stenosis and length$=4D$ (dash-dotted line) while $Re = 876$ and $A = 0.40$. The circumferential positions at which wall pressure was obtained are marked

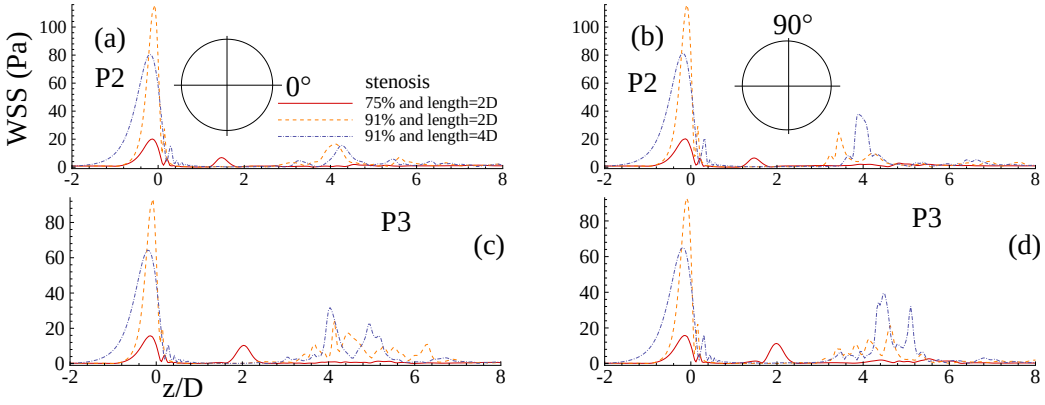

Figure 5.36: Effects of different percentages and lengths of stenosis: instantaneous wall shear stress (Pa) in non-spiral flow during phases $P2$ and $P3$ for (i) 75% stenosis and length$=2D$ (solid line), (ii) 91% stenosis and length$=2D$ (dashed line) and (iii) 91% stenosis and length$=4D$ (dash-dotted line) while $Re = 876$ and $A = 0.40$. The circumferential positions at which WSS was recorded are marked

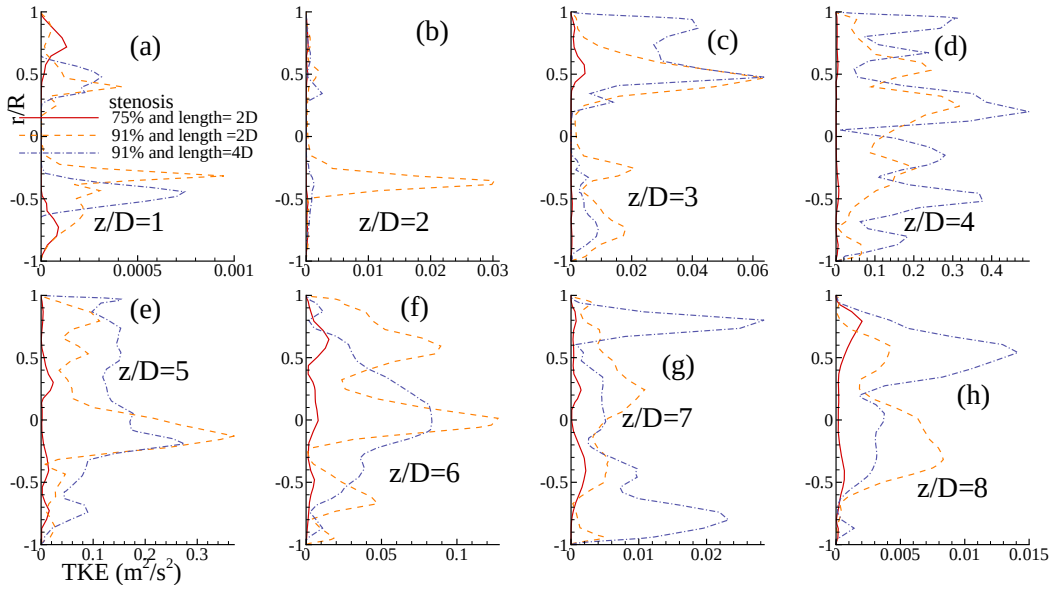

Figure 5.37: Effects of different percentages and lengths of stenosis: turbulent kinetic energy (TKE), $\frac{1}{2}\langle u_j'' u_j'' \rangle$ (m^2/s^2), in non-spiral flow during phase $P3$ at different indicated axial locations for (i) 75% stenosis and length$= 2D$ (solid line), (ii) 91% stenosis and length$= 2D$ (dashed line) and (iii) 91% stenosis and length$= 4D$ (dash-dotted line) while $Re = 876$ and $A = 0.40$.

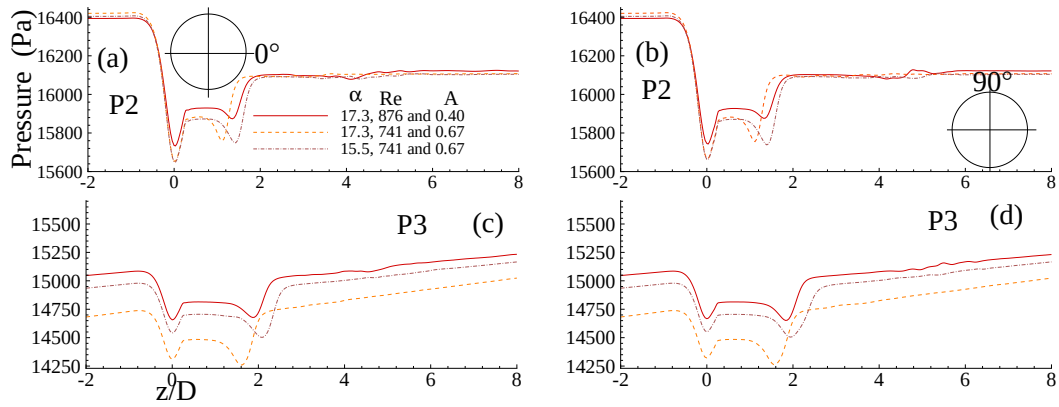

Figure 5.38: Effects of Womersley parameter and amplitude of pulsation: instantaneous wall pressure, $\bar{p}$ (Pa), in non-spiral flow during phases $P2$ and $P3$ for (i) Womersley parameter, $\alpha = 17.3$, $Re = 876$ and $A = 0.40$ (solid line), (ii) $\alpha = 17.3$, $Re = 741$ and $A = 0.67$ (dashed line) and (iii) $\alpha = 15.5$, $Re = 741$ and $A = 0.67$ (dash-dotted line) while the peak Reynolds number is same in all three cases, i.e. $Re_{pk} = 2400$. The circumferential positions at which WSS was recorded are marked

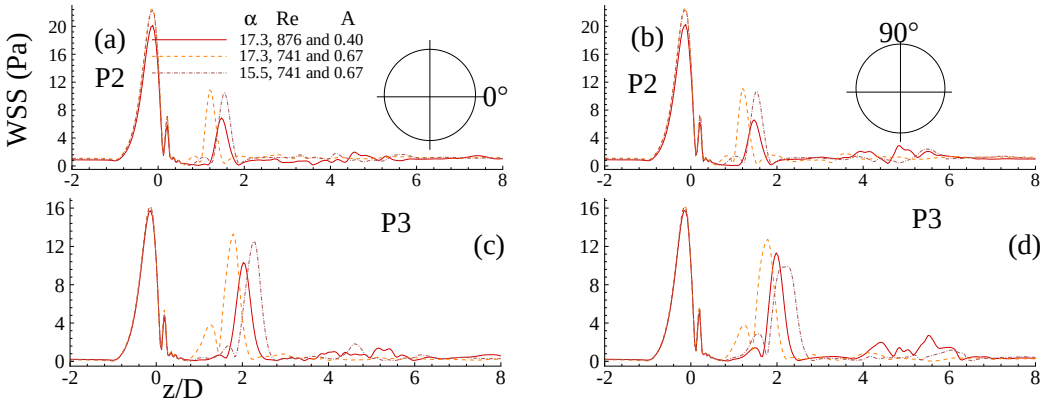

Figure 5.39: Effects of Womersley parameter and amplitude of pulsation: instantaneous wall shear stress (Pa) in non-spiral flow during phases $P2$ and $P3$ for (i) Womersley parameter, $\alpha = 17.3$, $Re = 876$ and $A = 0.40$ (solid line), (ii) $\alpha = 17.3$, $Re = 741$ and $A = 0.67$ (dashed line) and (iii) $\alpha = 15.5$, $Re = 741$ and $A = 0.67$ (dash-dotted line) while the peak Reynolds number is same in all three cases, i.e. $Re_{pk} = 2400$. The circumferential positions at which WSS was recorded are marked

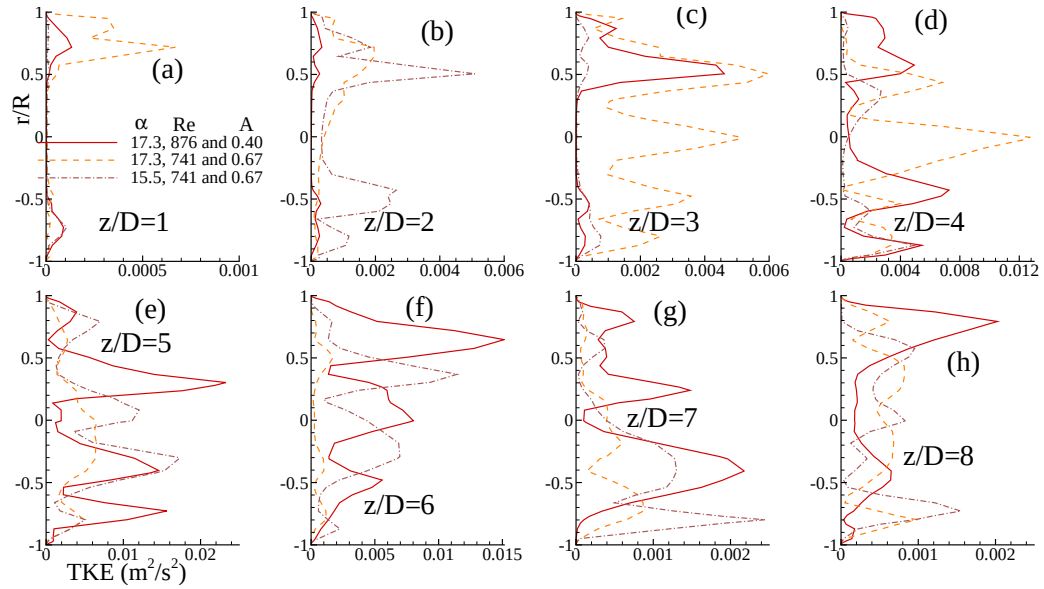

Figure 5.40: Effects of Womersley parameter and amplitude of pulsation: turbulent kinetic energy (TKE), $\frac{1}{2}\langle u_j'' u_j'' \rangle$ (m^2/s^2), in non-spiral flow during phase $P3$ at different indicated axial locations for (i) Womersley parameter, $\alpha = 17.3$, $Re = 876$ and $A = 0.40$ (solid line), (ii) $\alpha = 17.3$, $Re = 741$ and $A = 0.67$ (dashed line) and (iii) $\alpha = 15.5$, $Re = 741$ and $A = 0.67$ (dash-dotted line) while the peak Reynolds number is same in all three cases, i.e. $Re_{pk} = 2400$.

Chapter 6

LES of Physiological Pulsatile Non-spiral and Spiral Blood Flow through a Model of Irregular Arterial Stenosis

6.1 Introduction

All the available three-dimensional computational studies on blood flow through a model of arterial stenosis have been done using a stenosis of regular shape only, to the best of our knowledge. However, it is clear from the *in vitro* study of Back et al. [32], who used mildly atherosclerotic (about 50% area reduction) main coronary casting of man, that stenoses, in reality, are of irregular shape. Although an arterial stenosis generally tends towards a smooth curve, it has many small valleys and ridges (Sarifuddin [64]). Johnston and Kilpatrick [60] and Andersson et al. [61] have studied two-dimensional steady flow through an irregular stenosis with 48% area reduction for Reynolds numbers ranging from $Re = 10$ to 1000. Two-dimensional unsteady pulsatile flow through an irregular stenosis was investigated by Yakhot et al. [62], Chakravarty et al. [63] and Sarifuddin et al. [64]. The findings of these studies have been discussed in § 2.2.1 of Chapter 2. Simulation of blood flow through an irregular arterial stenosis model, which closely resembles real stenosis in artery, would, therefore, understandably provide better insight into transition-to-turbulence phenomena of blood flow through atherosclerotic artery.

In this Chapter, we investigate three-dimensional physiological pulsatile non-

spiral and spiral blood flow through a straight stenosed tube having a 75% area reduction irregular stenosis by applying Large Eddy Simulation technique with the Smagorinsky-Lilly dynamic subgrid model (Germano [115], Lilly [116] and Kim [123]). The irregular stenosis was formed by shifting the cross-sections of a cosine-type stenosis randomly to either x or y-direction. The first four harmonics of the physiological pulsatile flow and pressure pulse, as described in Chapter 5 were used at the inlet and outlet, respectively, to introduce pulsatile velocity profile at the inlet and pressure waveform at the outlet. In addition, like Chapter 5, one-sixth of physiological pulsatile bulk velocity was taken as tangential velocity at the inlet for generating spiral effect there.

The Smagorinsky-Lilly dynamic subgrid model is assessed in terms of the results of the Smagorinsky constant and the normalised SGS viscosity. The numerical results are presented in terms of streamlines, velocity vectors, vortices, wall pressure and shear stresses, turbulent kinetic energy, velocity and pressure fluctuations and their energy spectra to study the transition-to-turbulence of pulsatile non-spiral and spiral blood flow in the downstream of the irregular stenosis. The effects of the irregular stenosis on the pressure drop, wall shear stress and turbulent intensity are also assessed by comparing the flow results obtained from the pulsatile non-spiral blood flow through the irregular stenosis with the corresponding results from Chapter 5, i.e. from the flow through a cosine-type regular stenosis.

6.2 Problem Formulation

6.2.1 Model Geometry and Mesh arrangement

The model of arterial stenosis of irregular shape with rigid wall was developed by using GAMBIT 2.4 (Fluent Inc.) and is shown in Figure 6.1. The diameter of the model, the length of the stenosis, the upstream and downstream lengths from the stenosis centre were kept same as they were in Chapter 5. First a cosine-type regular stenosis of 75% area reduction was developed, then the cross-sections of the cosine-shaped stenosis were shifted maximum 0.5 mm randomly to either x or y-direction (positive or negative) to get the irregular stenosis of circular cross-section. Like previous chapters, a boundary layer was introduced inside the wall to have fine

resolution in the sublayer and also the finest mesh resolution was ensured at the centre and immediate downstream of the stenosis.

6.2.2 Governing Equations and Boundary Conditions

The filtered Navier-Stokes governing equations, which are given in § 3.4.1 of Chapter 3, were solved assuming the blood used in the study to be homogeneous, incompressible and Newtonian. The physiological pulsatile non-spiral and spiral blood flows at the inlet and the pressure waveform at the outlet remain same as in Chapter 5.

6.3 Results and Discussion

The simulations were run for Reynolds numbers, $Re = 438$, 584 and 876 while the Womersley number, α, and the amplitude of pulsation, A, were chosen as 17.3 and 0.40 respectively. Following the results in the previous chapters, the time-step, δt, was fixed at 10^{-3} for all the computations. As in Chapter 5, the simulations were carried out for 20 pulsatile cycles; the initial eight cycles were ignored and the last 12 cycles were taken for phase-averaged statistics. The same phases will be chosen to present and analyse the results as they were referred to in Chapter 5.

The layout of this section is as follows. Firstly, the results of the grid resolution study are presented in § 6.3.1. This is followed by the contribution of the subgrid model to the large scale motion in § 6.3.2. The instantaneous flow physics and the phase-averaged flow characteristics are presented in § 6.3.3 and § 6.3.4 respectively, while the turbulent flow characteristics are given in § 6.3.5. Lastly, the findings are summarised in § 6.4 under 'conclusion'.

6.3.1 Grid Resolution Study

A grid resolution study was done for $Re = 876$ in non-spiral flow taking three grids, namely Grid 1, Grid 2 and Grid 3. Grid 1 consists of $\approx 550,000$ control volumes which is increased by about 45% in Grid 2 so that Grid 2 has $\approx 800,000$ control volumes. The number of control volumes in Grid 3 was further increased by about 75% compared with Grid 2, resulting in $\approx 1,400,000$ control volumes in

Grid 3. Figures 6.2 and 6.3 show grid resolution results during phase $P3$ in terms of phase-averaged streamwise velocity, $\langle\langle\bar{w}\rangle\rangle$ (m/s), at different axial positions and wall shear stress (Pa), respectively. Note that the circumferential-averaged WSS was used for the phase averaging of WSS in Figure 6.3. The overall agreement between the results obtained for three different grids is quite good, given that LES results are dependent on the mesh resolution until LES grid resolution becomes fine enough to be used for DNS (Mittal et al. [88]; Paul and Molla [93]). Further, results for Grid 2 agree better with Grid 3 results compared with Grid 1. Hence the resolution of Grid 2 was used for the simulation of pulsatile non-spiral and spiral blood flow through the irregular stenosis model as its resolution seems adequate to resolve the transient flow in the model.

6.3.2 Contributions of the SGS Dynamic Model

Figure 6.4 presents the contour plots of the dynamic Smagorinsky constant, C_s, in non-spiral flow during phase $P3$ in the $z-x$ mid-plane for $Re = 438$, 584 and 876. The maximum value of C_s here is ≈ 0.05, whereas it was ≈ 0.045 in Chapter 5, i.e. the maximum value of C_s has increased due to the effects of irregular stenosis. Also, the locations of non-zero C_s increase in the downstream region of the stenosis when the Reynolds number is increased. It should be noted that the value of C_s in the upstream of the stenosis is very insignificant as compared with its downstream value where the flow is predicted to be turbulent.

The contribution of the SGS dynamic model to the large scale motion can be observed clearly from Figure 6.5, which shows the contour plots of normalised SGS eddy viscosity, μ_{sgs}/μ, in non-spiral flow during phase $P3$ for the investigated Reynolds numbers in the $z-x$ mid-plane. Though the maximum (normalised) eddy viscosity, which is also found in the downstream transition-to-turbulence region, for all the Reynolds numbers is same, i.e. ≈ 0.55, the effects of Reynolds number on it can be distinctly seen as the maximum eddy viscosity occurs at more places for higher Reynolds number (frame b-c). That means a maximum of 55% contribution is received from the SGS model for $Re = 438$, 584 and 876. Additionally, like C_s, the maximum eddy viscosity increases in the irregular stenosis model compared with its corresponding value in the regular stenosis model which was 0.5. Thus, the

SGS dynamic model in the irregular stenosis model contributes 5% more energy diffusion into the flow than that in the regular stenosis model. In spiral flow through the irregular stenosis model, the values of C_s and μ_{sgs}/μ are almost same as that in non-spiral flow.

6.3.3 Instantaneous Flow Physics

The contour plots of the instantaneous y-vorticity, $\Omega_y = (\frac{\partial \bar{w}}{\partial x} - \frac{\partial \bar{u}}{\partial z})$ (1/s), in non-spiral and spiral flow through the irregular stenosis during phase $P3$ of 20^{th} cycle for (a) $Re = 438$, (b) $Re = 584$ and (c) $Re = 876$ are shown in Figures 6.6(a-c) and 6.7(a-c), respectively. Note that the corresponding y-vorticity in both non-spiral and spiral flows through the regular stenosis for $Re = 876$ is appended in frame (d). Two vortices, one clockwise (blue) and the other anti-clockwise (red), are developed in the downstream region near the wall as the shear layers separate from the stenosis throat. The vortex-rings in non-spiral flow for a given Reynolds number resemble their counterparts in spiral flow. However, they become larger and move further downstream when the Reynolds number is increased. For $Re = 438$ in both non-spiral and spiral flow, the jet and shear layers break down at $z \approx 3D$; evidently, the flow undergoes transition to turbulence between $z = 3D$ and $4D$ with the flow reattachment by $z \approx 4D$ (frame a). The transition-to-turbulence region changes if the Reynolds number is increased. For $Re = 584$ in both non-spiral and spiral flow, the transition-to-turbulence region is within $3D \leq z \leq 5D$ (frame b), however, for $Re = 876$, apparently the flow transients to turbulence in non-spiral and spiral flow within $4D \leq z \leq 6D$ (Figure 6.6(c)) and $3D \leq z \leq 6D$ (Figure 6.7(c)), respectively.

In both non-spiral and spiral flows for $Re = 876$, the vortex-rings are stronger and stretch as far as $z/D \approx 2.5$ in frame (c) due to the effects of the irregular stenosis as compared with their counterparts in the regular stenosis in frame (d) where they stretch up to $z/D \approx 2.25$. Additionally, in spiral flow, though the shear layers break down at $z/D \approx 3$ in both the irregular and regular stenoses, the flow reattachment occurs at further downstream region by $z \approx 6D$ in the irregular stenosis (Figure 6.7(c)) ; whereas in the regular stenosis, the flow reattachment occurs by $z \approx 5D$ (Figure 6.6(d)). In non-spiral flow through both the irregular

and regular stenoses (Figure 6.6(c-d)), the shear layers breakdown and the flow reattachment occur at $z \approx 4D$ and $z \approx 6D$, respectively.

Figures 6.8(a-c) and 6.9(a-c) depict the instantaneous $z - x$ mid-plane streamlines in non-spiral and spiral flow, respectively, through the irregular stenosis during phase $P3$ for (a) $Re = 438$, (b) $Re = 584$ and (c) $Re = 876$. The corresponding streamlines in both flows through the regular stenosis for $Re = 876$ are appended in frame (d). In both non-spiral and spiral flow for all the Reynolds numbers, large recirculation regions are developed near the wall, right after the stenosis throat due to the occurrence of back flow there. The length of the recirculation region grows if the Reynolds number is increased. As mentioned in the previous chapter, these recirculation regions increase the blood residence time as the blood is recirculated in these regions during each cycle for a significant time, posing a potential risk of heart attack and brain stroke (Molla [90]). The corresponding streamlines in non-spiral and spiral flow resemble each other and the effect of spiral flow on the streamlines is negligible. The only difference in the pattern of streamlines in non-spiral and spiral flow which can be observed for $Re = 876$ (frame c) is the existence of an additional small recirculation region in non-spiral flow after $z = 4D$ (at the bottom wall), which is absent in the spiral flow case. However, the effects of the irregular stenosis on the recirculation region is obvious from frames (c-d) in both the figures. The recirculation region in the irregular stenosis is stronger than that in the regular stenosis; the flow reattachment in the irregular stenosis occurs at $z/D \approx 2.6$, whereas in the regular stenosis, it occurs at $z/D \approx 2.25$. It is clear from the above discussion that results in the irregular stenosis vary significantly from that in the regular stenosis and irregular stenosis should, therefore, be considered for getting clear picture of the flow physics in the downstream of the stenosis.

Further information on the flow characteristics of non-spiral and spiral flow through the irregular stenosis is revealed through cross-stream velocity vectors. The in-plane velocity vectors appended on the streamwise velocity, $\bar{w}$ (m/s), contours at different axial locations for $Re = 876$ during phase $P3$ in non-spiral and spiral flow are presented in Figures 6.10 and 6.11. The flow is apparently laminar at the throat of the stenosis (frame a) and $z = 1D$ (frame b) in both non-spiral and spiral flow; the streamwise velocity attains its maximum value at $z = 1D$ (frame b) and $z = 2D$ (frame c). However, in both non-spiral and spiral flow, the stenotic jet breakdown

starts at $z = 2D$ (frame c), resulting in the onset of transition-to-turbulence and the flow is very chaotic within $2 \leq z/D \leq 6$ (frame c-g). Relaminarisation process takes place subsequently, which is more obvious at $z = 8D$ (frame h) where the flow is almost undisturbed. It is interesting to note that the spiral pattern of the velocity vectors is found only up to the throat of the stenosis (Figure 6.11(a)) and it is lost subsequently as a result of intense turbulence activities in the further downstream region.

6.3.3.1 Instantaneous Wall Pressure

The instantaneous wall pressure, $\bar{p}$ (Pa), profiles at two circumferential locations (0° and 90°) of the wall during different phases of the last pulsatile cycle for $Re = 438$, 584 and 876 in both non-spiral (NSp) and spiral flow are shown in Figure 6.12. The corresponding wall pressure results for $Re = 876$ in non-spiral flow through the regular stenosis are also appended in the figure. It is important to note that the effects of spiral flow on the wall pressure is found only at some locations within $2 \leq z/D \leq 6$ where the pressure is of oscillating nature for $Re = 584$ and 876 and the maximum pressure drop remains almost unaffected by the spiral flow. As seen in the previous chapters, the pressure drops sharply at the stenosis throat and in the immediate post-stenotic region where the streamwise velocity is extremely high and the pressure drop increases with Reynolds number. The maximum pressure drop occurs during phase $P1$ and it is extremely high during phases $P2$ and $P3$ compared with the corresponding pressure drop during other phases.

Due to the effect of irregular stenosis, the pressure drop at 0° circumferential location differs significantly from that at 90° circumferential location, e.g. for $Re = 876$ in non-spiral flow, excess pressure drops (around the throat of the stenosis) of ≈ 132 Pa, ≈ 198 Pa and ≈ 125 Pa during phases $P1$, $P2$ and $P3$, respectively, are found at 0° circumferential location compared with the corresponding results at 90° circumferential location. Also the ridges in the profiles found between $z = -1D$ and $z = 1D$ are caused by the influence of the irregular stenosis. Furthermore, the maximum pressure drop increases significantly in the irregular stenosis compared with that in the regular stenosis. For example, the maximum pressure drops in non-spiral flow through the irregular stenosis during phases $P1$, $P2$ and $P3$ for $Re = 876$ are ≈ 883 Pa, ≈ 864 Pa and ≈ 567 Pa, respectively, whereas the

corresponding maximum pressure drops for the regular stenosis during phases $P1$, $P2$ and $P3$ are ≈ 685 Pa, ≈ 661 Pa and ≈ 426 Pa, respectively – which are equivalent to $\approx 29\%$, $\approx 31\%$ and $\approx 33\%$ increase in the maximum pressure drop in the irregular stenosis during phases $P1$, $P2$ and $P3$, respectively, compared with the the corresponding maximum pressure drops in the regular stenosis. The pressure drop agrees with the corrsponding results of in the similar studies of Johnston and Kilpatrick [60], Andersson et al. [61], Chakravarty et al. [63] and Sarifuddin et al. [64], but the magnitude of the pressure drop in the irregular stenosis in this study is higher than that in the regular stenosis. However, they reported that the pressure drop in a cosine-type regular stenosis increases (by 10% to 16%) compared with the corresponding pressure drop in an irregular stenosis – this is possibly due to the fact that their studies were limited to two-dimensional laminar flow through relatively mild stenosis (48% area reduction). The clinical implications of these extremely high pressure drops are potentially dangerous which, were also discussed in the previous chapters, include flow choking and rupture of the plaque cap (Wootton and Ku [6]; Li et al. [8]).

6.3.3.2 Instantaneous Wall Shear Stress

Figures 6.13, 6.14 and 6.15 illustrate the instantaneous wall shear stress (WSS) in both non-spiral and spiral flow for $Re = 438$, 584 and 876, respectively, at 0° and 90° circumferential locations of the wall during different phases of the last pulsatile cycle. Note that the corresponding wall shear stresses in non-spiral flow through the regular stenosis for the investigated Reynolds numbers are appended in the figures. For all the Reynolds numbers during all the phases, the WSS starts to rise at the pre-lip of the stenosis with sharp ridges due to effects of the irregular stenosis; and it attains its maximum value just before the stenosis throat. After this sharp rise it drops to almost its upstream value at the stenosis throat and continues with slightly decreasing value almost up to the post-lip of the stenosis; in the further downstream region the WSS takes oscillatory pattern. As seen in the results of wall pressure, the effects of spiral flow on the WSS can be observed only in the downstream region between $z \approx 1.25D$ and $7D$ where the WSS is of oscillating nature. The oscillatory WSS is implicated in arterial disease progression (Ku [3]; Paul and Molla [93]). Throughout the pulsatile cycle, the WSS is heavily depen-

dent on Reynolds number; it increases significantly when the Reynolds number is increased.

For all the investigated Reynolds numbers in Figures 6.13, 6.14 and 6.15, the maximum value of WSS occurs during phase $P2$ at 90° circumferential location of the wall (frame d); the maximum shear stresses around the stenosis throat during phase $P2$ (at 0° circumferential location) (frame c), $P1$ (frame a-b) and $P3$ (frame e-f) are also extremely large. For $Re = 438$, 584 and 876, the maximum shear stresses are ≈ 17 Pa (Figure 6.13(d)), ≈ 25 Pa (Figure 6.14(d)) and ≈ 48 Pa (Figure 6.15(d)), respectively. It is interesting to note that due to the effects of the irregular stenosis, the maximum value of the WSS at 90° circumferential location significantly differs from that at 0° circumferential location during a given phase, more specifically, it is greater at 90° circumferential location than that at 0° circumferential location. For example, the maximum shear stresses for $Re = 876$ during phases $P1$, $P2$ and $P3$ at 90° circumferential location are ≈ 47 Pa, ≈ 48 Pa and ≈ 38 Pa, respectively, whereas their counterparts at 0° circumferential location are ≈ 41 Pa, ≈ 41 Pa and ≈ 32 Pa, respectively. Furthermore, it is clear from the figures that for all the Reynolds numbers during all the phases, the maximum WSS increases in the irregular stenosis compared with the corresponding WSS in the regular stenosis. The maximum shear stresses (frame d) in the irregular stenosis rise by $\approx 126\%$, $\approx 126\%$ and $\approx 140\%$ for $Re = 438$, 584 and 876, respectively, compared with that in the regular stenosis. This result agree with the corresponding findings in the studies of Johnston and Kilpatrick [60], Andersson et al. [61], Chakravarty et al. [63] and Sarifuddin et al. [64], who also reported that WSS rises significantly in the irregular stenosis compared with that in the cosine-type regular stenosis.

The pathophysiological impacts of high WSS, as discussed in the previous chapters, are profoundly detrimental to cardiovascular health. According to Ku [3], high WSS may overstimulate platelet thrombosis, resulting in total occlusion of the vessel (Folts et al. [38]). Fry [36] reported that high WSS $> 37.9 \pm 8.5$ (SD) Pa may harm endothelial cells. Shear stress ≥ 10 Pa lead to deformation of the red blood cells (Sutera and Mehrjardi [37]) and > 7 Pa, according to Malek et al. [9], may induce thrombosis. It is, therefore, clear from the above three figures that wall shear stress reaches the clinically harmful level during all the phases for $Re = 876$, however, for $Re = 584$ and 438, it reaches the dangerous level only during phases $P1$,

$P2$ and $P3$.

6.3.4 Phase-averaged Flow Characteristics

It would be interesting to present some phase-averaged results and see how they behave. The phase-averaged streamwise velocity during phase $P3$ in both non-spiral (NSp) and spiral flow at different axial locations is presented in Figure 6.16(a-l) for Reynolds numbers $Re = 438$, 584 and 876. The corresponding results in non-spiral flow through the regular stenosis for $Re = 876$ are also appended in the figure. The streamwise velocity increases with Reynolds number. Its pattern is similar to that of fully developed Poiseuille flow at the pre-lip of the stenosis; it increases dramatically at the throat and in the immediate post-stenotic region (frames b-d). Due to the existence of the permanent re-circulation region observed in Figures 6.8 and 6.9, negative values of the streamwise velocity is observed near the wall in frames (c-d). As seen in the phase-averaged streamwise velocity profiles in Chapter 5, the effect of spiral flow is visible only in the transition-to-turbulence region, between $z = 2D$ and $6D$, where the profiles lose their jet-like character and tend to uniformity. The streamwise velocity in spiral flow increases at some places compared with that in non-spiral flow, e.g. for $Re = 876$, due to spiral flow, it increases at some places in frames (e-h) and decreases in frames (d, h). Flow tries to regain its upstream character in further downstream region as the relaminarisation process takes place. The effects of the irregular stenosis on the streamwise velocity is observed only between the throat and $z = 6D$. In the further downstream region, the velocity profiles in the regular stenosis match that in the irregular stenosis. The streamwise velocity in the irregular stenosis increases in frames (b-e, h) compared with that in the regular stenosis, however, the opposite happens at $z = 4D$ and $5D$ (frames f-g).

Figure 6.17 depicts the phase-averaged wall shear stress at 0° and 90° circumferential locations of the wall during phase $P3$ in both non-spiral and spiral flow for $Re = 438$, 584 and 876. Note that the corresponding phase-averaged results in non-spiral flow through the regular stenosis are also appended. As seen in Chapter 5, the phase-averaged wall shear stresses closely resemble the corresponding instantaneous results in Figures 6.13(e-f), 6.14(e-f) and 6.15(e-f) in both magni-

tude and pattern. The oscillating nature of the WSS, which was observed in the downstream region in the instantaneous results, is absent here as a result of phase-averaging. Therefore, instantaneous WSS is important for accurate description of its profile. The effect of spiral flow on the phase-averaged WSS is negligible. Like the instantaneous WSS in the irregular stenosis, the phase-averaged WSS in the irregular stenosis increases dramatically compared with the corresponding result in the regular stenosis. For example, the maximum phase-averaged shear stresses at 90° circumferential location in the irregular stenosis increase by $\approx 116\%$, $\approx 122\%$ and $\approx 137\%$ for $Re = 438$, 584 and 876, respectively, compared with the corresponding results in the regular stenosis.

6.3.5 Turbulent Characteristics

In this section, the effects of the irregular stenosis on both non-spiral and spiral turbulent flows are presented in terms of the root mean square (rms) of the streamwise velocity and pressure fluctuations, turbulent kinetic energy (TKE) and the energy spectra of the streamwise velocity and pressure fluctuations.

Figure 6.18 shows the root mean square (rms) of the streamwise velocity fluctuations, $\langle w'' \rangle_{rms}$ (m/s), at different axial locations during phase $P3$ in both non-spiral (NSp) and spiral flow for $Re = 438$, 584 and 876. Note that the corresponding results in non-spiral flow through the regular stenosis for $Re = 876$ are also appended. The maximum $\langle w'' \rangle_{rms}$ occurs at different places for different Reynolds numbers. For $Re = 438$ and 584, the maximum $\langle w'' \rangle_{rms}$ is found at $z = 4D$, whereas for $Re = 876$, it occurs at $z = 5D$. The magnitude of the maximum $\langle w'' \rangle_{rms}$ increases with Reynolds number. The streamwise velocity fluctuations at some places in spiral flow rises compared with that in non-spiral flow. Additionally, the maximum $\langle w'' \rangle_{rms}$ in the irregular stenosis is larger than that in the regular stenosis.

Further information on the effects of the irregular stenosis and spiral flow can be obtained from the TKE results. Figures 6.19, 6.20 and 6.21 illustrate the turbulent kinetic energy (TKE), $\frac{1}{2}\langle u_j'' u_j'' \rangle$ (m^2/s^2), at different axial locations during phase $P3$ in both non-spiral (NSp) and spiral flow through the irregular stenosis along with the corresponding results in non-spiral flow through the regular stenosis for $Re = 438$, 584 and 876, respectively. The TKE is very small at the post lip for all the

Reynolds numbers, it increases in the downstream region where the flow transients to turbulence and die away in the further downstream region as the relaminarisation process begins. It is clear from the above figures that the transition-to-turbulence region increases when the Reynolds number is increased; and the transition starts in the immediate downstream region for high Reynolds number, while it starts in the further downstream region for low Reynolds numbers. For example, the transition-to-turbulence regions for $Re = 438$, 584 and 876 are within $3D \leq z \leq 4D$, $3D \leq z \leq 5D$ and $2D \leq z \leq 6D$, respectively.

Like $\langle w'' \rangle_{rms}$, the maximum TKE increases when the Reynolds number is increased. Moreover, for all the Reynolds numbers, the maximum TKE in spiral flow (Figures 6.19(b), 6.20(d) and 6.21(e)) increases significantly compared with that in non-spiral flow. Also TKE at some other places rises sharply due to the effects of spiral flow. As observed in the previous chapters, this result contradicts the claims of Paul and Larman [17] and Stonebridge et al. [16]. The drawbacks of their studies will not be repeated here as they were discussed in detail in § 2.4 of Chapter 2. As for the effects of the irregular stenosis on TKE, the values of TKE at some locations in the irregular stenosis increase significantly compared with the corresponding results in the regular stenosis. In the pathological context, the large TKE in the transition-to-turbulence region may lead to the damage of the blood cell tissues inside a blood vessel (Ku [3]; Paul and Molla [93]).

The rms of wall pressure fluctuations, $\langle p'' \rangle_{rms}$ (Pa), in both non-spiral and spiral flow for Reynolds numbers $Re = 438$, 584 and 876 during phase $P3$ at 0° and 90° circumferential locations of the wall are shown in Figure 6.22. The corresponding results in non-spiral flow through the regular stenosis for $Re = 876$ are also appended in the figure. For $Re = 438$, the rms of wall pressure fluctuations in both non-spiral and spiral flow is very small as the wall pressure does not fluctuate much for low Reynolds number. The value $\langle p'' \rangle_{rms}$ increases when the Reynolds number is increased. In both non-spiral and spiral flow for $Re = 584$ and 876, $\langle p'' \rangle_{rms}$ increases significantly at around $z = 2D$; and in the further downstream region between $z \approx 3D$ and $7D$, its rise is of oscillatory pattern. The maximum $\langle p'' \rangle_{rms}$, which occurs at around $z = 2D$ at 0° circumferential location for $Re = 584$ and 876, in non-spiral flow increases as compared with that in spiral flow. Additionally, the maximum $\langle p'' \rangle_{rms}$ in non-spiral flow through the regular stenosis for

$Re = 876$, which occurs at around $z = 5D$, is much less than the corresponding result through the irregular stenosis. As discussed in Chapter 5, high level of pressure fluctuations are the main source of arterial murmurs, a key diagnostic condition of arterial stenosis detected by bio-acoustic techniques (Ask et al. [135]). As the value of pressure fluctuations in the irregular stenosis increases compared with that in the regular stenosis, the intensity of the arterial murmurs in the irregular stenosis would be higher than that in the regular stenosis. the same observation can be made for non-spiral and spiral flow, i.e. the intensity of arterial murmurs in spiral flow is less than that in non-spiral flow.

6.3.5.1 Cycle-to-cycle variations

Figure 6.23 presents cycle-to-cycle variations of the centreline cross-stream velocity fluctuations, u''/u''_{max} and v''/v''_{max}, and the centreline streamwise velocity fluctuations, w''/w''_{max}, at different axial positions in both non-spiral and spiral flow for $Re = 876$ over the last three cycles used for phase-averaged statistics. The magnitudes of the velocity fluctuations before $z = 2D$ are very small and not shown in the figure. It is clear from the figure that the centreline velocity fluctuations in both non-spiral and spiral flow are non-periodic and very big in magnitude in the downstream region of $3D \leq z \leq 6D$; they fade away in the further downstream region due to the decreasing influence of the stenosis there. Also the effects of the spiral flow on the centreline velocity fluctuations are clearly visible within $3D \leq z \leq 6D$.

The cycle-to-cycle variations of the TKE, $\frac{1}{2}\langle u''_j u''_j \rangle$ (m^2/s^2), at different axial locations on the centreline in both non-spiral and spiral flow for $Re = 876$ are shown in Figure 6.24. Note that the corresponding results in non-spiral flow through the regular stenosis are also appended in the figure. As seen in the previous chapter, the centreline TKE in spiral flow rises significantly during some phases at some locations compared with the corresponding result in non-spiral flow. In addition, due to the effects of the irregular stenosis, the maximum TKE in non-spiral flow through the irregular stenosis increases by $\approx 55\%$ compared with that through the regular stenosis. Hence the irregular stenosis should be considered in the simulation of blood flow through stenosis to accurately predict the turbulent characteristics in the post-stenotic region.

6.3.5.2 Turbulent Energy Spectra

Energy spectra, $E_{w''w''}$ of the normalised centreline streamwise velocity fluctuations, $(w''/\langle w''\rangle_{rms})^2$, and $E_{p''p''}$ of the normalised wall pressure fluctuations, $(p''/\langle p''\rangle_{rms})^2$, in both non-spiral (red coloured line) and spiral (green coloured line) flow at different axial positions for $Re = 876$ are shown in Figures 6.25 and 6.26, respectively. Along with $E_{w''w''}$, the lines of $(Sr)^{-5/3}$, $(Sr)^{-10/3}$ and $(Sr)^{-7}$ are also included in Figure 6.25, whereas for $E_{p''p''}$, the lines of $(Sr)^{-5/3}$, $(Sr)^{-7/3}$ and $(Sr)^{-7}$ are included in Figure 6.26. The calculation methods for the energy spectra have already been explained in § 5.4.5 of Chapter 5.

In the downstream region between $z = 2D$ and $6D$ in both non-spiral and spiral flow where the flow transients to turbulence, the inertial subrange region of $-5/3$ power slope in the velocity spectra in Figure 6.25 break into $-10/3$ power slope at higher frequencies, resulting in large range of broadband frequencies and very small viscous dissipation range of -7 power slope for this region (frame b-f). The broadband frequency range is very small at the post-lip and in the down stream region $z > 6D$ (frame a, g-i). The spectra changes from $-10/3$ power slope to -7 power slope at lower frequencies in the down stream region $z > 6D$ (frame g-i) as a result of weak turbulence intensity there, giving a large range of viscous dissipation frequencies. These findings are consistent with the experimental results of Gross et al. [138] and Lu et al. [47]. Additionally, it should be noted that at $z = 2D$ and $6D$, the broadband frequency range in the velocity spectra in non-spiral flow has larger range of frequencies than that in spiral flow (frame b,f), however in frames (c-e), the opposite happens, i.e. the inertial subrange in the velocity spectra in spiral flow has larger range of frequencies than that in non-spiral flow. In the region $z \geq 8D$, the viscous dissipation range in non-spiral flow is smaller than that in spiral flow as the spectra of -7 power slope in non-spiral flow roll off to another power slope inclining toward horizontal line at lower frequencies than that in spiral flow.

As seen in the velocity spectra, the pressure spectra in both non-spiral and spiral flow in Figure 6.26 has larger range of frequencies constituting the inertial subrange in the downstream region between $z = 2D$ and $6D$ (frame b-f). And at $z = 1D$ (frame a), the inertial subrange region in the pressure spectra is very small as well. The pressure spectra change from the broadband range of $-5/3$ power slope to the

break frequency region of $-7/3$ power slope at frequencies which represent the energy transfer from the pressure spectra to the sound spectra, a possible source of arterial stenosis murmurs (Paul and Molla [93]) which was also discussed in the previous chapter. Due to the effect of spiral flow on the pressure spectra, apart from the absence of the viscous dissipation range in non-spiral flow at $z = 3D$ (frame c), the change in the spectra rolling off to a power slope of interest is negligible.

It is to note that these findings on the turbulence power spectra in non-spiral and spiral flow through the irregular stenosis are quite similar to the corresponding results through the regular stenosis in Chapter 5.

6.4 Conclusion

In this chapter, Large Eddy Simulation with Smagorinsky-Lilly dynamic subgrid model (Germano [115], Lilly [116] and Kim [123]) has been employed to investigate the physiological pulsatile non-spiral and spiral blood flow through a straight tube having an irregular stenosis of 75% area reduction for $Re = 438$, 584 and 876. The results of non-spiral flow through the irregular stenosis are also compared with the corresponding results through a regular stenosis from Chapter 5 to assess the effects of the irregular stenosis. Although the maximum contribution from the SGS model is 55% in both non-spiral and spiral flow for all the Reynolds number, the maximum SGS contribution occurs at more places when the Reynolds number is increased. And due to the effect of the irregular stenosis, the maximum SGS contribution increases significantly.

The permanent recirculation regions near the wall after the throat of the stenosis found in both non-spiral and spiral flow are quite strong and increase due to the effects of the irregular stenosis. As seen in the previous chapter, the maximum wall pressure drop increases with Reynolds number; the effect of spiral flow on the wall pressure is found only in the downstream region within $2 \leq z/D \leq 6$ where the pressure is of oscillating form and the effect of spiral flow on the maximum pressure drop is negligible. The maximum pressure drop at one circumferential location of the wall differs significantly from that at other circumferential location as a result of the irregular stenosis. Also the maximum pressure drop through the irregular stenosis greatly increases compared with that through the regular stenosis.

For example, the maximum pressure drop during phase $P2$, i.e. under the inlet peak flow condition, for $Re = 876$ through the irregular stenosis increases by $\approx 31\%$ compared with that through the regular stenosis. Furthermore, the findings on WSS are quite similar to the wall pressure results. The effect of spiral flow is found only in the downstream region where the WSS is of oscillatory nature and the maximum WSS in the irregular stenosis rises sharply compared with the corresponding result in the regular stenosis. For example, the maximum WSS during phase $P2$ for $Re = 876$ in the irregular stenosis rises by $\approx 140\%$ compared with the corresponding result in the regular stenosis.

The transition-to-turbulence region and the TKE in both non-spiral and spiral flow increases with Reynolds number; the flow transients to turbulence in the immediate downstream region for high Reynolds number, whereas for low Reynolds number, the flow transition begins in the further downstream region. As seen in the previous chapter, the TKE increases significantly at some locations and phases due to spiral effect. This finding contradicts the claim made in similar studies (Paul and Larman [17]; Stonebridge et al. [16]) which was also discussed in the previous chapters. In addition, the maximum TKE in the non-spiral flow through the irregular stenosis rises sharply compared with corresponding result in non-spiral flow through the regular stenosis. In the pathological context, the irregular stenosis has devastating effects on the cardiovascular health of the patients. In the simulation of blood flow through stenosed artery, irregular stenosis should, therefore, be taken for accurate prediction of the flow field. As seen in the previous chapter, in both velocity and pressure spectra in non-spiral and spiral flow, the large broadband frequency range exists in the transition-to-turbulence region and the well-defined viscous dissipation range can be found in the further downstream region as the relaminarisation process starts there. At some locations in the transition region, the velocity spectra in spiral flow has larger range of broadband frequencies than that in non-spiral flow. The effects of spiral flow on the pressure spectra is negligible.

So far, we have studied non-spiral and spiral flow through stenosis only. But stenosis may be followed by an adjacent aneurysm in the same arterial segment (In et al. [13]). Hence it would be interesting to study physiological pulsatile non-spiral and spiral blood flow through a model of arterial stenosis with adjacent aneurysm in the next chapter.

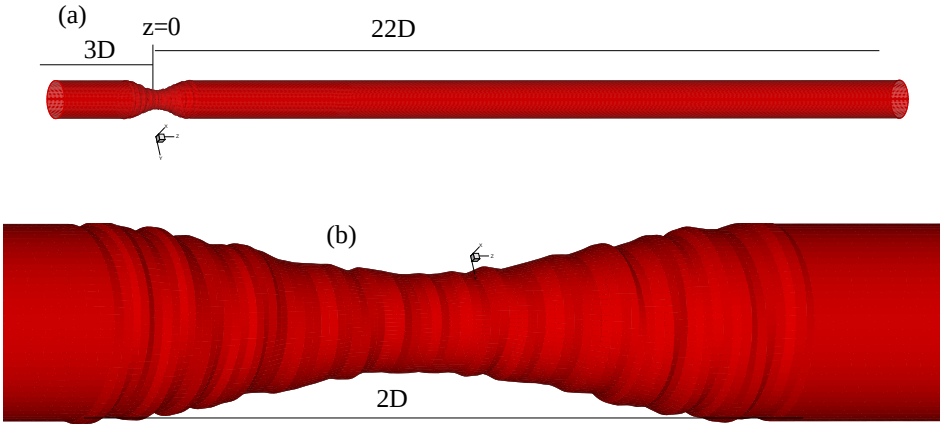

Figure 6.1: Three dimensional view of model artery having irregular stenosis: (a) the whole domain and (b) zoomed-in section on irregular stenosis.

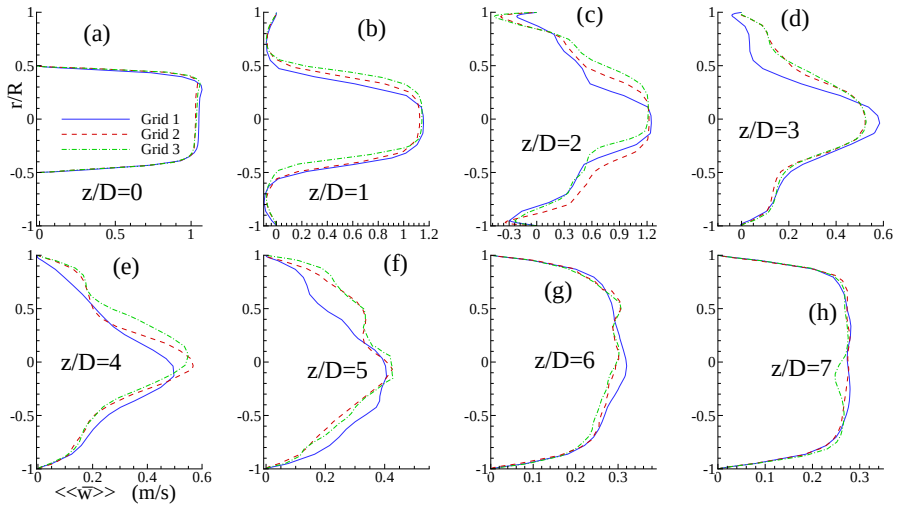

Figure 6.2: Grid resolution study for phase-averaged streamwise velocity, $\langle\langle\bar{w}\rangle\rangle$ (m/s), in non-spiral blood flow during phase $P3$ at different indicated axial locations while $Re = 876$.

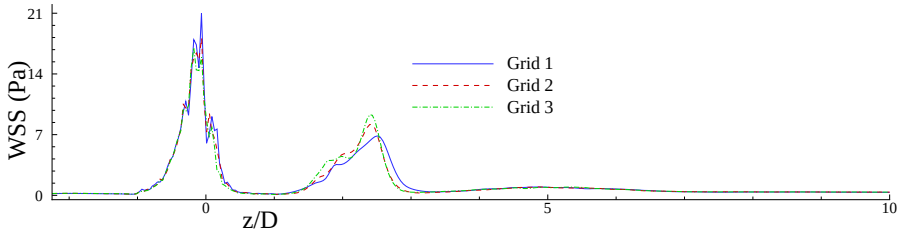

Figure 6.3: Grid resolution study for phase-averaged axial wall shear stress (Pa) in non-spiral blood flow during phase $P3$ while $Re = 876$. Phase averaging was done on the circumferential average WSS.

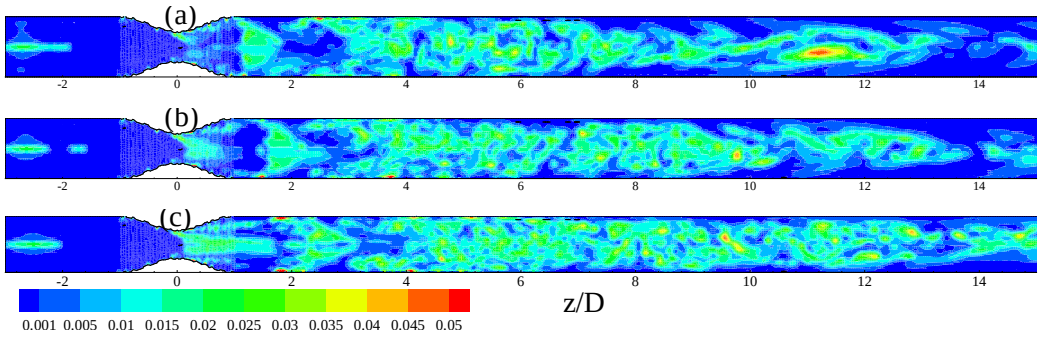

Figure 6.4: Dynamic Smagorinsky constant, C_s, in non-spiral blood flow during phase $P3$ for (a) $Re = 438$ and (b) $Re = 584$ and (c) $Re = 876$.

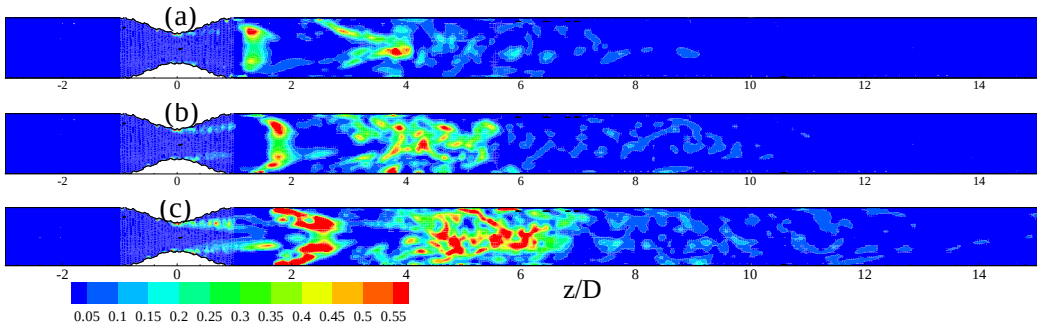

Figure 6.5: Normalised SGS eddy viscosity, μ_{sgs}/μ, in non-spiral blood flow during phase $P3$ for (a) $Re = 438$ and (b) $Re = 584$ and (c) $Re = 876$.

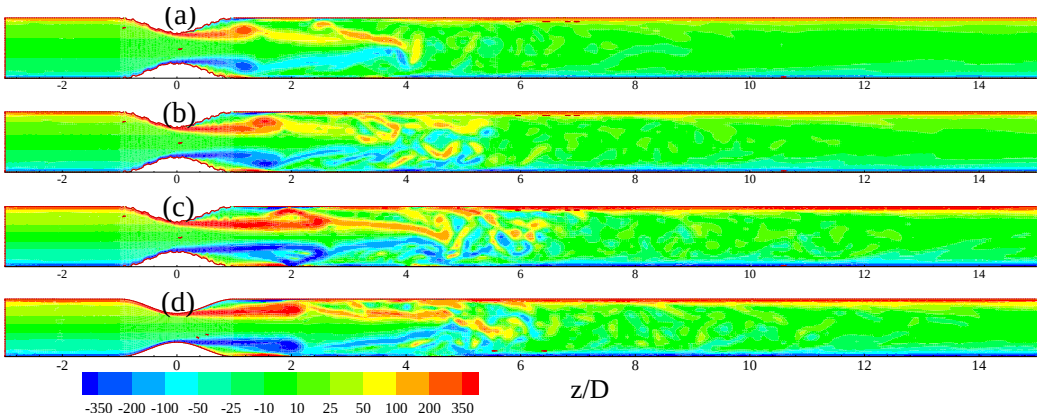

Figure 6.6: Instantaneous y-vorticity, Ω_y (1/s), in non-spiral flow during phase $P3$ for (a) $Re = 438$, (b) $Re = 584$ and (c) $Re = 876$. The corresponding Ω_y in non-spiral flow through the regular stenosis for $Re = 876$ is also appended in frame (d).

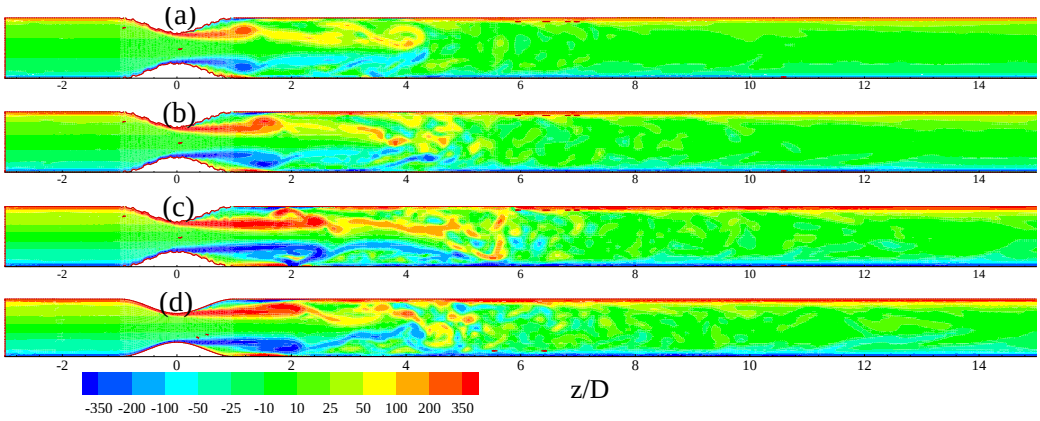

Figure 6.7: Instantaneous y-vorticity, Ω_y (1/s), in spiral flow during phase $P3$ for (a) $Re = 438$, (b) $Re = 584$ and (c) $Re = 876$. The corresponding Ω_y in spiral flow through the regular stenosis for $Re = 876$ is also appended in frame (d).

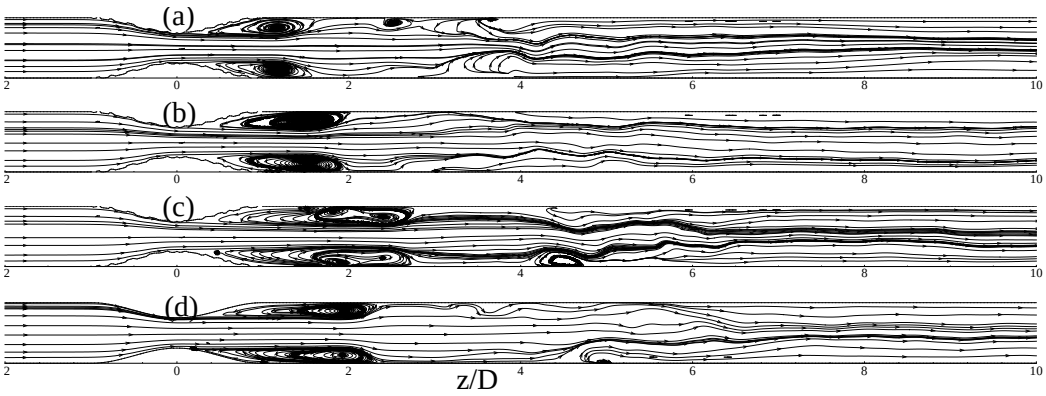

Figure 6.8: Instantaneous mid-plane streamlines in non-spiral blood flow during phase $P3$ for (a) $Re = 438$, (b) $Re = 584$ and (c) $Re = 876$. Note that the corresponding streamlines in non-spiral flow through the regular cosine-type stenosis for $Re = 876$ are also appended in frame (d).

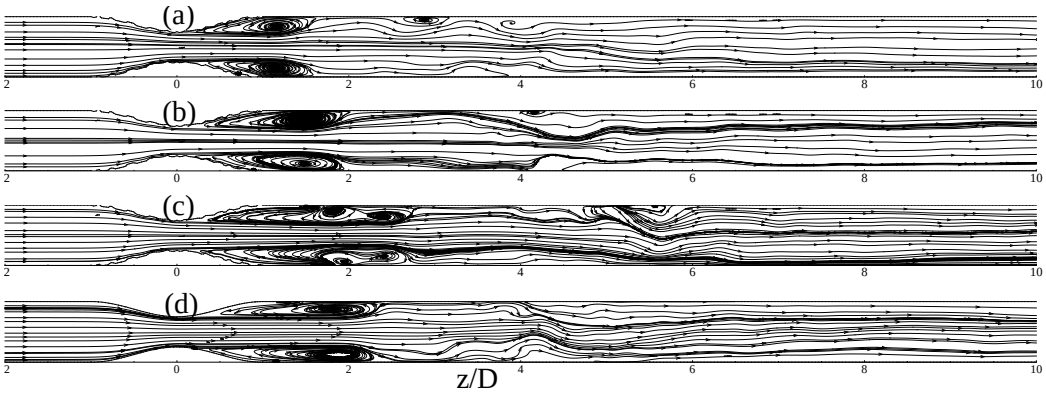

Figure 6.9: Instantaneous mid-plane streamlines in spiral blood flow during phase $P3$ for (a) $Re = 438$, (b) $Re = 584$ and (c) $Re = 876$. The corresponding streamlines in spiral flow through the regular stenosis for $Re = 876$ are also appended in frame (d).

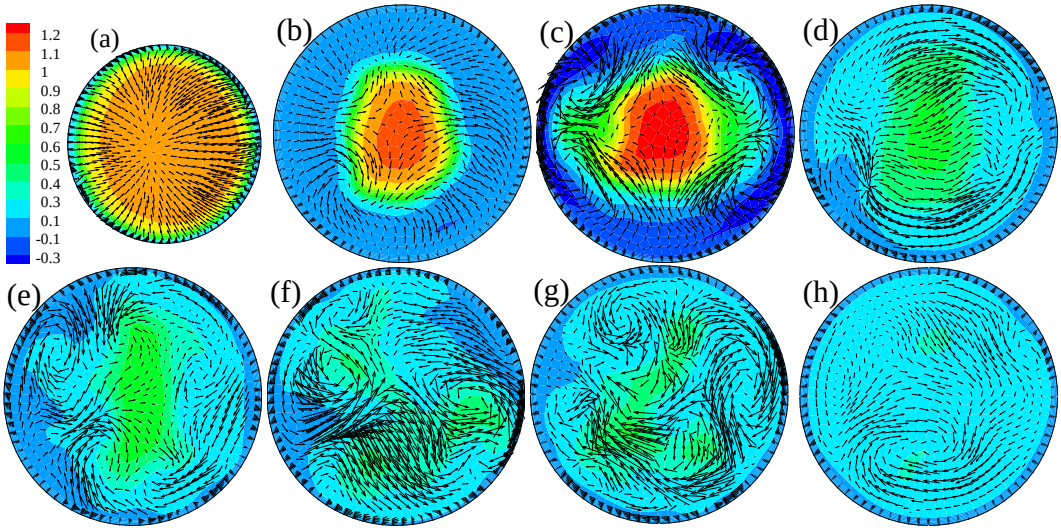

Figure 6.10: Instantaneous cross-sectional vectors appended on the contours of the streamwise velocity, $\bar{w}$, in non-spiral flow during phase $P3$ at (a) $z/D = 0$, (b) $z/D = 1$, (c) $z/D = 2$, (d) $z/D = 3$, (e) $z/D = 4$, (f) $z/D = 5$, (g) $z/D = 6$ and (h) $z/D = 8$ while $Re = 876$.

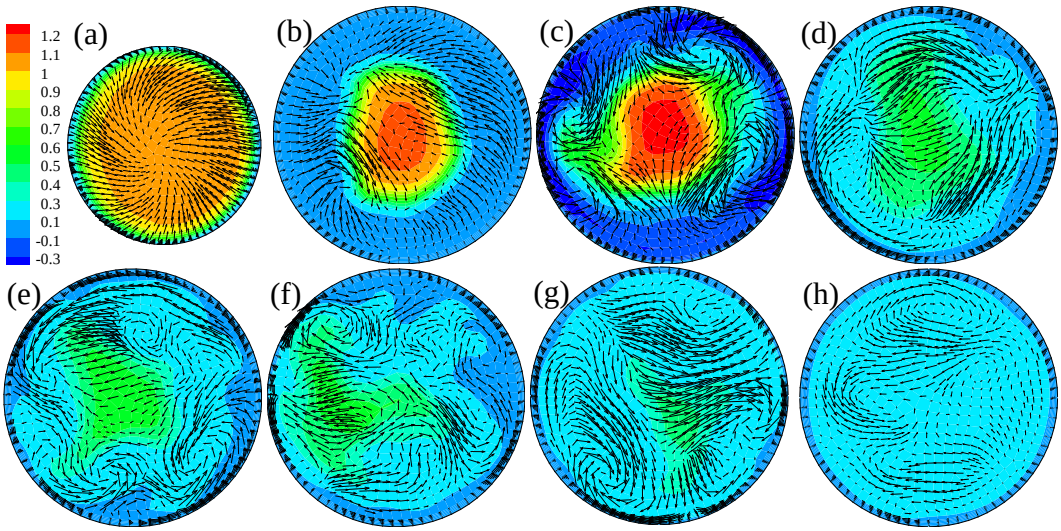

Figure 6.11: Instantaneous cross-sectional vectors appended on the contours of the streamwise velocity, $\bar{w}$, in spiral flow during phase $P3$ at (a) $z/D = 0$, (b) $z/D = 1$, (c) $z/D = 2$, (d) $z/D = 3$, (e) $z/D = 4$, (f) $z/D = 5$, (g) $z/D = 6$ and (h) $z/D = 8$ while $Re = 876$.

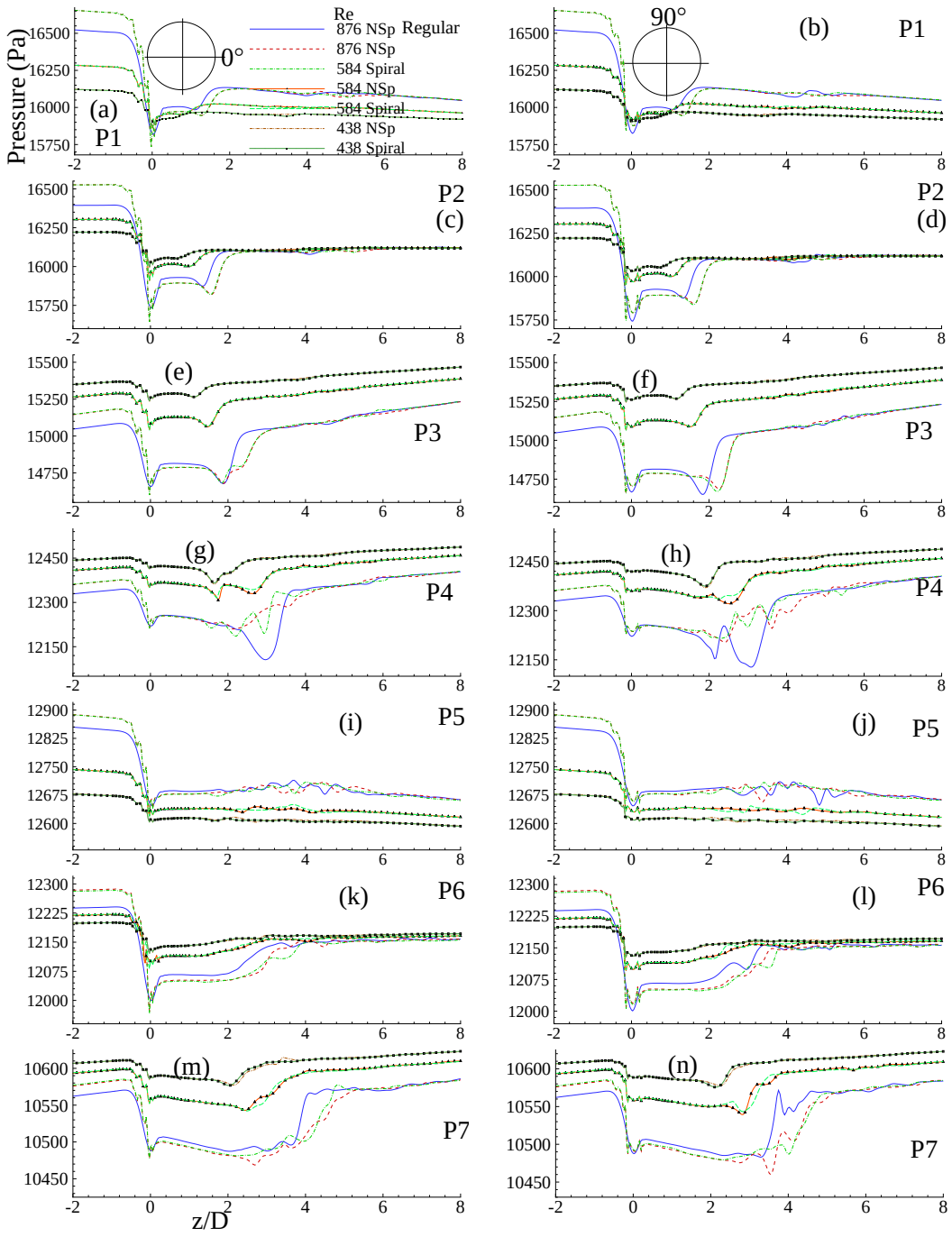

Figure 6.12: Instantaneous wall pressure, $\bar{p}$ (Pa), in both non-spiral (NSp) and spiral flow for the different Reynolds numbers, namely $Re = 438$, 584 and 876, during different phases of the last cycle at the two indicated circumferential locations. Note that the corresponding wall pressures for $Re = 876$ in non-spiral flow through the regular stenosis are also appended.

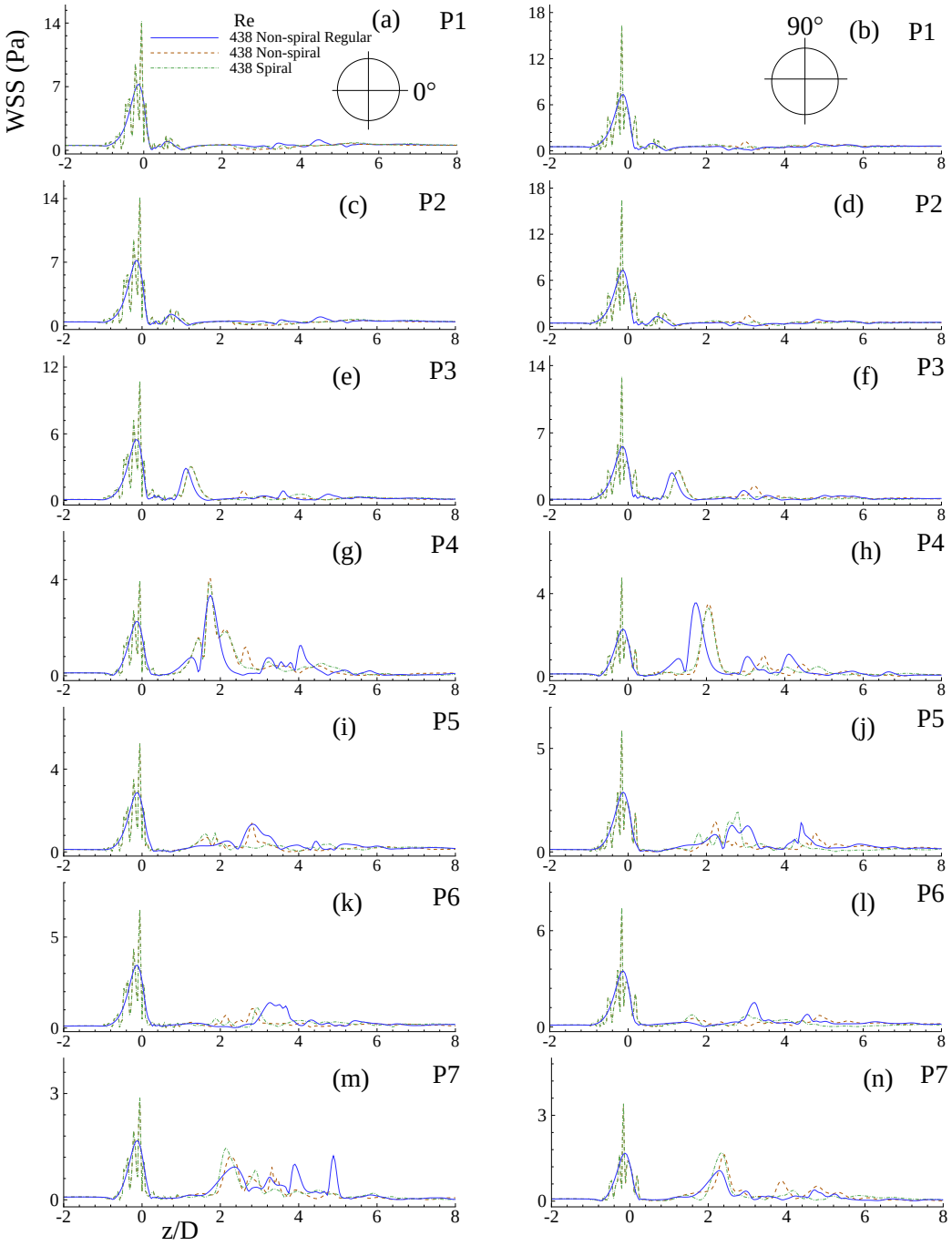

Figure 6.13: Instantaneous wall shear stress (Pa) for $Re = 438$ in both non-spiral and spiral flow during different phases of the last cycle at the two indicated circumferential locations. Note that the corresponding wall shear stresses for $Re = 438$ in non-spiral flow through the regular stenosis are also appended.

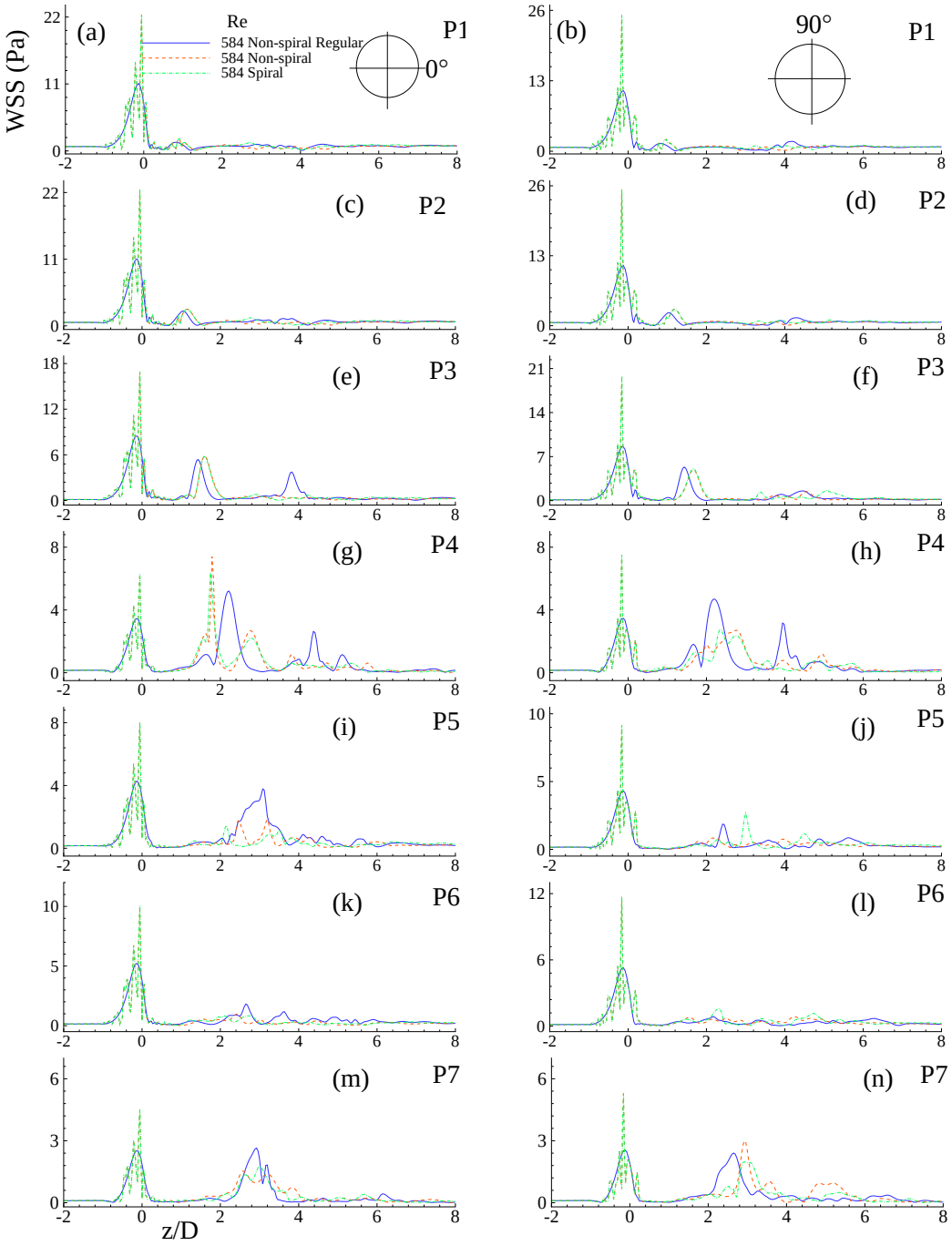

Figure 6.14: Instantaneous wall shear stress (Pa) for $Re = 584$ in both non-spiral and spiral flow during different phases of the last cycle at the two indicated circumferential locations. The corresponding wall shear stresses for $Re = 584$ in non-spiral flow through the regular stenosis are also appended.

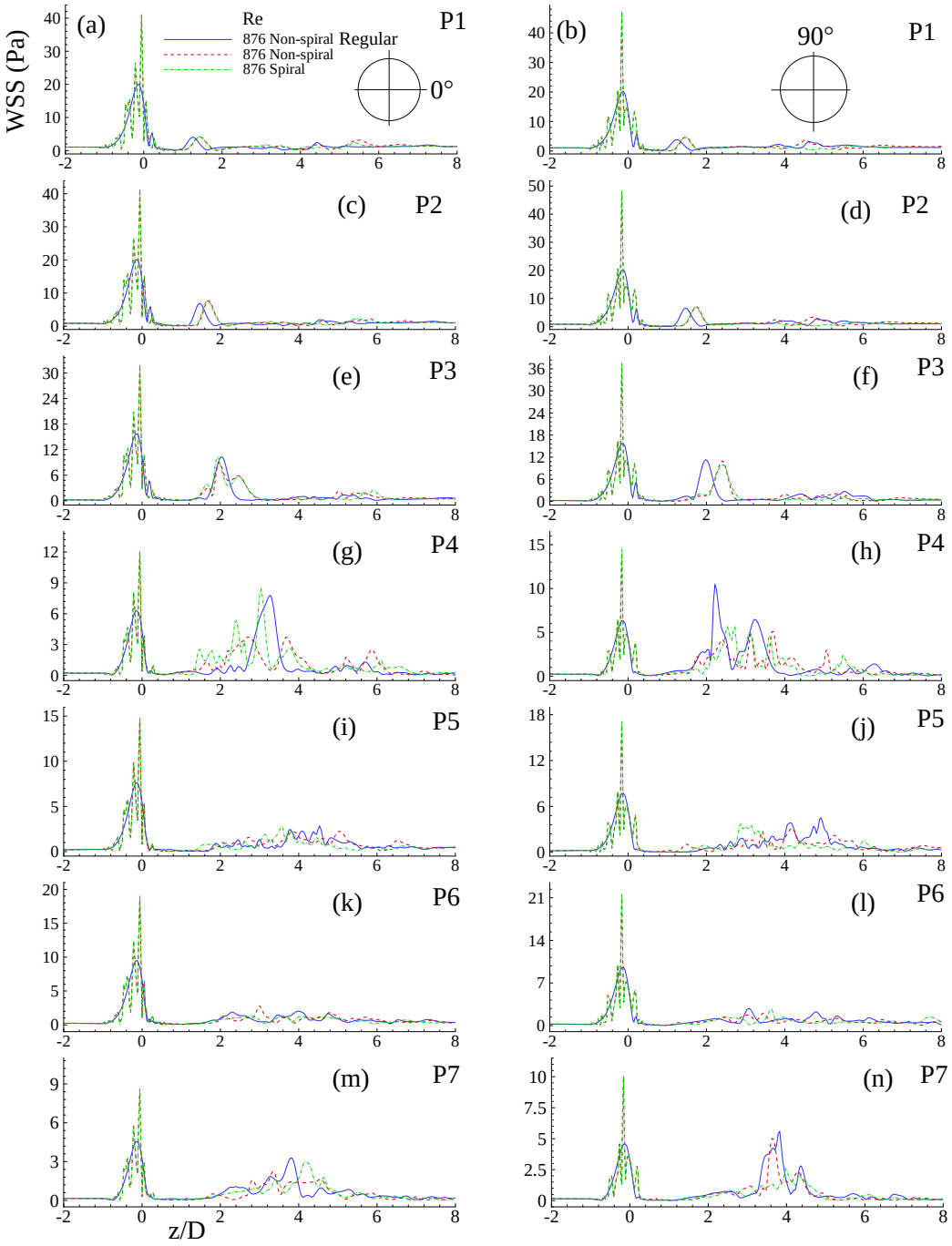

Figure 6.15: Instantaneous wall shear stress (Pa) for $Re = 876$ in both non-spiral and spiral flow during different phases of the last cycle at the two indicated circumferential locations. The corresponding wall shear stresses for $Re = 876$ in non-spiral flow through the regular stenosis are also appended.

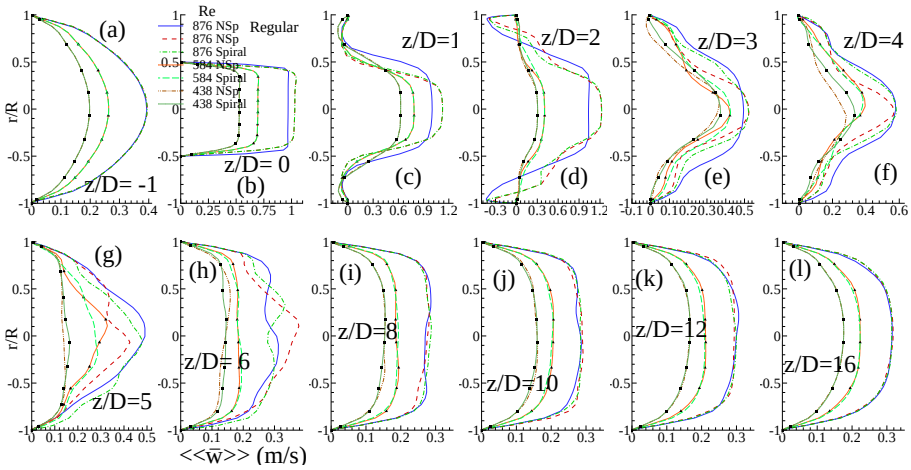

Figure 6.16: Phase-averaged streamwise velocity, $\langle\langle\bar{w}\rangle\rangle$ (m/s), in both non-spiral (NSp) and spiral flow for the different Reynolds numbers, namely $Re = 438$, 584 and 876, during phase $P3$ at different axial locations. Note that the corresponding $\langle\langle\bar{w}\rangle\rangle$ in non-spiral flow through the regular stenosis for $Re = 876$ are also appended.

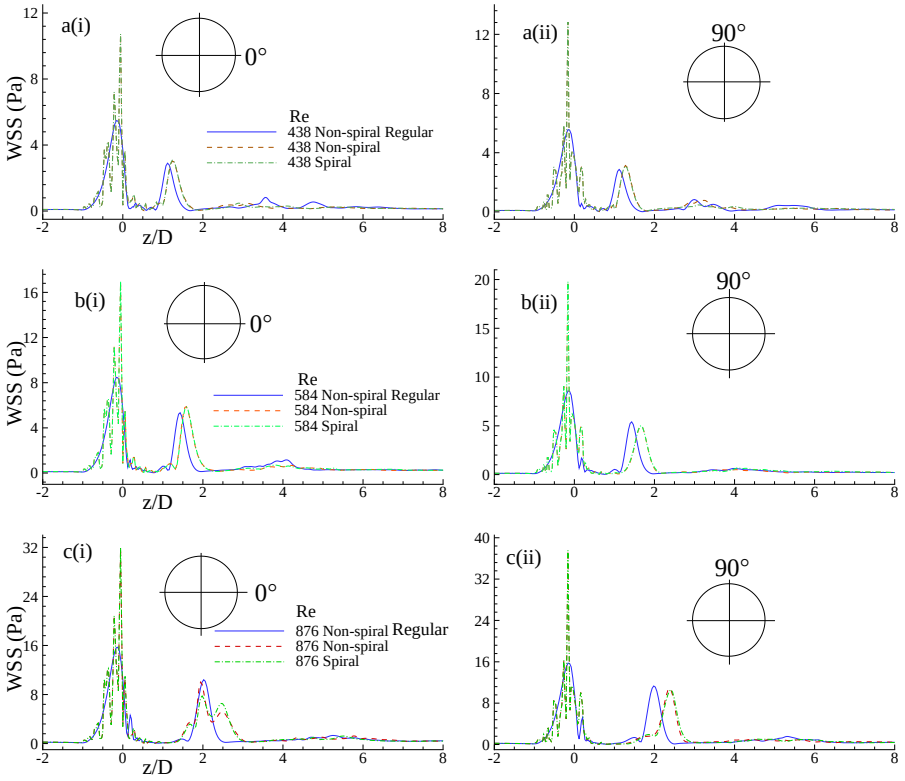

Figure 6.17: Phase-averaged wall shear stress (Pa) in both non-spiral and spiral flow during phase $P3$ at the two indicated circumferential locations for (a) $Re = 438$, (b) $Re = 584$ and (c)$Re = 876$. Note that the corresponding wall shear stresses in non-spiral flow through the regular stenosis for $Re = 438$, 584 and 876 are also appended in frame (a), (b) and c respectively.

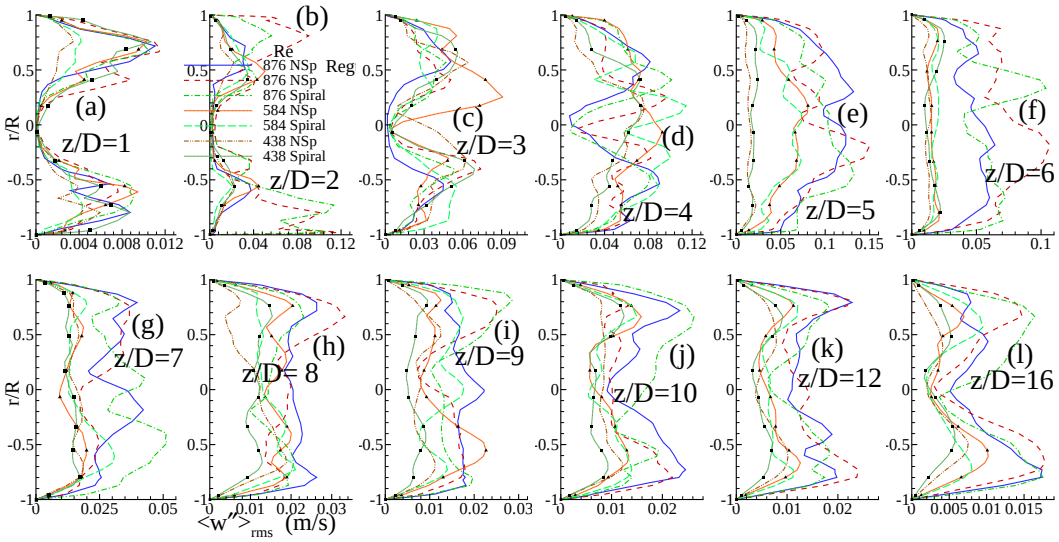

Figure 6.18: rms of the streamwise velocity fluctuations, $\langle w'' \rangle_{rms}$ (m/s), in both non-spiral (NSp) and spiral flow for the different Reynolds numbers, namely $Re = 438$, 584 and 876, during phase $P3$ at different axial locations. Note that the corresponding $\langle w'' \rangle_{rms}$ for $Re = 876$ in non-spiral flow through the regular stenosis are also appended.

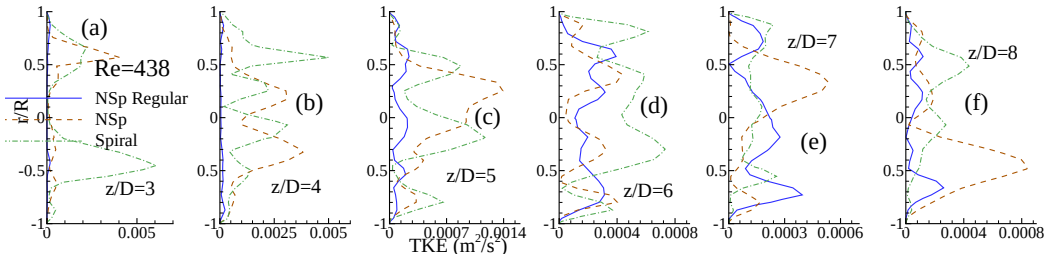

Figure 6.19: Turbulent kinetic energy, $\frac{1}{2}\langle u_j'' u_j'' \rangle$ (m^2/s^2), for Reynolds number $Re = 438$ in both non-spiral (NSp) and spiral flow during phase $P3$ at different axial locations. The corresponding $\frac{1}{2}\langle u_j'' u_j'' \rangle$ in non-spiral flow through the regular stenosis for $Re = 438$ are also appended.

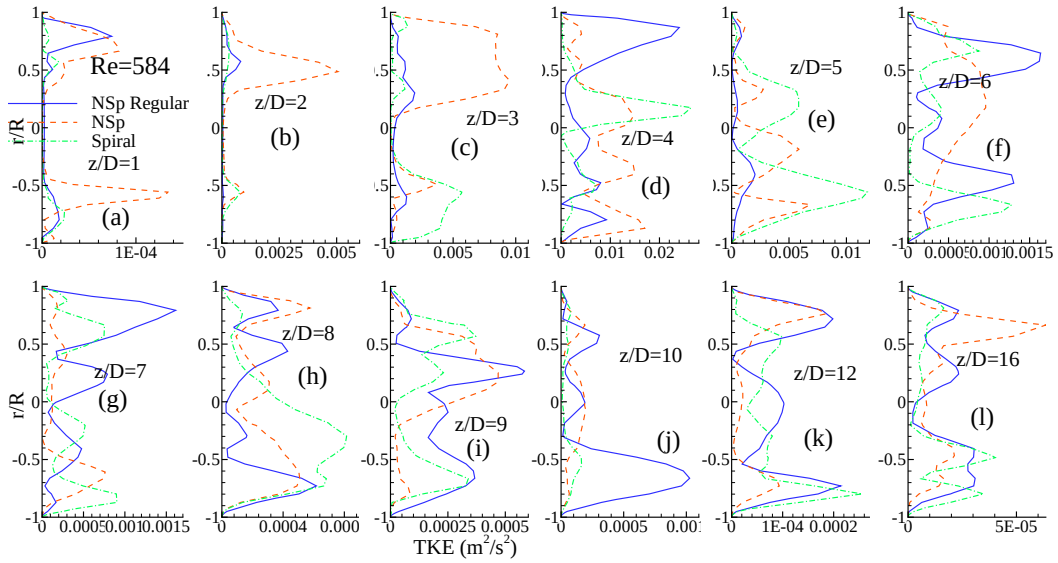

Figure 6.20: Turbulent kinetic energy, $\frac{1}{2}\langle u_j'' u_j'' \rangle$ (m^2/s^2), for Reynolds number $Re = 584$ in both non-spiral (NSp) and spiral flow during phase $P3$ at different axial locations. The corresponding $\frac{1}{2}\langle u_j'' u_j'' \rangle$ in non-spiral flow through the regular stenosis for $Re = 584$ are also appended.

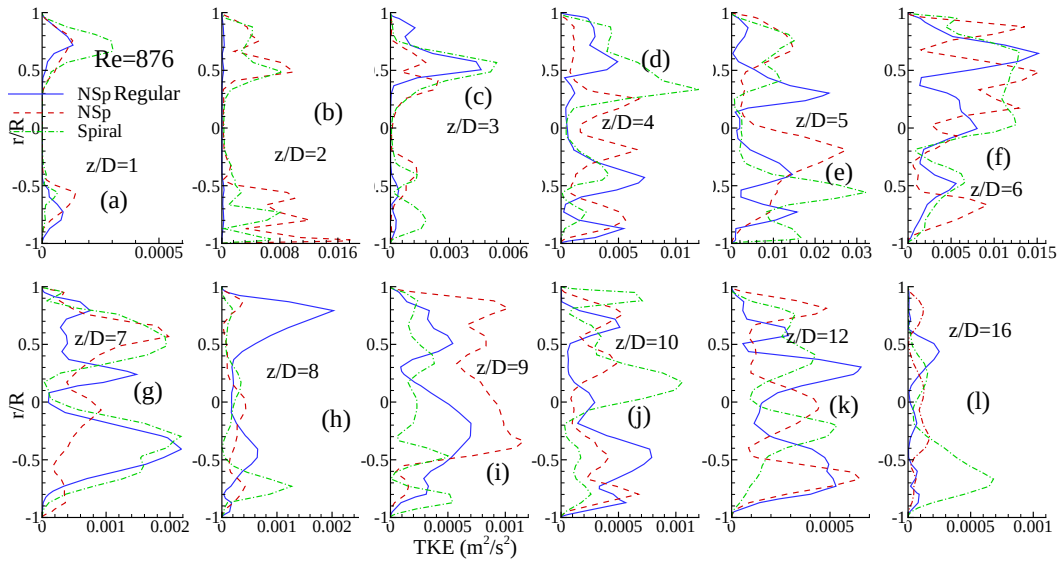

Figure 6.21: Turbulent kinetic energy, $\frac{1}{2}\langle u_j'' u_j'' \rangle$ (m^2/s^2), for Reynolds number $Re = 876$ in both non-spiral (NSp) and spiral flow during phase $P3$ at different axial locations. The corresponding $\frac{1}{2}\langle u_j'' u_j'' \rangle$ in non-spiral flow through the regular stenosis for $Re = 876$ are also appended.

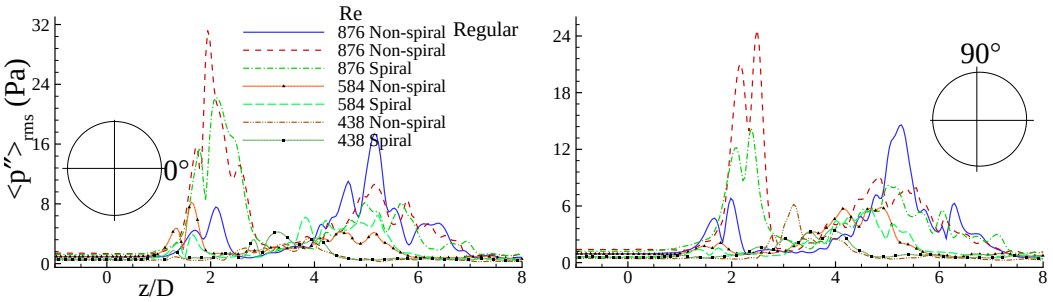

Figure 6.22: rms of wall pressure fluctuations, $\langle p'' \rangle_{rms}$ (Pa), in both non-spiral and spiral flow for the different Reynolds numbers, namely $Re = 438$, 584 and 876, during phase $P3$ at the two indicated circumferential locations. The corresponding $\langle p'' \rangle_{rms}$ for $Re = 876$ in non-spiral flow through the regular stenosis are also appended.

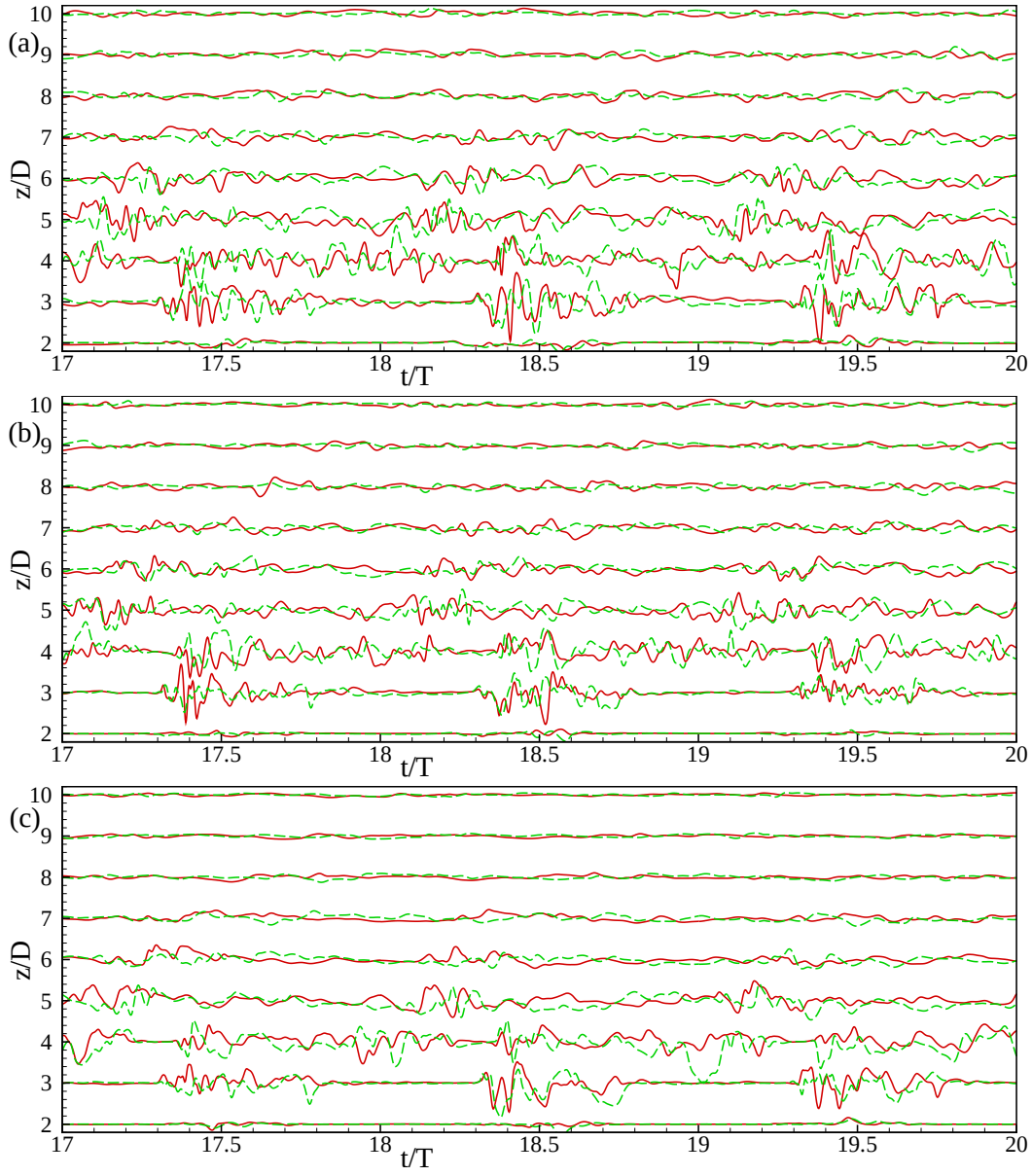

Figure 6.23: Time history of the centreline velocity fluctuations, (a) u''/u''_{max}, (b) v''/v''_{max} and (c) w''/w''_{max} at different axial locations for both non-spiral and spiral pulsatile blood flow while $Re = 876$. The red coloured solid line denotes velocity fluctuations for non-spiral flow while the green coloured dashed line corresponds to velocity fluctuations for spiral flow.

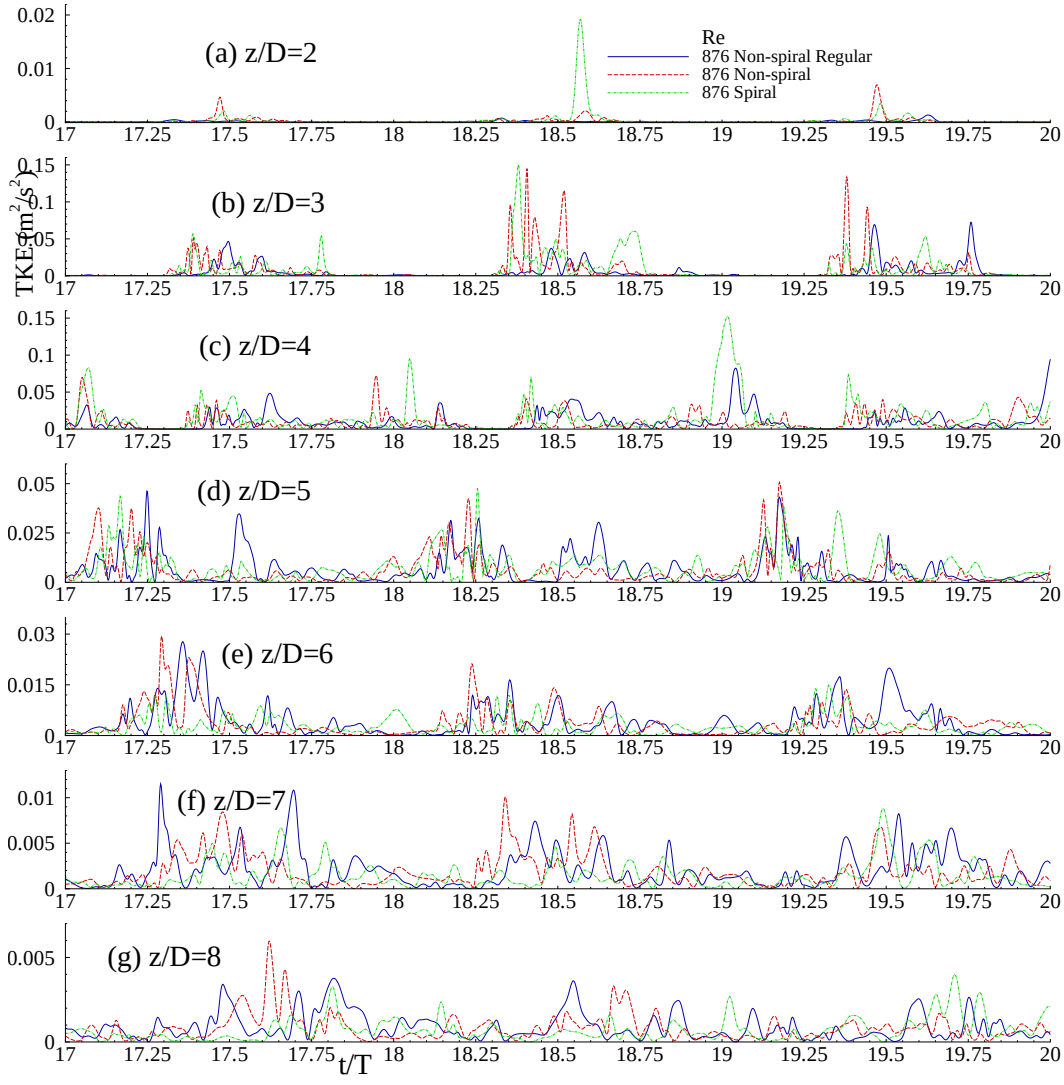

Figure 6.24: Time history of centreline turbulent kinetic energy (TKE), $\frac{1}{2}\langle u_j'' u_j'' \rangle$ (m^2/s^2), at different indicated axial locations for both non-spiral (red coloured dashed line) and spiral (green coloured dash-dot-dot line) pulsatile blood flow while $Re = 876$. Note that the corresponding $\frac{1}{2}\langle u_j'' u_j'' \rangle$ for $Re = 876$ in non-spiral flow through the regular stenosis (blue coloured solid line) are also appended.

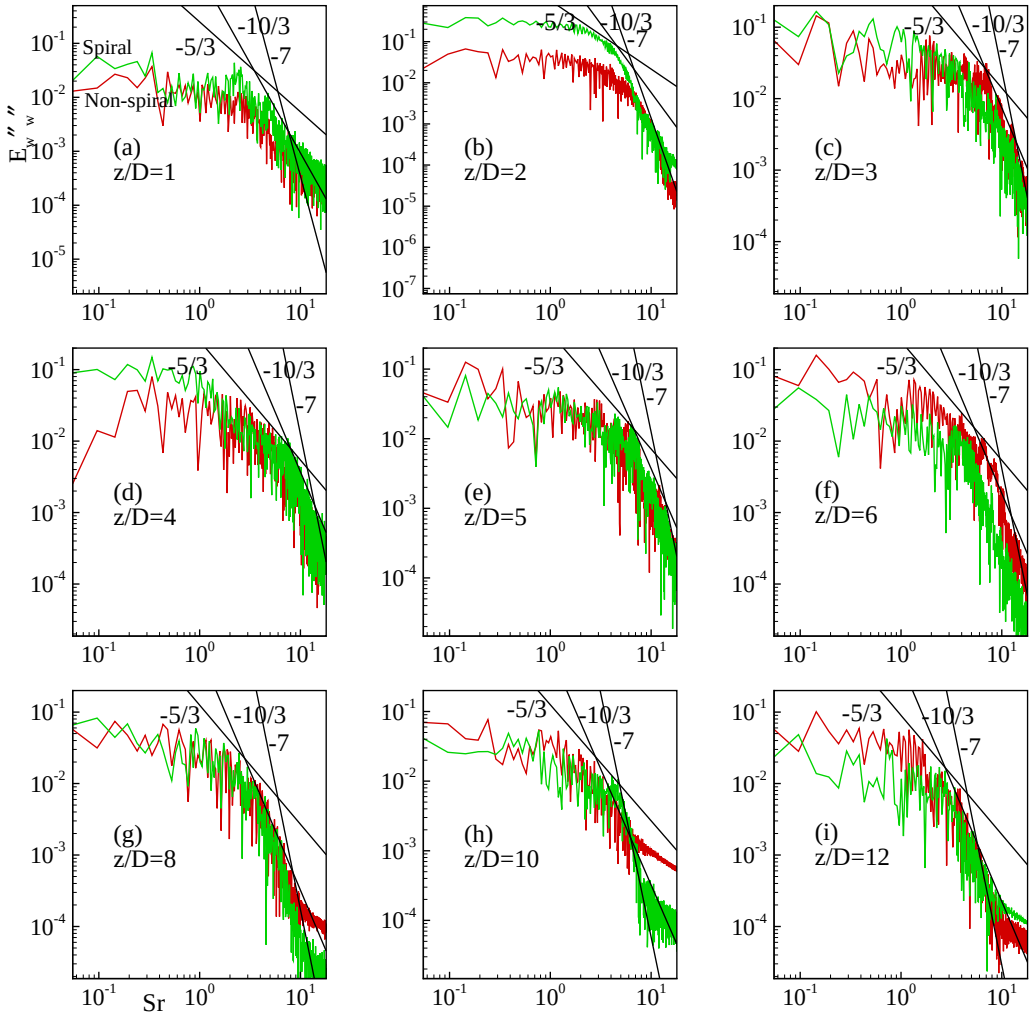

Figure 6.25: Energy spectra of centreline streamwise velocity fluctuations, w'', at different axial locations normalised by centreline $\langle w'' \rangle_{rms}$ at the same locations, for both non-spiral and spiral pulsatile flow while $Re = 876$. The red and the green coloured lines correspond to the energy spectra of velocity fluctuations for non-spiral and spiral flow, respectively.

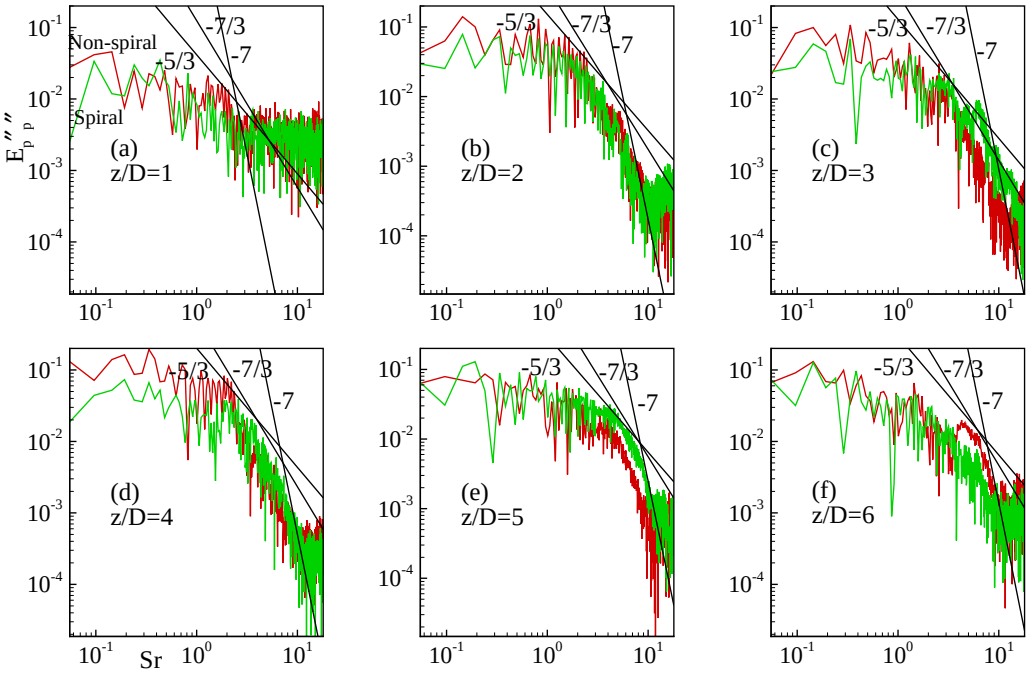

Figure 6.26: Energy spectra of wall pressure fluctuations, p'', at different axial locations normalised by wall $\langle p'' \rangle_{rms}$ at the same locations, for both non-spiral and spiral pulsatile flow while $Re = 876$. The red and the green coloured line corresponds to the energy spectra of wall pressure fluctuations for non-spiral and spiral flow, respectively.

Chapter 7

Physiological Pulsatile Non-spiral and Spiral Flow in a Model of a Stenosis with an Adjacent Aneurysm in Basilar Artery

7.1 Introduction

Atherosclerotic artery rarely has both stenosis and aneurysm in the same arterial segment. Until recently no reports on intracranial stenoses associated with adjacent aneurysms have been found (In et al. [13]). In et al. [13] reported the existence of a severe stenosis with an adjacent (pre-stenotic 'saccular' or post-stenotic 'fusiform') aneurysm in basilar artery. They defined a 'saccular' aneurysm as an aneurysm which has a smooth berry-shaped body and a neck and an 'atherosclerotic fusiform' aneurysm as an aneurysm having a dilated arterial segment without definite neck formation. Aneurysm has the potential for rupture of the vessel wall, which may lead to haemorrhage, complications to local organ function, and even death as aneurysm ruptures have high mortality and morbidity rates (Kassell et al. [139]). Hence, like severe stenosis, aneurysm could prove fatal if left without taking any therapeutic measures. When both stenosis and aneurysm exist in the same arterial segment, it would pose more danger to the patient than the existence of either of them in an artery. Therefore, it would really be interesting to study blood flow through a model of an arterial stenosis with an adjacent (post-stenotic) aneurysm in the same arterial segment as no studies (laminar or turbulence) have

been done on it, to the best of the author's knowledge.

In this Chapter, mainly Large Eddy Simulation (LES) with the Smagorinsky-Lilly dynamic subgrid model (Germano [115], Lilly [116] and Kim [123]) was applied to study physiological pulsatile non-spiral and spiral blood flow through a three-dimensional model of an irregular stenosis with an adjacent post-stenotic fusiform irregular aneurysm in basilar artery. The stenosis and the aneurysm were of 75% area reduction and 126% area enlargement, respectively, at their centres. The cross-sections of both cosine-type stenosis and aneurysm were shifted randomly to either x or y-direction to form irregular shape of them. Two-equation k-ω Transitional model was also applied to pulsatile non-spiral flow for the highest Reynolds number investigated. As described in Chapter 5, the first four harmonics of the physiological pulsatile flow and pressure pulse were employed at the inlet and outlet, respectively, to generate pulsatile velocity profile at the inlet and pressure waveform at the outlet. To introduce spiral velocity at the inlet, one-sixth of physiological pulsatile bulk velocity was taken as tangential velocity at the inlet, as seen in Chapters 5 and 6. Moreover, to investigate the effect of the magnitude of spiral velocity, spiral velocity was increased by taking one-fourth of physiological pulsatile bulk velocity as tangential velocity at the inlet.

The numerical results are presented in terms of velocity, vectors, streamlines, wall pressure and shear stress distributions, turbulent kinetic energy, velocity and pressure fluctuations and the energy spectra of the centreline streamwise velocity fluctuations to investigate the transition-to-turbulence of pulsatile non-spiral and spiral blood flow in the downstream of the irregular stenosis with the adjacent post-stenotic irregular aneurysm.

7.2 Problem Formulation

7.2.1 Model Geometry and Mesh arrangement

Figure 7.1 depicts the geometry of the model of an arterial stenosis with an adjacent post-stenotic aneurysm of irregular shape with rigid wall which was developed by using GAMBIT 2.4 (Fluent Inc.). The existence of a severe stenosis with an adjacent (pre- or post-stenotic) aneurysm is commonly found in basilar and vertebral

artery (In et al. [13]). Our model resembles basilar artery as it is a straight tube like basilar artery. The *in vivo* study of Pico et al. [140] shows that the diameter of basilar artery varies between 2.6 mm and 35 mm and the mean diameter of it in 159 subjects is 8 mm. The diameter of the unaffected section of the model was, therefore, taken as $D = 8$ mm. As seen in the previous chapters, the stenosis is centred at $z = 0$ and of length $= 2D$. As for aneurysm length, Neofytou et al. [141] and Molla [90] took four times diameter of the model tube and four times height of the channel, respectively, as the aneurysm segment length. So the adjacent aneurysm is taken of length $= 4D$ and centred at $z = 3D$. The upstream and downstream lengths of the model from the stenosis centre are $3D$ and $15D$, respectively, giving a total length of the model $18D$.

First a cosine-type stenosis of 75% area reduction with an adjacent post-stenotic cosine-type aneurysm of 126% area enlargement corresponding to $\approx 50.33\%$ diameter dilation was developed using the following relation:

$$\frac{r_0(z)}{R} = \begin{cases} 1 - \frac{\delta_c^1}{2}\left(1 + \cos\frac{z\pi}{D}\right) & \text{if} \quad -D \le z \le D \\ 1 + \frac{\delta_c^2}{2}\left(1 + \cos\frac{(z-3D)\pi}{2D}\right) & \text{if} \quad D \le z \le 5D \\ 1 & \text{elsewhere} \end{cases} \tag{7.1}$$

where r_0 and R are the cross-sectional radius and radius of the unaffected section of the model, respectively. Here δ_c^1 and δ_c^2 are the parameters that control the percentage of the area reduction in the stenosis and the area enlargement in the aneurysm, respectively. The values of δ_c^1 and δ_c^2 were fixed at 0.5 and $\sqrt{2} - 1$, respectively, to obtain a 75% reduction and 126% enlargement of the cross-sectional area at the centres of the stenosis and aneurysm, respectively. And then the cross-sections of both the stenosis and the aneurysm were shifted maximum 0.25 mm randomly to either x or y-direction (positive or negative) to get the irregular shape. It is to note that In et al. [13] defined aneurysm as an artery diameter greater than 1.5 times that of the adjacent normal lumen, which corresponds to greater than 125% area enlargement. As in previous chapters, a boundary layer was applied to the inside of the wall to get fine resolution in the sublayer; and the finest grid resolution was also ensured in the region from the centre of the stenosis to the immediate downstream region of the aneurysm.

7.2.2 Boundary Conditions

The equations for the inlet and outlet boundary conditions were described in § 5.2.1 of Chapter 5. The values of the angular frequency, η, density, ρ, and dynamic viscosity, μ, remain same as they were in Chapters 5 and 6. However, the Womersley number, $\alpha = R\sqrt{\frac{\rho\eta}{\mu}}$, becomes 6.92 as $R = 0.004$ in this chapter. The Reynolds numbers investigated, based on the diameter of the unaffected section of the tube, D, and steady inlet bulk velocity, $\bar{V}$, were $Re = 366$ and 440 with peak Reynolds numbers, $Re_{pk} \approx 1000$ and 1200, respectively, corresponding to a value of $A = 0.40$ in Equation (5.12). Note that the two-equation k-ω Transitional model was applied to non-spiral flow for Reynolds number $Re = 440$ only. To assess the effect of the magnitude of the spiral velocity, the spiral velocity was increased for $Re = 440$ by increasing the value of the control parameter for spiral velocity, C, in Equation (5.16) from $\frac{1}{6}$ to $\frac{1}{4}$. The inlet velocity profiles at different positions and phases and the outlet pressure profile are presented in Figures 7.2(a-d) and 7.3, respectively. The phases in the pulsatile cycle at which the results were obtained are indicated in Figure 7.2(a).

7.3 Results and Discussion

As in previous chapters, the time-step, δt, for all the computations in this chapter was also fixed at 10^{-3}. The simulations were performed for 20 pulsatile cycles; the last 12 cycles were used for phase-averaged statistics while the initial eight cycles were set aside for the flow development. A grid resolution study was done only in non-spiral flow and the chosen grid was deemed sufficient for both non-spiral and spiral flow.

7.3.1 Grid Resolution Study

Three grid arrangements, namely Grid 1, Grid 2 and Grid 3 were used in grid resolution study for $Re = 440$ in the non-spiral flow. Grid 1 has $\approx 500,000$ control volumes, whereas Grid 2 consists of $\approx 750,000$ control volumes, which is an increase of about 50% on Grid 1. Grid 3 is a further refinement of Grid 2 which has $\approx 1,350,000$ control volumes, i.e. a massive increase of about 80% on Grid 2.

Grid resolution results are shown in terms of phase-averaged streamwise velocity, $\langle\langle\bar{w}\rangle\rangle$ (m/s), at different axial positions and wall shear stress (Pa) during phase $P3$ in Figures 7.4 and 7.5, respectively. It is to note that the phase averaging of WSS in Figure 7.5 was done on the circumferential-averaged WSS. The agreement of the results for Grid 2 and Grid 3 are good indeed, considering the fact that LES results cannot be fully grid independent unless LES grid resolution becomes fine enough to be qualified for DNS (Mittal et al. [88]; Paul and Molla [93]). The resolution of Grid 2 appears to be adequate for resolving the transient flow in the model and it was, therefore, chosen for all the simulations in this chapter.

7.3.2 Contributions of the SGS Dynamic Model

The contour plots of the dynamic Smagorinsky constant, C_s, in non-spiral flow during phase $P3$ in the $z-x$ mid-plane for $Re = 366$ and 440 are depicted in Figure 7.6. The maximum value of C_s found in the downstream of the aneurysm which is ≈ 0.04. The locations of non-zero C_s inside the aneurysm and in the downstream region of the aneurysm increase with Reynolds number. Additionally, for both the Reynolds numbers, the value of C_s in the upstream of the stenosis is very small as the flow is laminar there.

Figure 7.7 presents the corresponding contour plots of the normalised SGS eddy viscosity, μ_{sgs}/μ. It is clear from the figure that the maximum contribution of the SGS dynamic model to the large scale motion for both the Reynolds numbers is $\approx 25\%$ and it is found in the downstream region of the aneurysm, where the flow is predicted to be turbulent. Like C_s, the non-zero μ_{sgs}/μ is found at more places for higher Reynolds number. The characteristics of C_s and μ_{sgs}/μ in spiral flow through the model are almost same as that in non-spiral flow.

7.3.3 Instantaneous Flow Field

The contour plots of the instantaneous streamwise velocity, $\bar{w}$ (m/s), in both non-spiral and spiral flow for $Re = 440$ during phase $P2$, i.e. peak inlet flow condition, are shown in Figure 7.8 . In both non-spiral and spiral flow, the flow reverses near the wall from the centre of the stenosis to the immediate downstream region of the aneurysm. The stenotic jet becomes weaker at around the post-lip of the aneurysm,

i.e. at $z \approx 5D$, and starts to break down; the flow appears to be very chaotic in the downstream region between $z \approx 5D$ and $z \approx 10D$. The effect of spiral flow on the instantaneous streamwise velocity during phase $P2$ is insignificant.

Figures 7.9(a-b) and 7.10(a-b) present the contour plots of the instantaneous streamwise velocity, $\bar{w}$ (m/s), in non-spiral and spiral flow, respectively, during phase $P3$ for $Re = 366$ and 440. Note that the corresponding results from non-spiral flow with k-ω Transitional model and increased spiral flow ($C = 1/4$) are also appended in Figures 7.9(c) and 7.10(c), respectively. As seen during phase $P2$ in Figure 7.8, during phase $P3$, the reverse flow near the wall occurs after the throat of the stenosis which is stretched up to the immediate downstream region of the aneurysm and the jet breaks down at $z \approx 5D$ in non-spiral and spiral flow for both the Reynolds numbers. The effects of Reynolds number on velocity magnitudes can be clearly seen from the figures; also the flow reattachment takes place by $z \approx 8D$ for $Re = 366$, whereas for Reynolds number $Re = 440$, it occurs in the further downstream region by $z \approx 10D$. It is interesting to note that in Figure 7.9, the velocity jet from k-ω Transitional model (frame c) is weaker than that from LES (frame b), though the streamwise velocity in k-ω Transitional model increases at some places in the region after $z = 8D$ compared with the corresponding LES results. As for the effects of spiral flow during phase $P3$, the magnitudes of the streamwise velocity in the downstream region, e.g. at $z = 6D$ for $Re = 366$ and at $z = 8D$ for $Re = 440$, decrease in spiral flows (7.10(a-b)) compared with those in non-spiral flows (7.9(a-b)). Moreover, when the magnitude of the spiral velocity is increased (7.10(c)), the jet in the region after $z = 6D$ becomes weaker and the magnitude of the streamwise velocity decreases compared with that in low spiral flow (7.10(b)).

Further information on the flow physics of non-spiral and spiral flow through the model can be obtained from cross-stream velocity vectors. Figures 7.11 and 7.12 depict the in-plane velocity vectors appended on the streamwise velocity, $\bar{w}$ (m/s), contours at different axial locations in non-spiral and spiral flow, respectively, during phase $P3$ for $Re = 440$. In both non-spiral and spiral flow, the stenotic jet appears to be stable, i.e. the flow is laminar up to $z = 4D$ (frames a-e) and the streamwise velocity is maximum at $z = 4D$ (frame e); the jet breaks down at $z = 5D$ (frame f), causing the flow to become recirculating and transitional. The

flow reattachment occurs by $z = 10D$ (frame k) and relaminarisation process starts subsequently in both the flows. It should be noted that the spiral pattern of the flow in Figure 7.12 disappears after the post-lip of the stenosis (frame b) due to the occurrences of disturbances in the flow in the further downstream region.

The instantaneous mid-plane streamlines in non-spiral and spiral ($C = 1/6$) flow during phase $P2$ for $Re = 440$ are presented in Figure 7.13. In both non-spiral and spiral flow, extremely large primary recirculation regions are created near the wall after the throat of the stenosis which are stretched up to $z \approx 6D$ and occupy almost half of the diameter of the model due to the existence of reverse flow or adverse pressure gradient in this region. Secondary recirculation regions are also found between $z \approx 6D$ and $z \approx 7D$. The effect of spiral flow on the streamlines during this phase is invisible.

Figures 7.14(a-b) and 7.15(a-b) show the streamlines in non-spiral and spiral flow, respectively, during phase $P3$ for $Re = 366$ and 440. Note that the corresponding streamlines for $Re = 440$ in non-spiral flow with k-ω Transitional model and in increased spiral ($C = 1/4$) flow are also included in Figures 7.14(c) and 7.15(c), respectively. During phase $P3$, the recirculation regions in both non-spiral (7.14(b)) and spiral (7.15(b)) flow appear to be less severe than those during phase $P2$ (Figure 7.13), however, the recirculation regions during phase $P3$ increase compared with those during phase $P2$. The recirculation region also increases when the Reynolds number is increased. Along with primary and secondary recirculation regions, tertiary recirculation region is also observed for higher Reynolds number.

It is interesting to note that, the recirculation regions observed in k-ω Transitional model (7.14(c)) are larger than those in LES (7.14(b)). As k-ω model gives time-averaged results, we can, therefore, safely say that the recirculation regions in the above figures are permanent. During phase $P3$ in spiral flow (7.15(a-b)), the primary recirculation regions become weaker and the secondary and tertiary recirculation regions become stronger than those in non-spiral flow (7.15(a-b)) while the total length of the regions remain almost same in both the flows. Furthermore, when the spiral velocity is increased (7.15(c)), the secondary and tertiary recirculation regions increase, causing the total length of the recirculation regions to be larger than that in low spiral flow (7.15(b)). In the pathological context, these extremely large recirculation regions are very harmful as they increase the blood residence time with

potential risk of stroke; and also they may induce blood clot or thrombosis inside the aneurysm (Molla [90]; Rayz et al. [106]).

7.3.3.1 Instantaneous Wall Pressure

The instantaneous wall pressure, $\bar{p}$ (Pa), distributions at two circumferential locations (0° and 90°) of the wall in both non-spiral (NSp) and spiral flow during different phases of the last pulsatile cycle for $Re = 366$ and 440 are presented in Figure 7.16. The corresponding pressure results for $Re = 440$ in non-spiral flow with k-ω Transitional model and in high spiral ($C = 1/4$) flow are also appended in the figure. For all the cases of the flows during all the phases and circumferential locations, the wall pressure drops sharply at the throat of the stenosis as seen in Chapters 5 and 6. However, it rises a little immediately after the stenosis throat and continues steadily with almost the same value up to $z \approx 4D$, where it starts to rise as the magnitude of the streamwise velocity decreases gradually in the further downstream region; and the pressure regains its undisturbed value by $z \approx 8D$ eventually. The ridges found in the pressure profiles around the stenosis throat are due to the effect of the irregular shape of the stenosis.

Additionally, the wall pressure drop varies considerably with the circumferential location as a result of the irregular shape of the model stenosis and aneurysm, e.g. for $Re = 440$ in non-spiral flow, excess pressure drops of ≈ 30 Pa, ≈ 28 Pa and ≈ 24 Pa during phases $P1$, $P2$ and $P3$, respectively, are observed at at 0° circumferential location compared with the corresponding pressure drops at 90° circumferential location. The pressure drops, for all the cases of the flows, are maximum during phase $P1$ at 0° circumferential location as seen in Chapter 6. They are extremely large during first three phases, i.e. during $P1$, $P2$ and $P3$, compared with the corresponding results during other phases. The pressure drop rises significantly if the Reynolds number is increased, e.g. the maximum pressure drops at 0° circumferential location in non-spiral flow during phases $P1$, $P2$ and $P3$ for $Re = 366$ are ≈ 900 Pa, ≈ 854 Pa and ≈ 588 Pa, respectively, whereas for $Re = 440$, the corresponding maximum pressure drops during phases $P1$, $P2$ and $P3$ are ≈ 1280 Pa, ≈ 1231 Pa and ≈ 859 Pa, respectively.

It is clear from the figure that the effect of spiral flow on the maximum pressure drop is very insignificant, e.g. the maximum pressure drop in high spiral ($C =$

$1/4$) flow decreases by only $\approx 0.23\%$ compared with that in non-spiral flow and this decrease in the maximum pressure drop in low ($C = 1/6$) spiral flow is even less than that in high ($C = 1/4$) spiral flow. However, the effects of spiral flow on the wall pressure can be observed clearly in the region between $z \approx 4D$ and $z \approx 10D$ where the pressure is of oscillating form, especially during phases $P3$, $P4$ and $P7$. It is interesting to note that an excellent agreement is found between the k-ω pressure results and the corresponding LES results. As described in the previous chapters, these extremely large pressure drops have severe impacts on the pathophysiology of the artery, such as flow choking and rupture of the plaque cap (Wootton and Ku [6]; Li et al. [8]).

7.3.3.2 Instantaneous Wall Shear Stress

Figures 7.17 and 7.18 depict the instantaneous wall shear stress (WSS) in both non-spiral and spiral ($C = 1/6$) flow through the model at 0° and 90° circumferential locations of the wall during different phases of the last pulsatile cycle for $Re = 366$ and 440, respectively. The corresponding WSS results for $Re = 440$ in non-spiral flow with k-ω Transitional model and in high spiral ($C = 1/4$) flow are also appended in Figure 7.18. For all the cases of the flows during all the phases and circumferential locations, as seen in the previous chapter, the WSS begins to rise at the pre-lip of the stenosis and reaches its maximum value just before the stenosis throat; it then falls to its upstream value right after the stenosis throat and continues with slightly decreasing value up to $z \approx 3D$. The WSS takes on oscillating form after the centre of the aneurysm, which is prominent during phases $P3$ and $P4$ (frames e-h) in the region between $z \approx 4D$ and $z \approx 8D$. The sharp ridges in the WSS distributions found in the stenosis region and in the last half of the aneurysm and the discrepancy in the magnitudes of WSS at different circumferential locations, e.g. the maximum value of the WSS at 90° circumferential location is greater than that at 0° circumferential location, are due to the effects of the irregular shapes of the stenosis and aneurysm.

The maximum WSS around the throat of the stenosis increases with Reynolds number. For both the Reynolds numbers, the cycle maximum and minimum of the maximum WSS around the throat of the stenosis occur at 90° circumferential location during phase $P1$ and 0° circumferential location during phase $P7$, respec-

tively. For example, the cycle maximum of the maximum WSS around the throat of the stenosis in non-spiral flow for $Re = 440$ is ≈ 98 Pa (Figure 7.18(b)) and the corresponding cycle minimum of the maximum WSS for $Re = 366$ is ≈ 16 Pa (Figure 7.17(m)).

Furthermore, it is clear from the above two figures that the effects of spiral flow on the maximum WSS around the centre of the stenosis is very insignificant, e.g. the maximum WSS around the stenosis centre for $Re = 440$ at 90° circumferential location during phase $P1$ in high ($C = 1/4$) spiral flow rises by $\approx 0.14\%$ (Figure 7.18(b)) compared with the corresponding result in non-spiral flow and this increase in the maximum WSS in low ($C = 1/6$) spiral flow is even less than that in high ($C = 1/4$) spiral flow. However, as seen in the wall pressure distributions, the effects of spiral flow on the WSS can be seen distinctly in the oscillatory pattern of the WSS in the region between $z \approx 4D$ and $z \approx 8D$ during phases $P3$ and $P4$ (frames e-h). It should be pointed out that the overall agreement between the k-ω WSS results and the corresponding LES results are quite good indeed (Figure 7.18), though the maximum WSS with k-ω Transitional model increases by $\approx 2\%$ compared with the corresponding LES result (Figure 7.18(b)).

The clinical implications of high WSS, as discussed in the previous chapters, include overstimulation of platelet thrombosis leading to total occlusion of the vessel (Ku [3]; Folts et al. [38]), endothelial cells damage for high WSS $> 37.9 \pm 8.5$ (SD) Pa (Fry [36]), deformation of the red blood cells for Shear stress ≥ 10 Pa (Sutera and Mehrjardi [37]) and induced thrombosis for Shear stress > 7 Pa (Malek et al. [9]). Owing to the above discussion, it is clear from the above two figures that the maximum values of the WSS around the throat of the stenosis are above the harmful level for both the investigated Reynolds numbers during all the phases. Also the oscillatory WSS is responsible for arterial disease progression (Ku [3]; Paul and Molla [93]). Is is interesting to note that the WSS rises significantly in the region between $z \approx 4D$ (beginning of the last quarter of the aneurysm) and $z \approx 8D$ during phases $P3$ and $P4$ (frames e-h). Salsac [142] observed that high shear stress may activate platelets, which can be transported to the regions of low shear stresses inside the aneurysm wall where they would build up, initiating the formation of the endothelial thrombus. Lasheras [12] noted that high shear stress and other anomalous conditions resulting from the separated flow on the endothe-

lial activity accelerates the expansion process of the aneurysm and an endoluminal thrombus is developed early in the expansion process. This thrombus covers the aneurysm's wall and leads to the destruction of the endothelial layer by hypoxia – a pathological condition in which a region of the body does not get adequate oxygen supply.

7.3.4 Phase-averaged Flow Characteristics

Phase-averaged streamwise velocity and wall shear stresses during phase $P3$ are presented in this section. Figure 7.19 shows the phase-averaged streamwise velocity, $\langle\langle\bar{w}\rangle\rangle$ (m/s), during phase $P3$ in both non-spiral (NSp) and spiral ($C = 1/6$) flow at different axial locations for Reynolds numbers $Re = 366$ and 440. It is to note that the corresponding results for $Re = 440$ in non-spiral flow with k-ω Transitional model and in high ($C = 1/4$) spiral flow are also appended in the figure. At the pre-lip of the stenosis, i.e. at $z = -1D$ (frame a) , the velocity profile is parabolic in shape as the flow is laminar there. When the flow passes through the centre of the stenosis, the velocity profile becomes plug-shaped jet and the jet remains stable up to $z = 4D$ (frame f). The break down of the jet starts at the post-lip of the aneurysm, i.e. at $z = 5D$ (frame g) and the profiles tend toward uniformity in the region between $z = 5D$ and $z = 10D$ (frames g-k) where the flow transients to turbulence. In the further downstream region the relaminarisation process starts and the velocity profiles incline to their inlet character (frame l). The negative values of the streamwise velocity in the region between $z = 1D$ and $z = 7D$ (frames c-i) near the wall, which covers almost half of the diameter of the tube are due to adverse pressure gradient. The streamwise velocity increases significantly with Reynolds number. It is interesting to note that k-ω Transitional results do not agree with the corresponding LES results, especially in the turbulent region because k-ω model gives only time-averaged results instead of time-accurate results (Scotti and Piomelli [75]) as mentioned in Chapter 5. Furthermore, the effects of spiral flow becomes significant only after $z = 4D$ (frame f). The maximum value of the phase-averaged streamwise velocity near the centre of the tube decreases in the subsequent frames except in frame (l) (at $z = 12D$) when the spiral velocity is increased. However, at some places near the wall, the streamwise velocity increases

with spiral flow.

The corresponding wall shear stress at 0° and 90° circumferential locations are shown in Figure 7.20. The phase-averaged wall shear stresses during phase $P3$ for $Re = 366$ in Figure 7.20(a)(i-ii) and for $Re = 440$ in Figure 7.20(b)(i-ii) closely resemble the corresponding instantaneous WSS in Figure 7.17(e-f) and Figure 7.18(e-f), respectively. All the characteristics of the instantaneous WSS remain same in the phase-averaged WSS except the oscillatory pattern in the downstream region, which become less prominent in the phase-averaged WSS. Hence, as discussed in Chapters 5 and 6, the instantaneous WSS should be considered for accurate representation of WSS distributions.

7.3.5 Turbulent characteristics

The root mean square (rms) of the streamwise velocity fluctuations, $\langle w'' \rangle_{rms}$ (m/s), in non-spiral and spiral ($C = 1/6$ and $C = 1/4$) flow for $Re = 366$ and 440 during phase $P3$ at different axial locations are presented Figure 7.21. The corresponding rms velocity fluctuations in non-spiral flow for $Re = 440$ with k-ω Transitional model are also included in the figure. The rms of the streamwise velocity fluctuations at the pre-lip of the stenosis is almost zero; it increases with the axial distance and is extremely high in the region between $z = 4D$ and $z = 10D$ (frames f-l) where the flow transition-to-turbulence takes place. In the further downstream region, the magnitude of $\langle w'' \rangle_{rms}$ decreases again as the relaminarisation process starts after $z = 10D$. As seen in the phase-averaged streamwise velocity, the rms of velocity fluctuations with k-ω model do not agree with the corresponding LES results as only time-averaged results can be obtained from k-ω model. It is clear from the figure that the velocity fluctuations increase with Reynolds number. Additionally, the magnitude of $\langle w'' \rangle_{rms}$ in spiral flow increases significantly at some locations compared with the corresponding result in non-spiral flow. But the effects of high ($C = 1/4$) spiral flow on $\langle w'' \rangle_{rms}$ remain unclear as the magnitude of $\langle w'' \rangle_{rms}$ in low ($C = 1/6$) spiral flow rises at some places compared with the corresponding result in high ($C = 1/4$) spiral flow and the opposite happens at other places.

Further information on the transition-to-turbulence of non-spiral and spiral flow

can be obtained from the turbulent kinetic energy results. Figures 7.22 and 7.23 show the turbulent kinetic energy (TKE), $\frac{1}{2}\langle u_j'' u_j'' \rangle$ (m^2/s^2), in non-spiral and spiral ($C = 1/6$) flow during phase $P3$ at different axial locations for $Re = 366$ and 440, respectively. Note that the corresponding TKE for $Re = 440$ in non-spiral flow with k-ω Transitional model and in high ($C = 1/4$) spiral flow are also appended in Figure 7.23. The TKE behaves like $\langle w'' \rangle_{rms}$. That is the maximum TKE increases dramatically with Reynolds number. The disagreement between the k-ω and LES results show the unsuitability of k-ω model for simulating pulsatile flow as it gives only time-averaged results instead of time-accurate results (Scotti and Piomelli [75]), which was also discussed in Chapter 5. At most of the locations, the TKE in spiral flow rises sharply compared with that in non-spiral flow – similar findings were observed in the previous chapters. Moreover, it is clear from Figure 7.23 that the maximum TKE in high ($C = 1/4$) spiral flow occurs in the further downstream region of the aneurysm at $z = 8D$ with a slight ($\approx 5.8\%$) drop in its magnitude (frame j) compared with the maximum TKE in low ($C = 1/6$) spiral flow at $z = 7D$ (frame i). However, the TKE in high ($C = 1/4$) spiral flow generally increases compared with that in low ($C = 1/6$) spiral flow.

The rms of the wall pressure fluctuations, $\langle p'' \rangle_{rms}$ (Pa), in non-spiral and spiral ($C = 1/6$) flow during phase $P3$ at 0° and 90° circumferential locations of the wall for $Re = 366$ and 440 are presented in Figure 7.24. The corresponding $\langle p'' \rangle_{rms}$ results for $Re = 440$ in non-spiral flow with k-ω Transitional model and in high ($C = 1/4$) spiral flow are also appended in the figure. It is interesting to note that $\langle p'' \rangle_{rms}$ is strongly oscillating in the transition-to-turbulence region between $z \approx 4D$ and $z \approx 10D$. Like other results, the maximum $\langle p'' \rangle_{rms}$ increases with Reynolds number, but it occurs in the further downstream region of the aneurysm for high Reynolds number than that for low Reynolds number. As seen in the other turbulent results, the k-ω Transitional model $\langle p'' \rangle_{rms}$ results do not agree with the corresponding LES results. Unlike the maximum pressure drop, the maximum $\langle p'' \rangle_{rms}$ occurs at 90° circumferential location of the wall. Additionally, the maximum $\langle p'' \rangle_{rms}$ in spiral ($C = 1/6$) flow, which occurs at $z/D \approx 7.2$, rises by $\approx 117.2\%$ compared with that in non-spiral flow, which occurs in the further downstream region at $z/D \approx 7.7$. Like the maximum TKE, the magnitude of the maximum $\langle p'' \rangle_{rms}$ in high ($C = 1/4$) spiral flow falls by $\approx 5.8\%$ compared with

that in low ($C = 1/6$) spiral flow. The extreme pressure fluctuations are implicated in arterial murmurs in the presence of arterial stenosis (Ask et al. [135]), which was also discussed in Chapters 5 and 6.

7.3.5.1 Cycle-to-cycle variations

The cycle-to-cycle variations of the velocity fluctuations and the TKE would be presented in this section. Figure 7.25 illustrates cycle-to-cycle variations of the centreline cross-stream velocity fluctuations, u''/u''_{max} and v''/v''_{max}, and the centreline streamwise velocity fluctuations, w''/w''_{max}, at different axial positions in both non-spiral and spiral ($C = 1/6$) flow for $Re = 440$ over the last three cycles used for phase-averaged statistics. The centreline velocity fluctuations before $z = 4D$ are very small in magnitude and, therefore, are not shown in the figure. It can be observed from the figure that the centreline velocity fluctuations in both non-spiral and spiral flow are non-periodic and significantly large in the region within $5D \leq z \leq 10D$; the magnitudes of these centreline velocity fluctuations keep decreasing in the further downstream region of the aneurysm as the relaminarisation process starts. In addition, the effects of spiral flow on the centreline velocity fluctuations can be distinctly seen in the figure.

The cycle-to-cycle variations of the centreline TKE, $\frac{1}{2}\langle u''_j u''_j \rangle$ (m^2/s^2), at different axial locations in non-spiral and spiral (both high and low, i.e. $C = 1/4$ and $C = 1/6$) flow for $Re = 440$ are presented in Figure 7.26. It is clear from the figure that in the region between $4D \leq z \leq 7D$, the magnitudes of the centreline TKE are mostly significantly large during $0.2 \leq t/T \leq 0.6$ of the pulsatile cycle and zero during other phases of the cycle; however, in the further downstream region, they are generally very insignificant during $0.4 \leq t/T \leq 0.7$ of the pulsatile cycle. As seen in Chapters 5 and 6, the centreline TKE in spiral (both $C = 1/6$ and $C = 1/4$) flow increases significantly during some phases. Also the maximum value of the centreline TKE in spiral flow (frame e) is greater than that in non-spiral flow (frame f). Furthermore, the maximum TKE in high ($C = 1/4$) spiral flow during the last pulsatile cycle drops by $\approx 12.8\%$ compared with that in low ($C = 1/6$) spiral flow, whereas this drop is $\approx 33.3\%$ when the last three cycles are considered (frame e).

7.3.5.2 Turbulent Energy Spectra

Energy spectra, $E_{w''w''}$ of the normalised centreline streamwise velocity fluctuations, $(w''/\langle w'' \rangle_{rms})^2$, in both non-spiral (red coloured line) and spiral ($C = 1/6$) (green coloured line) flow at different axial positions for $Re = 440$ are depicted in Figure 7.27. As seen in Chapters 5 and 6, the lines of $(Sr)^{-5/3}$, $(Sr)^{-10/3}$ and $(Sr)^{-7}$ are also appended in the figure. At $z = 4D$, the inertial subrange region of $-5/3$ power slope is very small while the viscous dissipation range of -7 power slope is quite large. The velocity spectra changes from $-5/3$ power slope to $-10/3$ power slope at higher frequencies in the downstream region of $5D \leq z \leq 10D$ (frames b-g), giving a large range of frequencies for the inertial subrange region in the transition-to-turbulence region of the flow. In the further downstream region (frames h-i), the inertial subrange region becomes smaller again as the turbulence intensity decreases there. In addition, after $z = 5D$, the velocity spectra in spiral flow has slightly larger range of frequencies constituting the inertial subrange region than the velocity spectra in non-spiral flow; and also in the downstream region after $z = 8D$, the viscous dissipation region in the velocity spectra in non-spiral flow are almost absent.

7.4 Conclusion

Large Eddy Simulation with the Smagorinsky-Lilly dynamic subgrid model (Germano [115], Lilly [116] and Kim [123]) and k-ω Transitional model were employed to investigate the physiological non-spiral and (both low and high) spiral blood flow through a three-dimensional model of an irregular stenosis with an adjacent post-stenotic fusiform irregular aneurysm in basilar artery for $Re = 366$ and 440. In this chapter, the maximum contribution from the SGS model is $\approx 25\%$ in both non-spiral and spiral flow, which is smaller than those in Chapters 5 and 6. The effects of Reynolds number on all the flow results are observed, e.g. the recirculation regions, the maximum pressure drop and the maximum WSS around the throat of the stenosis, the TKE, etc. increase with Reynolds number. As seen in Chapter 5, the turbulent results obtained from the k-ω Transitional model do not agree with the corresponding LES results, though other results such as wall pressure and shear

stress from the k-ω Transitional model agree quite well with the corresponding LES results – this shows unsuitability of k-ω model for pulsatile flow simulation.

In both non-spiral and spiral flow, large permanent recirculation regions are generated right after the throat of the stenosis which are stretched beyond the aneurysm. The length of the recirculation regions increases when the spiral velocity is increased. During all the phases in both non-spiral and spiral flow, the wall pressure drops significantly at the throat of the stenosis and does not rise to get its undisturbed value before the last quarter of the aneurysm, i.e. $z = 4D$. The maximum pressure drop in non-spiral flow for $Re = 440$ is 1280 Pa, which occurs during phase $P1$ at 0° circumferential location of the wall. The effect of (both low and high) spiral flow on the pressure drop is very insignificant; the spiral effects on the wall pressure can only be seen in the downstream region after $z = 4D$ where the pressure takes oscillatory form. In both non-spiral and spiral flow, the maximum value of the WSS, which is found around the throat of the stenosis, reaches clinically dangerous level during all the phases of the pulsatile cycle for both the Reynolds numbers. The cycle maximum WSS in both non-spiral and spiral flow occurs during phase $P1$ at 90° circumferential location of the wall, which is 98 Pa in non-spiral flow for $Re = 440$. As seen in the wall pressure, the effects of spiral flow on the WSS are visible only in the oscillatory pattern of the WSS in the downstream region after $z \approx 4D$.

In both non-spiral and spiral flow, the transition-to-turbulence of the flow occurs in the downstream region between $z \approx 4D$ and $10D$, i.e. the transition starts in the last quarter of the aneurysm, not in the immediate downstream region of the stenosis as seen in the previous chapters. The TKE is large in this region and it fades away in the further downstream region as the relaminarisation process starts there. Due to the influence of spiral flow, the TKE in spiral flow increases significantly compared with that in non-spiral flow. However, the maximum value of the TKE in high spiral flow drops considerably compared with that in low spiral flow.

Furthermore, the velocity spectra in the transition-to-turbulence region in both non-spiral and spiral flow have large range of frequencies making up the inertial subrange region. The inertial subrange regions in spiral flow have slightly larger range of frequencies than that in non-spiral flow. Also the viscous dissipation region in non-spiral flow is almost absent in the downstream region after $z = 8D$.

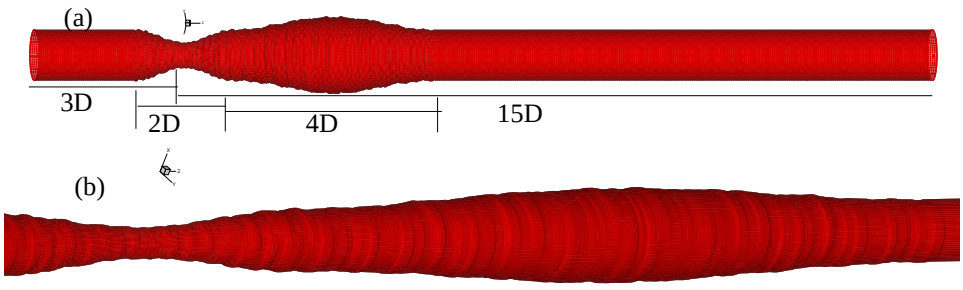

Figure 7.1: Three dimensional view of model artery having irregular stenosis with adjacent irregular aneurysm (a) the whole domain and (b) zoomed-in section on irregular stenosis with adjacent irregular aneurysm.

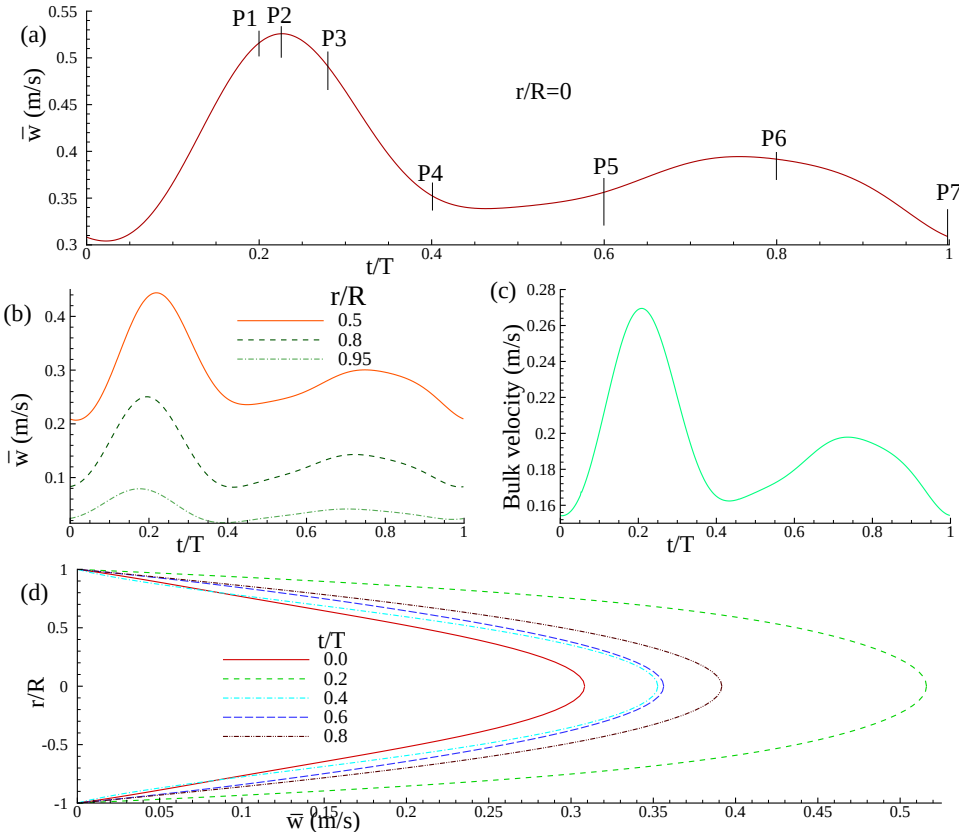

Figure 7.2: Inlet physiological 4th harmonic pulsatile velocity profiles, $\bar{w}$ (m/s), for a time cycle (a) at the centre of the tube, (b) at different locations between the wall and the centre, (c) bulk velocity profile and (d) during different phases of a time cycle while $A = 0.40$, $Re = 440$ and the Womersley parameter $\alpha = 6.92$. Reference phases at which results are obtained are also marked.

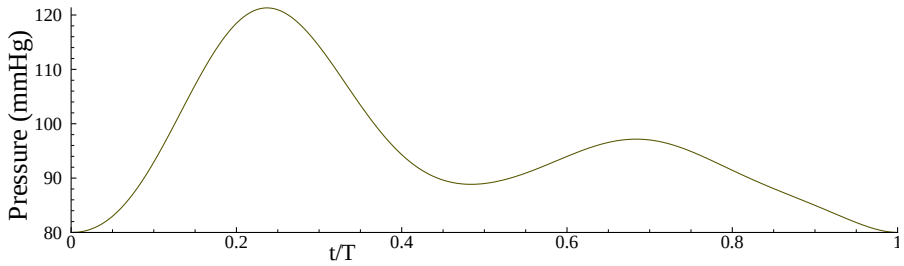

Figure 7.3: Outlet physiological 4th harmonic pulsatile pressure profiles, $\bar{p}$ (mmHg), for a time cycle while $A = 0.40$, $Re = 440$ and the Womersley parameter $\alpha = 6.92$. (1 mmHg$=$ 133.32 Pa.)

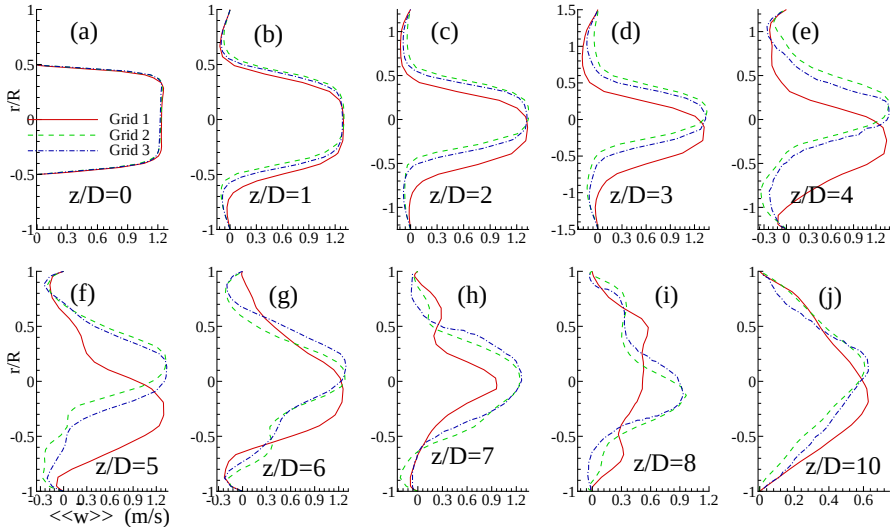

Figure 7.4: Grid resolution study for phase-averaged streamwise velocity, $\langle\langle\bar{w}\rangle\rangle$ (m/s), in non-spiral blood flow during phase $P3$ at different indicated axial locations while $Re = 440$.

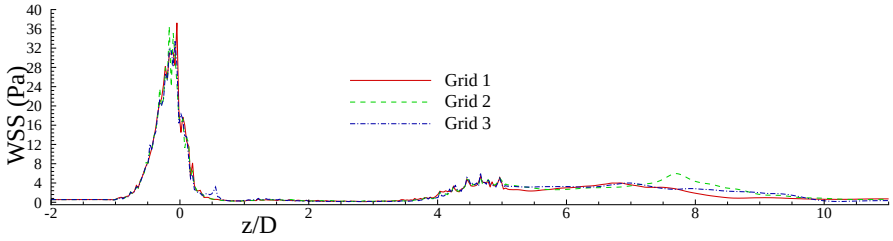

Figure 7.5: Grid resolution study for phase-averaged axial wall shear stress (Pa) in non-spiral blood flow during phase $P3$ while $Re = 440$. Phase averaging was done on the circumferential average WSS.

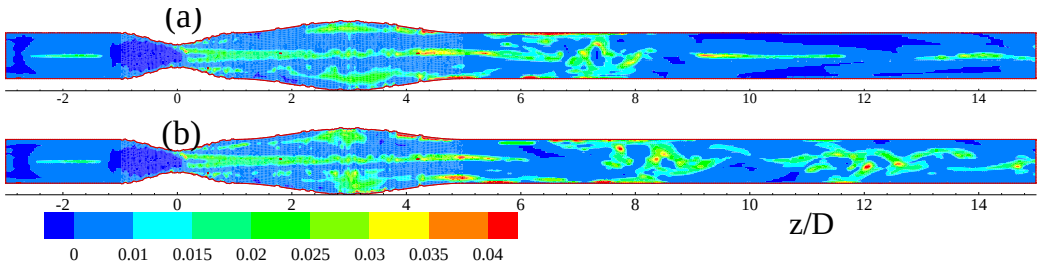

Figure 7.6: Dynamic Smagorinsky constant, C_s, in non-spiral blood flow during phase $P3$ for (a) $Re = 366$ and (b) $Re = 440$.

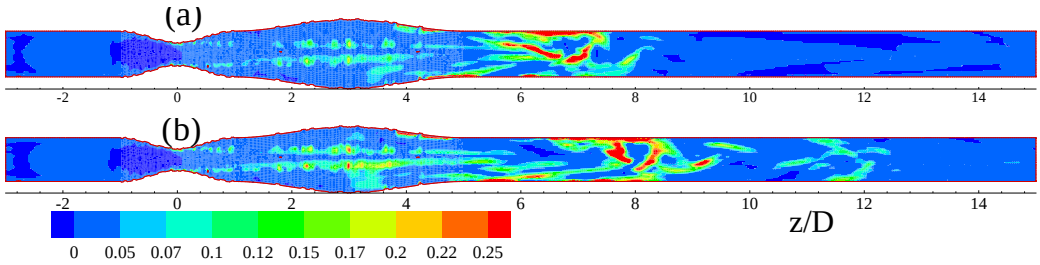

Figure 7.7: Normalised SGS eddy viscosity, μ_{sgs}/μ, in non-spiral blood flow during phase $P3$ for (a) $Re = 366$ and (b) $Re = 440$.

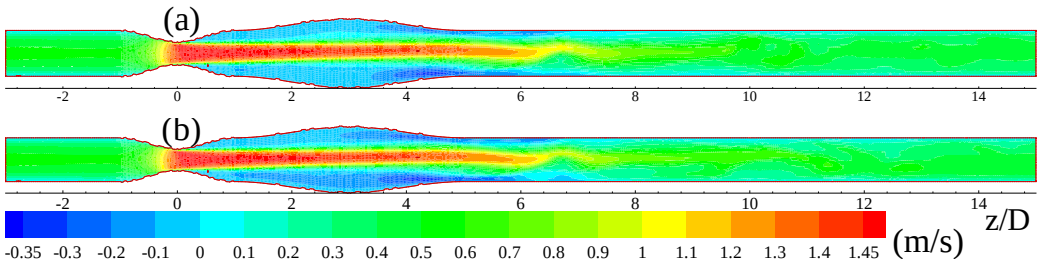

Figure 7.8: Contour plot of the instantaneous mid-plane streamwise velocity, $\bar{w}$ (m/s), for $Re = 440$ during phase $P2$ in (a) non-spiral and (b) spiral blood flow while $C = 1/6$.

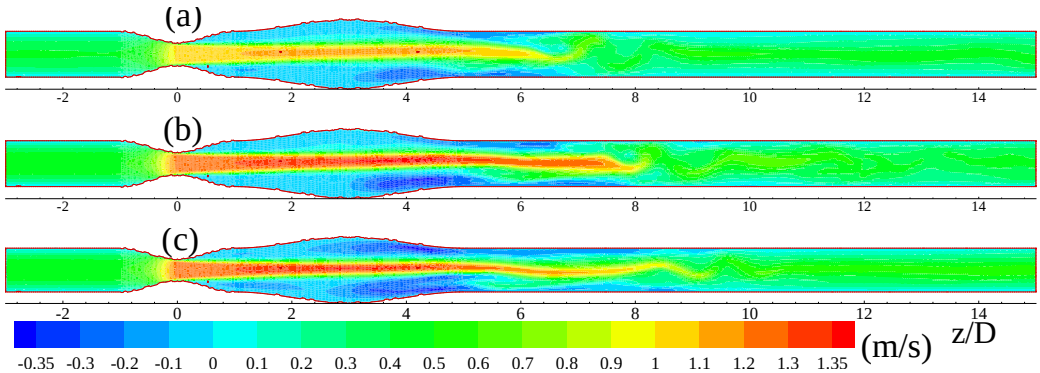

Figure 7.9: Contour plot of the instantaneous mid-plane streamwise velocity, $\bar{w}$ (m/s), in non-spiral blood flow during phase $P3$ for (a) $Re = 366$ and (b) $Re = 440$ and (c) the corresponding $\bar{w}$ from k-ω Transitional model in non-spiral flow for $Re = 440$.

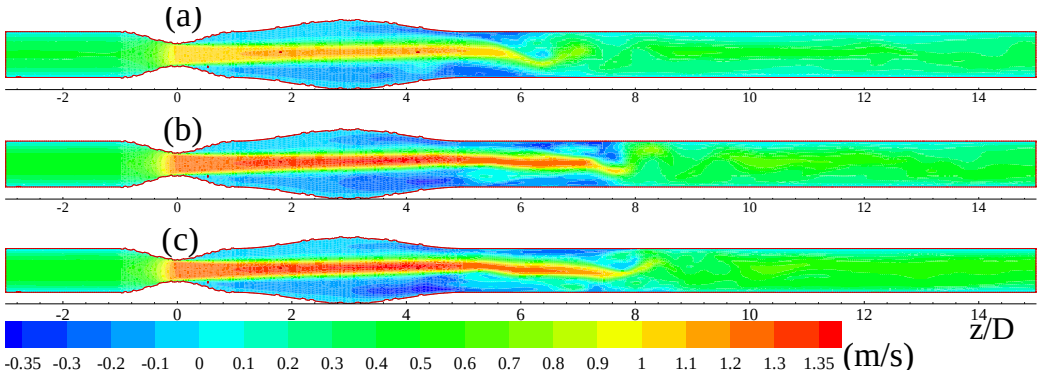

Figure 7.10: Contour plot of the instantaneous mid-plane streamwise velocity, $\bar{w}$ (m/s), in spiral blood flow during phase $P3$ for (a) $Re = 366$ while $C = 1/6$, (b) $Re = 440$ while $C = 1/6$ and (c) $Re = 440$ while $C = 1/4$.

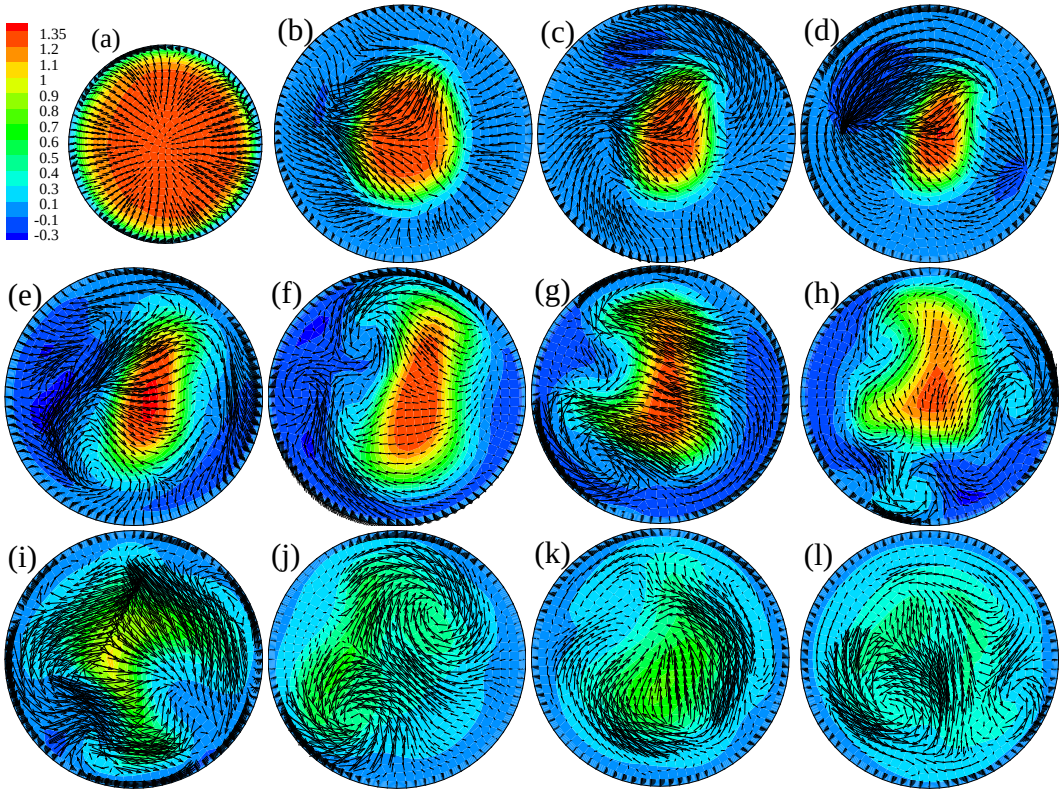

Figure 7.11: Instantaneous cross-sectional vectors appended on the contours of the streamwise velocity, $\bar{w}$, in non-spiral flow during phase $P3$ at (a) $z/D = 0$, (b) $z/D = 1$, (c) $z/D = 2$, (d) $z/D = 3$, (e) $z/D = 4$, (f) $z/D = 5$, (g) $z/D = 6$, (h) $z/D = 7$, (i) $z/D = 8$, (j) $z/D = 9$, (k) $z/D = 10$ and (l) $z/D = 12$ while $Re = 440$.

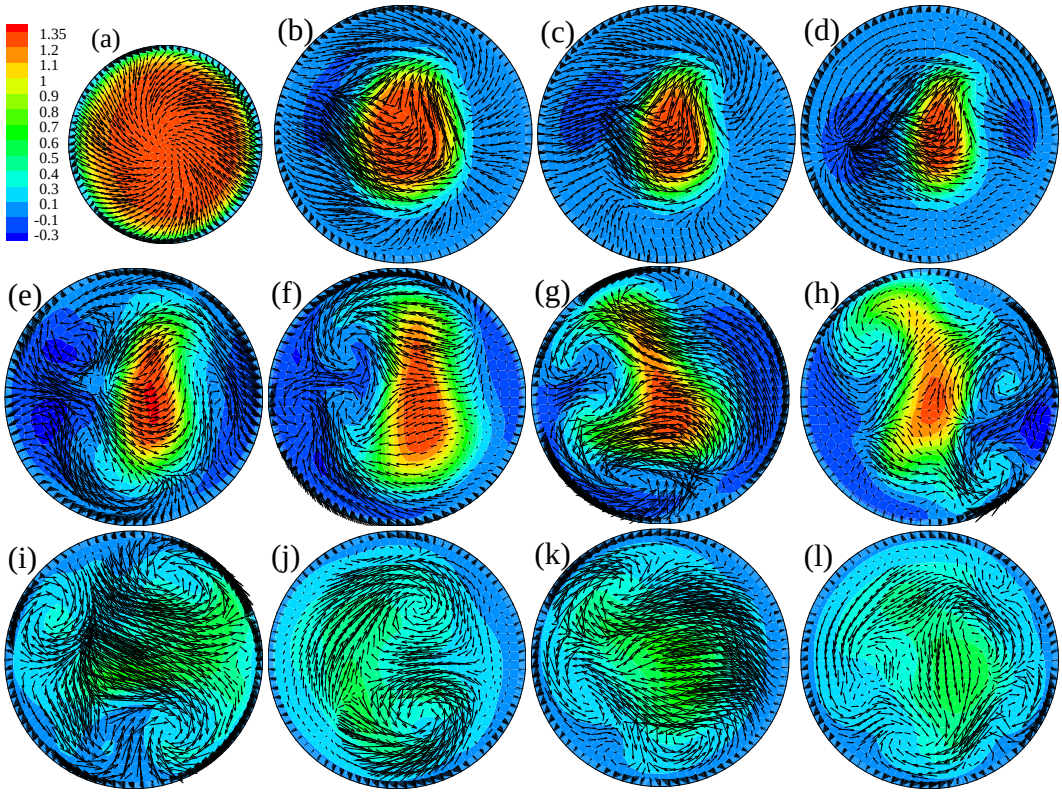

Figure 7.12: Instantaneous cross-sectional vectors appended on the contours of the streamwise velocity, $\bar{w}$, in spiral flow during phase $P3$ at (a) $z/D = 0$, (b) $z/D = 1$, (c) $z/D = 2$, (d) $z/D = 3$, (e) $z/D = 4$, (f) $z/D = 5$, (g) $z/D = 6$, (h) $z/D = 7$, (i) $z/D = 8$, (j) $z/D = 9$, (k) $z/D = 10$ and (l) $z/D = 12$ while $Re = 440$.

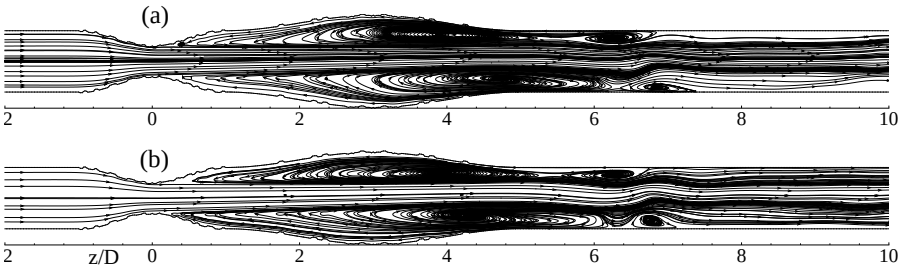

Figure 7.13: The instantaneous mid-plane streamlines for $Re = 440$ during phase $P2$ in (a) non-spiral and (b) spiral blood flow while $C = 1/6$.

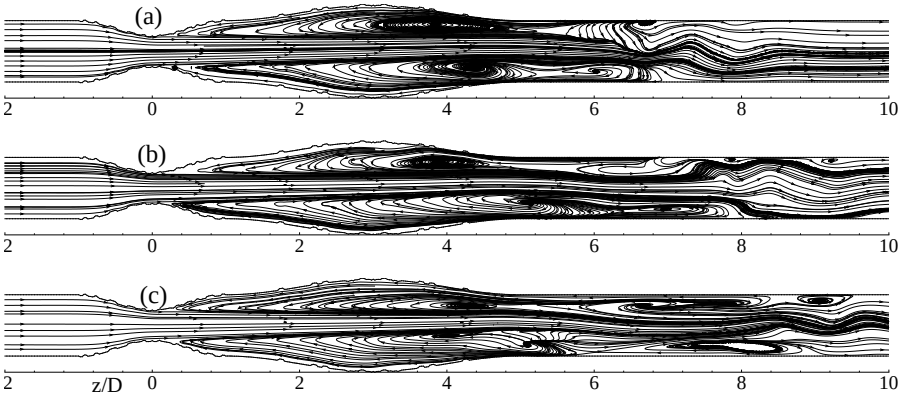

Figure 7.14: The instantaneous mid-plane streamlines in non-spiral blood flow during phase $P3$ for (a) $Re = 366$ and (b) $Re = 440$ and (c) the corresponding streamlines from k-ω Transitional model in non-spiral flow for $Re = 440$.

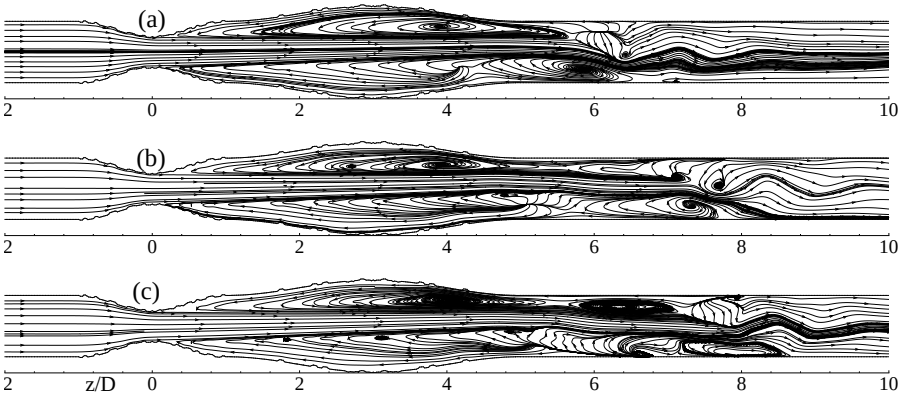

Figure 7.15: The instantaneous mid-plane streamlines in spiral blood flow during phase $P3$ for (a) $Re = 366$ while $C = 1/6$, (b) $Re = 440$ while $C = 1/6$ and (c) $Re = 440$ while $C = 1/4$.

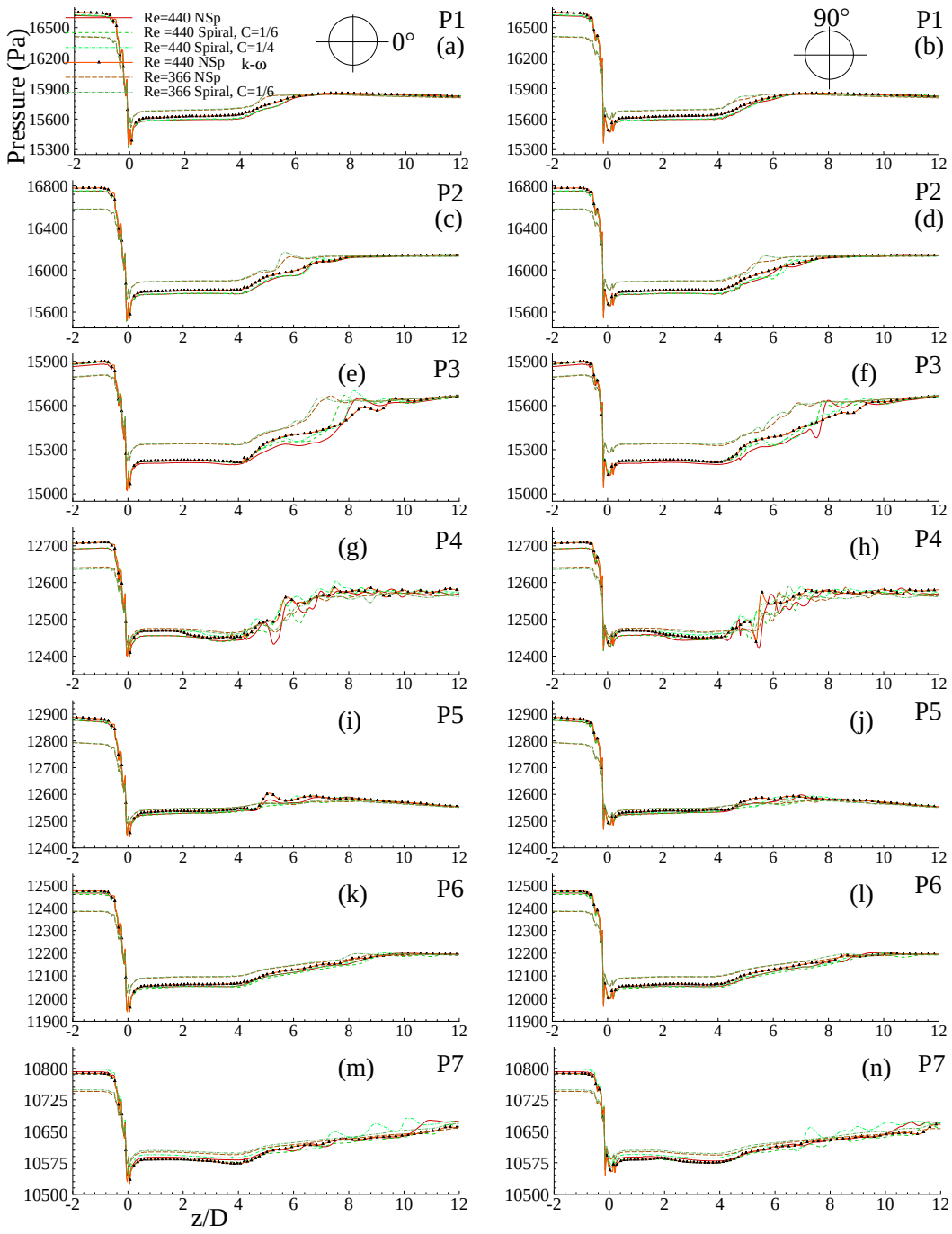

Figure 7.16: The instantaneous wall pressure, $\bar{p}$ (Pa), in both non-spiral and spiral flow for Reynolds numbers $Re = 366$ (while $C = 1/6$) and $Re = 440$ (while $C = 1/6$ and $C = 1/4$) during different phases of the last cycle at the two indicated circumferential locations. The corresponding k-ω Transitional results in non-spiral flow for $Re = 440$ are also appended.

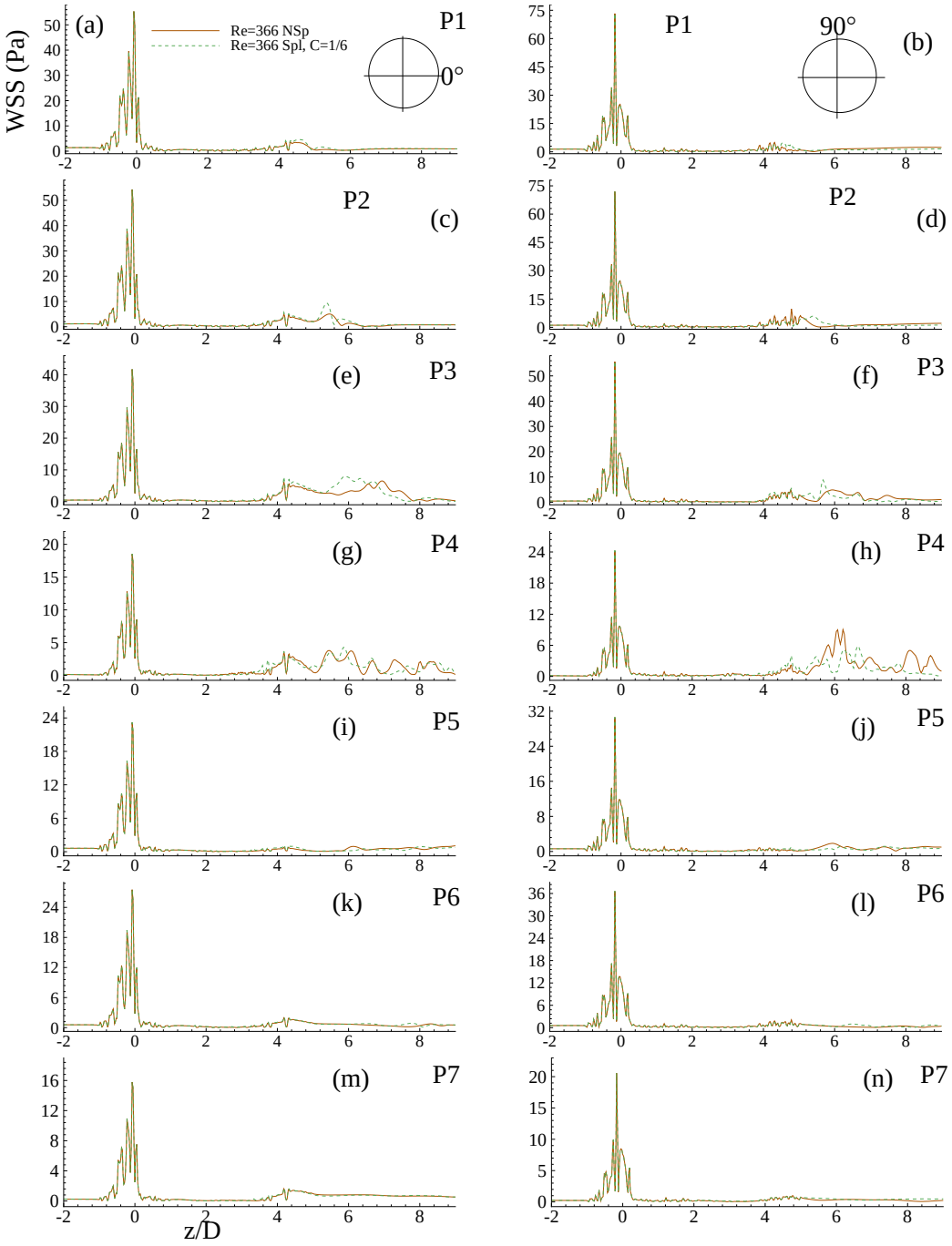

Figure 7.17: The instantaneous wall shear stress (Pa) for $Re = 366$ in both non-spiral and spiral ($C = 1/6$) flow during different phases of the last cycle at the two indicated circumferential locations.

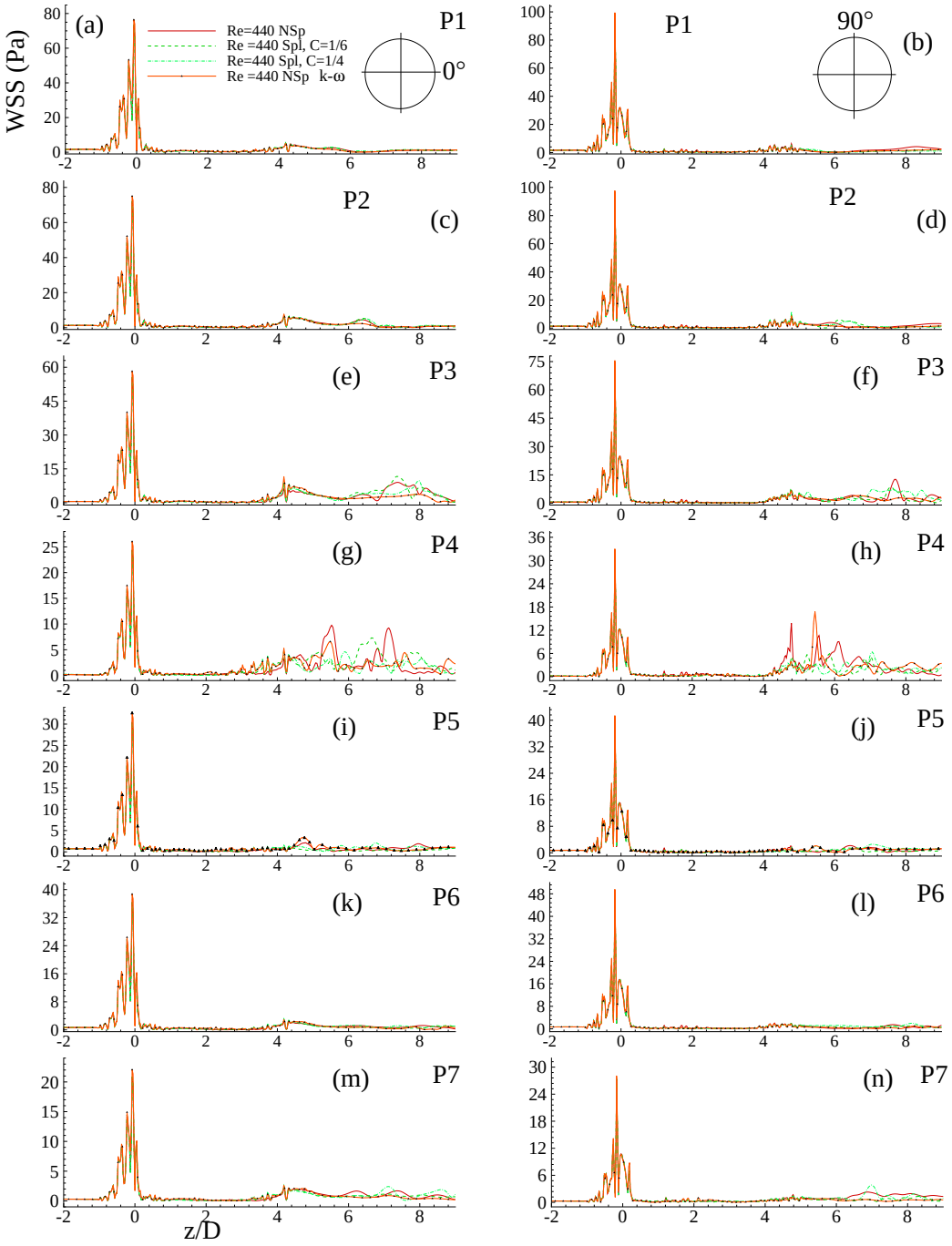

Figure 7.18: The instantaneous wall shear stress (Pa) for $Re = 440$ in both non-spiral and spiral ($C = 1/6$ and $C = 1/4$) flow during different phases of the last cycle at the two indicated circumferential locations. Note that the corresponding k-ω Transitional results in non-spiral flow are also appended.

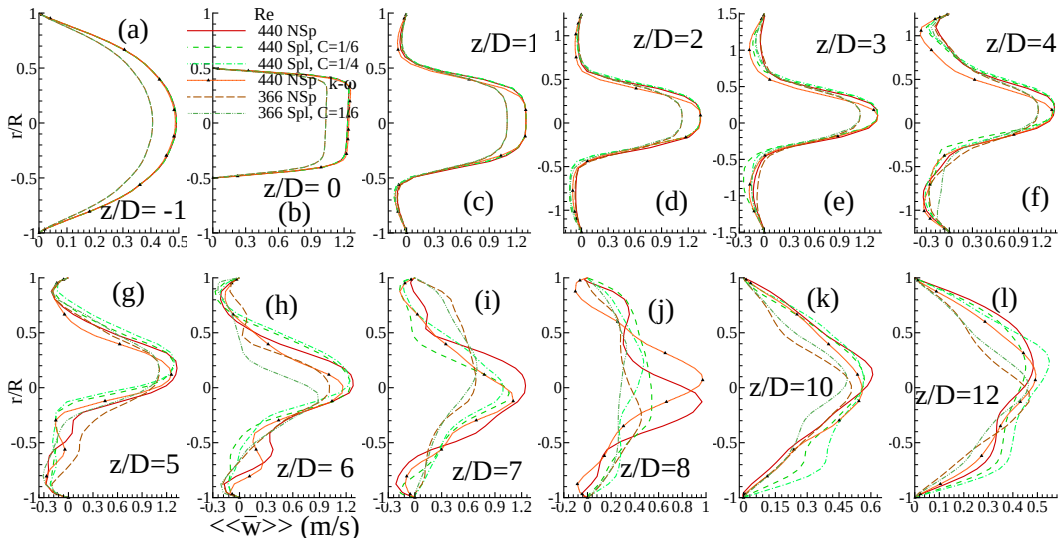

Figure 7.19: Phase-averaged streamwise velocity, $\langle\langle\bar{w}\rangle\rangle$ (m/s), in both non-spiral and spiral flow for Reynolds numbers $Re = 366$ (while $C = 1/6$) and $Re = 440$ (while $C = 1/6$ and $C = 1/4$) during phase $P3$ of the last cycle at different axial locations. Note that the corresponding k-ω Transitional results in non-spiral flow for $Re = 440$ are also appended.

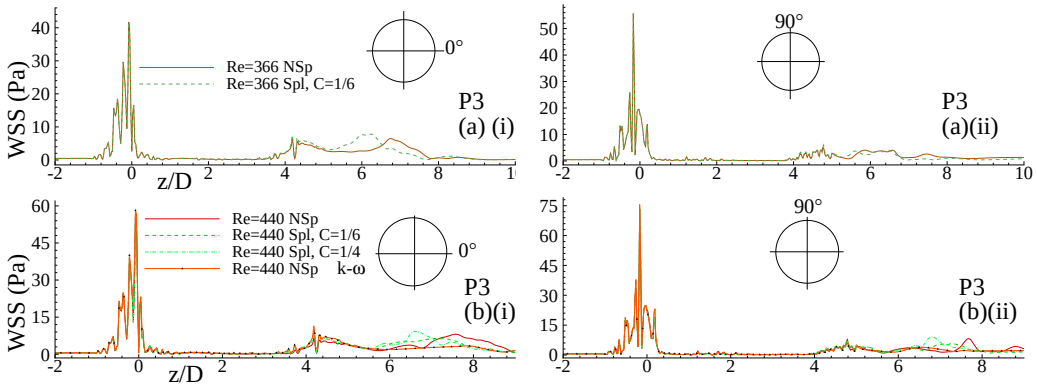

Figure 7.20: Phase-averaged wall shear stress (Pa) in both non-spiral and spiral flow during phase $P3$ for (a) $Re = 366$ (while $C = 1/6$) and (b) $Re = 440$ (while $C = 1/6$ and $C = 1/4$) at the two indicated circumferential locations. The corresponding k-ω Transitional results in non-spiral flow for $Re = 440$ are also appended in (b).

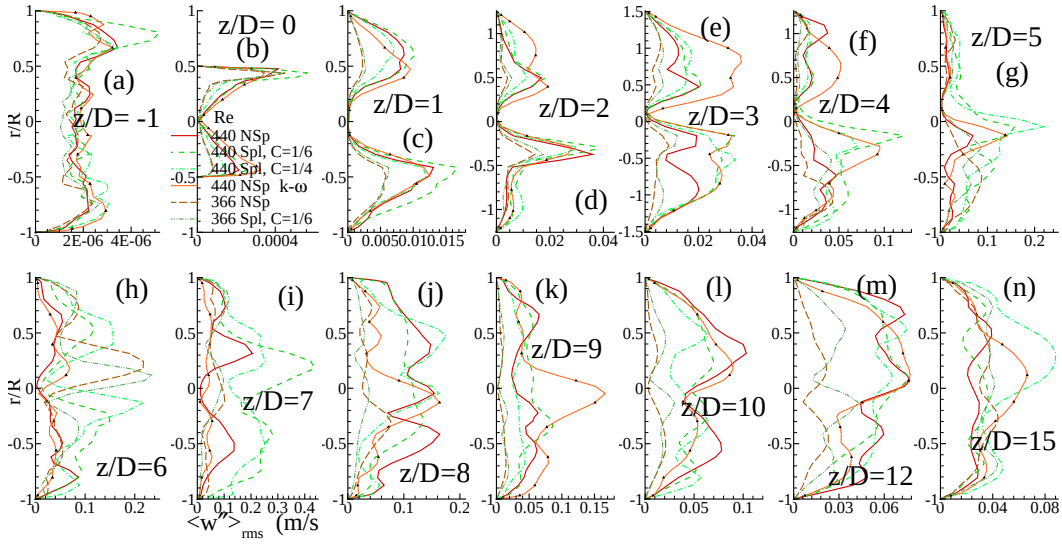

Figure 7.21: rms of the streamwise velocity fluctuations, $\langle w'' \rangle_{rms}$ (m/s), in both non-spiral and spiral flow for Reynolds numbers $Re = 366$ (while $C = 1/6$) and $Re = 440$ (while $C = 1/6$ and $C = 1/4$) during phase $P3$ at different axial locations. Note the corresponding k-ω results in non-spiral flow for $Re = 440$ are also appended.

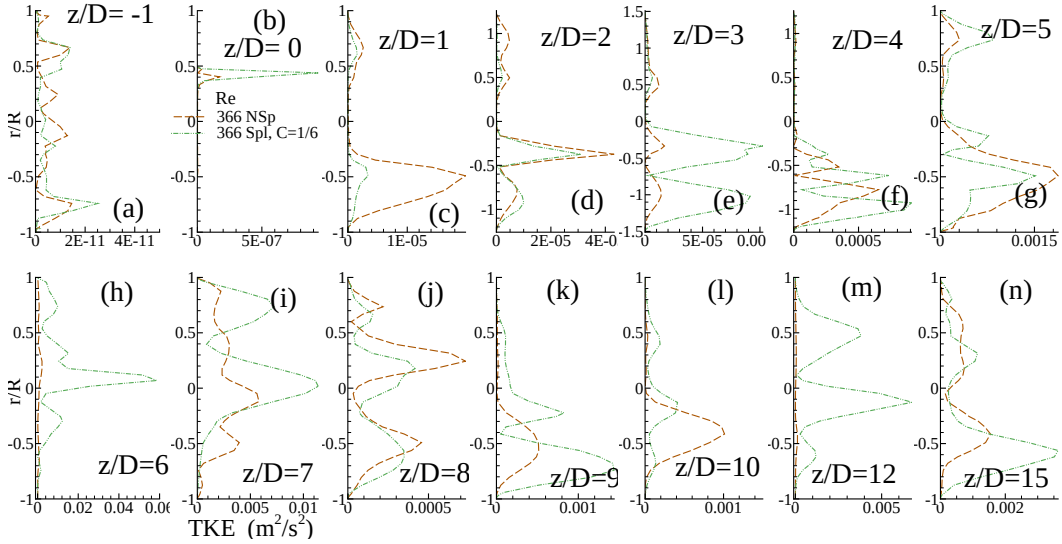

Figure 7.22: Turbulent kinetic energy (TKE), $\frac{1}{2}\langle u_j'' u_j'' \rangle$ (m^2/s^2), in both non-spiral and spiral ($C = 1/6$) flow for Reynolds numbers $Re = 366$ during phase $P3$ at different axial locations.

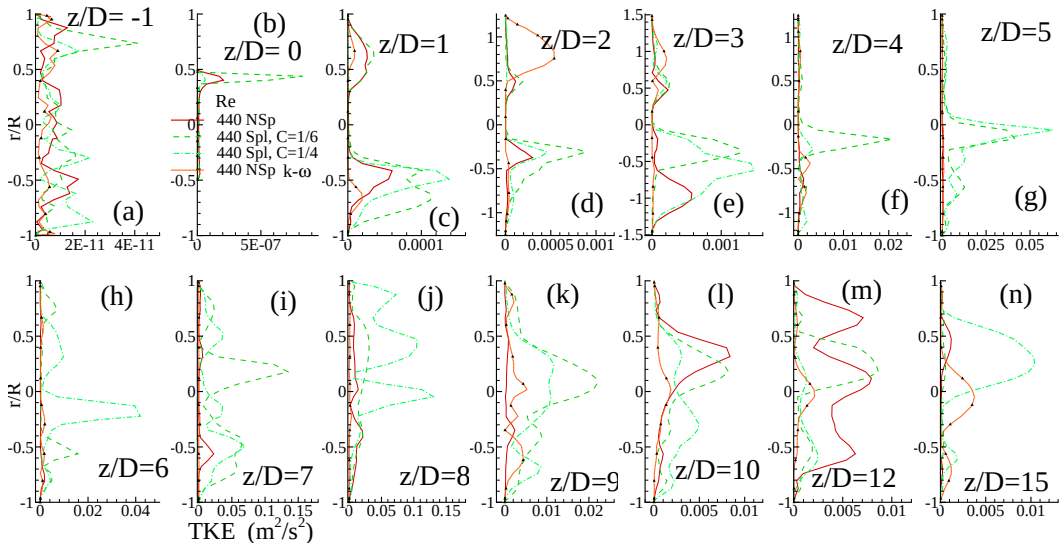

Figure 7.23: Turbulent kinetic energy (TKE), $\frac{1}{2}\langle u_j'' u_j'' \rangle$ (m^2/s^2), in both non-spiral and spiral ($C = 1/6$ and $C = 1/4$) flow for Reynolds numbers $Re = 440$ during phase $P3$ at different axial locations. Note the corresponding k-ω results in non-spiral flow for $Re = 440$ are also appended.

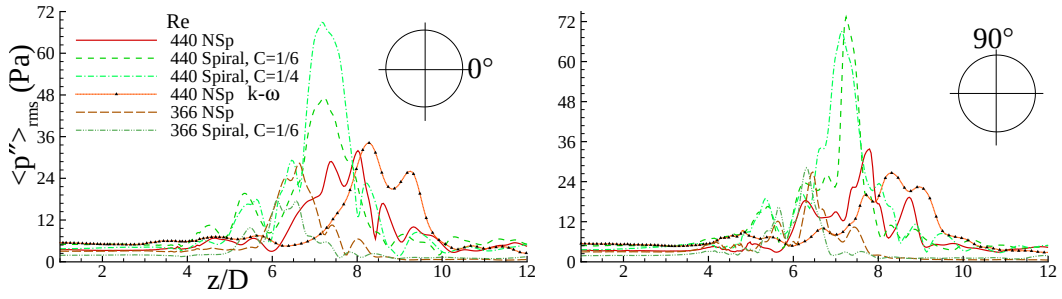

Figure 7.24: rms of wall pressure fluctuations, $\langle p'' \rangle_{rms}$ (Pa), in both non-spiral and spiral flow for Reynolds numbers $Re = 366$ (while $C = 1/6$) and $Re = 440$ (while $C = 1/6$ and $C = 1/4$) during phase $P3$ at the two indicated circumferential locations. The corresponding k-ω results in non-spiral flow for $Re = 440$ are also appended.

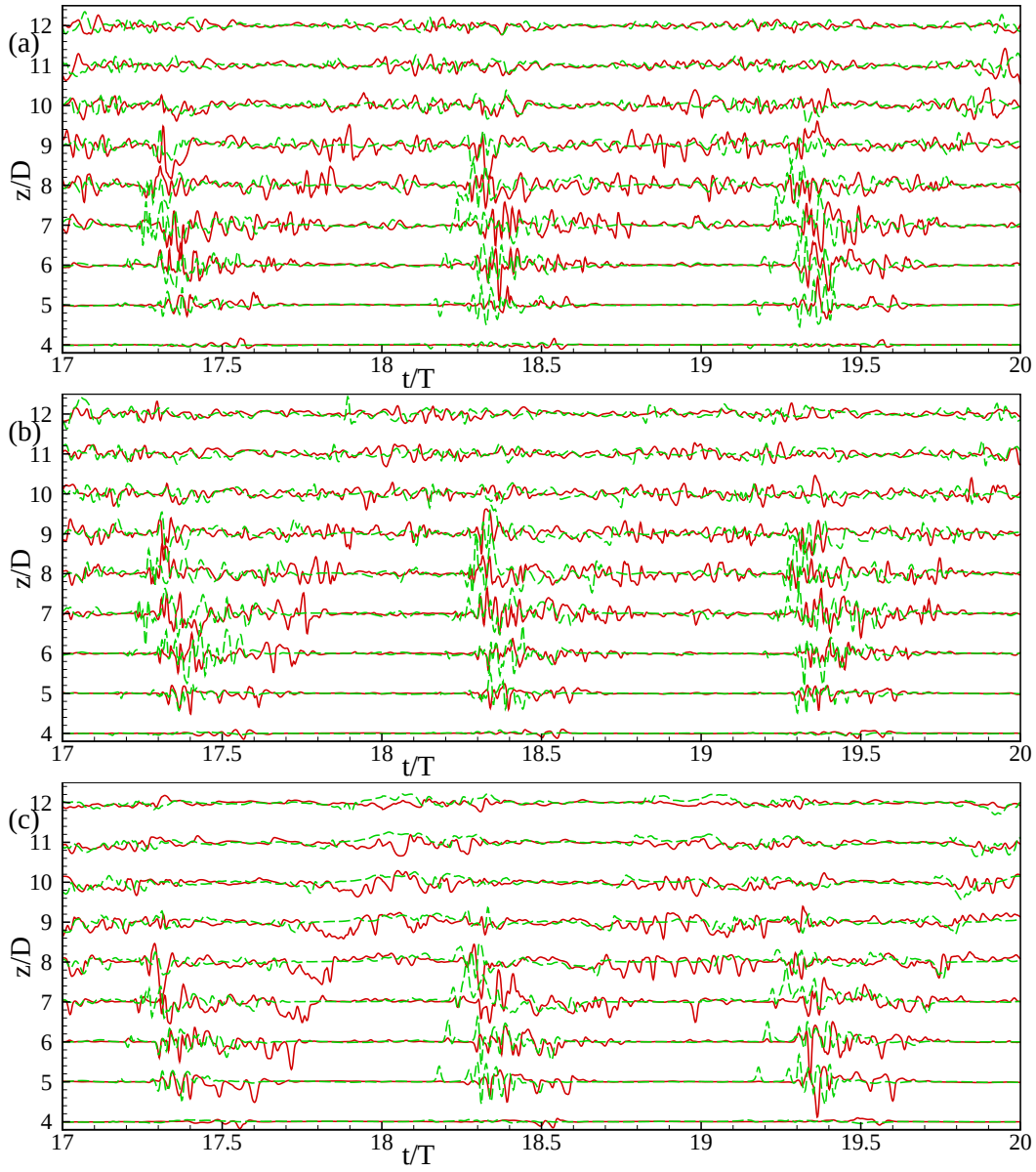

Figure 7.25: Time history of the centreline velocity fluctuations, (a) u''/u''_{max}, (b) v''/v''_{max} and (c) w''/w''_{max} at different axial locations for both non-spiral and spiral ($C = 1/6$) pulsatile blood flow while $Re = 440$. The red coloured solid line denotes velocity fluctuations for non-spiral flow while the green coloured dashed line corresponds to velocity fluctuations for spiral flow.

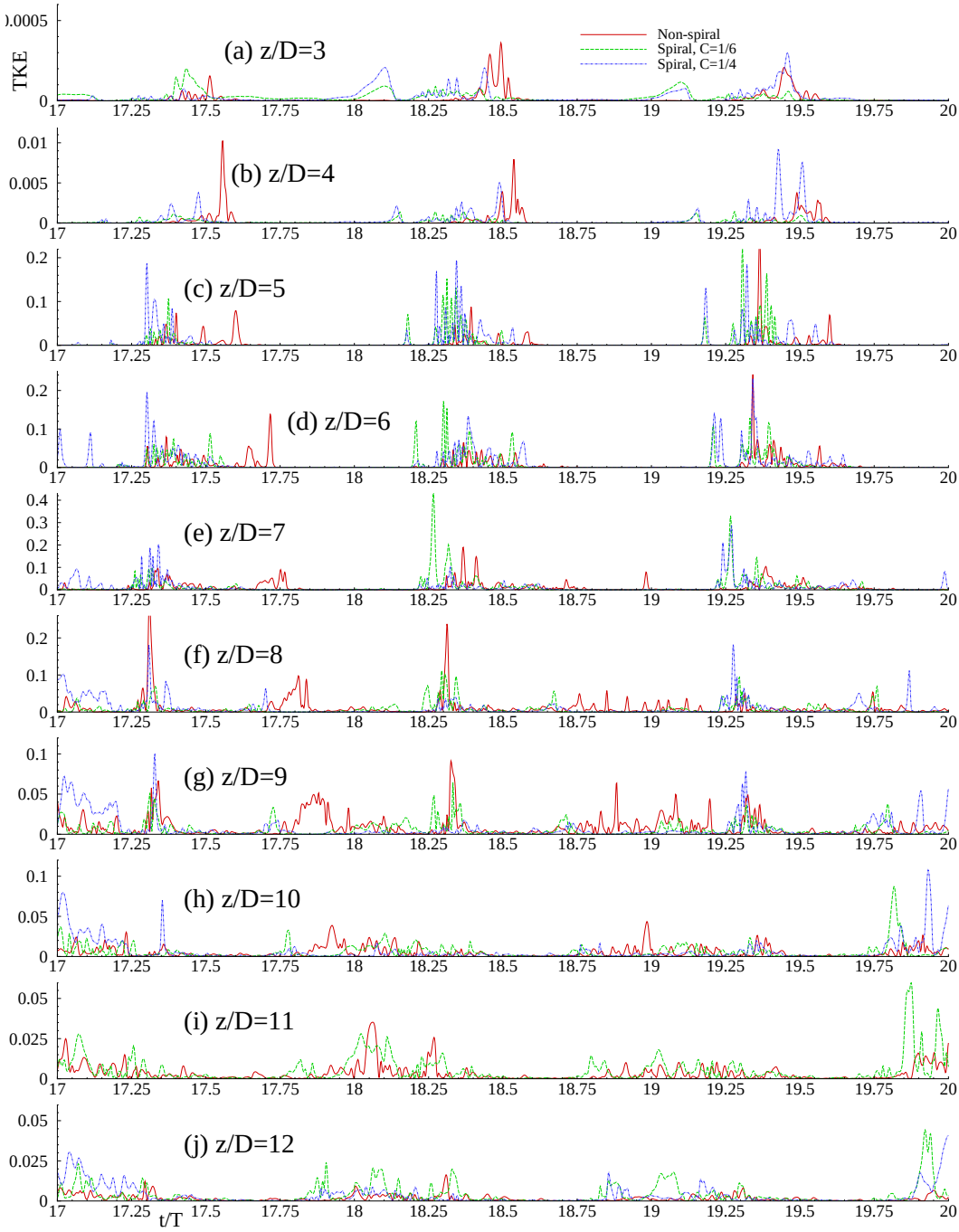

Figure 7.26: Time history of centreline turbulent kinetic energy (TKE), $\frac{1}{2}\langle u_j'' u_j'' \rangle$ (m^2/s^2), at different indicated axial locations for both non-spiral and spiral flow while $Re = 440$. The red coloured solid line denotes TKE for non-spiral flow while the green coloured dashed line and blue coloured dash-dot-dot line correspond to TKE for spiral flow corresponding to $C = 1/6$ and $C = 1/4$ respectively.

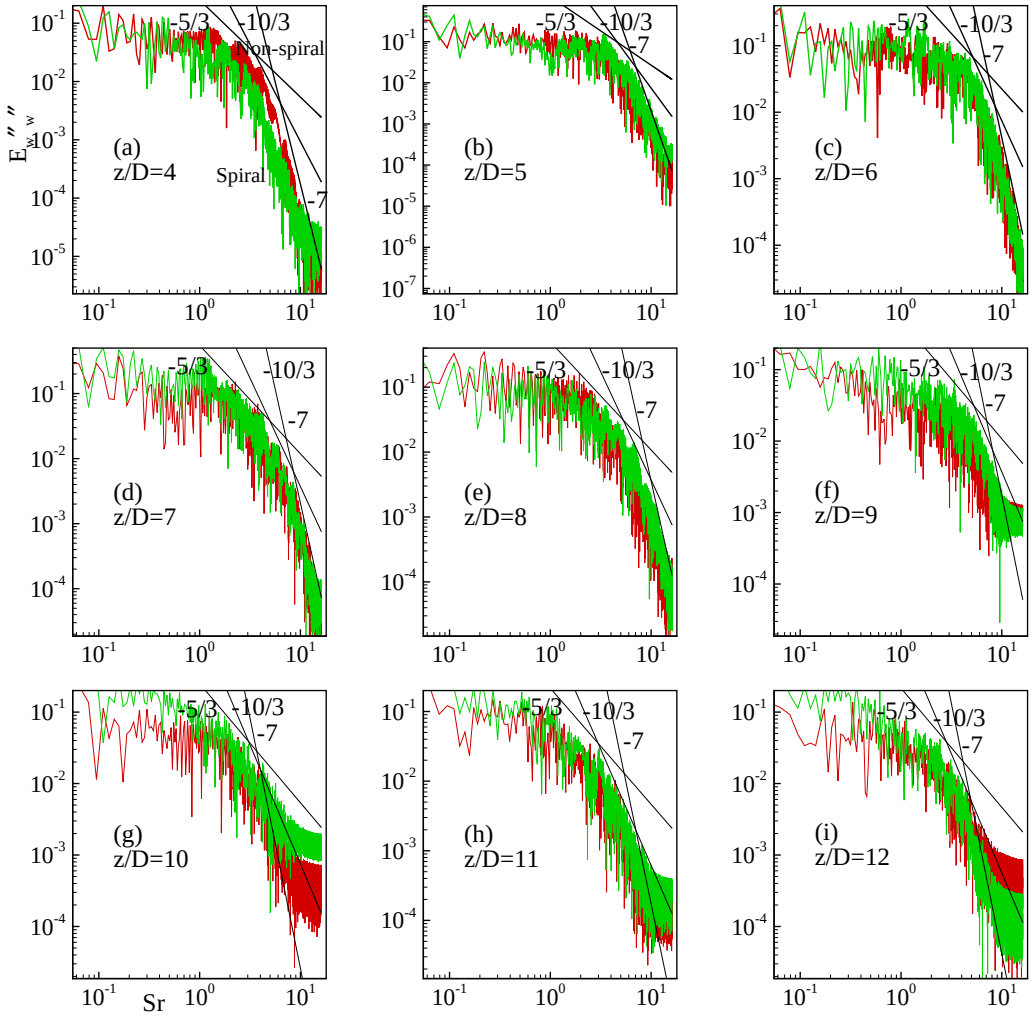

Figure 7.27: Energy spectra of centreline streamwise velocity fluctuations, w'', at different axial locations normalised by centreline $\langle w'' \rangle_{rms}$ at the same locations, for both non-spiral and spiral ($C = 1/6$) pulsatile flow while $Re_{pk} = 1200$. The red and the green coloured lines correspond to the energy spectra of velocity fluctuations for non-spiral and spiral flow, respectively.

Chapter 8

Conclusions and Suggestions for Future Research

In this chapter, the findings of the thesis are summarised in § 8.1 and some suggestions on future research are made in § 8.2.

8.1 Conclusions

Large Eddy Simulation and two-equation k-ω Transitional model were employed to investigate the transition-to-turbulence of non-spiral and spiral blood flow through different models of arterial stenosis and aneurysm for different Reynolds numbers. The findings of the thesis are summed up chapter-wise and are presented below.

In Chapter 4, the steady spiral blood flow in 75% area reduction arterial stenosis models without and with upstream curved segments of $60°$, $90°$ and $120°$ angle of curvature for Reynolds numbers $Re = 500$, 1000, 1500 and 2000 by using the standard k-ω Transitional model and LES with Smagorinsky-Lilly dynamic subgrid model (Germano [115], Lilly [116] and Kim [123]) has been numerically investigated. Excellent agreement between LES results for non-spiral flow in the straight stenosed tube for $Re = 1000$ and 2000 and the corresponding experimental results (Ahmed and Giddens [27; 28]) were found when the appropriate inlet perturbations were introduced. In the models with an upstream curved segment, no significant effect of spiral flow on any flow property was found for the investigated Reynolds numbers. The spiral pattern of the flow introduced at the inlet disappears before the stenosis in the models with an upstream curved segment, whic may be due to the constraints imposed in the simulations such as steady flow and rigid wall of the mod-

els. Contrary to the claims of Paul and Larman [17] and Stonebridge et al. [16], the TKE in spiral flow through the straight stenosed tube for the investigated Reynolds numbers increases compared with the corresponding result in non-spiral flow. However, the effect of spiral flow on the WSS and wall pressure is negligible. The effects of the curved upstream model can be seen mainly in the maximum TKE, the maximum pressure drop and the maximum WSS, which in curved upstream model generally increase significantly compared with the corresponding results in straight stenosed tube.

In Chapter 5, mainly LES with Smagorinsky-Lilly dynamic subgrid model was applied to investigate the transition-to-turbulence of the physiological pulsatile non-spiral and spiral blood flow through a straight stenosed tube having 75% area reduction stenosis for $Re = 438$, 584 and 876. For $Re = 438$ in non-spiral flow through the model, the two-equation Standard k-ω Transitional model was also employed to assess its suitability for pulsatile flow simulation. For $Re = 876$ in both non-spiral and spiral flow, the maximum contribution from the SGS model to large scale motion is 50%. The turbulent results obtained from k-ω model differ significantly from the corresponding LES results which is expected because the k-ω model gives time-averaged results rather than instant results. Flow-choking and even rupture of the plaque in pulsatile flow can take place due to the occurrence of extremely high pressure drop in both non-spiral and spiral flow at the throat of the stenosis during phases $P1$, $P2$ and $P3$ compared with other phases. In addition, the sharp rise of the WSS just before the stenosis throat, which is also extremely large during phases $P1$, $P2$ and $P3$, may induce thrombosis and deformation of red blood cells. The effect of spiral flow on both the maximum pressure drop and maximum WSS is very insignificant as seen in Chapter 4. The spiral effects on the wall pressure and WSS can only be seen in their oscillatory pattern within $2 \leq z/D \leq 6$.

The transition-to-turbulence in non-spiral flow occurs in the further downstream region than that in spiral flow. As seen in Chapter 4, the TKE in pulsatile spiral flow also increases significantly at some places and phases compared with the corresponding result in pulsatile non-spiral flow. In both non-spiral and spiral flow, the occurrence of the high level of turbulent fluctuations in the downstream region has serious pathological implications as it may activate the blood platelets and also damage the blood cell materials, leading to many pathological diseases (Ku [3]; Paul

and Molla [93]). The break frequencies of energy spectra for velocity and pressure fluctuations from $-5/3$ power slope to $-10/3$ power slope and $-7/3$ power slope, respectively, are observed in the downstream transition-to-turbulence region in both non-spiral and spiral flow. At some locations in the transition region, the velocity spectra in spiral flow has larger inertial subrange region than that in non-spiral flow. The effects of spiral flow on the pressure spectra is insignificant.

Additionally, we have also studied the effects of percentage of area reduction in stenosis, length of stenosis, amplitude of pulsation and Womersley number, α, in Chapter 5. The maximum pressure drop, the maximum WSS and the TKE rise sharply when the area reduction in the stenosis is increased. As for the effects of length of the stenosis, the maximum WSS falls significantly and the maximum TKE rises sharply due to the increase in the length of the stenosis; but the maximum pressure drop is almost unaffected by the increase in the stenosis length. The increase in the amplitude of pulsation causes both the maximum pressure drop and the maximum WSS to increase significantly under the inlet peak flow condition, i.e. during phase $P2$. While the increased amplitude of pulsation decrease the maximum TKE, it is nonetheless responsible for the sharp rise in TKE found at some places in the transition-to-turbulence region. The decrease in the Womersley number causes the maximum TKE to increase dramatically; however, the maximum pressure drop and the maximum WSS decrease slightly during phase $P2$ as a result of the decrease in the Womersley number.

In Chapter 6, LES was applied to investigate the physiological pulsatile non-spiral and spiral blood flow through a straight tube having an irregular stenosis of 75% area reduction for $Re = 438$, 584 and 876. The results of non-spiral flow through the irregular stenosis are also compared with the corresponding results through a regular stenosis from Chapter 5 to assess the influence of the irregular stenosis. In both non-spiral and spiral flow, the maximum contribution from the sub-grid scale to the large scale motion in the irregular stenosis for all the investigated Reynolds numbers is 55%, which is larger than that in the regular cosine-type stenosis. The effects of spiral flow on the wall pressure and WSS are observed only in the downstream region where the pressure and WSS are of oscillatory nature. Due to the effects of the irregular stenosis, the maximum wall pressure drop and the maximum WSS at one circumferential location of the wall differ significantly from

those at other circumferential location of the wall. Also, the maximum wall pressure drop, the maximum WSS and the maximum TKE in non-spiral flow through the irregular stenosis rise significantly compared with the corresponding results in non-spiral flow through the regular stenosis. As seen in Chapters 4 and 5, the TKE rises significantly at some locations and phases if the spiral effect is introduced at the inlet. From the pathological point of view, the irregular stenosis has devastating impacts on the cardiovascular health of the patients. In the simulation of blood flow through stenosed artery, irregular stenosis instead of regular stenosis should, therefore, be taken to accurately predict the flow field.

In Chapter 7, the physiological non-spiral and (both low and high) spiral blood flow through a three-dimensional model of an irregular stenosis with an adjacent post-stenotic fusiform irregular aneurysm in basilar artery have been studied for $Re = 366$ and 440 by applying LES. The two-equation k-ω Transitional model was also applied in non-spiral flow for $Re = 440$ to crudely assess the LES results as no experimental or computational study of blood flow through this kind of geometry is available in the literature. The maximum contribution from the SGS model to the large scale motion is $\approx 25\%$, relatively small compared with those in Chapters 5 and 6. Although wall pressure and shear stress from the k-ω Transitional model agree quite well with the corresponding LES results, the turbulent results obtained from the k-ω Transitional model differ significantly from the corresponding LES results – this shows unsuitability of k-ω model for pulsatile flow simulation. Throughout the pulsatile cycle in both non-spiral and spiral flow, the wall pressure falls significantly at the throat of the stenosis and does not rise to regain its undisturbed value before the start of the last quarter of the aneurysm, i.e. $z = 4D$. The maximum value of the WSS in both non-spiral and spiral flow, which is found just before the stenosis throat, attains clinically harmful level during all the phases of the pulsatile cycle for both the Reynolds numbers. In both non-spiral and spiral flow, the cycle maximum pressure drop and WSS occur during phase $P1$ at 0° and 90° circumferential location of the wall, respectively. The effects of (low or high) spiral flow on the wall pressure and WSS are visible only in the downstream region after $z \approx 4D$ where they take oscillatory pattern. The transition-to-turbulence in both non-spiral and spiral flow occurs in the downstream region between $z \approx 4D$ and $10D$, i.e. the transition does not start before the last quarter of the aneurysm. The TKE in

spiral flow rises significantly compared with that in non-spiral flow. However, the maximum value of the TKE in high spiral flow drops considerably compared with that in low spiral flow.

Modelling transitional blood flow through arterial stenosis and aneurysm is very challenging. Accuracy of the simulation depends mainly on suitable numerical approach, realistic model geometry and boundary conditions. The suitability of LES in this kind of investigations has been shown in the present study and also in similar studies by Paul and Molla [93], Molla [90], Gårdhagen et al. [95], Mittal et al. [88], Scotti and Piomelli [75] and Liang and Papadakis [143]. The present study was simplified by taking rigid walls for the arterial models; even so, we do believe that it makes a breakthrough in understanding the non-spiral and spiral transient blood flows through arteries having stenosis and stenosis with adjacent post-stenotic aneurysm. The results presented in the thesis would, therefore, help the interested groups such as pathologists, medical surgeons and researchers greatly in gaining better insight into transient non-spiral and spiral blood flow through models of arterial stenosis and aneurysm.

8.2 Future Research

Only a handful of studies of transient non-spiral flow in models of stenosis or aneurysm by applying LES are available and no report of LES of transitional spiral flow through stenosis and/or aneurysm can be found in the literature, which was also discussed in Chapter 2. This thesis has shown that LES can be potentially applied to investigate both non-spiral and spiral blood flow through various models of stenosis and aneurysm. LES, in our view, can also be employed to study fluid-structure interaction in transient non-spiral and spiral blood flow in various models of stenosis and/or aneurysm. In the light of the findings of this project, the following proposals are put forward for future research.

- The stenoses taken in this study are axisymmetric. Models of eccentric stenosis of irregular shape could be taken for future investigation of non-spiral and spiral transient blood flow through such models.

- We have studied non-spiral and spiral transitional flow in a model of basilar

artery having both stenosis and adjacent post-stenotic fusiform aneurysm. So, LES of non-spiral and spiral blood flow through models of artery having both stenosis and adjacent pre-stenotic fusiform or saccular aneurysm would be an interesting investigation in future.

- Unlike compliant arterial wall in real biological system, the arterial wall in this project was considered rigid. Arterial murmurs in the presence of an arterial stenosis are produced due to vibration of the arterial wall, which is again associated with the pressure fluctuations in the transient blood flow. Also, the velocity profiles at the inlet and the pressure profile at the outlet were theoretically derived. Therefore, the more realistic approach would be investigation of transient non-spiral and spiral blood flow through patient based compliant model geometry with patient based velocity and pressure waveform. Hence a potential future study would be simulation of fluid-structure interactions in diseased arteries using the LES technique.

- Bifurcated arteries are commonly associated with stenosis and spiral flow. So, it would be interesting to employ LES for studying transition-to-turbulence of non-spiral/spiral flow through models of bifurcation stenosis.

References

[1] A. J. Lusis, "Atherosclerosis," *Nature*, vol. 407, pp. 233–241, 2000.

[2] D. F. Young, "Fluid mechanics of arterial stenoses," *ASME J. Biomech. Eng.*, vol. 101, pp. 157–173, 1979.

[3] D. N. Ku, "Blood flows in arteries," *Annu. Rev. Fluid Mechanics*, vol. 29, pp. 399–434, 1997.

[4] S. S. Varghese, S. H. Frankel, and P. F. Fischer, "Direct numerical simulation of stenotic flows. Part 1. Steady flow," *J. Fluid Mech.*, vol. 582, pp. 253–280, 2007.

[5] D. N. Ku and B. N. McCord, "Cyclic stress causes rupture of the atherosclerotic plaque cap," *Suppl. to Circulation*, vol. 88 (1), pp. 1362–1375, 1993.

[6] D. M. Wootton and D. N. Ku, "Fluid mechanics of vascular systems, diseases, and thrombosis," *Annu. Rev. Biomed. Eng.*, vol. 01, pp. 299–329, 1999.

[7] W. W. Nichols and M. F. O'Rourke, *McDonald's Blood Flow in Arteries: Theoretical, Experimental and Clinical Principles*, 4th ed. Oxford University Press, 1998.

[8] Z.-Y. Li, V. Taviani, T. Tang, U. Sadat, V. Young, A. Patterson, M. Graves, and J. H. Gillard, "The mechanical triggers of plaque rupture: shear stress vs pressure gradient," *The British Journal of Radiology*, vol. 82, pp. S39–S45, 2009.

[9] A. M. Malek, S. L. Alper, and S. Izumo, "Hemodynamic shear stress and its role in atherosclerosis," *J. Ameriacn Medical Association (JAMA)*, vol. 282, pp. 2035–2042, 1999.

[10] A. Frydrychowicz, A. Harloff, B. Jung, M. Zaitsev, E. W. Eigang, T. A. Bley, M. Langer, J. Henning, and M. Markl, "Time-resolved, 3-Dimensional magnetic resonance flow analysis at 3 T: visualization of normal and pathological aortic vascular hemodynamics," *J. Comput. Assist. Tomogr.*, vol. 31(1), pp. 9–15, 2007.

[11] B. V. R. Kumar and K. B. Naidu, "Hemodynamics in aneurysm," *Computers and Biomedical Research*, vol. 29 (2), pp. 119–139, 1996.

[12] J. C. Lasheras, "The biomechanics of arterial aneurysms," *Annu. Rev. Fluid Mechanics*, vol. 39, pp. 293–319, 2007.

[13] H. S. In, H. Y. Lee, J. Y. Park, S. Y. Kim, J. H. Jung, J. S. Kim, S. J. Kim, and D. C. Suh, "Intracranial stenting in patients with atherosclerotic stenosis associated with various aneurysms in the same diseased arterial segment," *AJNR Am J Neuroradiol*, vol. 31, pp. 1895–1898, Nov-Dec 2010.

[14] P. A. Stonebridge and C. M. Brophy, "Spiral laminar flow in arteries?" *The Lancet*, vol. 338, pp. 1360–1361, 1991.

[15] P. A. Stonebridge, P. R. Hoskins, P. L. Allan, and J. F. F. Belch, "Spiral laminar flow in vivo," *Clinical Science*, vol. 91, pp. 17–21, 1996.

[16] P. A. Stonebridge, C. Buckley, A. Thompson, J. Dick, G. Hunter, J. A. Chudek, J. G. Houston, and J. J. F. Belch, "Non spiral and spiral (helical) flow patterns in stenoses — in vitro observations using spin and gradient echo magnetic resonance imaging (mri) and computational fluid dynamic modeling," *International Angiology*, vol. 23, no. 3, pp. 276–283, 2004.

[17] M. C. Paul and A. Larman, "Investigation of spiral blood flow in a model of arterial stenosis," *Medical Engineering & Physics*, vol. 31, pp. 1195–1203, 2009.

[18] D. F. Young and F. R. Tsai, "Flow characteristics in models of arterial stenosis -i. steady flow," *J. Biomechanics*, vol. 6, pp. 395–410, 1973.

[19] D. F. Young and F. R. Tsai, "Flow characteristics in models of arterial stenosis -ii. unsteady flow," *J. Biomechanics*, vol. 6, pp. 547–559, 1973.

[20] C. Clark, "The fluid mechanics of aortic stenosis–I. Theory and steady flow experiments," *J. Biomechanics*, vol. 9, pp. 521–528, 1976.

[21] C. Clark, "The fluid mechanics of aortic stenosis–II. Unsteady flow experiments," *J. Biomechanics*, vol. 9, pp. 567–573, 1976.

[22] R. A. Cassanova and D. P. Giddens, "Disorder distal to modeled stenoses in steady and pulsatile flow," *J. Biomechanics*, vol. 11, pp. 441–453, 1978.

[23] W. Yongchareon and D. F. Young, "Initiation of turbulence in model arterial stenoses," *J. Biomechanics*, vol. 12, pp. 185–196, 1979.

[24] A. M. A. Khalifa and D. P. Giddens, "Analysis of disorder in pulsatile flows with application to poststenotic blood velocity measurement in dogs," *J. Biomechanics*, vol. 11, pp. 129–141, 1978.

[25] A. M. A. Khalifa and D. P. Giddens, "Characterization and evolution of poststenotic flow disturbances," *J. Biomechanics*, vol. 14 (5), pp. 279–296, 1981.

[26] L. J. D'Luna, V. L. Newhouse, and D. P. Giddens, "In vitro Doppler detection of axisymmetric stenosis from transverse velocity measurements," *J. Biomechanics*, vol. 15(9), pp. 647–660, 1982.

[27] S. A. Ahmed and D. P. Giddens, "Velocity measurement in steady flow through axisymmetric stenosis at moderate Reynolds number," *J. Biomechanics*, vol. 16 (7), pp. 505–516, 1983.

[28] S. A. Ahmed and D. P. Giddens, "Flow disturbance measurements through a constricted tube at moderate Reynolds numbers," *J. Biomechanics*, vol. 16 (12), pp. 955–963, 1983.

[29] L. H. Back and E. J. Roschke, "Shear-layer flow regimes and wave instabilities and reattachment lengths downstream of an abrupt circular channel expansion," *J. Applied Mechanics*, vol. 39, pp. 677–681, 1972.

[30] S. A. Ahmed and D. P. Giddens, "Pulsatile poststenotic flow studies with Laser Doppler Anemometry," *J. Biomechanics*, vol. 17 (9), pp. 695–705, 1984.

[31] S. A. Ahmed, "An experimental investigation of pulsatile flow through a smooth constriction," *Exp. Therm. Fluid Sci.*, vol. 17, pp. 309–318, 1998.

[32] L. Back, Y. Cho, D. Crawford, and R. Cuffel, "Effect of mild atherosclerosis on flow resistance in a coronary artery casting of man," *ASME J. Biomech. Eng.*, vol. 106, pp. 48–53, 1984.

[33] D. L. Bruns, "A general theory of the cause of murmurs in the cardiovascular system," *American J. Medicine*, vol. 27, pp. 360–374, 1959.

[34] E. L. Yellin, "Hydraulic noise in submerged and bounded liquid jets," *Proceedings of ASME Biomedical Fluid mechanics Symposium*, pp. 209–221, 1966.

[35] R. S. Lees and C. F. Dewey, Jr., "Phonoangiography: a new noninvasive diagnostic method for studying arterial disease," *Procsedings of the National Academy of Science*, vol. 67(2), pp. 935–942, Oct. 1970.

[36] D. L. Fry, "Acute vascular endothelial changes associated with increased blood velocity gradients," *Circulation Res.*, vol. 22, pp. 165–197, 1968.

[37] S. P. Sutera and M. H. Mehrjardi, "Deformation and fragmentation of human red blood cells in turbulent flow," *Biophysical J.*, vol. 15, pp. 1–10, 1975.

[38] J. D. Folts, E. B. Crowell Jr., and G. G. Rowe, "Platelet aggregation in partially obstructed vessels and its elimination with aspirin," *Circulation*, vol. 54 (3), pp. 365–370, 1976.

[39] P. Stein, F. J. Walburn, and H. N. Sabbah, "Turbulent stresses in the region of aortic and pulmonary valves," *ASME J. Biomech. Eng.*, vol. 104 (3), pp. 238–244, 1982.

[40] M. H. Friedman, G. M. Hutchins, C. B. Bargeron, O. J. Deters, and F. Mark, "Correlation between intimal thickness and fluid shear in human arteries," *Atherosclerosis*, vol. 39, pp. 425–436, 1981.

[41] D. N. Ku, D. P. Giddens, C. K. Zarins, and S. Glagov, "Pulsatile flow and atherosclerosis in the human carotid bifurcation. Positive correlation between

plaque location and low oscillating shear stress," *Atherosclerosis*, vol. 5, pp. 293–302, 1985.

[42] T. A. Salam, A. B. Lumsden, W. D. Suggs, and D. N. Ku, "Low shear stress promotes intimal hyperplasia thickening," *J. Vasc. Invest.*, vol. 2 (1), pp. 12–22, 1996.

[43] X. He and D. N. Ku, "Pulsatile flow in the human left coronary artery bifurcation: average conditions," *ASME J. Biomech. Eng.*, vol. 118, pp. 74–82, 1996.

[44] B. M. Kim and W. H. Corcoran, "Experimental measurements of turbulence spectra distal to stenosis," *J. Biomechanics*, vol. 7 (4), pp. 335–342, 1974.

[45] C. Clark, "Turbulent velocity measurements in a model of aortic stenosis," *J. Biomechanics*, vol. 9, pp. 677–687, 1976.

[46] C. Clark, "Turbulent wall pressure measurements in a model of aortic stenosis," *J. Biomechanics*, vol. 10, pp. 461–472, 1977.

[47] P. C. Lu, D. R. Gross, and N. H. C. Hwang, "Intravascular pressure and velocity fluctuations in pulmonic arterial stenosis," *J. Biomechanics*, vol. 13 (3), pp. 291–300, 1980.

[48] P. C. Lu, C. N. Hui, and N. H. C. Hwang, "A model investigation of the velocity and pressure spectra in vascular murmurs," *J. Biomechanics*, vol. 16 (11), pp. 923–931, 1983.

[49] R. J. Tobin and I.-D. Chang, "Wall pressure spectra scaling downstream of stenoses in steady tube flow," *J. Biomechanics*, vol. 9 (10), pp. 633–640, 1976.

[50] D. P. Giddens, R. F. Mabon, and R. A. Cassanova, "Measurements of disordered flows distal to subtotal vascular stenoses in the thoracic aortas of dogs," *Circulation Research*, vol. 39, pp. 112–119, 1976.

[51] S. A. Jones and A. Fronek, "Analysis of break frequencies downstream of a constriction in a cylindrical tube," *J. Biomechanics*, vol. 20 (3), pp. 319–327, 1987.

[52] J. S. Lee and Y. C. Fung, "Flow in locally constricted tubes at low Reynolds numbers," *J. Applied Mechanics*, vol. 37, pp. 9–16, 1970.

[53] M. D. Deshpande, D. P. Giddens, and R. F. Mabon, "Steady laminar flow through modelled vascular stenoses," *J. Biomechanics*, vol. 9 (4), pp. 165–174, 1976.

[54] L. C. Cheng, M. E. Clark, and J. M. Robertson, "Numerical calculations of oscillating flow in the vicinity of square wall obstacles in plane conduits," *J. Biomechanics*, vol. 5, pp. 467–484, 1972.

[55] B. J. Daly, "A numerical study of pulsatile flow through stenosed canine femoral arteries," *J. Biomechanics*, vol. 9 (7), pp. 465–475, 1976.

[56] V. O'Brien and L. W. Ehrlich, "I. Simple pulsatile flow in an artery with a constriction," *J. Biomechanics*, vol. 18 (2), pp. 117–127, 1985.

[57] S. Cavalcanti, "Hemodynamics of an artery with mild stenoses," *J. Biomechanics*, vol. 28 (4), pp. 387–399, 1995.

[58] G. R. Zendehbudi and M. S. Moayeri, "Comparison of physiological and simple pulsatile flows through stenosed arteries," *J. Biomechanics*, vol. 32 (9), pp. 959–965, 1999.

[59] P. F. Marques, M. E. C. Oliveira, A. S. Franca, and M. Pinotti, "Modeling and simulation of pulsatile blood flow with a physiologic wave pattern," *Artificial Organs*, vol. 27 (5), pp. 478–485, 2003.

[60] P. R.Johnston and D. Kilpatrick, "Mathematical modelling of flow through an irregular arterial stenosis," *J. Biomechanics*, vol. 24 (11), pp. 1069–1077, 1991.

[61] H. I. Andersson, R. Halden, and T. Glomsaker, "Effects of surface irregularities on flow resistance in differently shaped arterial stenoses," *J. Biomechanics*, vol. 33, pp. 1257–1262, 2000.

[62] A. Yakhot, L. Grinberg, and N. Nikitin, "Modeling rough stenoses by an immersed-boundary method," *J. Biomechanics*, vol. 38, pp. 1115–1127, 2005.

[63] S. Chakravarty, P. K. Mandal, and Sarifuddin, "Effects of surface irregularities on unsteady pulsatile flow in a compliant artery," *Int. J. Non-Linear Mechanics*, vol. 40, pp. 1268–1281, 2005.

[64] Sarifuddin, S. Chakravarty, P. K. Mandal, and G. C. Layek, "Numerical simulation of unsteady generalized newtonian blood flow through differently shaped distensible arterial stenoses," *J. Medical Engineering & Technology*, vol. 32 (5), pp. 385–399, 2008.

[65] M. C. Melaaen, "Analysis of fluid flow in constricted tubes and ducts using body-fitted non-staggered grids," *Int. J. Numer. Meth. Fluids*, vol. 15, pp. 895–923, 1991.

[66] C. Bertolotti and V. Deplano, "Three dimensional numerical simulations of flow through a stenosed coronary bypass," *J. Biomechanics*, vol. 33 (8), pp. 1011–1022, 2000.

[67] J. S. Stroud, S. A. Berger, and D. Saloner, "Influence of stenosis morphology on flow through severely stenotic vessels: implications for plaque rupture," *J. Biomechanics*, vol. 33, pp. 443–455, 2000.

[68] A. S. Dvinsky and M. Ojha, "Simulation of three-dimensional pulsatile flow through an asymmetric stenosis," *Med. Biol. Eng. Comput.*, vol. 32 (2), pp. 138–142, 1994.

[69] Q. Long, X. Y. Xu, K. V. Ramnarine, and P. R. Hoskins, "Numerical investigation of physiologically realistic pulsatile flow through arterial stenosis," *J. Biomechanics*, vol. 34, pp. 1229–1242, 2001.

[70] F. Ghalichi, X. Deng, A. De Champlain, Y. Douville, M. King, and R. Guidoin, "Low Reynolds number turbulence modeling of blood flow in arterial stenoses," *Biorheology*, vol. 35 (4-5), pp. 281–294, 1998.

[71] S. S. Varghese and S. H. Frankel, "Numerical Modeling of pulsatile turbulent flow in stenotic vessels," *ASME J. Biomech. Eng.*, vol. 125, pp. 445–460, 2003.

[72] T. S. Lee, W. Liao, and H. T. Low, "Numerical simulation of turbulent flow through series stenoses," *Int. J. Numer. Meth. Fluids*, vol. 42, pp. 717–740, 2003.

[73] T. S. Lee, W. Liao, and H. T. Low, "Numerical study of physiological turbulent flows through series arterial stenoses," *Int. J. Numer. Meth. Fluids*, vol. 46, pp. 315–344, 2004.

[74] M. X. Li, J. J. Beech-Brandt, L. R. John, P. R. Hoskins, and W. J. Easson, "Numerical Analysis of pulsatile blood flow and vessel wall mechanics in different degrees of stenoses," *J. Biomechanics*, vol. 40, pp. 3715–3724, 2007.

[75] A. Scotti and U. Piomelli, "Turbulent models in pulsating flows," *AIAA Journal*, vol. 40 (3), pp. 537–544, 2002.

[76] P. R. Spalart and S. R. Allmaras, "A one-equation turbulence model for aerodynamic flows," *La Recherche Aerospatiale*, vol. 1 (1), pp. 5–21, 1994.

[77] P. G. Saffman and D. C. Wilcox, "Turbulence-model predictions for turbulent boundary layers," *AIAA Journal*, vol. 12, pp. 541–546, 1974.

[78] P. A. Durbin, "Separated flow computations with the k-ϵ-v^2 model," *AIAA Journal*, vol. 33, pp. 659–664, 1995.

[79] J. Ryval, A. G. Straatman, and D. A. Steinman, "Two-equation turbulence modelling of pulsatile flow in a stenosed tube," *ASME J. Biomech. Eng.*, vol. 126, pp. 625–635, 2004.

[80] F. Mallinger and D. Drikakis, "Instability in three-dimensional, unsteady, stenotic flows," *Int. J. Heat and Fluid Flow*, vol. 23, pp. 657–663, 2002.

[81] F. Mallinger and D. Drikakis, "Laminar-to-turbulent transition in pulsatile flow through a stenosis," *Biorheology*, vol. 39, pp. 437–441, 2002.

[82] S. J. Sherwin and H. M. Blackburn, "Three-dimensional instabilities and transition of steady and pulsatile axisymmetric stenotic flows," *J. Fluid Mech.*, vol. 533, pp. 297–327, 2005.

[83] H. M. Blackburn and S. J. Sherwin, "Instability modes and transition of pulsatile stenotic flow: pulse-period dependence," *J. Fluid Mech.*, vol. 573, pp. 57–88, 2007.

[84] S. S. Varghese, S. H. Frankel, and P. F. Fischer, "Direct numerical simulation of stenotic flows. Part 2. Pulsatile flow," *J. Fluid Mech.*, vol. 582, pp. 281–318, 2007.

[85] S. S. Varghese, S. H. Frankel, and P. F. Fischer, "Modelling transition to turbulence in eccentric stenotic flows," *ASME J. Biomech. Eng.*, vol. 130, pp. 0 145 031–7, 2008.

[86] F. P. P. Tan, N. B. Wood, G. Tabor, and X. Y. Xu, "Comparison of les of steady transitional flow in an idealized stenosed axisymmetric artery model with a rans transitional model," *ASME J. Biomech. Eng.*, vol. 133, pp. 0 510 011–12, 2011.

[87] R. Mittal, S. P. Simmons, and H. S. Udaykumar, "Application of Large-eddy simulation to the study of pulsatile flow in a modelled arteria stenosis," *ASME J. Biomech. Eng.*, vol. 123, pp. 325–332, 2001.

[88] R. Mittal, S. P. Simmons, and F. Najjar, "Numerical study of pulsatile flow in a constricted channel," *J. Fluid Mech.*, vol. 485, pp. 337–378, 2003.

[89] O. R. Tutty, "Pulsatile flow in a constricted channel," *ASME J. Biomech. Eng.*, vol. 114, pp. 50–54, 1992.

[90] M. M. Molla, "Les of pulsatile flow in the models of arterial stenosis and aneurysm," PhD Dissertation, University of Glasgow, Department of Mechanical Engineering, May 2009.

[91] M. C. Paul, M. M. Molla, and G. Roditi, "Large-eddy simulation of pulsatile blood flow," *Medical Engineering & Physics*, vol. 31, p. 153159.

[92] M. M. Molla, M. C. Paul, and G. Roditi, "Les of additive and non-additive pulsatile flows in a model arterial stenosis," *Computer Methods in Biomechanics and Biomedical Engineering*, vol. 13 (1), pp. 105–120, 2010.

[93] M. C. Paul and M. M. Molla, "Investigation of physiological pulsatile flow in a model of arterial stenosis using large-eddy and direct numerical simulations," *Applied Mathematical Modelling*, vol. 36, pp. 4393–4413, 2012.

[94] R. Gårdhagen, J. Lantz, F. Carlsson, and M. Karlsson, "Quantifying turbulent wall shear stress in a stenosed pipe using large eddy simmulation," *ASME J. Biomech. Eng.*, vol. 132 (6), pp. 0 610 021–0 610 027, 2010.

[95] R. Gårdhagen, J. Lantz, F. Carlsson, and M. Karlsson, "Large eddy simmulation of stenotic flow for wall shear stress estimation - validation and application," *WSEAS Transactions on Biology and Biomedicine*, vol. 8 (3), pp. 86–99, 2011.

[96] T. J. Barber and A. Simmons, "Large eddy simulation of a stenosed artery using a femoral artery pulsatile flow profile," *Artificial Organs*, vol. 35 (7), pp. E155–E160, 2011.

[97] P. W. Scherer, "Flow in axisymmetrical glass model aneurysms," *J. Biomechanics*, vol. 6, pp. 695–700, 1973.

[98] C. J. Egelhoff, R. S. Budwig, D. F. Elger, T. A. Khraishi, and K. H. Johansen, "Model studies of the flow in abdominal aortic aneurysms during resting and exercise conditions," *J. Biomechanics*, vol. 32, pp. 1319–1329, 1999.

[99] A. V. Salsac, S. R. Sparks, J. M. Chomaz, and J. C. Lasheras, "Evolution of the wall shear stresses during the progressive enlargement of symmetric abdominal aortic aneurysms," *J. Fluid Mech.*, vol. 560, pp. 19–51, 2006.

[100] V. Deplano, Y. Knapp, E. Bertrand, and E. Gaillard, "Flow behaviour in an asymmetric compliant experimental model for abdominal aortic aneurysm," *J. Biomechanics*, vol. 40, pp. 2406–2413, 2007.

[101] S. O. Wille, "Finite element simulations of the pulsatile blood flow patterns in arterial abnormalities," R. H. Gallagher (Ed.) et al.., *Finite Elements in Biomechanics*,John Wiley, New York, pp. 39–60, 1982.

[102] K. Perktold, K. Gruber, T. Kenner, and H. Florian, "Calculation of pulsatile flow and particle paths in an aneurysm-model," *Basic Research in Cardiology*, vol. 79, pp. 253–261, 1984.

[103] K. Perktold, "On the paths of fluid particles in an axisymmetrical aneurysm," *J. Biomechanics*, vol. 20 (3), pp. 311–317, 1987.

[104] B. V. R. Kumar, "A space-time analysis of blood flow in a 3D vessel with multiple aneurysms," *Computation Mechanics*, vol. 32, pp. 16–28, 2003.

[105] B. Utter and J. S. Rossmann, "Numerical simulation of saccular aneurysm hemodynamics: Influence of morphology on rupture risk," *J. Biomechanics*, vol. 40, pp. 2716–2722, 2007.

[106] V. L. Rayz, L. Boussel, M. T. Lawton, G. Acevedo-Bolton, L. Ge, W. L. Young, R. T. Higashida, and D. Saloner, "Numerical modeling of the flow in intracranial aneurysms: prediction of regions prone to thrombus formation," *Annals of Biomedical Engineering*, vol. 36 (11), pp. 1793–1804, 2008.

[107] I. Chatziprodromou, A. Tricoli, D. Poulikakos, and Y. Ventikos, "Haemodynamics and wall remodelling of a growing cerebral aneurysm: A computational model," *J. Biomechanics*, vol. 40, pp. 412–426, 2007.

[108] A. A. Valencia, A. M. Guzmán, E. A. Finol, and C. H. Amon, "Blood flow dynamics in saccular aneurysm models of the basilar artery," *ASME J. Biomech. Eng.*, vol. 128, pp. 516–526, 2006.

[109] A. Valencia, H. Morales, R. Rivera, E. Bravo, and M. Galvez, "Blood flow dynamics in patient-specific cerebral aneurysm models: The relationship between wall shear stress and aneurysm area index," *Medical Engineering & Physics*, vol. 30, pp. 329–340, 2008.

[110] K. M. Khanafer, J. L. Bull, and R. Berguer, "Fluid-structure interaction of turbulent pulsatile flow within a flexible wall axisymmetric aortic aneurysm model," *European Journal of Mechanics B/Fluids*, vol. 28, pp. 88–102, 2009.

[111] M. D. Deshpande and D. P. Giddens, "Turbulence measurements in a constricted tube," *J. Fluid Mech.*, vol. 97, pp. 65–89, 1979.

[112] D. A. McDonald, "The relation of pulsatile pressure to flow in arteries," *J. Physiology*, vol. 127, pp. 533–552, 1955.

[113] S. K. Lam, G. S. K. Fung, S. W. K. Cheng, and K. W. Chow, "A computational study on the biomechanical factors related to stent-graft models in the thoracic aorta," *Med Biol Eng Comput*, vol. 46, pp. 1129–1138, 2008.

[114] R. M. Nerem, "Vascular fluid mechanics, the arterial wall, and atherosclerosis," *ASME J. Biomechanical Engineering*, vol. 114 (3), pp. 274–282, 1992.

[115] M. Germano, U. Piomelli, and W. Cabot, "A dynamic subgrid-scale eddy viscosity model," *Physics of Fluids A*, vol. 3 (7), pp. 1760–1765, 1991.

[116] D. K. Lilly, "A Proposed Modification of the Germano Subgrid-Scale Closure Method," *Physics of Fluids A*, vol. 4 (3), pp. 633–635, 1992.

[117] T. J. Pedley, *The fluid mechanics of large blood vessels*. Cambridge University Press, 1980.

[118] Y. C. Fung, *Biomechanics: Circulation*, 2nd ed. Springer, 1997.

[119] D. C. Wilcox, *Turbulence modelling for CFD*. La Cãnada, California: DCW Industries, 2002.

[120] F. R. Menter, "Two-equation eddy-viscosity turbulence models for engineering applications," *AIAA J.*, vol. 32 (8), pp. 1598–1605, 1994.

[121] A. Leonard, "Energy cascade in Large-Eddy Simulations of turbulent fluid flows," *Adv. Geophys.*, vol. 18A, pp. 237–248, 1974.

[122] J. Smagorinsky, "General circulation experiment with the primitive equations. i. the basic experiment," *Monthly Weather Rev.*, vol. 91, pp. 99–164, 1963.

[123] S. E. Kim, "Large eddy simmulation using unstructured meshes and dynamic subgrid-scale turbulence models," AIAA paper 2004-2548, Tech. Rep., Jun. 2004, (34th Fluid Dynamics Conference and Exhibit).

[124] G. Erlebacher, M. Y. Hussaini, C. G. Speziale, and T. A. Zang, "Toward the large-eddy simulation of compressible turbulent flows," *J. Fluid Mech.*, vol. 238, pp. 155–185, 1992.

[125] *Fluent 6.3: User's Guide*, Fluent Inc., Sep. 2006.

[126] J. P. Vandoormaal and G. D. Raithby, "Enhancements of the simple method for predicting incompressible fluid flows," *Numer. Heat Transfer*, vol. 7, pp. 147–163, 1984.

[127] R. I. Issa, "Solution of implicitly discretized fluid flow equations by operator splitting," *J. Computational Physics*, vol. 62, pp. 40–65, 1986.

[128] C. M. Rhie and W. L. Chow, "Numerical study of the turbulent flow past an airfoil with trailing edge separation," *AIAA Journal*, vol. 21 (11), pp. 1525–1532, 1983.

[129] B. B. Lieber and D. P. Giddens, "Post-stenotic core flow behavior in pulsatile flow and its effects on wall shear stress," *J. Biomechanics*, vol. 23 (6), pp. 597–605, 1990.

[130] *MATLAB: The Language of Technical Computing*, The Mathworks Inc., Feb. 2008, (Release 7.6).

[131] J. R. Womersley, "Method for the calculation of velocity, rate of flow and viscous drag in arteries when the pressure gradient is known," *J. Physiology*, vol. 127, pp. 553–563, 1955.

[132] K. B. Chandran, *Cardiovascular Biomechanics*. New York University Press, 1992.

[133] N. W. McLachlan, *Bessel Functions for Engineers*, 2nd ed. Clarendon Press, 1955.

[134] H. Choi and P. Moin, "Effect of the computational time step on numerical solutions of turbulent flow," *J. Computational Physics*, vol. 111, pp. 1–4, 1994.

[135] D. L. P. Ask, B. Hok and H. Terio, "Bio-acoustic signals from stenotic tube flow: state of the art and perspectives for future methodological development," *Med. Bio. Engn. Comput.*, pp. 669–675, 1995.

[136] H. Tennekes and J. L. Lumley, *A first course in turbulence*. The MIT press, 1972.

[137] J. O. Hinze, *Turbulence*. McGraw-Hill, 1975.

[138] D. R. Gross, P. C. Lu, K. T. Dodd, and N. H. Hwang, "Physical characteristics of pulmonary artery stenosis murmurs in claves," *Am. J. Physiol.- Heart Circ. Physiol.*, vol. 238 (6), pp. H876–H885, 1980.

[139] N. F. Kassell, J. C. Torner, E. C. Haley Jr., J. A. Jane, H. P. Adams, and G. L. Kongable, "The international cooperative study on the timing of aneurysm surgery. Part 1: Overall management results," *J. Neurosurgery*, vol. 73 (1), pp. 18–36, 1990.

[140] F. Pico, J. Labreuche, I. Gourfinkel-An, and P. Amarenco, "Basilar artery diameter and 5-year mortality in patients with stroke," *Stroke*, vol. 37, pp. 2342–2347, 2006.

[141] P. Neofytou, S. Tsangaris, and M. Kyriakidis, "Vascular wall flow-induced forces in a progressively enlarged aneurysm model," *Computer Methods in Biomechanics and Biomedical Engineering*, vol. 11 (6), pp. 612–626, 2008.

[142] A. V. Salsac, S. R. Sparks, and J. C. Lasheras, "Hemodynamic changes occurring during the progressive enlargement of abdominal aortic aneurysm," *Annals Vascular Surgery*, vol. 18 (1), pp. 14–21, 2004.

[143] C. Liang and G. Papadakis, "Large eddy simulation of pulsatile flow over a circular cylinder at subcritical Reynolds number," *Computers and Fluids*, vol. 36, pp. 299–312, 2007.